University of Alberta

Homogeneity of Metal Matrix Composites Deposited by Plasma Transferred Arc Welding

by

Tonya Brett Bunton Wolfe

A thesis submitted to the Faculty of Graduate Studies and Research
in partial fulfillment of the requirements for the degree of

Doctor of Philosophy

in

Materials Engineering

Department of Chemical and Materials Engineering

Spring 2010
Edmonton, Alberta

Examining Committee

Dr. Hani Henein, Chemical and Materials Engineering

Dr. Adrian Gerlich, Chemical and Materials Engineering

Dr. Anthony Yeung, Chemical and Materials Engineering

Dr. Andre McDonald, Mechanical Engineering

Dr. Ravi Ravindran, Mechanical and Industrial Engineering, Ryerson University

To all the mothers in non-traditional careers…

Yes, We Can!

Abstract

Tungsten carbide-based metal matrix composite coatings are deposited by PTAW (Plasma Transferred Arc Welding) on production critical components in oil sands mining. Homogeneous distribution of the reinforcement particles is desirable for optimal wear resistance in order to reduce unplanned maintenance shutdowns. The homogeneity of the coating can be improved by controlling the heat transfer, solidification rate of the process and the volume fraction of carbide.

The degree of settling of the particles in the deposit was quantified using image analysis. The volume fraction of carbide was the most significant factor in obtaining a homogeneous coating. Lowering the current made a modest improvement in homogeneity. Changes made in other operational parameters did not effect significant changes in homogeneity.

Infrared thermography was used to measure the temperature of the surface of the deposit during the welding process. The emissivity of the materials was required to acquire true temperature readings. The emissivity of the deposit was measured using laser reflectometry and was found to decrease from 0.8 to 0.2 as the temperature increased from 900°C to 1200°C. A correction algorithm was applied to calculate the actual temperature of the surface of the deposit. The corrected temperature did increase as the heat input of the weld increased.

A one dimensional mathematical model of the settling profile and solidification of the coatings was developed. The model considers convective and radiative heat input from the plasma, the build-up of the deposit, solidification of the deposit and the settling of the WC particles within the deposit. The model had very good agreement with the experimental results of the homogeneity of the carbide as a function of depth. This fundamental model was able to accurately predict the particle homogeneity of an MMC deposited by an extremely complicated process. It was shown that the most important variable leading to a homogeneous coating is to operate at the packing saturation limit of the reinforcement. In the case of the MMC explored, a fully homogeneous coating was obtained with 50 vol% WC in a NiCrBSi matrix.

Acknowledgments

This thesis is dedicated to my husband, Daniel. Without you, I wouldn't have started this program and I certainly would not have finished it. You really were the foundation of this work. This degree is half yours.

To my loving children Max and Ripley, who were both born within the timeframe of this thesis – here is irrefutable proof that I really do know something when you state, "Mom, you don't know anything!". I'm looking forward to finally being a real mom and I promise to make you lots of cookies and eat them in our playforts.

To my parents, who always wished I would become a doctor. Oh well, close enough.

To the members of AMPL and CME who have all found much more delicious pastures, thank you for your friendship and support – Arvind, Errol, Elliot, Junfang, Joel, Larissa, Heather, Matt, Christine and Preston.

To Syncrude for your support, both financially and otherwise – Stefano Chiovelli, Shane Hoskins, Mike Anderson, Tim Revega, thank you for prioritizing my work and making me feel part of the team. A sincere thanks to Lillian Darichuk and Robert Skwarok who provided me countless hours of their time and whose dedication and expertise is directly shown in the results section of this thesis.

Thank you to the Advanced Materials Group at Alberta Research Council (Alberta Innovates – Technology Futures). Your patience and support while I completed this degree were invaluable. I appreciate all the resources you allocated, especially in obtaining XRD scans of the materials quickly.

Thank you to NETZCHE for completing the calorimetric work.

And finally, a heartfelt thank you to Hani Henein. We certainly did become friends during this journey and I thank you for all your mentorship. I hope you gained as much from this as I did.

Table of Contents

Table of Figures

List of Tables

List of Symbols

Upper Case Letters

C – factor to concentrate arc heat input
C_A – added mass coefficient
C_D – drag coefficient
D – container size (m)
H – plasma enthalpy (J/kg)
F – forces acting on sphere (N)
I – current (A)
J_a – anode current density (A/m^2)
L – length (m)
M – radiative energy (W/m^2)
R – gas constant (J/mol K)
T – temperature (K)
U – instantaneous velocity of particle (m/s)
U_o – terminal velocity of the particle (m/s)
U_h – hindered settling velocity of particles (m/s)
Q – heat input (W/m^2)
Q" – internal heat generation (W/m^3)
W – molecular weight
V – voltage (V)
Bi – Biot number
Re – Reynolds number
Pe – Peclet number
Pr – Prandtl number
Nu – Nusselt number

Lower Case Letters

a – thermal accommodation coefficient (0.8)
b - Wien displacement constant (2.897×10^{-3} m K)
c – speed of light (m/s)
c_p – heat capacity (J/kg)
d – diameter of the particle (m)
f_l – fraction of liquid
e – electron charge (C)
g – gravitational acceleration (m/s^2)
h - heat transfer coefficient (W/m^2 K)
h_P – Planck's constant (6.626×10^{-34} J s)
k – thermal conductivity (W/m K)
k_B – Boltzmann constant (1.38×10^{-24} J/K)
m – mass (kg)
n – ratio of specific surfaces

r – radius (m)
t – time (s)
x – direction ordinate
y – direction ordinate
z – direction ordinate

Greek Letters

α – thermal diffusivity (m^2/s)
β – Richardson-Zaki exponent for hindered settling
ρ – density (kg/m^3)
μ – viscosity of the liquid (kg/ms)
θ – concentration of particles
Λ – latent heat (J/kg)
γ – ratio of densities (ρ_p/ ρ_l)
λ – wavelength (m)
ω - magnetic permeability (H/m)
χ – specific heat ratio of plasma gas
ν – travel speed (m/s)
η – welding efficiency
ψ – sphericity
Φ – work function (V)
υ – kinematic viscosity (kg/s m)
σ – Stefan-Boltzmann constant (5.67×10^{-8} $w/m^2 K^4$)
ε – emissivity

Subscript

a - anode
b – boundary layer
c - convection
e - electron
f – gas fluid
i - initial
l/L – liquid
p – particle
r - radiation
s - surface
sub – substrate
w – near the vicinity of the particle surface

1 Introduction

1.1 The Need for a Durable Wear Resistant Coating

The mining and oil & gas sectors in Canada spend approximately $2.5 billion per year on damage caused by wear [NRC1987]. There are three general methods that are used to extend component life in oil sands mining operations. The first is to change the base material of the component to an abrasion resistant steel. The second option is to overlay the component with chrome-iron or chrome-carbide overlays. The final option is to use tungsten carbide overlays. Each individual material upgrade can increase the component life by three to ten times.

If the process flow of a typical 100 000 barrel/day oil sands production train is interrupted, the down time costs are approximately $3-6M/day [HOS2008]. If a component that experiences a high degree of wear is part of a production critical stream, there is a huge incentive to improve the material's wear resistance. In such environments, the best solution to extend the component life is to apply a tungsten carbide based composite coating onto a substrate by plasma transferred arc welding (PTAW). The coating is a metal-matrix composite (MMC): a combination of a hard ceramic particulate reinforcement and a tough corrosion- and wear-resistant metal alloy. The matrix and reinforcement particles are initially in powder form and are injected into and melted by a moving plasma torch. They solidify on a metal substrate to form a layer of thick MMC coating.

Examples of critical components are teeth on crusher rolls, shovel buckets or cyclofeeder sieve cloths, shown in Figure 1.1. The MMC which has shown the best wear resistance in this application has been a NiCrBSi matrix with 65 wt% monolithic WC reinforcement particle deposited by PTAW. The total cost of these powders in service is approximately $100/kg, where 30% of the price of the coating is due to the MMC powder itself and 70% is due to the machine

equipment and operator time. This does not include the cost of the parts themselves.

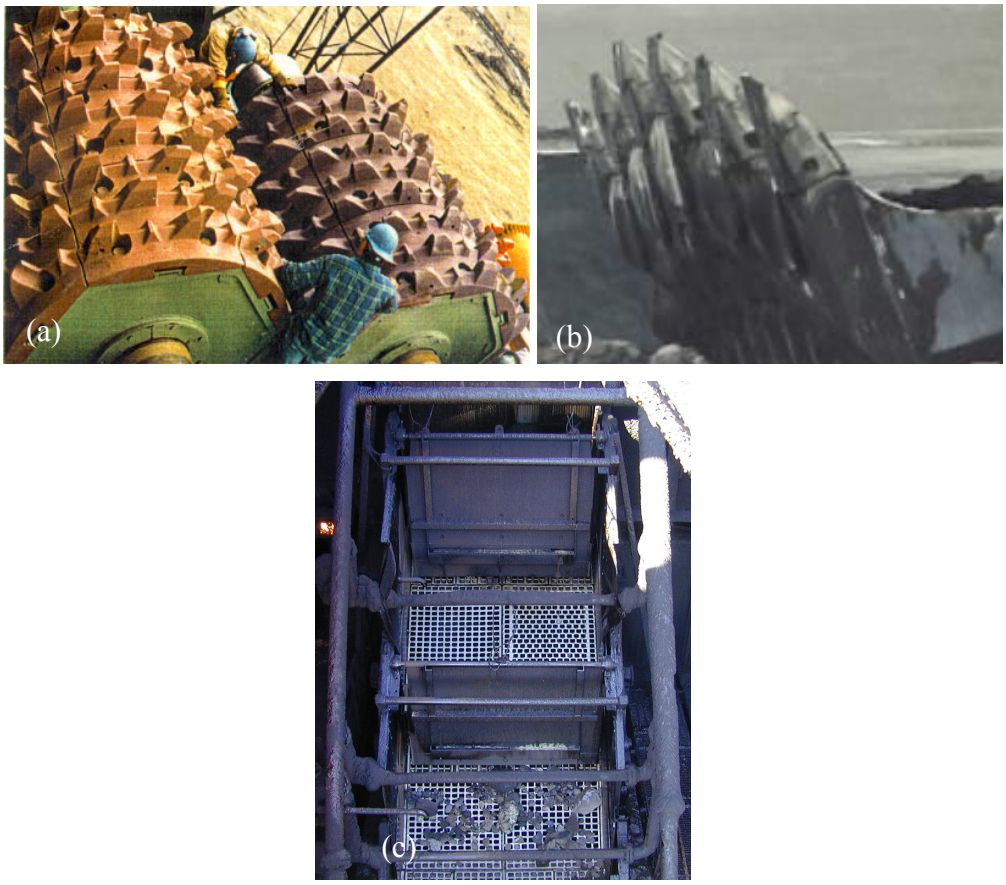

Figure 1.1: Examples of oil sands mining components that require tungsten carbide based wear resistant coatings – (a) the crusher teeth on a rotating digging wheel, (b) the shovel teeth on the end of a bucket and (c) cyclofeeder sieves, courtesy of Syncrude Canada, Inc.

The coating life is unfortunately shorter than expected, as it either spalls off or wears prematurely, such that the unplanned shut down costs to replace critical components in the plant are very high. Homogeneity of the reinforcement particles within the coating is believed to be the main contributing factor to premature equipment failure.

1.2 Plasma Transferred Arc Welding

The overlay is formed by depositing a metal powder, which passes through a nozzle into a plasma, onto the component substrate. The plasma heats the

particles to very high temperatures and a metallurgical bond is formed between the coating and substrate. The torch moves over the workpiece to cover the substrate with the coating in a variety of patterns. A schematic of the process is shown in Figure 1.2a. In PTAW, there are three gas inlets, shown in Figure 1.2b: the plasma gas, the shielding gas and the carrier gas. The gases used are inert (such as argon) and are chosen based on their ionization potentials. The plasma gas provides the self-sustaining welding arc. The shielding gas protects the arc and molten coating from air entrainment and the carrier gas transports the powder from the hopper to the nozzle. The coating thickness for one pass can be between 2-10 mm. The result is a homogeneous dispersion of hard ceramic in a metal matrix, which has very good wear properties.

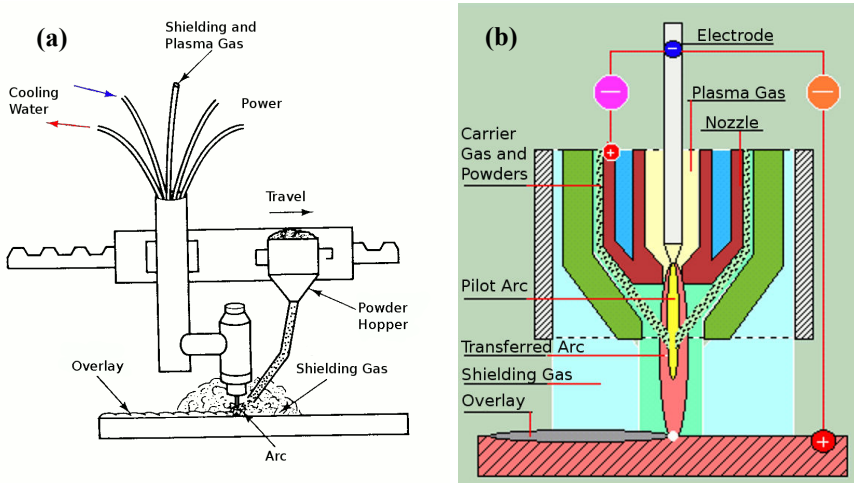

Figure 1.2: (a) Schematic of Plasma Transferred Arc Welding [modified from BUD1988] and (b) detailed view of torch depicting gas and powder inlets [modified from PLA2005].

A selection of the myriad operating variables that must be optimized in order to obtain a good PTA weld are: current, voltage, plasma gas flow rate, torch travel speeds, gas composition, substrate material, nozzle configuration, powder gas flow, stand-off distance, and electrode configuration. A typical NiCrBSi-WC MMC coating will be successfully deposited under the conditions listed in Table 1.

Table 1: Typical deposition conditions for NiCrBSi-WC applied by PTAW.

Parameter	*Range*
Current (A)	120-180
Voltage (V)	20-25
Travel Speed (mm/s)	3.81
Plasma Gas Flow (lpm)	2-2.5
Shielding Gas Flow (lpm)	9-11
Carrier Gas Flow (lpm)	1.4

1.3 Project Rationale

The PTAW process is complex: the effect of operating variables on the coating life differs for every application and is time consuming and costly to understand. A desirable coating consists of the following deliverables: high toughness, high abrasion resistance, and homogeneity of reinforcement particles throughout the thickness. The coatings are applied multiple times in order to increase the in-service time of the component. However, as the number of layers increases, the tendency for spalling and cracking of the coating also increases. An understanding of the effect of slower cooling rates experienced by multi-pass coatings on the particle settling and phase distribution may lead to the cause of premature coating failure.

The hard phases developed during solidification of the molten metal powders ultimately determine the toughness and contribute to the hardness of the coating. The powders are exposed to very high temperatures in the plasma, which are very difficult to measure. An analysis of the phases present in the coating can give insight to the temperatures the particles are exposed to, the hardness and wear resistance of the coating and an understanding of the solidification of the coating. This information assists in order to optimize the wear resistance through operational and powder chemistry modifications.

This project will only address control of homogeneity of the coatings. In this thesis, good homogeneity means that the volume fraction of reinforcement

particle is similar through the thickness of the coating. The homogeneity of the coating can be improved by controlling the heat transfer and solidification rate of the process. An investigation into the solidification of the coating and settling of the reinforcement particles will give insight to those operating parameters which contribute to poor coating performance. The real temperature of the substrate and coating will be measured using non-contact methods by acquiring infrared thermographic images of the process. The settling of the particles in the MMC will be quantified using image analysis to identify the parameters that lead to a homogeneous coating.

1.4 Thesis Overview

In Chapter 2, the literature on arc welding, including plasma transferred arc welding, as well as the development of wear resistant coatings, the settling of metal matrix composites and experimental benchmarks on infrared thermal measurements of welding are presented.

The experimental methods used to quantify the homogeneity of the MMC coating and to capture the temperatures attained by the deposit during the process both qualitatively and quantitatively are conveyed in Chapter 3. The results are discussed in Chapter 4.

The modeling efforts to understand the solidification of the coating and settling of the WC particles are presented in Chapter 5. The operating conditions predicated by the model that obtained a more homogeneous coating are presented in Chapter 6.

The conclusions of this body of work and proposed future work are summarized in Chapter 7.

2 Literature Review

As mentioned in the previous chapter, the particle homogeneity in a metal matrix composite (MMC) coating is critical for improving wear resistance. The coatings are deposited by plasma transferred arc welding (PTAW) onto mining equipment that in service experiences a high degree of abrasive wear. In order to predict the operating conditions which yield improvements in coating homogeneity, an understanding of welding and PTAW as well as wear resistant coatings and materials selection, is required.

This chapter reviews the relevant literature leading up to the development and experimental verification of a model which will predict conditions resulting in improvements in coating homogeneity. Since a portion of the model is verified using infrared thermography, a review of infrared theory and uses of thermography in welding is included.

2.1 Wear Resistant Coatings: Deposition

Wear is a form of material degradation, usually physical in nature. The material is removed by one or a combination of several mechanisms in mining applications [MCK1997], as briefly discussed:

- **Abrasion** – occurs when two surfaces are in contact with each other by sliding. A series of grooves is formed in the softer material due to the wear particles originating from the harder material or the environment. A combination of hardness and toughness are critical to coating longevity.
- **Impact** – occurs when the surface is repeatedly stressed by an intense mass. Material toughness will extend the life of the component.
- **Erosion** – occurs when a continuous stream of particles is inundated on the material surface. Low angle particle erosion is similar to low stress abrasion. Slurry erosion is a combination of low-stress abrasion and

liquid flow and in order to resist liquid flow, a tenacious stable oxide is required.

- **Corrosion** – occurs when sliding between two materials is introduced to a corrosive environment. Corrosion acts to accelerate material degradation by several means such as pitting and stress-corrosion cracking. Erosion and corrosion are usually coupled.

In order to improve the in-service time of mining components, a wear-resistant coating is applied. Hardfacing is a technique that involves the application of materials that have superior properties than those of the substrate to which it is applied. These coatings are applied in industrial applications exposed to high wear such as mining equipment, blades and edges.

2.1.1 Methods of Deposition

Several techniques are currently being used industrially to deposit a tough, wear resistant coating onto the components which are prone to high wear rates. The techniques predominantly used are:

- Thermal spraying;
- Laser cladding;
- Plasma transferred arc welding (PTAW).

These techniques are being utilized because the power densities of these processes in the weld region are from 10^7 to 10^{12} W/m^2; whereas conventional welding processes are between 10^4 and 10^5 W/m^2 [RAV2001].

Thermal spraying of the coatings is carried out by igniting a gas through a torch which produces a high temperature high velocity fluid. The material can initially be in powder or wire form. The very high kinetic energy of particles striking the substrate surface do not require the particles to be fully molten to form high quality coatings. Since the heat input is typically low, most substrates can easily accept the application without a loss to its original properties. However, a

mechanical bond is obtained, whose strength is significantly lower than the metallurgical bond produced in PTAW. In addition, the coatings thicknesses are limited to about 2.5 mm.

Distinct differences in microstructure between the PTA coating and the spray and fused coating were observed [KIM1999]. The carbides and borides in the spray and fused deposition are finer than from PTA deposition and are needle shaped, which is due to the higher solidification rate. However, porosities in the spray and fused coating are present in the vicinity of the interface and have been shown to have detrimental effects in corrosion resistance.

High Velocity Oxy-Fuel (HVOF) thermal spray coatings tend to erode quickly [KRE1998] due to the inherent microstructural features present in HVOF coatings, such as pores, micro cracks and oxide layers at the splat interface. The formation and propagation of fatigue cracks initiate cavitation erosion in HVOF coatings as crack growth is enhanced by the presence of pores and brittle phases.

Laser cladding has gained some popularity in the application of hardfacing coatings due to the high power density of the laser resulting in rapid localized heating and cooling. However, the equipment is expensive and the rate of deposition is slow since the bead width is small.

Both laser cladding and PTA welding provide a melt pool having convection streams and usually 100% melting of the powder [OBE1992]. Very smooth surfaces were produced, and further improvement in smoothness was obtained by subsequent remelting using a laser without powder injection and shorter beam-substrate interaction times. In addition, laser remelting the surface and subsequent rapid solification led to an overlay with high hardness which was partly amorphous.

Plasma transferred arc welding is very popular in industrial applications. The following sections discuss the welding process and PTAW in depth.

2.2 Arc Welding

The process of welding is defined by the American Welding Society as the joining of materials by the application of heat with or without adding pressure, or by pressure alone, and with or without the use of filler material [JEN2001]. Welding processes are categorized according to the mode of energy transfer. Table 2.1 lists many of the groups and processes, along with their short form designation.

Table 2.1: A selection of AWS processes and designations [PAT1998]

Group	*Welding Process*	*Short Form Designate*
Arc welding	Carbon Arc	CAW
	Flux Cored Arc	FCAW
	Gas Metal Arc	GMAW
	Gas Tungsten Arc	GTAW
	Plasma Arc	PAW
	Shielded Metal Arc	SMAW
	Submerged Arc	SAW
Brazing	Diffusion Brazing	DFB
	Dip Brazing	DB
Oxyfuel Gas Welding	Oxyacetylene Welding	OAW
Resistance Welding	High Frequency Resistance	HFRW
	Projection Welding	RPW
	Resistance-Seam Welding	RSEW
	Resistance-Spot Welding	RSW
	Upset Welding	UW
Solid State Welding	Diffusion Welding	DFW
	Explosion Welding	EXW
	Forge Welding	FOW
	Friction Welding	FRW
	Hot Pressure Welding	HPW
	Ultrasonic Welding	USW
Other Welding Processes	Electron Beam	EBW
	Electroslag	ESW
	Induction	IW
	Laser Beam	LBW
	Thermit	TW

There are indeed many unique welding processes; however, arc welding is the most prominent method used to join metals. The heat source is generated by an arc which melts the filler and the base metals to form a fusion weld. The arc is a conductive plasma, self-sustained between an anode and cathode that carries high currents at low voltages.

2.2.1 Arc Physics and Plasmas

A plasma is an electrically conductive ionized gas that has a high enthalpy content. Shown in Figure 2.1, the plasma is constrained between an anode and cathode and is typically bell-shaped.

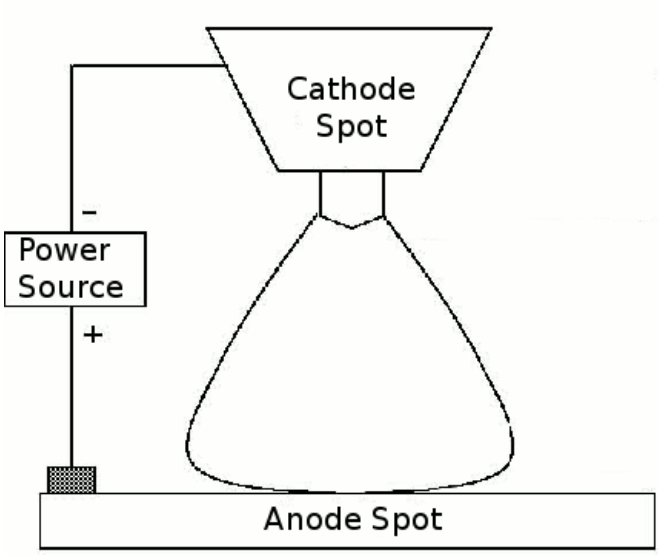

Figure 2.1: Schematic of welding arc [modified from YAR2005]

The plasma arc is self-sustaining, due to a voltage drop between the electrode and the substrate [MIL1968], described as follows. Electrons are emitted at the electrode by thermionic emission, which is a result of joule heating of the cathode due to the applied current [KEY1993]. This occurs when the electron energy at the cathode tip exceeds the work function, defined as the energy required to remove an electron from an atom.

Ionization of the gas occurs by transfer of kinetic energy from the electrons to the gas molecules. Ions are attracted towards the cathode, and upon impact at the cathode, release energy to maintain thermionic temperatures required to generate more electrons. The electrons are accelerated by the potential gradients of the arc column and anode fall space towards the anode spot. This high concentration of electrons results in intense heating resulting in a weld pool of molten metal [MIL1960].

This explanation of the arc initiation process applies only to the direct current electrode negative processes, where the tungsten electrode is the cathode. Electrodes most often emitted from tungsten due to their favourable work function, but commonly are doped with thoria (2.2 wt% ThO_2), zirconia (0.4 wt% ZrO_2), or ceria (3.0 wt% CeO_2), to lower the work function in order to achieve thermionic emission at lower temperatures and avoid melting the cathode tip [JEN2001].

Generally, plasmas are not stable and very turbulent, but by applying boundary conditions, such as a nozzle, result in laminar and self-stabilizing behaviour. The nozzle acts to constrict the arc column, which results in uniform electron convection thus defining the path of the plasma [MIL1968]. The axial flow of the gas is laminar and the colder gas which surrounds the hot core also acts to constrict and lengthen the arc. The gases must be properly metered in order to supply a constant flow rate to stabilize the plasma.

Argon gas is the most common gas used in arc welding as it is inert and the lower voltage drops needed to sustain the plasma arc are preferred. Higher arc voltages are required for diatomic gases such as H_2, but these gases also have higher enthalpies and thus, have higher temperatures. As the thermal conductivity of the gas decreases, the arc column narrows and the temperature of the arc increases. Other gases such as helium, nitrogen, hydrogen, and carbon dioxide are

sometimes added to the argon to modify the heat of the arc and the fluidity of the weld pool [HIC1991].

Key to understanding arc plasmas is the development of plasma jets. These are formed by changes in current density between the cathode and anode. A radial electromagnetic Lorentz force is generated due to the variations in magnetic field intensity produced by the welding current [MIL1960]. As current density increases, the compressive force increases, which results in a change in pressure along the length of the arc [MIL1968]. The net result is an axial pressure drop from the cathode to the anode that accelerates electrons and ions. The formation of plasma jets becomes very important in PTAW, where the constriction of the nozzle causes the formation of high velocity plasma jets and results in a high amount of convective heat transfer towards the anode.

2.3 Plasma Transferred Arc Welding (PTAW)

This thesis concentrates solely on plasma transferred arc welding. Plasma arc welding is defined as an arc welding process that joins metals by heating them with a constricted arc between an electrode and the work piece (transferred arc) or the electrode and the constricting nozzle (non-transferred arc).

The high velocity-high temperature plasma arc created by PTAW allows for a variety of applications such as welding, cutting, surfacing and spraying. PTAW can be operated by two methods: melt-in or keyhole. In melt-in, the plasma melts the surface to some depth and is similar to gas tungsten arc welding (GTAW). Keyhole mode forces the plasma arc to pass completely through the workpiece to produce a fully penetrated weld. The arc moves over the surface and the hole solidifies behind the arc.

A schematic comparing the GTAW and PTAW processes in shown in Figure 2.2. PTAW and GTAW are similar in that they are both free burning plasma arcs

initiated by a tungsten electrode and an ionizing gas such as argon. The difference lies in the energy density of the two plasma arcs. Since the arc in PTAW is significantly constricted due the presence of the nozzle and the electrode tip is positioned inside the nozzle rather than outside like in GTAW, the energy density is 10 times greater [PIN1973]. The shape of the arc in PTAW is more columnar than the traditional GTAW bell shaped plasma, which leads to the increase in energy density and improved arc stability. In industrial gains, this allows for higher welding speeds.

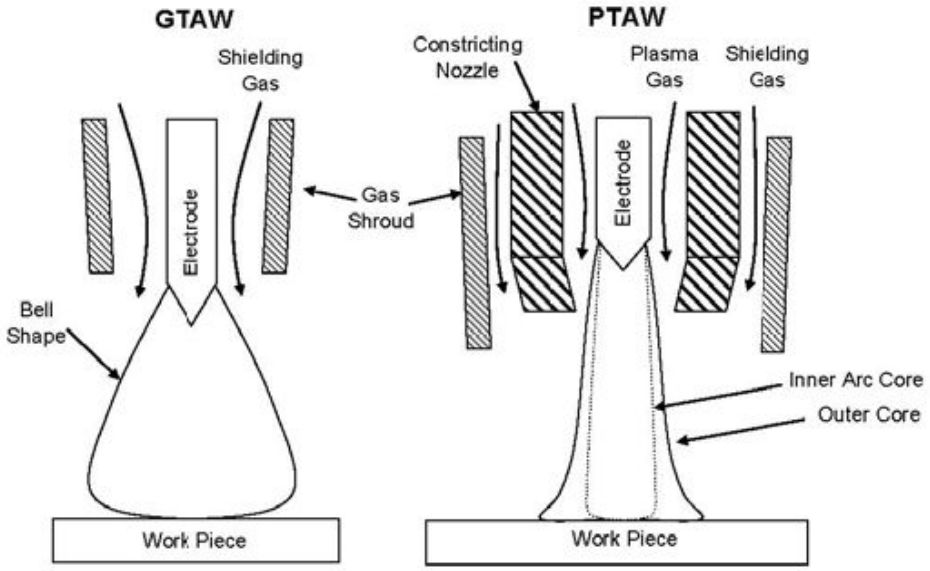

Figure 2.2: Schematic comparing GTAW and PTAW. Note the differences in plasma shape due to the constricting nozzle [YAR2005].

2.3.1 Process

A schematic of the PTAW process for depositing a coating is shown in Figure 1.2a/b. In PTAW, there are three gas inlets: the plasma gas, the shielding gas and the carrier gas.

The general operating sequence for PTAW is as follows:

1. A pilot arc is initiated between the electrode (cathode) and the substrate (anode).
2. The argon plasma gas passes through the nozzle between the cathode and anode and is ionized.

3. The ionized argon gas sustains a current path for the transferred arc between the electrode and the substrate.
4. The powder alloy is transported from the hopper and through the torch by a carrier gas, where it exits from multiple orifices at the nozzle. It intersects the plasma arc and is heated and accelerated to the substrate surface.
5. A molten weld puddle is formed on the substrate surface, protected from oxidation by a curtain of argon shielding gas. The torch moves over the workpiece to cover the substrate in a variety of patterns with the molten alloy.
6. The molten alloy solidifies on the surface of the substrate. As a result of the metallurgical bonding achieved between the coating and substrate in PTAW, there is excellent coating-substrate adhesion. The coating thickness for one pass can be between 2-10 mm. The amount of dilution between the coating and substrate in PTAW is usually less than 5%.

The result is a homogeneous dispersion of hard ceramic in a metal matrix, which has very good wear properties. The deposition rate is 2-10 kg/hr, which is higher than all other welding processes, with the exception of submerged arc welding, and is economic for industrial applications. The disadvantage to this method is the high cost of both the equipment and the specialty powders.

2.3.2 Process Parameters and Welding Output

The operating parameters in PTAW are numerous: current, voltage/stand-off distance, plasma gas flow rate, torch travel speeds, gas composition, substrate material, nozzle configuration, carrier gas flow, shielding gas flow rate, alloy composition and electrode configuration. Every coating has a different set of operating parameters that are determined experimentally, which contribute to an optimal coating. Superior coatings are characterized by low dilution, no porosity, smooth surface, and uniform distribution of reinforcement particles.

The following sections highlight various studies regarding the important factors which contribute to an ideal weld using PTAW.

2.3.2.1 Current

Arc current is one of the primary components in the heat input of the plasma arc. Increasing arc current adds more heat into the process and raises the temperature of both the coating overlay and the substrate. At very high currents, the smaller powder particles may be vaporized [BAB1986]. At lower currents, insufficient heat is produced to melt the powder or the substrate and there is poor adherence of the overlay with the substrate. The weld current and the movement of the torch mainly influence the substrate/overlay dilution [DIL2001].

2.3.2.2 Plasma Gas Flow Rate

The plasma gas flow rate dictates the magnitude of the arc collimation and the plasma velocity. If the plasma gas flow rate and main arc current are too high, the penetration into the substrate and the formation of pores and oxides increases and vaporization of both the substrate and powder occurs [KOU1985]. To avoid finger shaped penetration, the energy in plasma arc should be distributed homogeneously. This is achieved by reducing plasma gas flow rate while the main current is used to control the energy input for melting the base material and the powder.

2.3.2.3 Powder Feed Rate and Powder Size Distribution

The feed rate of the powder depends on the carrier gas flow rate and the bucket wheel speed. If the bucket wheel speed is too low or the carrier gas is too high, there will be an inconsistent flow of powder to the substrate. Conversely, a low carrier gas flow may not have sufficient energy to transport the powder to the torch nozzle.

Particles are limited to a narrow range to reduce feeding problems. As a general rule, the particle size should be restricted to no less than one third of the smallest

diameter experienced in the travel path. Determined through experimental investigations, finer powders (50 to 90 μm) led most frequently to obstructions in the feeding system [HAL1992]. Suggested maximum particle sizes for PTA have been recorded as 250 μm [KAM1991] and ideally in the range of 50-150 μm [DEU1998].

2.3.2.4 Voltage and Torch Stand-off Distance

The voltage is directly related to the torch stand-off distance; the closer the torch stand-off distance, the lower the voltage drop. The voltage is another component of the heat input of the system; higher voltages increase the heat input. The length between the torch and the workpiece is labeled the stand-off distance. The deposit can become diluted with iron from the substrate due to melting of the substrate, as such, the amount of iron in the coating decreases with increasing the torch stand-off distance [OBE1992]. An upper limit for the stand off distance of 10-15 mm was suggested [DEU1998].

2.3.3 Obtaining a Good Hardfacing Coating

In order to reduce the experimental time required to identify the optimal operating conditions, a factorial [HER1993] and a Taguchi-regression [TU2006] analysis of PTAW was performed. The factorial analysis revealed that the important factors were identified as current, plasma gas, transport gas, oscillation frequency, weld speed and torch standoff distance. An increase in plasma gas flow rate, weld speed and current result in a decrease of deposit height, which is related to the heat development of the bead overlay. The Taguchi analysis indicated that lower voltage, higher current, lower powder feed rate, lower waving oscillation, higher plasma gas flow rate and lower preheat improved wear resistance of hardfacing coatings.

It was determined that PTA parameters had an influence on the microstructure of the deposit and that an improvement in mechanical properties due to a finer structure was achieved by faster solidification [HAL1992]. Those properties

highlighted were an increase in surfacing speed and a reduction in plasma gas flow rate.

The selection of the material for the wear resistant coating is just as important as the process and conditions required for application. The following selection discusses the design parameters required in material selection.

2.4 Wear Resistant Coatings: Material Selection

When designing a MMC material system, the following parameters must be considered:

- Matrix composition
- Reinforcement particle composition
- Reinforcement particle size and volume fraction

2.4.1 Matrix Composition

To maximize coating hardness, the metal alloys contain a variety of elements, which when heated will form an assortment of hard phases. Several types of metal alloys and their primary applications are listed in Table 2.2. The two most common alloy systems are iron-chromium for high abrasion resistance and nickel-based alloys for general wear and corrosion resistance. A hard reinforcing ceramic particle, such as tungsten carbide, is added to the alloy when high stress abrasion is present.

Table 2.2: Examples of alloys used in hardfacing and their applications [MCK1997]

Metal Alloy	*Purpose*
Cobalt-base alloys	wear and corrosion resistance
Copper-base alloys	rebuilding worn machinery parts
Iron chromium alloys	high stress abrasion
Manganese steel	wear application
Nickel-base alloys	metal-to-metal wear resistance
Tool steel	tooling, wear application

Several materials systems currently explored by the mining industry for wear resistant applications are iron-based alloys, nickel-based alloys and cobalt based alloys.

2.4.1.1 Iron-based Alloys

Iron based alloys with the addition of chromium carbides (in the form M_7C_3) have a wear resistance which is strongly dependent on the amount of carbide present, and are used in low stress abrasion but are very brittle [COL2003]. Stainless steels are also able to resist metal to metal, impact, abrasion and erosion environments.

2.4.1.2 Nickel-based Alloys

Nickel based alloys are varied in the additive components such as boron, tungsten, silicon and carbon. Nickel based alloys have good wear resistance, high temperature stability, corrosion resistance, and good toughness. The additives act to enhance wear resistance, either by forming intermetallics or by solid solution strengthening of the nickel dendrites. The resulting microstructures of NiCrSiB consist of nickel solid solution, M_7C_3, chromium carbides, nickel and chromium borides, and Ni_5Si_2 [SU1997A]. The volume fraction of nickel-phase dendrites typically ranges from 40-70%, separated by a eutectic matrix of silicide, carbide and boride phases [COC2002]. Boron and silicon are added to suppress the melting point by forming low melting point glasses [MOS1980]. Further microscopy revealed that the dendrites are γ-nickel and the interdendritic phase constitutes primarily of binary eutectic of γ-nickel and nickel boride. There are two types of borides present: $(Ni,Fe)_3B$ and Cr_5B_3 [LIM1998B]. The chromium carbides are angular and blocky, whereas the chromium borides are floret-like [GUR2007]. Both improve the wear resistance of the deposit.

2.4.1.3 Cobalt-based Alloys

Cobalt based alloys are known for their work hardening abilities and good galling resistance. Carbide type cobalt alloys, such as Stellite, are hardened by Laves phases and $Mo(Co,Si)_2$. The addition of carbide composites such as WC, TiC, TaC and VC are highly resistant to low stress abrasion.

2.4.2 Reinforcement Particle Composition

Reinforcement particles are added to enhance the abrasion resistance of the coating. Reinforcement particles should be chosen such that they have low solubility in the matrix and that the melting temperature should be higher than matrix [COL2003]. The secondary phases formed in the deposit are a function of the composition of the matrix and the reinforcement particles and their reactivity, solubility and melting ranges. The carbide may experience dissolution in the matrix and this results in undesirable (or desirable) effects. Typical carbides and their relative properties are shown in Table 2.3.

Table 2.3: Properties of carbides used in wear resistant coatings.

Carbide	*Hardness (Hv)*	*Density (g/cm^3)*	*Melting Point (°C)*
B_4C [c]	3670	2.5	2450
TiC [a]	3000	4.9	3100
W_2C [f]	3100	17.2	2785
VC [a]	2900	5.7	2700
NbC [a]	2000	7.8	3600
WC [a]	2200	15.7	2870
Cr_7C_3 [b d]	1630	6.9	1755
Cr_3C_2 [a]	1400	6.7	1800
Fe_3C [d e]	1020	7.5	1252

Ref: [a][GAU1995], [b][PIE1996], [c][SCH1991], [d][XIA2009], [e][TAJ1993], [f][GUB2005].

Tungsten carbide is primarily used in the harshest abrasion conditions due to its combination of high hardness, toughness, strength and lower cost. The most prevalent types of tungsten carbides are:

- a cast and crushed (eutectic) with a composition of WC and W_2C resulting in a carbon content of 3.9 wt%. The melting point is 2730°C.
- a macrocrystalline tungsten carbide containing only WC with a carbon concentration of 6.1 wt%. The melting point of the macrocrystalline carbide is 2870°C.

Adding (V,W)C produced the most wear resistant of the iron based composite coatings, W_2C/WC was most effective in nickel-based and $(W,Ti)C_2$ was most effective in cobalt based systems [SAL1986]. TiC particles showed minimal

particle cracking and good particle-matrix attachment in an aluminum matrix [DEU1997A].

If there is a significant density difference between the reinforcement particle and the matrix, the solidified deposit will exhibit non-homogeneous properties. The low density of TiC caused the particles to float in iron- or cobalt-based overlays, whereas WC had the opposite problem: dispersed carbides tended to sink in nickel-based overlays [SAL1986]. The microstructure of the WC/W_2C overlays showed that the carbides segregated to the bottom of the overlay [BAB1986]. Due to the lighter density of V, the (V,W)C carbide allows particles to float in the weld pool instead of sink to the bottom as is the case for pure WC.

2.4.2.1.1 Interactions between WC Particles and the Matrix

Although WC is the most common carbide used in Ni-based MMCs, there are significant interactions between the particle and the matrix. This can be beneficial (increase in matrix hardness) or deleterious (decrease in fracture toughness).

According to the W-C phase diagram shown in Figure 2.3, there are two primary tungsten carbides: WC (δ) and W_2C (β). The primary phase is hexagonal WC, which is stable between 300 K and 3030-3050 K [KUR2006]. Decomposition of WC occurs incongruently into graphite and liquid. WC does not have a stable liquid phase and will transform easily into other phases if the carbon content is nonstoichiometric [RAN1986].

The eutectic W_2C, exists as three polymorphs β" (low temperature), β' (intermediate), and β (high temperature). The homogeneity range of β –W_2C is from $WC_{0.34}$ to $WC_{0.52}$. The eutectic starts to decompose below 1250°C into W and WC [PIE1996], but is found in commercial powders.

An unstable carbide, γ-WC_{1-x}, is formed only at temperatures above 1530 °C, but can be found at room temperature after rapid quenching.

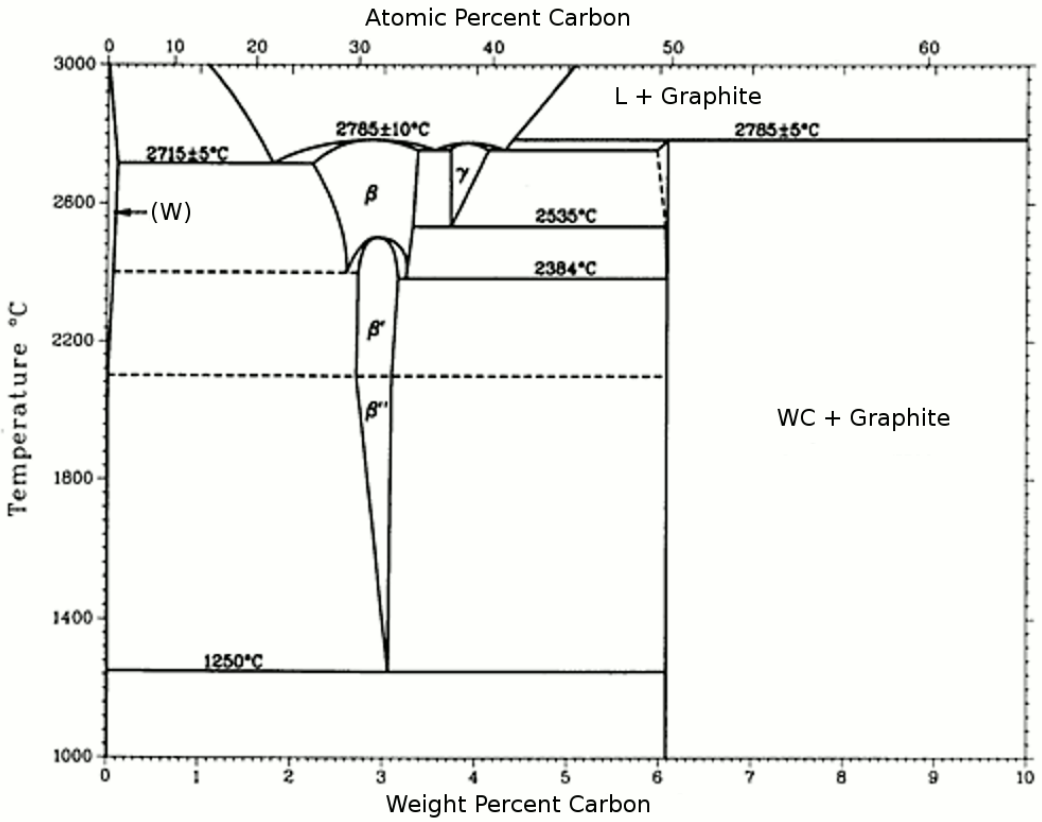

Figure 2.3: Phase diagram of W-C [modified from BAK1992]

The WC particles have been shown to dissolve into the liquid matrix to form W_2C and M_6C (M=Co, Ni, Fe) [LOU2003]. As the heat input increases, WC can dissolve and react with the matrix to from Ni_2W_4C until no WC remains [WU2003]. Thermodynamically, WC dissolves in Ni-rich liquid, and reprecipitates from the liquid upon cooling [BAB2002]. The standard formation free energies of tungsten carbides are high, therefore W does not form a stable binary carbide [ARA1993]. Dissolved WC particles can precipitate in the cooling molten alloy as WC, W_2C or eta (η) phase complex carbide. These η carbides, often found in many ternary carbide systems, are in the form M_6C or $M_{12}C$ in the Ni-W-C and Fe-W-C systems. Other complex carbides are described as $(NiSi)_A(CrW)_BC$ with A and B in the ranges (2.5-2.9) and (2.5-3.6) respectively [HAM1992], M_7C_3 and $M_{23}C_6$, or a mixed carbide $(W, Cr, Ni, Fe)_xC_y$ [QIA1998].

The η phases were found surrounding the WC particles and non-uniformly throughout the nickel base [BUC1991]. The formation of η phases occurs primarily at the surface when the temperature exceeds 900°C [LIA1997]. It is not desirable to have W_2C or η carbides form as they are more brittle and have less corrosion resistance than WC. It is stressed that the formation of the complex carbides is due to exposure to higher temperatures and longer deposition duration such that complete dissolution of the original WC particle can occur [KNO1981]. The degree of carbide dissolution decreases with powder feed rate in PTAW processing [LIM1998B]. As the heat input decreases, there is less dissolution of the carbides and a higher amount of unmelted WC, thus increasing overall coating hardness.

The addition of WC in a NiCrBSi alloy has refined the dendritic structure compared to the alloy alone and formed carbides containing 47 wt% W, 39 wt% Cr and 14 wt% C [ZHA2003]. A eutectic was identified with composition γ-(Fe, Ni) + $Fe_{23}B_6$, determined from TEM analysis. If the heat input is sufficient to melt the WC, up to 6 at% W has been found in the matrix eutectic. Tungsten has increased diffusion in the γ-(Fe, Ni) phase. Other sources report the matrix to be composed of γ-Ni dendrites and a γ-Ni + Ni_3B eutectic [LI1999]. However, the temperature and residence times of the reaction between the tungsten carbide is unknown.

2.4.3 Particle Size and Volume Fraction of Carbide

It is well known that abrasive wear properties depend on size and fraction of carbides as well as on the type of abrasive. The main contribution to excellent wear resistance is provided by a homogeneous distribution of the hard precipitates.

Carbides with a narrow grain size distribution have shown to result in a coating which has higher erosion and erosion-corrosion resistance. The smallest WC particles gave the most homogeneous structure (1.53 μm compared to 6.3 μm)

[KIM2001], whereas coating with the coarsest WC particles revealed relatively large areas of pure metal phase (5 μm compared to 1 μm) [BER1998].

As the WC particle size decreases, the mean-free path for reactions between WC and the matrix shortens. Since there is an increase in the fraction of WC per unit area, there is a higher probability of secondary carbide particle formation which results in an increase in hardness [KIM2001]. The secondary carbides particles found were dependent on the matrix, but followed similar compositions such as M_3W_3C (M=Co,Ni).

Increasing the volume fraction of SiC, Al_2O_3 or TiC reinforcement particles in an aluminum matrix reduced both the coating thickness and aluminum dendritic cell size [DEU1997A]. The secondary particles are rejected by the solidifying front to the interdendritic regions. It was assumed that the rejected particles contributed to a higher solidification front velocity, thus resulting in a smaller dendritic cell size. As the volume fraction of the particles increased, the depth to which the particles could penetrate into the weld pool also increased as their momentum increased.

Increasing the reinforcement particle volume density, for a constant reinforcement size, resulted in a higher dislocation density in the aluminum matrix [DEU1997B]. This increase in dislocation density is also due to the higher difference in the coefficient of thermal expansion of the reinforcement and matrix. A higher dislocation density can lead to higher corrosion rates. Ideally, the thermally expansion coefficients of the reinforcement particle and the matrix should match.

2.4.4 Multiple Passes of Coating Application

Multiple passes are desirable in order to increase the thickness of the wear resistant coating. Generally, a thicker coating will increase the service life of the component. The coating thickness is controlled by the powder feed rate, the

travel speed and by the number of applications. The effect of applying multiple passes in order to increase thickness of the coating is highlighted. However, in general, the hardness decreases with multi-pass clad layers as compared to the single pass, due to the effect of multiple thermal cycles. The additional heat can lead to coarsening of the dendritic structure, a transition from finer, angular mixed carbides to coarse leaf-like ones or increased dissolution of WC particles in nickel-based hardfacing alloys [QIA1998A] [COC1997]. It was observed that the number of angular hard phases in nickel-based alloys appeared to be less in the single pass regions and tended to line up in the overlay region [LIM1998B]. The abrasion resistance of a WC-NiCrBSi MMC was very sensitive to changes in current between 70 and 170 A for single pass coatings, but not in multiple pass coatings [BAD2008].

The region shared between two passes may result in cracking due to dissolution of tungsten carbide and the formation of deleterious intermetallics in nickel-based matrices. It was suggested that reducing the hardness of the matrix material in order to lower the concentration of intermetallics improves the longevity of the coating. A second approach was to modify the welding parameters so that settling of the carbides does occur at the surface. When another pass of coating is added, the carbides are not melted and the result is a congruent multipass coating [AND2003].

2.4.5 Wear Testing

Wear testing is conducted to measure the rate of mass loss of a coating in order to evaluate the effectiveness of the MMC chosen. The industrial standard test is the ASTM G65 Dry Sand/Rubber Wheel Tests [ASTMG65]. Silica sand of a known size is gravity fed between a rubber wheel and the specimen. The specimen is held in contact with the rubber wheel by a weight. As the wheel rotates, the sand abrades the coating surface. At the conclusion of the test, the mass loss of the specimen is calculated. With most MMCs used in mining applications, the softer matrix will abrade faster than the carbide thus exposing the carbide. The carbide

provides the majority of the wear resistance of the coating. As the applied load increases, the deformation in the coating will increase, which can lead to work hardening in the coating and could decrease the rate of wear resistance. At low speeds, the debris generated from the wear test is not ejected from the wear track and will continue to contribute to the track wear process in the form of abrasive wear.

In terms of comparing the wear performance of MMCs, it was found that:

- WC-Ni-based alloy exhibited a better wear resistance than Colmonoy 6 and 88, which are worn more readily due to the largely eutectic borides and softer mixed carbides [QIA1998].
- The weight losses of overlay alloys with TiC and VC were lower than others upon performing a wear test [ARA1993].
- Aging improves wear of a high Cr-high Ni alloy due to the precipitation of α- phase in γ-phase [TOM1998].
- The wear rate difference between PTA and open arc weld surfaced overlays is explained by difference in the eutectic contents [KIM1999].
- Increasing the volume fraction of the carbide phase increases the size and number of secondary phase precipitates [SU1997B].

The wear test is often repeated over the same scar in order to obtain a steady state result. This is because the surface is often depleted of carbide due to the settling of the dense reinforcing particles. A fully homogeneous coating will yield superior wear resistance. Although designed experiments have revealed operating parameters which yield improvements in the wear resistance of MMC coatings, modeling and predictive efforts would eliminate a majority of the labour intensive experiments. The following section examines the literature to date of the complexities of modeling the deposition of MMC by PTAW. The modeling efforts explored include arc welding and settling in MMCs.

2.5 Modeling Welding Heat Transfer

Arc welding modeling has been studied analytically, numerically and experimentally. Most of the research has been conducted in the area of gas tungsten arc welding, a process very similar to plasma arc welding, except that the arc is not constricted.

The transfer of thermal energy within the welding workpiece is dictated by transient conduction of heat, shown in equation 2.1 [JEN2001]. This equation includes heat flow in the *x* (welding direction), *y* (transverse to welding) and *z* (normal to surface) directions. The rate of internal heat generation (*Q''*) is only included when energy is added below the surface, such as in submerged arc welding. Heat is lost by a combination of convection and radiation to the environment, or by conduction through the base metal.

$$\frac{\partial}{\partial x}\left[k(T)\frac{\partial T}{\partial x}\right]+\frac{\partial}{\partial y}\left[k(T)\frac{\partial T}{\partial y}\right]+\frac{\partial}{\partial z}\left[k(T)\frac{\partial T}{\partial z}\right]=\rho c_p(T)\frac{\partial T}{\partial t}-Q'' \qquad (2.1)$$

The distribution of heat applied to the surface to form the weld bead can be expressed in two methods:

- at the surface, characterized by a heat flux distribution *q(x,y)*, expressed in W/mm^2.
- internally throughout the weld by *Q*.

Initially, the process was studied as a quasi-stationary thermal problem in order to obtain an analytical solution. Quasi-stationary models were developed which simplified equation 2.1 to become a two-dimensional problem. A number of assumptions were made to obtain a model which predicted the temperatures of the weldment using the quasi-stationary method. The assumptions required are a uniform heat source moving a constant speed unidirectionally, a uniform cross-section and that the process has achieved steady state [ROS1941] [FRI1975].

The shape of the arc heat distribution influences the size, shape and metallurgy of the weldment. A significant amount of work has been conducted to quantify the heat distribution of a plasma arc in welding, which will be discussed in the next section.

2.5.1 Arc Heat Input - Concentrated Source

The heat generated by the arc was initially modeled either as a point, line or plane heat source [ROS1941] [ROS1946] [RYK1974] [PAL1975] [OKA1988]. The concentrated heat input distribution are ideal when the thermal cycle of the weldment is not of interest and become more accurate as the distance increases from the heat source. However, the point source heat input estimation (equation 2.2), which is the primary heat input equation still used today, considers the current (I), voltage (V), travel speed (v) and efficiency (η) of the arc.

$$Q = \eta \frac{VI}{v} \tag{2.2}$$

The efficiency term varies for each welding scenario, and its value has been estimated but never agreed upon. It is an estimation of the amount of heat transferred from the arc to the work piece that is used for melting. It has been shown that welds cannot be characterized by this calculation of heat input, as changes in voltage, current and travel speed have varying effects on the weld output [YAR2005].

In order to estimate the efficiency term, a heat balance of the arc is required. The arc heat input at the anode can be estimated using the values of process parameters, and is categorized into anode effects, convention/conduction and radiation. The relative contributions of heat transfer to the workpiece, comparing a 10 kW PTAW and a 1.6 kW GTAW process, are shown in Figure 2.4. The plasmas generated in the PTAW and GTAW processes are similar in that they are both free burning plasma arcs initiated by a tungsten electrode and an ionizing gas such as argon. Since the arc in PTAW is significantly constricted due the nozzle,

the energy density is ten times greater. This results in a higher efficiency: 60% for PTAW compared to 47% for GTAW. Secondly, convection is the largest source of power input for PTAW, whereas anode effects dominate GTAW.

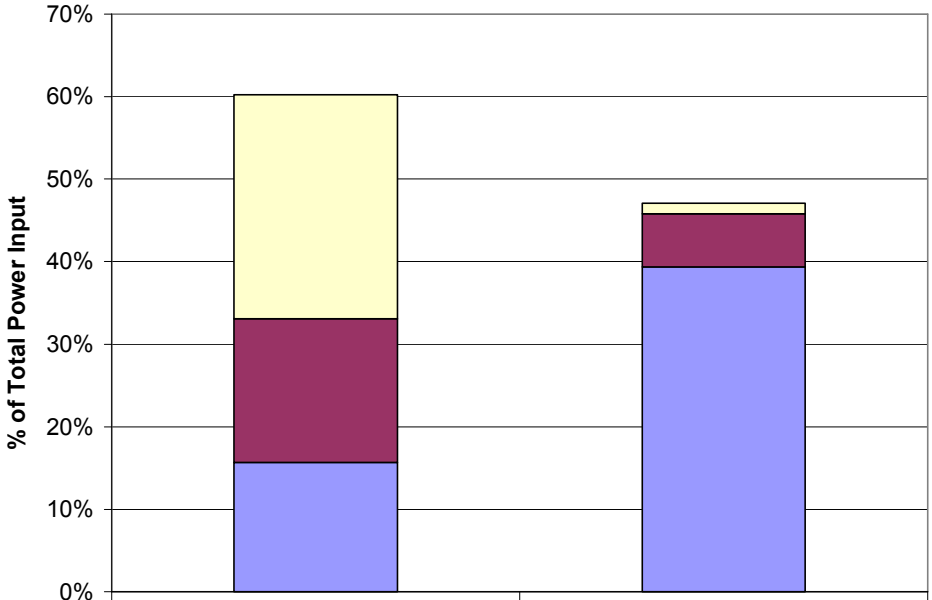

	PAW	GTAW
Convection	27%	1%
Radiation	17%	6%
Anode Effect	16%	39%

Figure 2.4: Comparison of arc heat inputs of PTAW [MET1975] and GTAW [QUI1973].

In GTAW, it is shown that the anode effects are the dominant mode of heat transfer. The heat transferred to the anode (Q_a) by arc welding is shown in equation 2.3 [COB1955], and comprises of the work function (Φ), anode fall effects (V_a) and the Thomson effect also known as the electron thermal energy in the plasma. The work function is the potential energy released by an electron on entering a metal and is typically 4 V for most metals. The anode fall region is located between the arc column and the anode. The temperature decreases quickly in this region and ionization decreases resulting in a voltage drop. When electrons flow from a hot plasma to a cool anode, they carry heat as well as

current – a phenomenon known as the Thomson effect. This is a function of the kinetic energy of the electrons at the mean plasma temperature.

$$Q_a = I\left(\Phi + V_a + \frac{3k_B T}{2e}\right) \tag{2.3}$$

The contributions of heat flow to the anode in GTAW were primarily due to the work function (26.2%), the anode fall region (9.4%), conduction (4.4%) and the Thomson effect (3.8%) [QUI1973].

However, convection is the dominant mode in PTAW. This is because the plasma gas velocity increases from 80-150 m/s in GTAW to 300-2000 m/s in PTAW. This calculation confirmed that the majority of heat available to the weld in PTAW is produced by convection – that is, the plasma gas flow and size of the arc are important factors.

The variables used in the PTAW process specific to this thesis were applied to the methodology described by Metcalfe and Quigley [MET1975]. The heat transfer mechanisms of plasma arc welding were obtained by analyzing the arc heat input components. It was calculated that 50% of the heat transfer is due to convection, 30% is due to anode effects and 2% due to radiation. This increases the efficiency of the process to over 80%. The efficiency term for plasma arc welding was evaluated to be 0.47 and 0.67 for gas tungsten arc welding [DUP1995]. Neither of these simulations included powder deposition. Other reports state PTAW efficiency to over 95% [AND2003].

It is shown here that the assumptions made to obtain a concentrated heat source results in variations in the results due to the complexities of the process. The heat input is highly dependent on the efficiency term. Hence, a more complex heat input model was developed – the distributed source, discussed next.

2.5.2 Arc Heat Input - Distributed Source

The first welding simulations had weld pools that were oval shaped, with no tapering at the trail end. A notable experiment performed by Nestor [NES1962], revealed that the heat intensity of a plasma arc is distributed with a peak at the centre and decreases with the plasma radius. By modifying the arc heat input to a Gaussian distribution [PAV1969] [RYK1974] (equation 2.4), a more realistic temperature profile of the substrate was obtained. The Gaussian distribution assumes that 95% of the arc heat input lies within a given radius. Inside this circle, the heat input increases exponentially to the centre.

$$Q_{anode}(r) = Q_{\max} \exp(-Cr^2) \tag{2.4}$$

The factor C concentrates the arc and can be modified to account for the heat input of any welding process. This method enables more sophisticated heat models to be developed by incorporating the Gaussian distributions in both axisymmetric [KIM1997A] and double ellipsoid forms [GOL1984].

The first analytical solution for the temperature profile of the arc was performed in one dimension by Glickenstein [GLI1979]. The heat flux at the anode was estimated as a combination of plasma convection, Q_c, electron thermal energy, Q_e, and plasma radiation, Q_r, as shown in equation 2.5 [USH1982]. The radiation term is the heat transfer from the arc to the weld pool. In addition, there are small heat losses from the pool that are due to evaporation of metal ions and radiation. The contribution of radiation (Q_r) to the total heat flux (Q_a) was determined to be less than 5%, and has been neglected.

$$Q_a(r) = Q_c(r) + Q_e(r) + Q_r \qquad (2.5)$$

where

$$Q_e(r) = \frac{5}{2} k_B (\alpha T_b - T_a) \frac{J_a}{e} + J_a V_a + J_a V_f$$

$$Q_c(r) = \frac{0.515}{\mathrm{Pr}_a} \left(\frac{\mu_b \rho_b}{\mu_a \rho_a} \right)^{0.11} \left[\mu_b \rho_b \frac{U_f}{r} \right] \left[H_b - H_a \right]$$

An improved understanding of plasma physics and an increase in computational ability led to a drastic increase in the complexity of welding models. Plasma models based on both continuity, Navier-Stokes momentum and the Maxwell equations are able to predict velocity, temperature and current density profiles [MCK1986] [CHO1990].

With this advance, interactions between the arc and the substrate were explored in both 2 and 3 dimensions [LI1997] [KIM1997B] [JOU2003]. Several models investigated the temperature, velocity, current densities of the arc fluid when varying the electrode tip angle [GOO1998] [LEE2002] and degree of surface deformation [WU2004]. A sharp electrode angle flattens the heat flux distribution resulting in a wider, shallower weld pool. A stationary TIG model was successful in modeling the electrode, plasma and substrate behaviour [CHO1990] [TAN2002]. At a current of 200 A and a stand-off distance of 10 mm, the temperature of the plasma arc ranges from 21 000 K near the electrode to 14 000 K at the outer surface [JON1994]. Models of the temperature and current density isotherms of high intensity plasmas have been well studied.

The models were verified by calorimetery [NES1962] [TSA1985], spectrometry [HSU1983] [COU1993], or arc pressure [LIN1986]. A unique approach for collecting the temperature of the plasma was by use of a line-profile analysis using laser scattering [TAN1999].

Shown in Figure 2.5 is a comparison of the heat flux of a GTA plasma determined numerically using the heat flux input shown in equation 2.5, a Gaussian approximation based on the form shown in equation 2.4, and experimental data. The agreement between methods is good. This figure shows that the heat input of the arc is distributed and axi-symmetric without the injection of particles, unlike the conditions on the arc in the PTAW case presented in this thesis. The effect of the particles on the shape of the arc heat input is not documented.

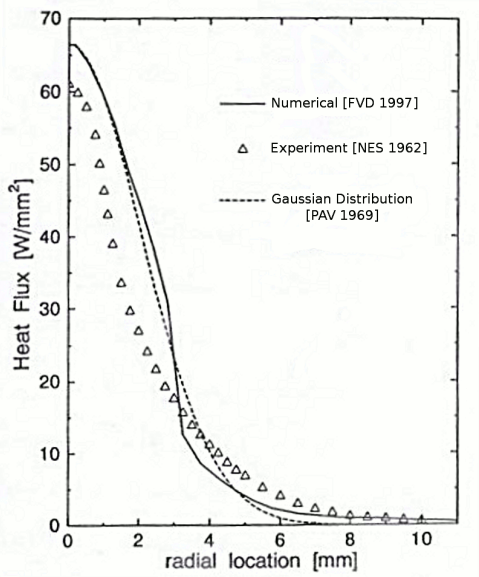

Figure 2.5: Heat Flux of a gas tungsten arc weld [modified from FUD1997]

Although GTAW and PTAW are similar, the arc heat inputs are slightly different due to the addition of the nozzle which constricts and collimates the arc. Unlike the GTAW scenarios, very few models have investigated plasma arc welding because of the complexity of the nozzle constriction and the increased gas flows. Highlights of the work undertaken to understand the heat input of the PTAW arc are summarized.

The conservation of energy, mass and momentum equations used to model the PTAW are similar to the GTAW models and have been used to predict the arc profile [DOW1994]. By separating the problem into a nozzle domain and an external domain, velocity and temperature profiles were obtained for currents of

100 and 150 A [AIT1998]. The axial component of the velocity dropped from a range of 1000 to 1400 m/s over a distance of 8 mm. The corresponding axial temperature ranged from 16 000 to 24 000 K over the same distance. The temperature of the anode was found to be 1 600°C at the same position the arc was a temperature of 11 000 °C [CHU2004]. Simulations of keyhole welding using PTAW were successfully carried out that were able include three dimensions [KEA1993], and the monitoring of the solid/liquid interface [HSU1988] [FAN1999]. The only work which models deposition of a coating using plasma transferred arc welding identified optimized process conditions to obtain a smooth surface [WIL2006].

A significant amount of research has been conducted in order to understand the heat flow of welding processes. With the increase in computational ability, the sophistication of the models has increased such that the arc, substrate and interactions between the two have evolved. However, the effect of particle injection on the heat input of the welding arc has not been studied.

The next section examines the modeling of the coating at it solidifies and the settling of the reinforcement particles in the liquid melt.

2.6 Settling of Reinforcement Particles in MMCs

This section reviews the current models and experiments dedicated to particle settling in the MMC coatings. The particle distribution in the WC-NiCrBSi MMC is influenced primarily by the settling of the reinforcing particles due to gravity since the density of WC is almost twice that of the matrix. The modeling of the homogeneity of metal matrix composites has not been well developed; however, the settling of two-phase systems has been well established.

2.6.1 Single Particle Settling

Consider a spherical particle of a given diameter fully immersed in an infinite and less dense fluid. A schematic of the forces acting on the sphere is shown in Figure 2.6 and a balance of the forces on the sphere is given by equation 2.6. The problem was modeled by balancing the forces on a sphere accelerating though a liquid, where m_{sphere} is the mass of the sphere, U is the instantaneous velocity and F are the forces acting on the sphere.

$$\frac{d}{dt}\left(m_{sphere}U\right)=\sum F \tag{2.6}$$

The forces shown to act on the sphere are:

- gravity ($F_G = m_{sphere}g$);
- buoyancy ($F_B=m_{disp}g$, where m_{disp} is the mass of fluid displaced by the sphere);
- drag generated by the difference in velocity between the sphere and fluid ($F_D=C_D\pi d^2\rho U|U|/8$, where d is the diameter of the sphere, U is its velocity through the fluid, ρ is the fluid density, C_D is the drag coefficient). Shown in Figure 2.7 are the drag coefficients for a sphere as a function of Reynolds number. Reynolds number is a dimensionless number given as the ratio between the inertial forces (ρU^2) to viscous forces ($\mu U/L$) (equation 2.7);
- added mass which allows for acceleration of the sphere and results in acceleration of the liquid around it ($F_A=C_Am_{disp}(dU/dt)$, where C_A=1/2 [LAN1959].

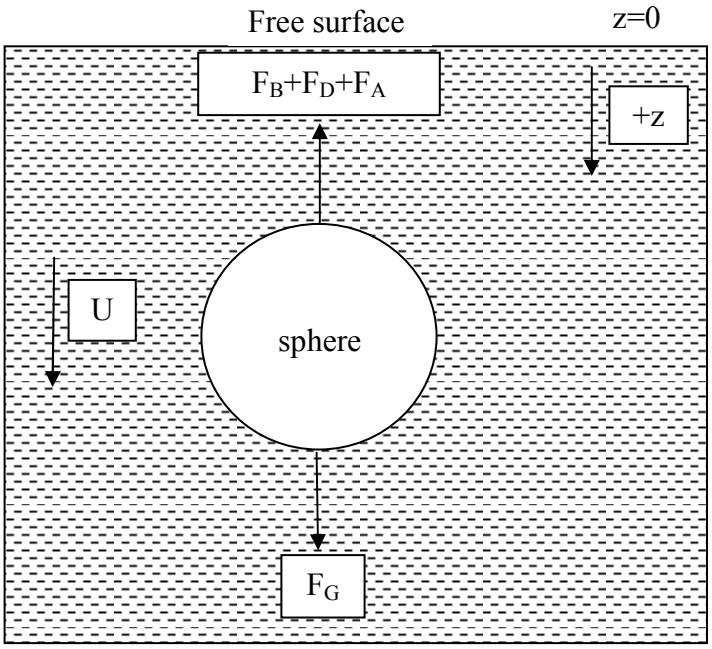

Figure 2.6: Schematic of forces on sphere accelerating through a fluid.

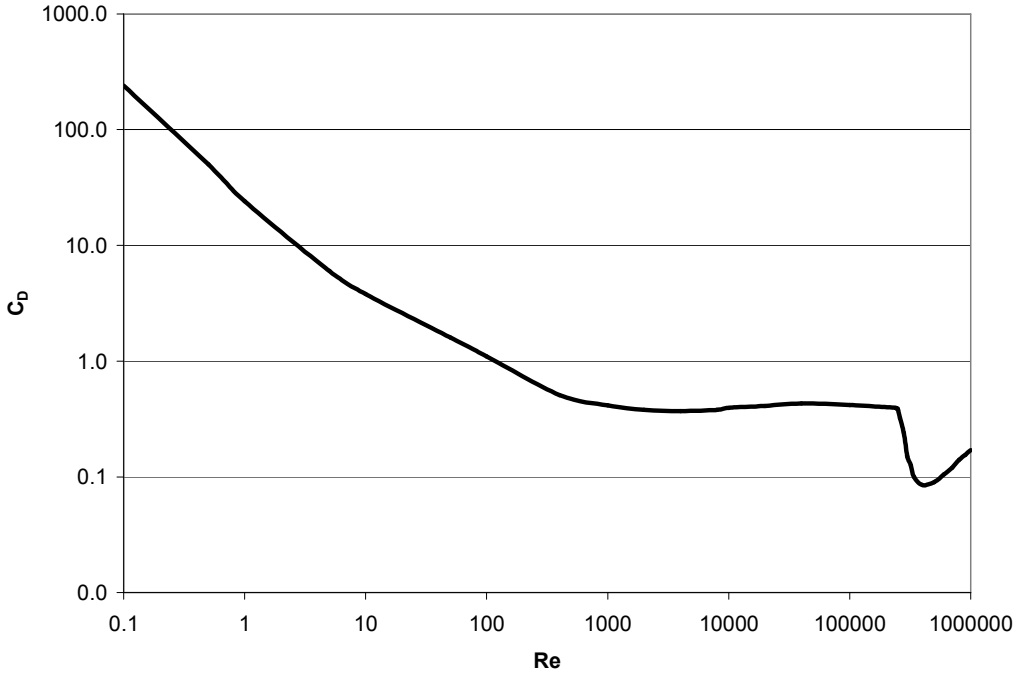

Figure 2.7: Drag coefficient for spheres as a function of the Reynolds number [KRE2005].

$$\mathrm{Re} = \frac{U_f \rho_f d}{\mu_f} = \frac{Ud}{\upsilon} \tag{2.7}$$

Rewriting equation 2.6 with the forces listed above, with an initial condition that at t=0, z=0 and U=0, results in equation 2.8. The term γ is the ratio of the density of the particle to the density of the liquid. By integrating this equation over the domain, the displacement and velocity of the particle can be tracked. With the added mass term, the trajectory of the particle is well modeled, even when heat transfer is involved [GUT1975] [GUT1976].

$$\frac{dU}{dt} = -\frac{(1-\gamma)g}{(\gamma + C_A)} - \frac{3C_D U|U|}{4d(\gamma + C_A)} \tag{2.8}$$

When the Reynolds numbers are small, which is true for very small particles such as those seen in MMCs, the drag force can be calculated by Stokes' law. If the particles are falling in a viscous fluid due to gravity, then the terminal velocity is reached when this drag force combined with the buoyant force exactly balance the gravitational force. When inertia is neglected, the flow is creeping and the settling velocity is calculated from Stokes' Law (equation 2.9) [STO1880]. If inertia cannot be neglected, the drag coefficient must be correlated through experimental means and the velocity can be tracked by using equation 2.8.

$$U_o = \frac{g d_p{}^2 \left(\rho_p - \rho_L\right)}{18\mu_L} \tag{2.9}$$

2.6.2 Hindered Settling

Stokes' Law no longer holds true as the particle concentration increases beyond a dilute solution. Velocity gradients surrounding the particle are affected by its nearby particles. The Richardson-Zaki [RIC1954] equation, a semi empirical

relationship between the settling velocity single particle and the velocity of multi-particle settling (hindered settling), is given by equation 2.10. Through experimental fluidization studies with spheres, β was determined to be in the range 2.4-4.65 as the Reynolds number decreased. As the particle concentration (θ) increases, the particle velocity (U_h) decreases significantly. This is shown in Figure 2.8 for β =2.4 and 4.65. A higher exponent results in a lower particle velocity.

$$\frac{U_h}{U_o} = (1-\theta)^{\beta} \tag{2.10}$$

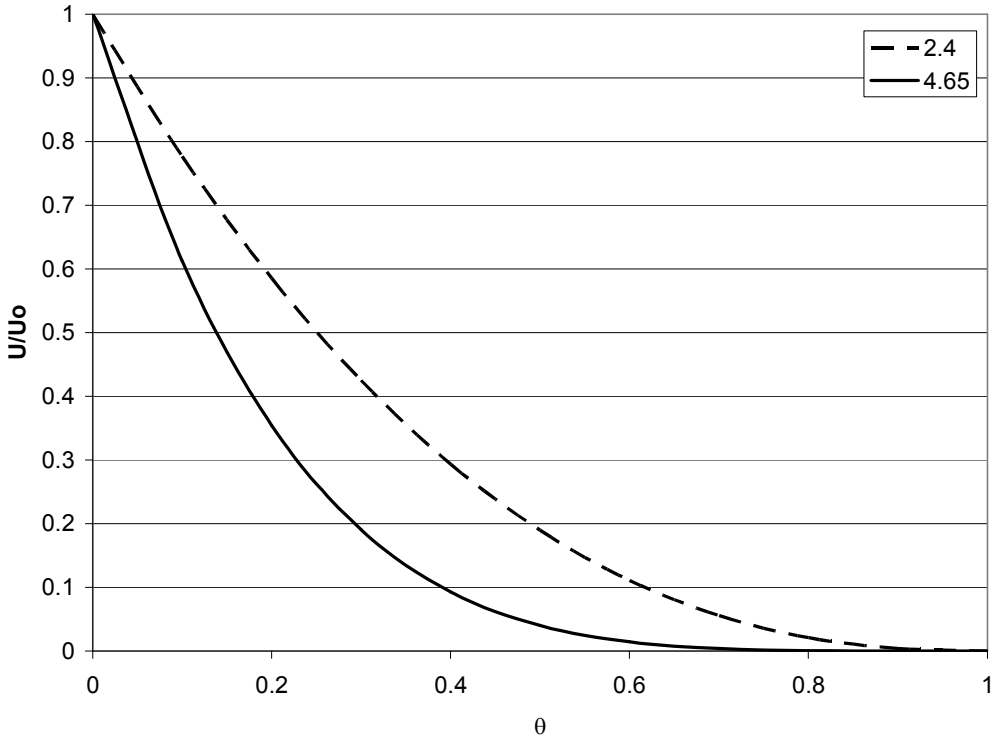

Figure 2.8: Dimensionless settling velocity as a function of concentration, where β = 2.4 and 4.65.

The empirical results for the parameter β, depend on the particle size (d_p), the container size (D) and the Reynolds number (Re). The results are summarized below (equation 2.11) [RIC1954].

$$\beta = 4.65 + 19.5\frac{d_p}{D}, \quad for \quad \mathrm{Re} < 0.2$$
$$\beta = \left(4.35 + 17.5\frac{d_p}{D}\right)\mathrm{Re}^{-0.03}, \quad for \quad 0.2 < \mathrm{Re} < 1.0$$
$$\beta = \left(4.45 + 18\frac{d_p}{D}\right)\mathrm{Re}^{-0.1}, \quad for \quad 1.0 < \mathrm{Re} < 200 \qquad (2.11)$$
$$\beta = 4.45\,\mathrm{Re}^{-0.1}, \quad for \quad 200 < \mathrm{Re} < 500$$
$$\beta = 2.39, \quad for \quad 500 < \mathrm{Re}$$

Further approximations of β have also included relationships with volume fraction [CHE1997] and fluid trapping on rough particles [MAN1986]. Most of the hindered settling studies have been approximating systems where the volume fraction is less than 30%. In high concentration systems, the settling velocity is significantly reduced to that of the immobile bed [BAL2004], verified in coastal applications. Greater settling is achieved when particle clustering occurs. The settling rate is also dependent on the particle size and shape.

In order to predict the settling of particles in a fluid bed, the laminae concept model was proposed by Mercer et al. [MER1999] in order to develop even dispersions for recording media. The column is divided into discrete sections, and the net solids flux and change in mass are calculated at each time interval. The particle size and concentration distribution was modeled in a similar manner: a mass flow calculation was performed based on Stokes' Law over a column divided into finite elements [BOU2001]. This method was applied to the separation of aluminum hydrate within the Bayer process in an alumina plant.

2.6.3 Settling of reinforcement particles in MMC melts

There are few studies that model MMC's and those that have been validated experimentally are even fewer. Most of the MMC studies involve modeling the solidification rate, as that is deemed the most important factor affecting the final microstructure. The sedimentation front settling velocity characterizes the

hindered settling rates, but it is difficult to measure in opaque materials. The system explored most frequently was SiC-Al MMCs.

The initial experimental studies of carbide overlays revealed that the low density of TiC caused the particles to float in the overlay, whereas WC had the opposite problem: dispersed carbides tended to sink [SAL1986] [BAB1986]. The WC was uniformly distributed close to the substrate interface and up to the middle of the deposit in nickel based matrix overlays [WLO1993]. Small particles tended to cluster before settling begins, which acts to increase the effective particle diameter and accelerate settling [IRO1995]. As the particle volume fraction increased, the particle settling is less severe [WU2001].

Further work also incorporated energy conservation to account for solidification, where the liquid, solid and particles phases were tracked, in both 1 and 2 dimensions. This model is based on conservation of mass and momentum using multiphase flow theory coupled with appropriate constitutive equations. The drag force is based on the creeping flow regime and Stokes' velocity. The velocity and concentration of the solid phase are solved simultaneously as a function of time and position. The models are heavily dependent on the Richardson-Zaki exponent, although it was determined that relationship overestimates settling rates as it is not dependent on particle-dendrite interactions [HAN1996]. An electric resistance probe has been used to measure the particle density in a settling Al/SiO_2 MMC and for validation of the mathematical model [HAN1992]. The solidification results were well validated by experimental means, however; the particle tracking models only had a moderate correlation when comparing to water/glass bead suspensions [GAO2001]. Regions of higher liquid metal velocity were void of reinforcement particles [FEL1997]. The settling rate of the particles was estimated by measuring the size of the particle free zone [OUR2001]. It was found that increasing the holding time and melt temperature would increase the settling region. The settling of high volume fractions of

carbide in MMCs has not been documented, nor has the settling profiles of a particle significantly more dense than the liquid.

A comprehensive solidification model was developed in order to quantify particle pushing and entrapment [XIO2006]. Using a multizone adaptive grid generation scheme, the solidification interface was accurately tracked. The model predicted the particles formed a circular pattern above the solidus interface due to the thermal convection of the molten metal. Particle vacancies were caused by anticlockwise convection and high axial or radial velocities, which would transport particles away from the interface. This study indicates that further depletion of carbide from the surface is due to natural convection of the melt; however, once the carbide is removed from the surface, the velocity of the liquid is very small compared to that of the settling velocity of the reinforcement particle.

2.7 Validation of Thermal Models of Welding

In order to validate the model predictions of the thermal profile of the deposit, measurements of the temperature of the weld are required. Thermocouples directly measure the temperature of the welding substrate. Thermocouples are appropriate for measuring temperature at a point, but it is difficult to measure a temperature field, as many thermocouples are required. If too many thermocouples are used, the temperature distribution may be altered. In addition, measurement of the temperature in the arc just at the liquid surface is not possible with thermocouples, as the temperature is too high. One example of temperature measurement using thermocouples in welding applications is the use of tungsten-rhenium thermocouples [COR1986] to measure centerline surface temperature. The thermocouples were inserted from the underside of the sample piece through predrilled holes to just below surface. It is difficult to determine whether this technique recorded true peak temperatures.

An indirect thermal measurement was conducted by Nestor [NES1962], who measured the heat flux of an arc using a calorimetric approach. This is not feasible for in-situ studies of welding.

Another option for capturing the thermal profile of the weld is to measure the temperature at the weld surface. The need for verification of complex heat balance models and development of welding control requires a specialized device: the infrared camera. This non-contact temperature measurement device allows for high temperature real-time measurements of the welding surface. The temperature field can be measured by this non-contact method and the response time is limited to the data transfer speed.
The following sections will discuss the theory behind infrared thermography and the current uses of the technique to measure temperature in welding applications.

2.7.1 Infrared Theory

All objects emit radiation along the electromagnetic spectrum within the infrared wavelengths (0.75 to 1000 μm). Its position on the electromagnetic spectrum is located between visible light and microwave regions. All bodies emit infrared radiation, which behaves similar to visible light except that it is not detected by the naked human eye. There are four subsets of infrared radiation:

- near infrared (0.77-1.5 μm);
- mid infrared (1.5-6 μm);
- far infrared (6-10 μm);
- very far infrared (10-1000 μm).

The sensor in an infrared camera measures the radiation intensity emitted by an object within a specific infrared wavelength range. The camera detector consists of many pixels that generate an output signal and reconstruction of the individual signals creates the image.

The theory behind the camera operation lies on two equations: the Planck radiation formula and the Stefan-Boltzmann law.

2.7.1.1 Planck Radiation Formula

The thermal energy radiated by an object is expressed in relation to the energy radiated at the same temperature by a perfect radiator - a black body. A blackbody absorbs all the radiation it receives and has the strongest emission power. It is used as the standard against all other objects. Mathematically, this is described by the Wien-Planck radiation given in equation 2.12 [SEI1981].

This equation describes that the radiation emitted per unit area (M) at a specific wavelength, λ, will increase with increasing temperature, T, for a black body whose emissivity , ε, is equal to one. In the equation, c is the speed of light (3×10^8 m s^{-1}), h_P is Planck's constant (6.626×10^{-34} J s) and k_B is Boltzmann constant (1.38×10^{-24} J K^{-1}). There is a distribution of radiant exitance over wavelength at each temperature and the peak wavelength decreases as temperature increases (Figure 2.9). Hence, at higher temperatures, the near infrared wavelengths contain more energy and are more sensitive to changes in temperature than the longer wavelengths. This equation is integrated over the wavelength range of the camera's sensor in order to obtain a relationship between exitance, temperature and emissivity for non black body objects where $0 \leq \varepsilon \leq 1$ for real objects and is a function of both λ and T.

$$M = \varepsilon(\lambda, T) \frac{C_1}{\lambda^5 \exp(\frac{C_2}{\lambda T} - 1)} \tag{2.12}$$

where $C_1 = 2\pi c^2 h_P$ and $C_2 = \frac{h_P c}{k_B}$

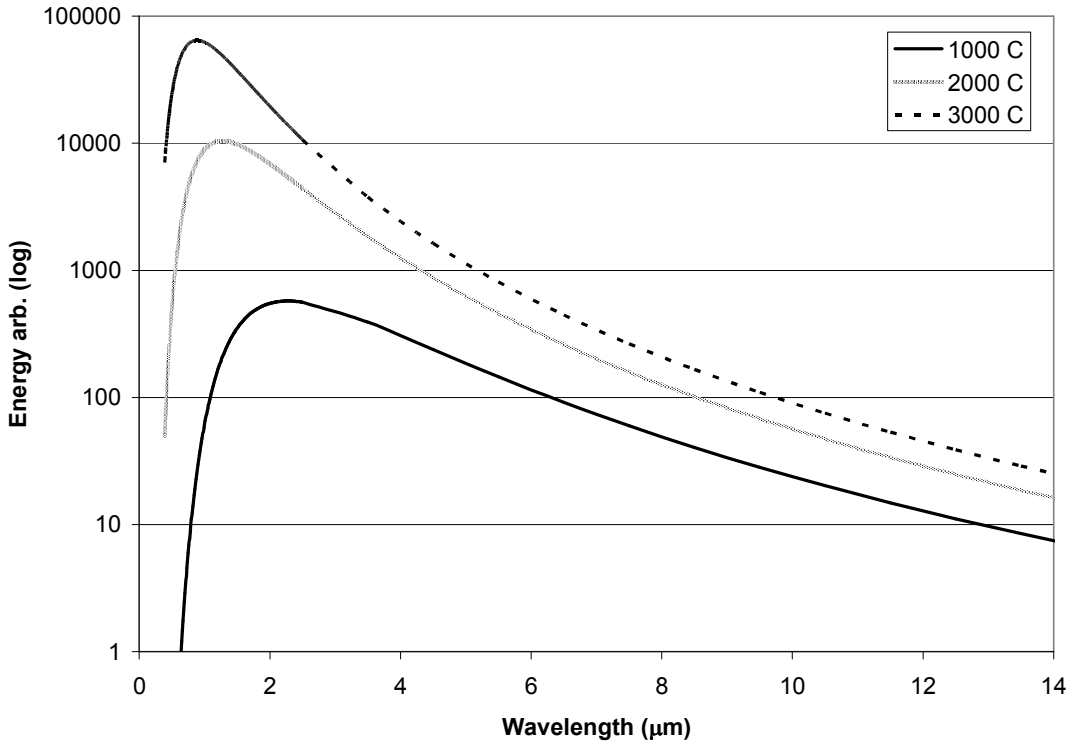

Figure 2.9: Blackbody radiation exitance for wavelengths between 0.8 and 14 μm at temperatures of 1000°C, 2000°C and 3000°C

2.7.1.2 Stefan-Boltzmann Law

Stefan observed that the total energy emitted by a black body is proportional to the temperature raised to the fourth power, shown in equation 2.13 [BUS2001], where σ is the Stefan-Boltzmann constant (5.67×10^{-8} w/m^{2}K^4). This was derived from the Planck formula by integrating over the wavelength range from zero to infinity.

$$M_{Total} = \varepsilon(T)\int_0^\infty M d\lambda = \varepsilon(T)\sigma T^4 \ (\mathrm{W/m^2}) \qquad (2.13)$$

It was shown in Figure 2.9 that as the temperature increased, not only did the amount of energy increase, but the wavelength at which the radiation is at a maximum shifts to lower wavelengths. The wavelength which corresponds to the

maximum spectrum radiation power at each temperature is designated λ_m. The relationship between T and λ_m is shown in equation 2.14 and plotted in Figure 2.10, where *b* is the Wien displacement constant (2.897 x 10^{-3} m K). This is called Wein's Displacement Law (BUS2001). For example, if the surface temperature of the weld is estimated at 3000K, the wavelength which emits the most radiation is 0.97 μm.

$$\lambda_m T = b \tag{2.14}$$

2.7.1.3 Emissivity

Emissivity is defined as the ratio of the radiative energy emitted by an object at a specific temperature and wavelength to that of a blackbody under the same conditions. Radiative emission is a result of the oscillations or transitions of electrons in a material and is dependant on the thermal nature of the material.

Since most objects are not a black body, their absorptivity is selective such that the emissivity is less than 1. Infrared cameras measure the radiative energy from a body, which could be a combination of emitted, reflected or transmitted infrared energy. Calibration is critical, as the grey levels of the image depend on many factors, which can be interrelated: radiation wavelength, radiation intensity, surrounding conditions, the atmosphere the radiation is travelling through, type of material, distance, and surface condition. The radiation received by an object such as an infrared camera is more complex than the relation given by equation 2.12. Because of the complexity of these variables, their effect on the radiation received by an object is often lumped into an effective emissivity, ε_{eff}. It is common to refer to an effective emissivity for a common surface rather than a true emissivity. In this thesis, discussions about emissivity refer to the materials' effective emissivity.

Metals typically exhibit a decrease in emissivity with wavelength. Emissivity and effective emissivity are typically determined by three methods [ASTME1933]:

1. By referring to published tables;
2. By comparing the IR camera measurement with a thermocouple measurement or other standard;
3. By measuring the effective reflectance of an emitting object (Kirchoff's Law states that the effective emissivity + effective reflectance = 1) [REI1965].

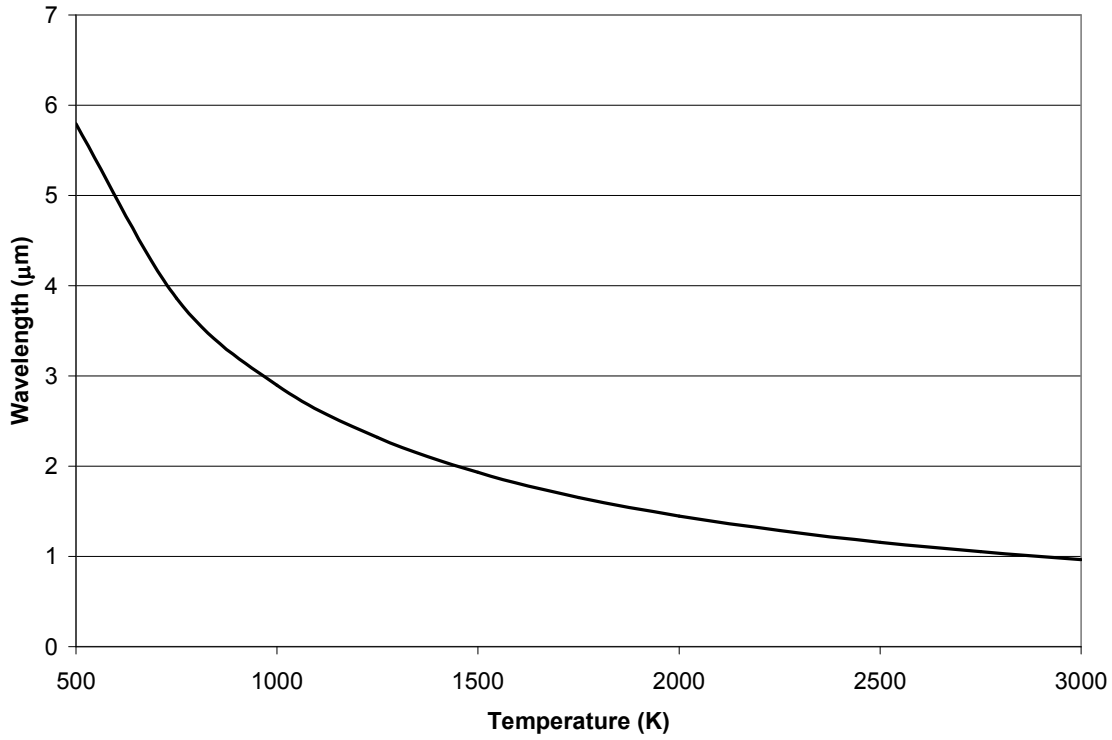

Figure 2.10: Maximum radiative wavelength for a corresponding temperature.

Method 1 is viable only for well documented applications, under steady state conditions. Method 2 is the best solution when the object of interest can by physically touched or the temperatures are low enough to apply black paints or tapes. However, in the PTAW scenario, the third method is the most practical to

apply in order to obtain emissivity values of the coating at high temperatures during solidification and as it cools.

Research in measuring emissivity or effective emissivity of metals at high temperatures with phase change is rare. The standard methodology does not apply to collect emissivity at high temperatures. A database of emissivities of metals at high temperatures over a range of wavelengths was mentioned [KOB1999], but the results were not made public.

2.7.2 IR Camera Use in Welding Applications

When selecting a non-invasive method for measuring temperature in welding research, several applications and approaches have been explored. Cooling rates were measured using an InSb (2-5.6 μm) camera [LUK1982]. The position of the heat affected zone [DOU1990] and the joint penetration depth [CHE1990] was monitored using an 8-14 μm HgCdTe detector. Mirrors were used to reflect the best field of view of the weld to the camera. Using a high speed camera, surface temperatures were obtained by measuring the spectral directional emissive power and spectral directional emissivity at specific wavelengths and angles through a HeNe laser [KRA1989]. The surface temperature of the solid area during thermal plasma processing was collected using a 1-spot low temperature monochromatic pyrometer, a 1-spot multiwavelength pyromenter and a 10x10 pixel high temperature monochromatic pyrometer [BER2000]. CCD cameras give clear, grey or colour pictures in the wavelength spectrum of 0.4-1.1μm. Filters of λ_1=0.8046 μm and λ_2=0.8943 μm were chosen to construct a two colour CCD thermal imager [JIL2003]. The camera was calibrated only in a narrow temperature range.

Many of the early IR temperatures reported were based not on absolute temperatures but on relative temperatures with respect to a reference on the plate. Infrared thermography was able to detect perturbations that result in welding flaws, such as joint mismatch and joint gaps [CHI1983]. In addition, because of

the costly nature of IR equipment, its application has been limited in welding research. Most measurements typically use low-cost point IR sensors, such as thin-film thermopiles for submerged arc welding process control [FAN2003].

Plasmas are highly luminescent and emit radiation in the UV range. For example, radiation interference in argon plasmas (Ar I – first energetic state) is prominent between 0.43 and 1.8 μm, shown in Figure 2.11 [RAL2008]. As the temperature of the plasma increases, more ionization levels are obtained. Even if all ionization levels were attained (Argon I - Argon IV), the radiation is limited to wavelengths less than 2 μm (Figure 2.12). To circumvent this, a bandpass filter and a shield were used with some success to remove the argon arc signal captured from a silicon photodiode detector [FAR1998].

More recently, infrared imaging in welding applications has been limited to studies of the back of the substrate [COB2007] [MAT2009], and the temperature field outside the area covered by the arc [HUA2007]. The current literature does not address definitively the camera type and data collection requirements in order to obtain temperatures of the weld pool while the welding is occurring. While it is evident from previous work that cameras capturing thermal intensities in both long- and short-wavelength range have been attempted, as well as a variety of lenses and camera angles, a direct and rigorous comparison of different infrared cameras operating within various wavelength range as well as filters and lenses in PTAW or any other welding operation has not yet been carried out. The above discussion shows that cameras capturing thermal intensities in both long- and short-wavelength regions were attempted, as well as a variety of lenses and camera angles. Further in this work, such a comparison will be presented along with the implications of the measurements obtained to understand the thermal history of the coating.

Accurate temperatures have yet to be reliably acquired during welding processes. Arc radiation interference and the knowledge of the variation of effective

emissivity with temperature, especially during a phase change, remain the principal challenges to address for reliable IR measurement of welding phenomena.

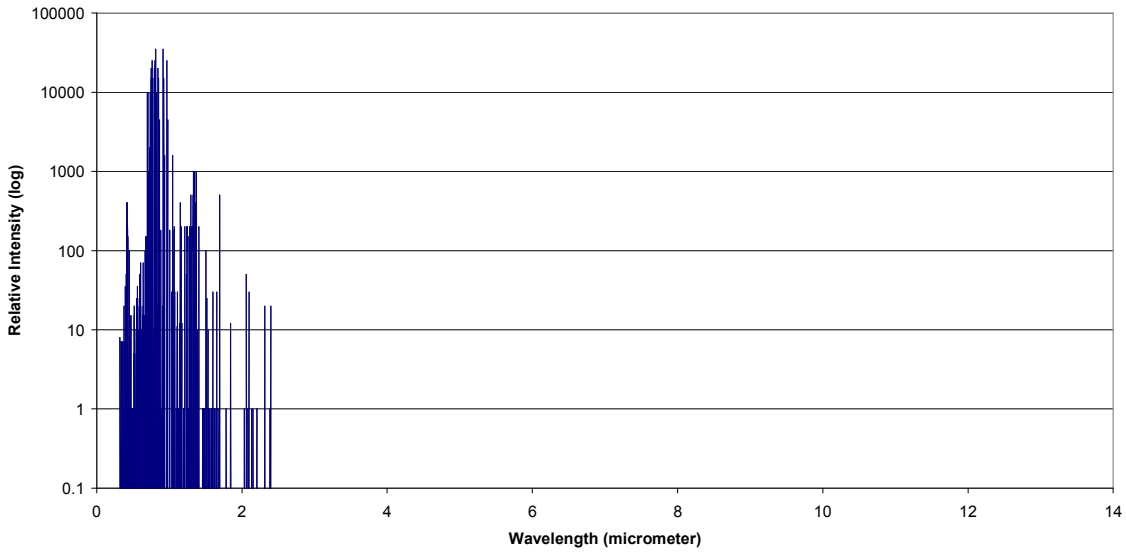

Figure 2.11: Argon I spectrum as a function of wavelength

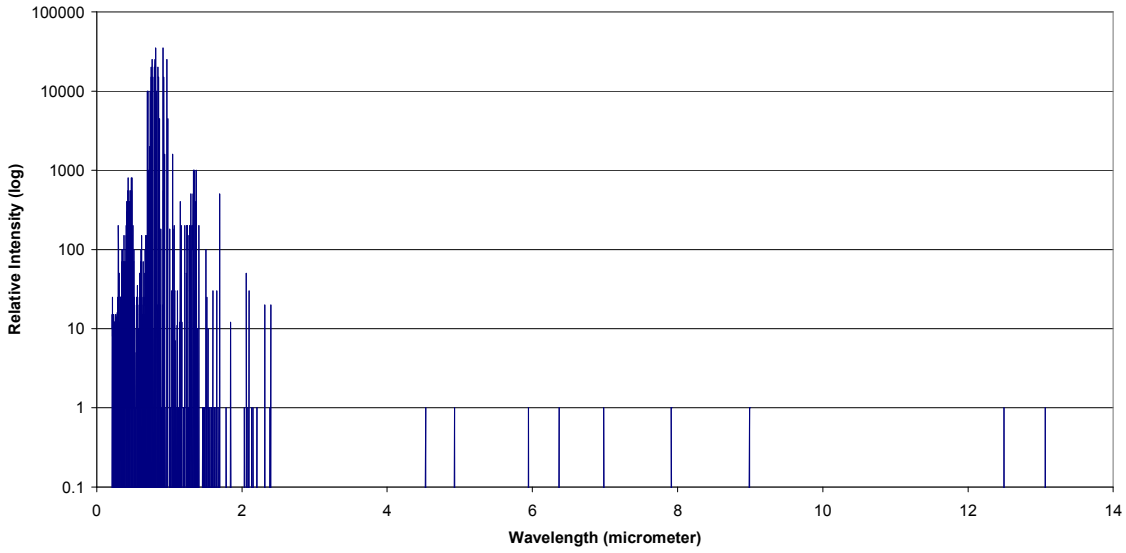

Figure 2.12: Argon I-IV spectrum as a function of wavelength

2.8 Summary

This chapter reviewed the relevant literature with regards to both the operational and modeling aspects of plasma transferred arc welding processes and the current prediction models to obtain a homogeneous metal matrix composite. The current phase analysis of the NiCrBSi-WC system was explored. The use of infrared thermal imaging measurements in welding systems was presented. The gaps of knowledge that this thesis will bridge are:

- a coupled solidification-settling model of the deposition of NiCrBSi-WC MMC using plasma transferred arc welding;
- the effects of powder injection on the symmetry of the plasma arc;
- the effect of heat input on the phases evolved in the NiCrBSi-WC system;
- a method for measuring actual temperatures of welds over phase changes using infrared thermography.

The following chapters will present the experimental procedures, results and analysis in order to obtain these knowledge gaps.

3 Experiment

In order to investigate the solidification and assess the coating homogeneity, the following experiments were conducted:

- Characterization of powder materials,
- Quantification of the WC distribution within the coatings,
- Measurement of the liquidus and solidus of the matrix metal,
- Measurement of coating temperature during deposition,
- Capture of the shape and intensity of the plasma arc,
- Identification of the secondary carbides and matrix of the deposit by scanning electron microscopy, and
- Abrasion resistance of the coating.

The degree of coating homogeneity was explored under a variety of PTAW operating conditions. In order to understand the solidification of the coating and heat transfer of the process, the melting range of the powder was measured, thermal imaging of the coating was performed and the shape of the plasma arc was characterized. The microstructure of coating was characterized to explore changes in the carbide with operating parameter. The effect of operating parameter on abrasion resistance was investigated.

The experimental methodology is detailed in this chapter.

3.1 Materials

3.1.1 Powder Material

The powder used was a combination of a NiCrBSi alloy, the matrix powder (Figure 3.1a), and tungsten carbide reinforcement particles (Figure 3.1b). The suppliers of the powders are proprietary. The chemistry of the matrix powder is shown in Table 3.1, as documented by the supplier. The hardness of the matrix

was 30 HR_C. The matrix and carbide powders were analyzed using a Siemens D5000 x-ray diffraction (XRD) Unit with a Cu source and energy of 45 kV and 30 mA. The XRD scan reveals that the matrix is primarily Ni based, with Ni_3B and $Ni_{16}Cr_6Si_7$ (Figure 3.2) and the tungsten carbide is macrocrystalline WC (Figure 3.3).

The standard MMC powder was a factory premix containing 50 v% matrix NiCrBSi and 50 v% monolithic angular WC. This will subsequently be referred to as the MMC mixed powder. The powders were sieved to measure the particle size range, and the data is presented in Appendix A. The size range of the MMC mixed powders is 45 to 180 μm. The WC powder size ranged from 63 to 106 μm, whereas the NiCrBSi powder ranged from 63 to 180 μm.

Mixtures of powders containing 10, 20, 30, 40 and 50 v% monolithic angular WC with NiCrBSi were also prepared. The conversion between volume percent and mass percent of WC in the MMC powders is tabled in Appendix A. This conversion is required for accurately mixing powders with a varying amount of WC.

Table 3.1: Elemental composition of Ni alloy powder

Element	***Wt%***
C	0.26
Ni	Balance
Fe	1.4
Cr	5.8
Si	3.9
B	.96
O_2	0.0068

A spherical cast W_2C/WC carbide (40-150μm) was also used as a reinforcement particle. There were two compositions, PS and RPS, as shown in Table 3.2. Energy dispersive x-ray (EDX) techniques were used to identify phase and elemental composition. The EDX equipment is described further in section 3.9.

The PS carbide contains less carbon than the RPS carbide. Shown in Figure 3.4 is the diffraction pattern of the PS carbide powder. The peaks indicate that there is a mixture of WC, W_2C as well as free tungsten and carbon. The RPS carbide powder diffraction pattern is shown in Figure 3.5. A mixture of WC, W_2C and free carbon is identified.

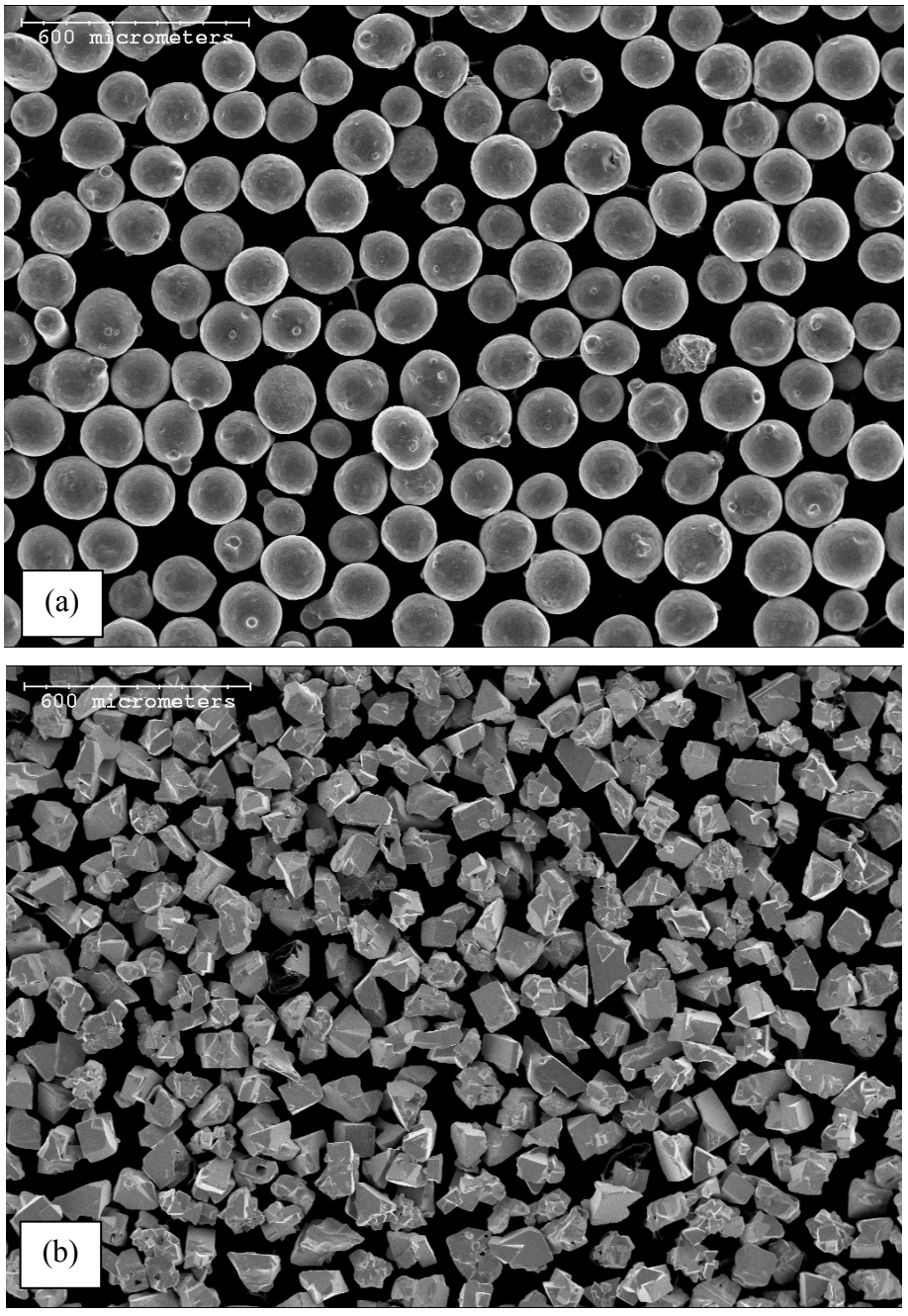

Figure 3.1: NiCrBSi powder (a) and monolithic WC (b), secondary electron image from SEM

Table 3.2: Semi-quantitative compositional analysis of spherical (WC/W_2C) powders determined from EDX quantification.

Powder	*W (wt%)*	*C (wt%)*
PS	95.51	4.49
RPS	91.56	8.44

3.1.2 Characterization of Packing Fraction of Powders

The random loose packing fraction of the angular and the spherical carbide powders with NiCrBSi was determined using the rapid inversion procedure [EPS1962] [EAS1969]. The fully packed monocrystalline powder yielded 50 vol%, whereas the spherical powders packed more densely to a value of 60 vol%. The spherical powders were also deposited with a volume fraction of 27 vol%, in order to note differences in weldability with the spherical powders. The values are summarized in Table 3.3, and both the morphology of the particles as well as their composition.

Table 3.3: Tungsten carbide powders used in MMC mixtures

Carbide Type	*Composition*	*Mass% of carbide in MMC*	*Vol% of carbide in MMC*
Standard angular	monocrystalline WC	65 (nominal)	50
Fully packed angular	monocrystalline WC	65	50
PS fully packed spherical	eutectic WC/W_2C	73	60
PS spherical	eutectic WC/W_2C	40	27
RPS spherical	eutectic WC/W_2C	40	27

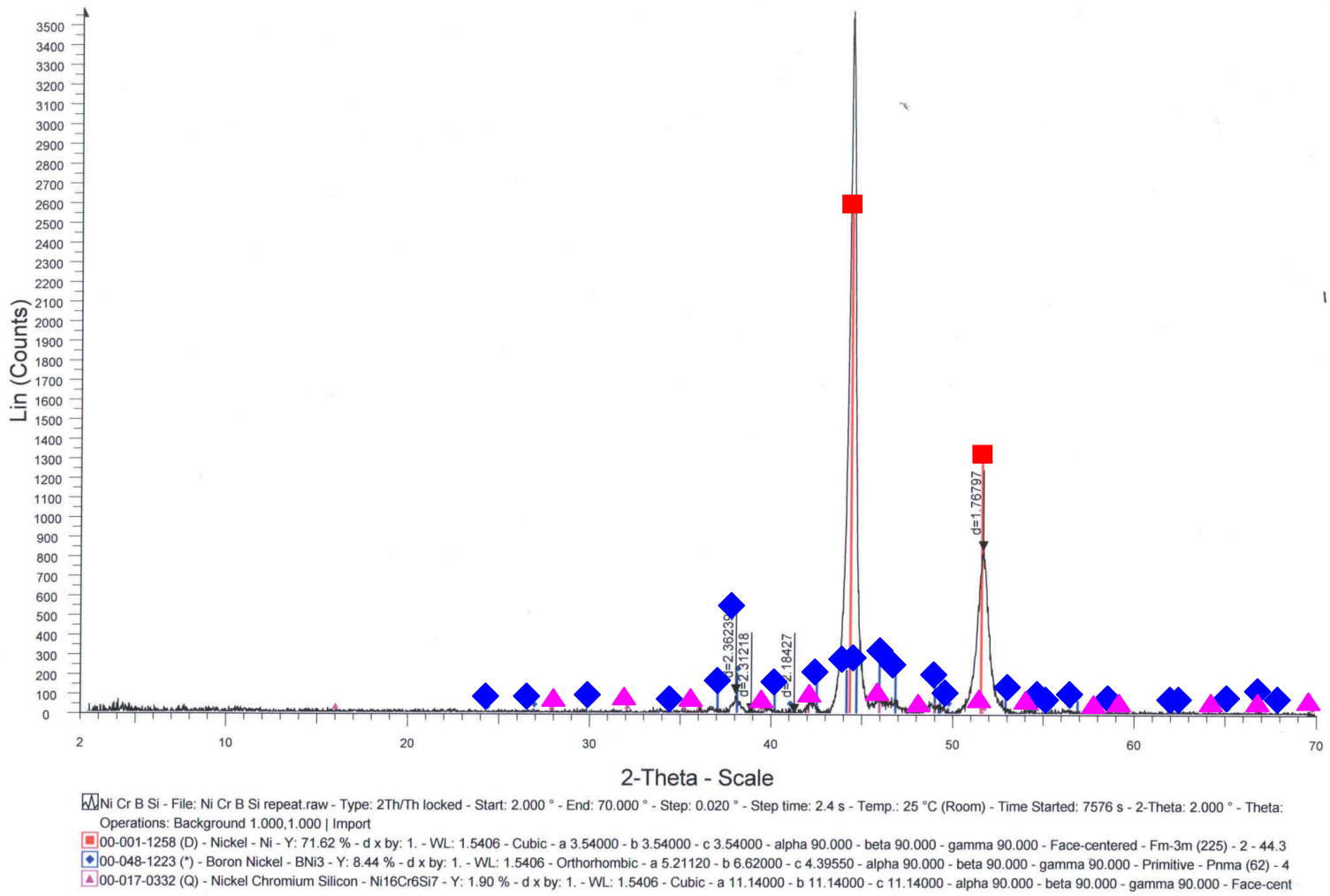

Figure 3.2: XRD scans of NiCrBSi (HRC 30). The matrix is primarily Ni (red square), but also Ni_3B (blue diamond) and a combination of Ni, Cr and Si ($Ni_{16}Cr_6Si_7$ - purple triangle).

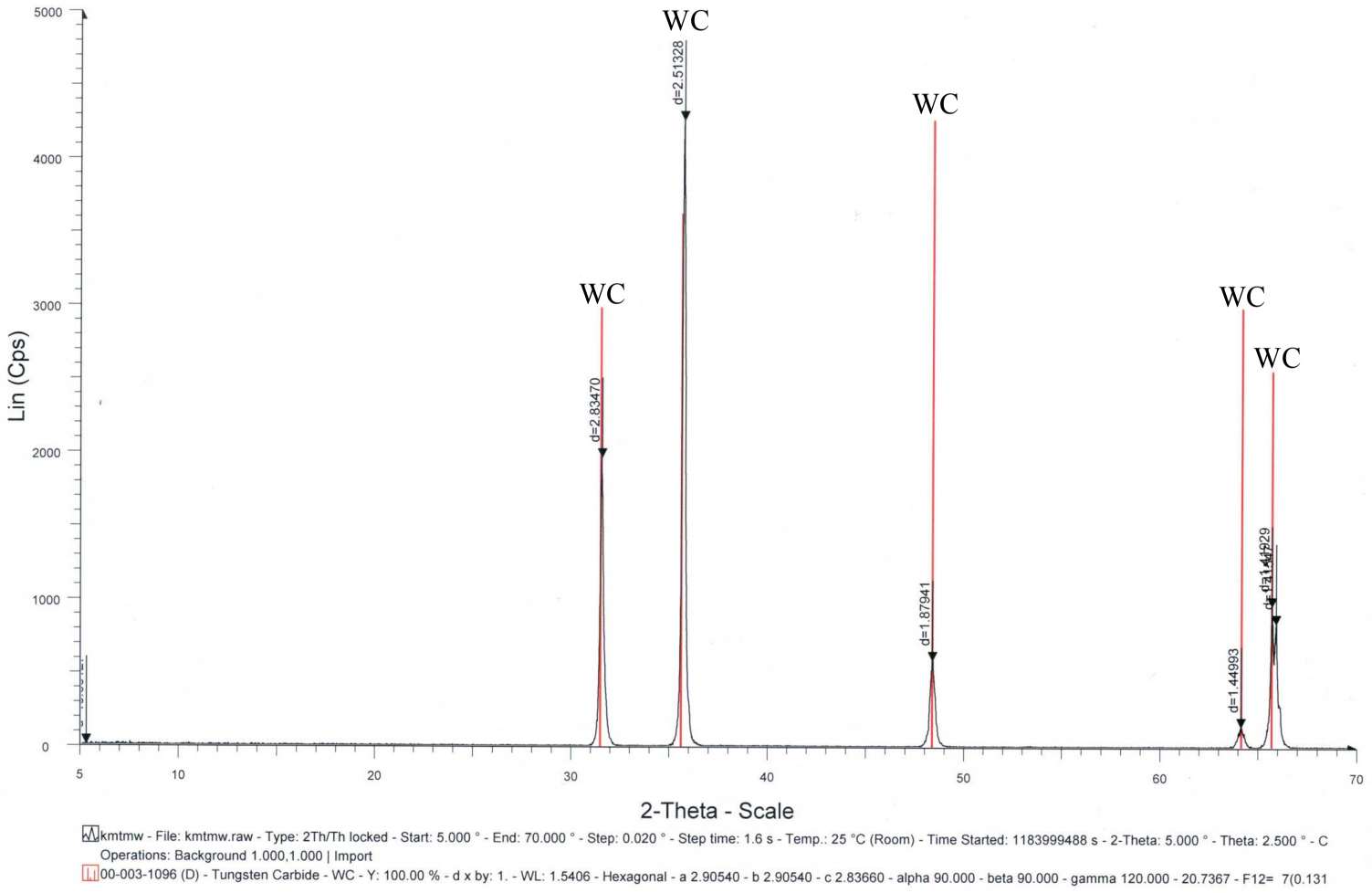

Figure 3.3: XRD scans of macrocrystalline tungsten carbide (WC).

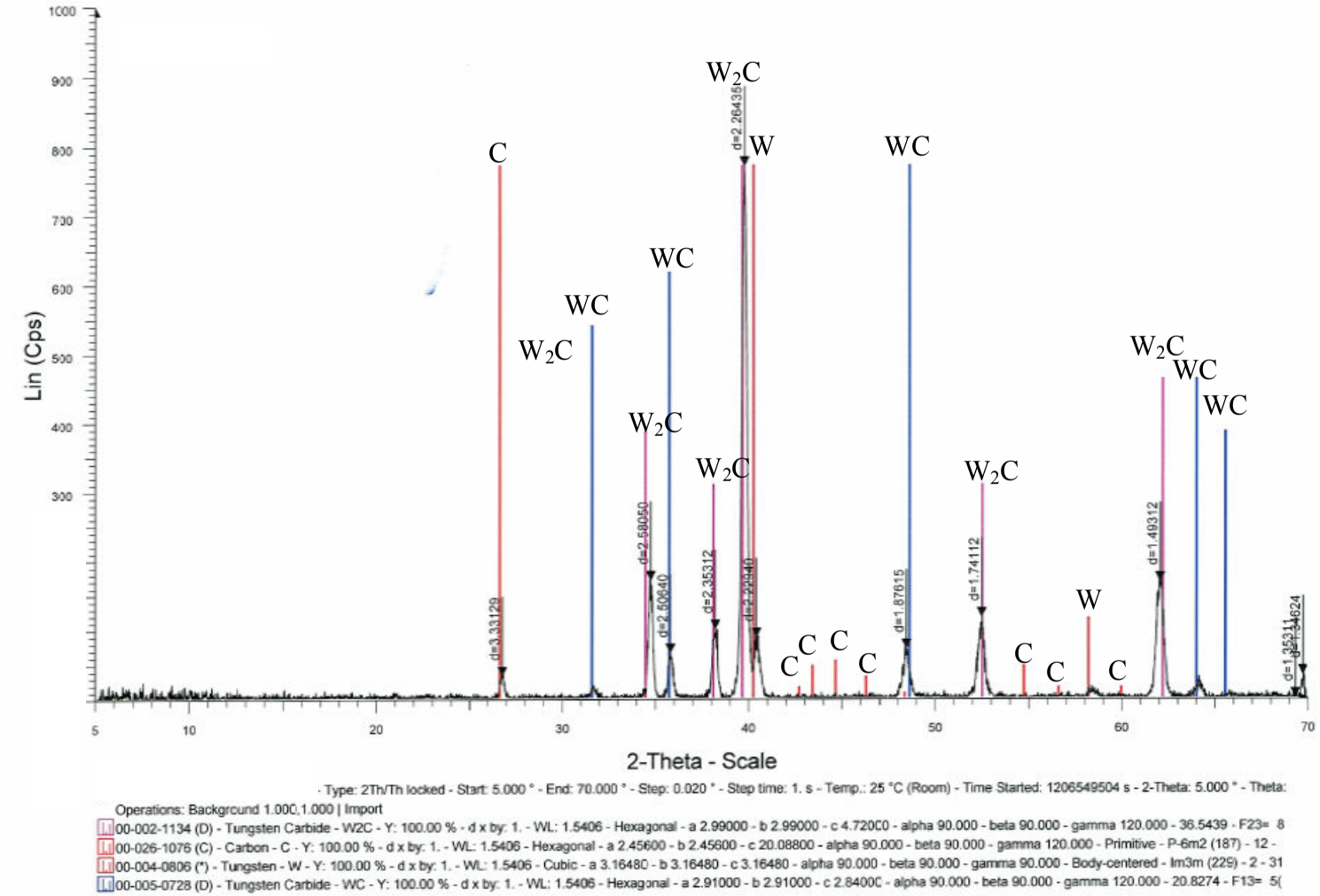

Figure 3.4: XRD scans of spherical tungsten carbide PS, a combination of WC and W_2C as well as free W and C.

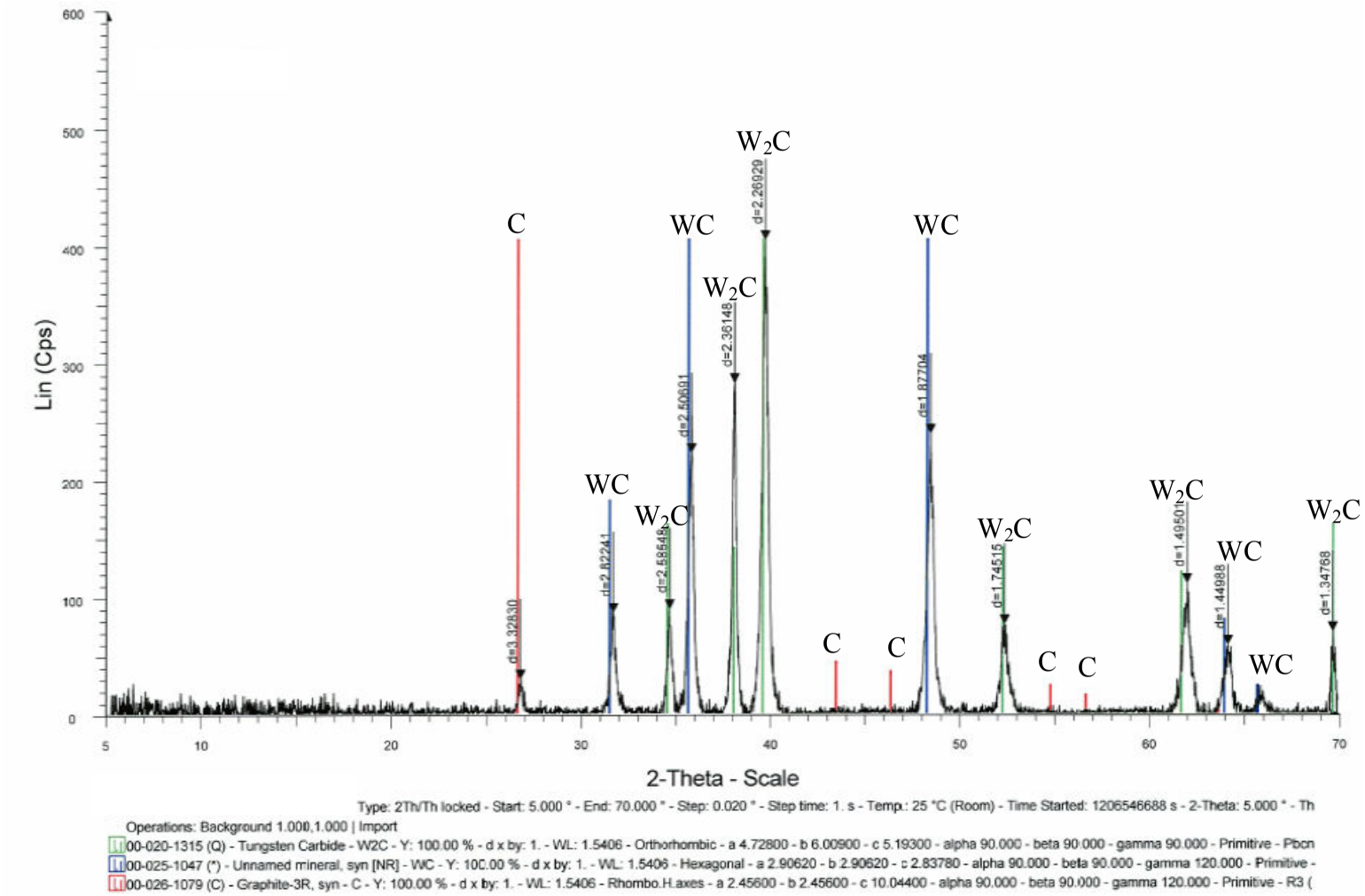

Figure 3.5: XRD scans of spherical tungsten carbide RPS. The carbides are a combination of WC and W_2C as well as free C.

3.2 PTA Equipment

The coatings were deposited using PTAW. This comprised of a EuTronic GAP 3000 AC/DC constant current power source, an EP 1 powder feeder, and a GAP E 52 torch (Castolin Eutectic Group, Eutectic Canada Inc., Granby, Quebec). The system is shown in Figure 3.6 as an image and in Figure 3.7 as a schematic. The 4 mm diameter thoriated-tungsten electrode was ground to an angle of 20° with a 0.5 mm diameter tip. The electrode tip was held 1 mm above the lower edge of the plasma nozzle bore. The torch was stationary and the table motion was controlled with the aid of a computer. Torch motion, welding speed, and the nozzle offset distance were set prior to each weld run. The powder was pre-mixed and poured into a single hopper. The speed of the bucket wheel controlled the rate that the powder was deposited into a venturi feeder. Argon gas was metered through the venturi as a constant flow rate to carry the powder to the nozzle. The powder was fed through the nozzle from 2 ports positioned 45° on opposite sides of the rear of the torch. Both stringer beads (5 mm wide) and 25 mm wide zig-zag coatings were deposited. Argon (99.9%) was used for the plasma gas, shielding gas and carrier gas. The gas flow rates were individually metered by ball valves.

The substrate used in the experiment was grade CSA 44W, which is typical as the base material of the mining equipment. The substrate dimensions were 38 mm wide x 19 mm high and 355 mm long. The substrate was clamped to the welding table to minimize thermally induced distortion.

3.3 Operational Parameters

3.3.1 Standard Tungsten Carbide Tests

A standard stringer bead was deposited under the conditions shown in

Table 3.4; the experimental range explored is also included. The powder used was the standard Ni-based powder with macrocrystalline angular WC. The deposition rate of the mixed powder was 27.22±0.32 g/min when the carrier gas flow was 1.4 lpm.

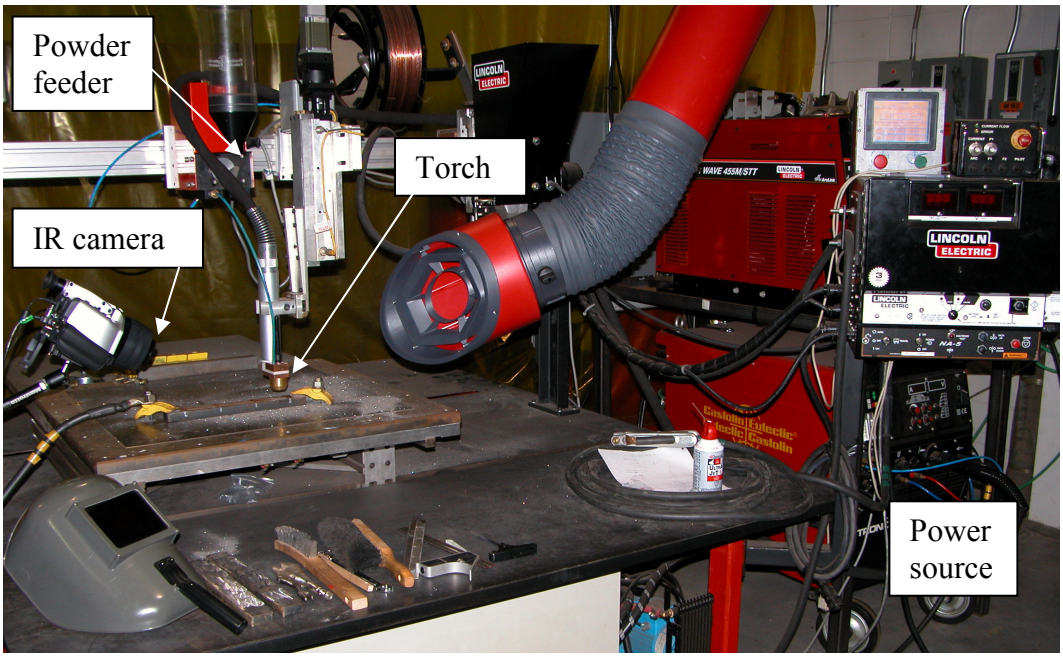

Figure 3.6: PTAW Equipment with Infrared Camera

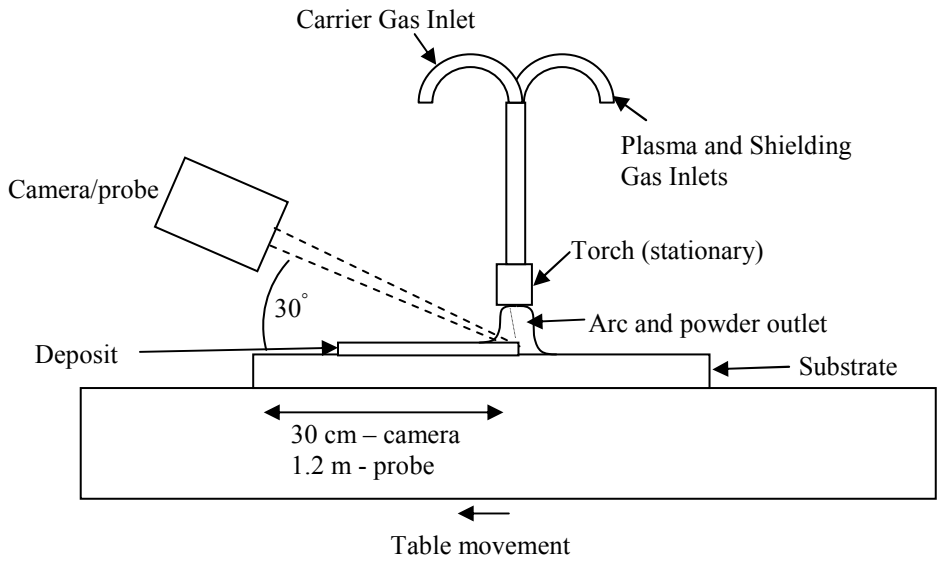

Figure 3.7: Schematic of experimental setup with infrared camera/emissivity probe.

Table 3.4: Experimental operational parameters tested for standard angular WC.

Parameter	*Standard*	*Experimental Range*
Current (A)	130	110-150
Voltage (V)	23.5	20-25
Travel Speed (mm/s)	3.81	3.81-7.62
Plasma Gas Flow (lpm)	2	1-4
Shielding Gas Flow (lpm)	9	7-11
Carrier Gas Flow (lpm)	1.4	1-2
Number of Passes	1	1-3
Volume % WC	50	10-50
Bucket Wheel Speed (%)	50	50

3.3.2 Other Tungsten Carbide Powders

Several types of tungsten carbide particles were tested. The angular monolithic WC powder was the standard configuration, however, spherical cast W_2C/WC carbide (40-150μm) was also briefly considered.

The deposition parameters to allow for a good coating are a function of the matrix and carbide type, as well as carbide fraction. Thus, the deposition parameters were adjusted slightly for the fully packed angular carbide and the spherical carbide, shown in Table 3.5. These powders were deposited as a 25 mm wide (nominal) bead as opposed to a stringer bead. The welding table moves in a zig-zig pattern under the torch rather than uni-directionally to form the deposit. The zig-zag pattern is that used in industrial application of the coating on the substrate. Thus, there are two speeds required to complete the zig-zag pattern: one transverse (oscillation speed) and one longitudinal (travel speed). The amplitude is the width of the oscillation. A bead width of 25 mm is required for abrasion wear testing.

Table 3.5: Experimental operational parameters tested for tungsten carbide variation

Parameter	*Standard*	*Fully packed angular*	*Spherical*
Current (A)	130	145	145-147
Voltage (V)	23	23	23
Travel Speed (mm/s)	0.64	0.64	0.43-0.51
Oscillation Speed (mm/s)	9.1	9.1	7.6-9.1
Amplitude (mm)	22.5	22.5	19.5
Plasma Gas Flow (lpm)	2	2	2
Shielding Gas Flow (lpm)	9	9	9
Carrier Gas Flow (lpm)	2.5	2.5	1.7

3.4 Sample Preparation

The coatings were prepared metallographically. A section from the deposit was cut at least 3 cm from the start of the deposit to ensure steady state conditions were achieved. A schematic of the location the samples were cut from the deposit is shown in Figure 3.8. The cuts were made with a Buehler cut off saw using a 12" Dynacut® resin bond diamond impregnated blade and a 12" Buehler aluminum oxide with resin blade (10-4410) (Buehler Canada, Whitby, Ontario, Canada). A small slice was cut from the section using the Struers Accutom-5® with a feed rate of 0.02-0.04 mm/s using a diamond impregnated 330CA blade at a speed of 3000 rpm with HIGH force (Struers Ltd., Mississauga, Ontario, Canada). Both longitudinal and transverse sections were captured. The sections were mounted in Struers DuroFast® and MultiFast® using the Struers Labo-Press 3®. The pressing conditions for a 40 mm mount included a heating time of 6 minutes at 180°C, a cooling time of 3 minutes and a pressing force of 30 kN. The mounted samples were polished on a Struers TegraPol-31® system using the TegraDoser-5® and TegraForce-5® attachments. The polishing sequence is listed in Table 3.6.

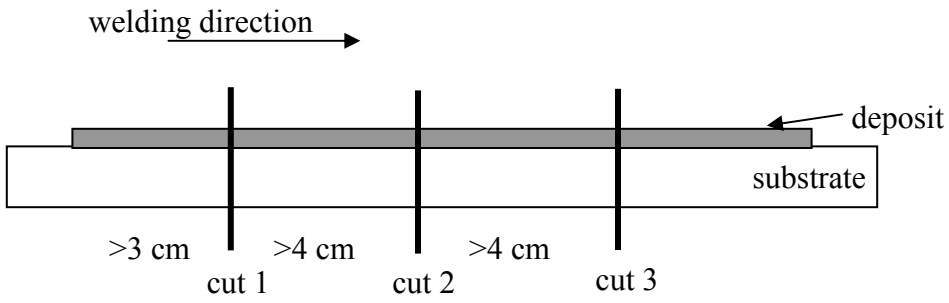

Figure 3.8: Schematic of sample location from deposit

Table 3.6: Polishing sequence of WC/NiCrBSi using Struers™ products

Condition	*Surface*			
	Piano 220®	***Allegro®***	***Pan®***	***Chem®***
Speed (rpm)	300	150	150	150
Abrasive	-	DiaPro Allegro/Largo® (9 μm)	DP-Susp® 3 μm	OP-S® 0.04μm
Lubrication	Water	-	DP-Green	
Time (min)	2	7	5	1

3.5 Quantification of Homogeneity

The carbide distribution in the deposit was visible under an Olympus PMG3 optical microscope. Images were taken with 50x magnification of the entire deposit sample. The images were captured with an Olympus Q Colour 5 camera and Quartz PCI v5 software. The sequence of quantifying the amount of WC particles as a function of depth in the coating is illustrated in Figure 3.9 and is described below. The images shown here are for a 50vol% WC MMC run under standard operating conditions. Individual images were stitched together, and processed using the image analysis toolbox within MATLABv7. The programming code is found in Appendix C. The original images (Figure 3.9a) were converted to black and white; the edges were found (Figure 3.9b) and filled (Figure 3.9c). The image was cropped to only include the deposit (Figure 3.9d). The image was sliced into 20 vertical and horizontal sections (Figure 3.9e) and the percent of white pixels was calculated for each section. This number of

sections was chosen in order to appropriately quantify the amount of carbide settling. The average and standard deviation are calculated along each row. Measurements were only taken with full thickness deposits.

Shown in Figure 3.10, sectioning the image into 20 vertical slices yields the best balance between resolution and noise. As the number of sections decrease below 20, the resolution in the depth below 40% is deteriorated. If the number of sections increases beyond 20, the size of the section becomes smaller than the carbide size and the signal becomes noisy. When the number of sections decrease below 20, the measurement sensitivity is compromised. The size of each vertical section is dependent on the number of slices. Shown in Figure 3.11 is the size of the cell in terms of the number of nodes, or slices taken, for a deposit with a thickness of 3 mm. If 20 slices are taken, the cell size is approximately 0.15 mm, or 150 μm. The mean reinforcement particle size is 150 μm. As the number of slices increases past 20, the cell size gets much smaller than the particle size. The sensitivity of the measurement and the size of the cell need to be balanced, and it was shown that the best combination occurs with 20 slices.

The percentage of white pixels was the amount of WC present in the section. The WC distribution could be measured through the depth or length. Shown in Table 3.7 are the measured values of carbide for the image presented in Figure 3.9 as the average value for each section and the horizontal variation. There is some variation over the horizontal sections due the small changes in coating thickness as the coating is deposited (shown in Figure 3.9a). This method of quantifying carbide fraction was verified against a similar one used by Neville et al. [NEV2006]. The method illustrated in Figure 3.9 resulted in a total value of 51.6 vol% WC and that of Neville was 51.53 ± 0.02 %vol WC. It can be concluded that the carbide quantification method used in this thesis correlates well with that used by other researchers. The measurements taken in this approach are area fractions and not volume fractions. However, DeHoff [DEH1968] concluded that area percent is a satisfactory measure of volume percent.

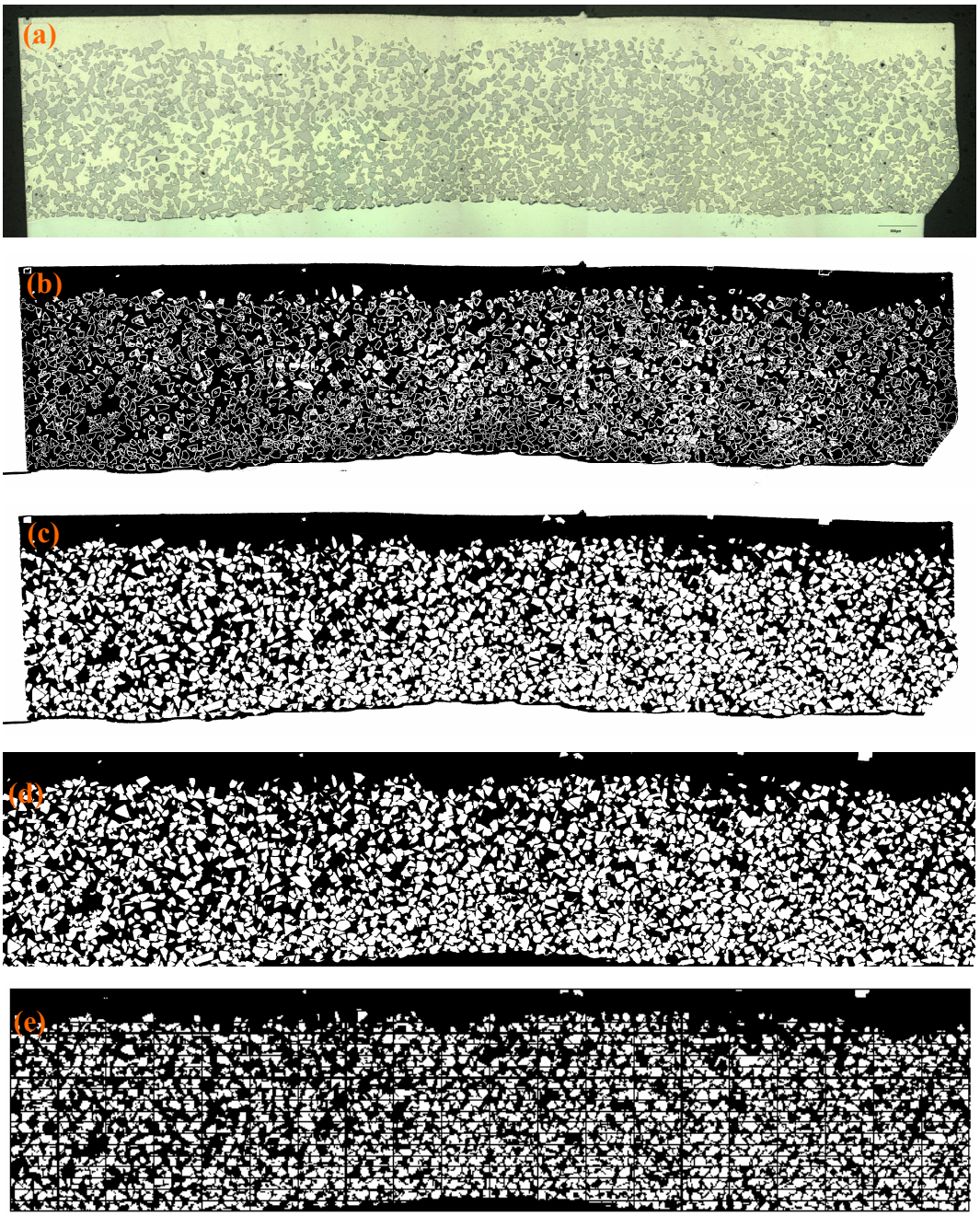

Figure 3.9: Image analysis map for quantifying WC distribution, (a) optical microscopy, (b) outline, (c) fill, (d) crop, (e) section. The thickness of the coating is approximately 3 mm.

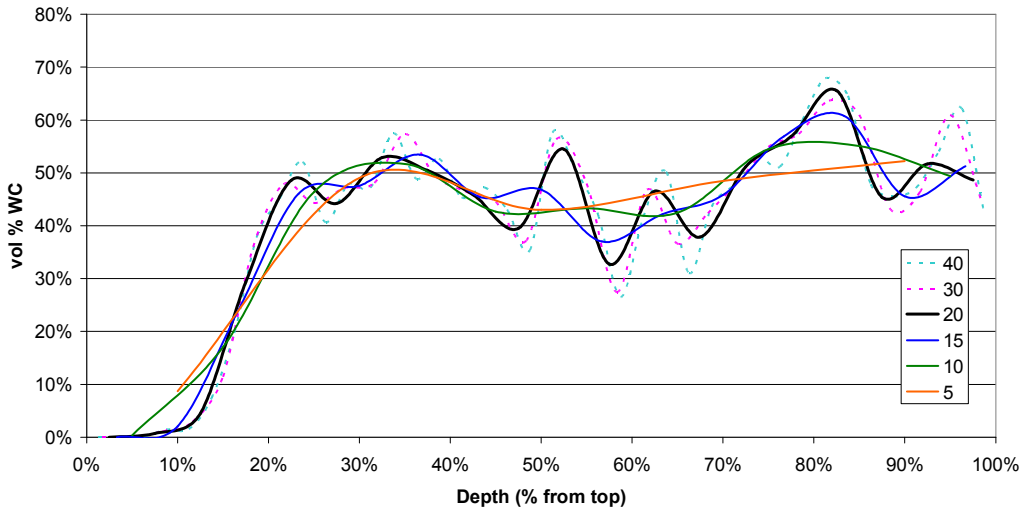

Figure 3.10 : Sensivity of number of sections above image is divided into on homogeneity through the depth.

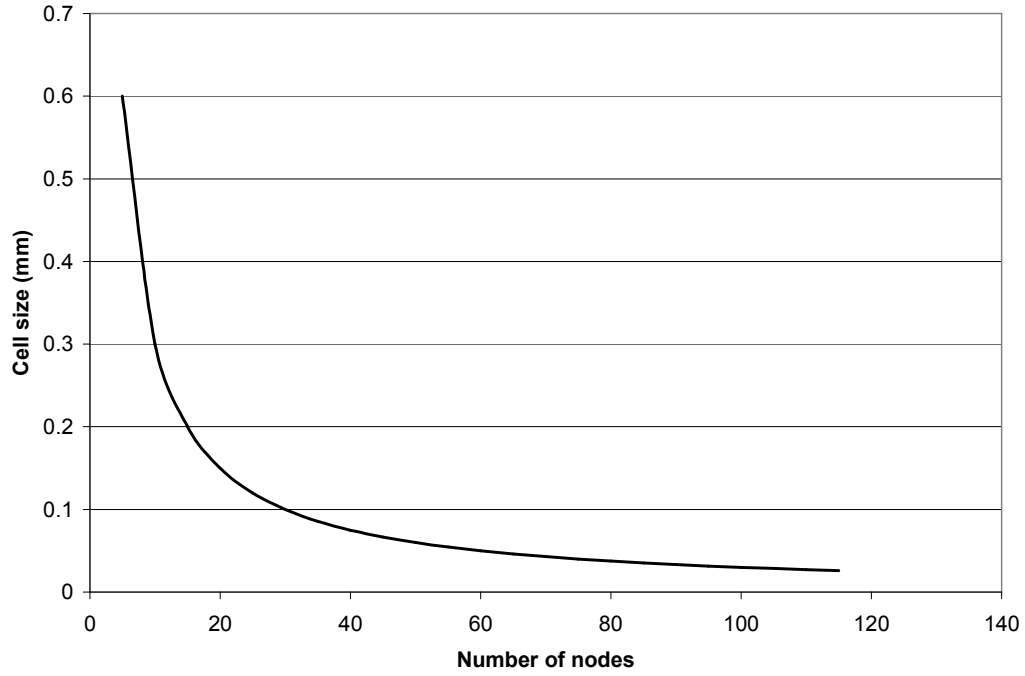

Figure 3.11: Relationship between cell size and number of vertical slices for a deposit thickness of 3 mm. The typical particle size is 0.15 mm.

Table 3.7: Measured values of fraction of white pixels (carbide) from Figure 3.9, showing the average value and variation for each section across the image.

Depth (from surface), %	*Average in cell,%*	*Horizontal variation,%*
5	40	15
10	53	11
15	57	8
20	49	20
25	50	15
30	54	9
35	56	7
40	54	8
45	55	10
50	54	10
55	56	11
60	55	9
65	56	7
70	58	7
75	58	7
80	54	9
85	51	9
90	47	11
95	38	11
100	35	12
Overall	51.6	6.6

3.6 Differential Scanning Calorimetry

The liquidus and solidus of the matrix and the matrix and carbide were measured using high temperature differential scanning calorimetry equipment from Netzsch (Netzsch Instruments N.A. LLC., Capitola, CA, USA). The STA 449 C Jupiter® simultaneous thermal analyzer measured the mass change and transformation energetics of the powders. The system was equipped with a SiC furnace and operated over the temperature range of 25 to 1200°C. The heating rate was 10 K/min in an inert environment of argon with 2% H_2. The sample holder was a TG-DSC type S and the crucible was Pt-Rh with an alumina liner (yttria coated).

The sample masses were 47.33 mg and 46.22 mg for the NiCrBSi and NiCrBSi + WC powders, respectively.

3.7 Temperature Measurement

Several methods to measure the temperature of the coating during the deposition process were attempted. Initially, contact methods were considered to obtain temperature data of the substrate. Although this method yielded no results, the experimental setup is described below.

Since the maximum temperature thermocouples can read in this environment is approximately 1800°C and it is unsafe to immerse a thermocouple into a welding arc, a non-contact method to determine the surface temperature – in particular, the coating temperatures next to the arc – was required. This method will be described in section 3.7.2.

3.7.1 Contact Methods

The substrate was instrumented with both Type B and Type K thermocouples, inserted into the side of the substrate. The type B thermocouple was a single ceramic sheathed exposed thermocouple; the diameter of the wire was 1.27 mm and the diameter of the sheath was 1.8 mm. The type K thermocouple was metal sheathed with an unexposed end with the same dimensions. The thermocouples were kept in constant contact with the substrate by a supporting device and clamps. Shown in Figure 3.12 is a schematic of the instrumented substrate; the torch is moving perpendicular to the page. The support bar is secured to the welding table. The thermocouples were inserted through the support bar and into the substrate. The engineering drawings for the placement of thermocouples into the substrate and the thermocouple support system are shown in Figure 3.13a and b. The size of the holes were 1.9 mm in diameter, located 2 mm from the top and bottom surface, as well as at the centerline. The thermocouple data was collected in real-time by an INSTRUNET data acquisition system.

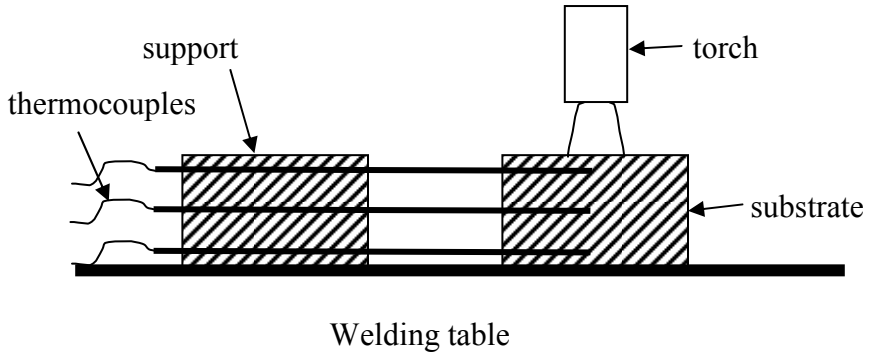

Figure 3.12: Schematic of placement of thermocouples during welding

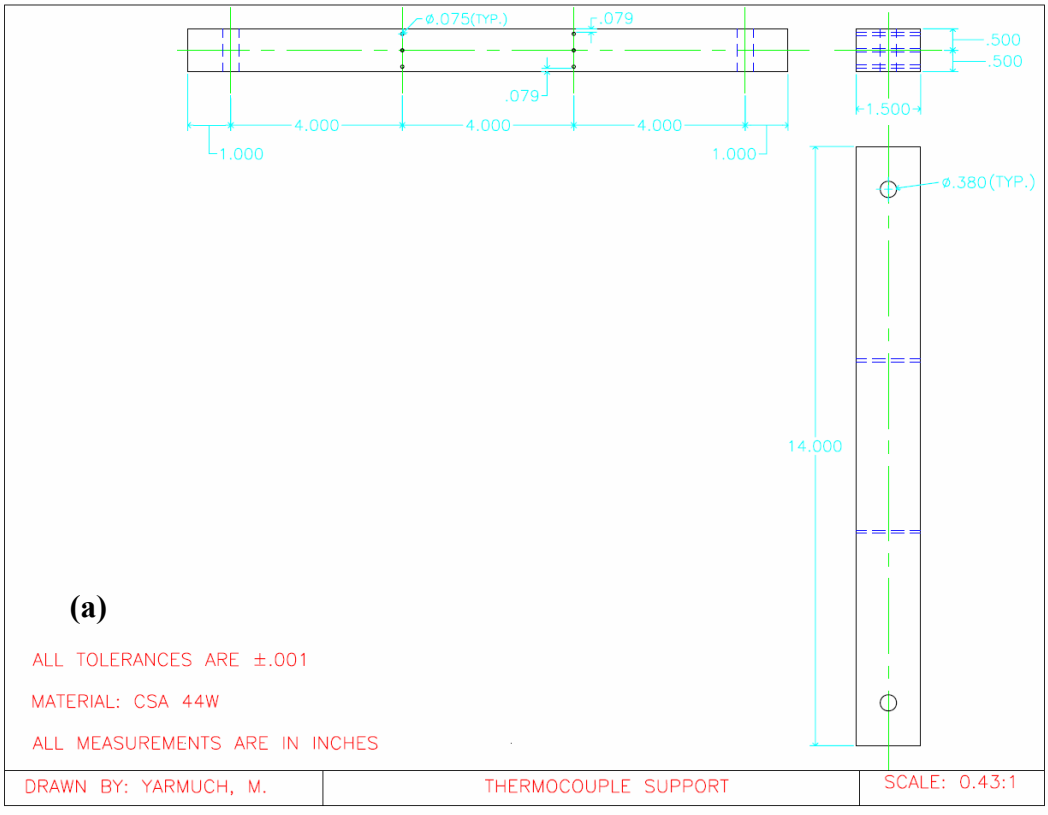

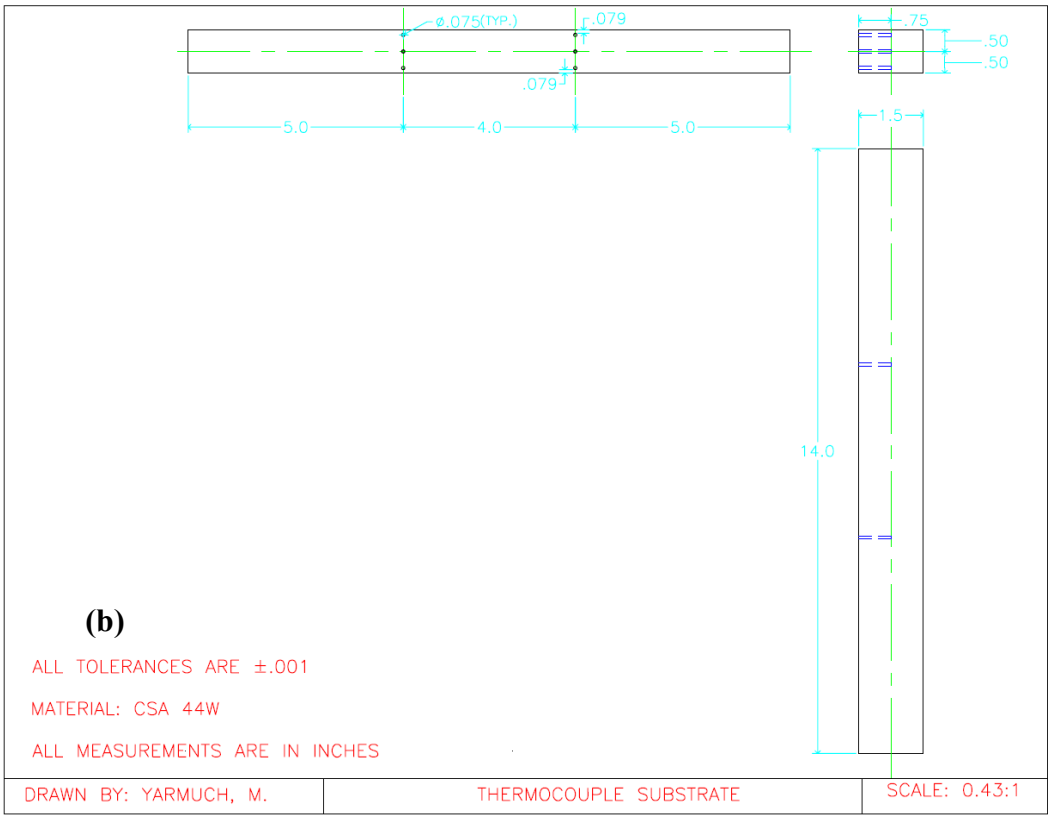

Figure 3.13: Thermocouple Support (a) and Substrate (b) Drawings

3.7.2 Infrared Thermography

To select a camera to measure temperatures of a welding operation, the issues that need to be considered are temperature sensitivity, background interference, size of the region of interest and focal distance, temperature range, and data acquisition rate. In this work, three cameras were selected: one in the near infrared region (0.9-1.7 μm) and two in the long wavelength (8-14 μm) region. The cameras were chosen based on the need to have good sensitivity at high temperatures and to eliminate or reduce the interference of the argon arc on the image. The temperatures and resulting images obtained during welding were evaluated.

It is challenging to select an IR camera that has good sensitivity at higher temperatures but shows no interference with argon plasma radiation. The relative sensitivity of a blackbody was shown in Figure 2.10; as the wavelength increases

there is very little difference in the energy absorbed from a body at 1000°C or 3000°C. To optimize signal sensitivity, it is desirable to limit the sensor wavelength to less than 2.5 μm for this application – ideally between 0.8 and 2 μm. Commercial IR cameras are available in the near-IR (0.9-1.7 μm), mid-IR (2-5 μm) and long-IR (8-14 μm) ranges. In addition, the lower the wavelength range of the camera, the less susceptible the temperature error due to changes in the object's emissivity.

A camera with the best sensitivity at the higher temperature regions would experience significant interference with the plasma, that is, the camera would absorb radiation from not only the substrate but the plasma as well. The welding arc (argon plasma) emits radiation at wavelengths up to 1.6μm (Figure 2.12). A camera with the best sensitivity at the higher temperature regions would experience significant interference with the plasma; the camera would absorb radiation from not only the substrate but the plasma as well. There are no reports of any spectral activity above 2.5 μm in the argon I spectrum, which made the long wavelength cameras ideal for measure surface temperatures of coatings during welding as the arc would be invisible. To alleviate the interference problem at the low wavelength region, the lens could be fitted with a filter which is not transmissive in the regions of high argon intensity. A lower wavelength camera is more desirable as the error in changes in the surface emissivity is significantly smaller than at higher wavelengths.

The IR cameras used to capture the surface temperatures of the coating during deposition were the MiKron 7600Pro (Alpha), the MiKron M9103 (Gamma) and the FLIR ThermaCAM P640 (Beta) (MiKron Infrared, Inc., Oakland, New Jersey, USA, FLIR Systems Ltd., Burlington, Ontario, Canada)– a summary of basis specifications is listed in Table 3.8. The 7600Pro and the P640 are essential identical in operation in that they are both long wavelength cameras (8-14 μm), however the resolution of the 7600Pro is 320x240 pixels and the P640 is 640x480 pixels. Both cameras can measure temperatures up to 2000°C. The M9103 is a

narrow band near IR wavelength camera (around 1μm), is more suitable for high temperature measurements and has a resolution of 640x480 pixels. The M9103 was also outfitted with a narrow lens filter of 1.06 to 1.08 μm. All three cameras capture real-time sequences of the process. Images can be selected from the sequences and the thermal data can be analyzed in any geometric configuration as a profile in a single image, or as an average/maximum/minimum over time.

Table 3.8: Key specifications of three infrared cameras used to measure weld pool temperature of PTAW.

Specification	*MiKron 7600Pro*	*FLIR ThermaCAM P640*	*MiKron M9103*
Wavelength	8-14 μm	7.5-13 μm	Around 1 μm
Image resolution	320x240 pixels	640x480 pixels	640x480 pixels
Camera capture rate	60 fps	60 fps	30 fps
Focal length (min)	0.3 m	0.3 m	1 m
Temperature range	-40°C to 2000°C	-40°C to 2000°C	600°C to 4000°C
Accuracy	2% or 2°C	2% or 2°C	1% or 1°C
Resolution	0.6°C	0.06°C	1°C

The two long wave cameras were mounted approximately 0.3 m away from the torch in order to obtain the best possible image with the lenses available, shown in Figure 3.6 and Figure 3.7. The M9103 camera had a focal length of 1.2 to 2 m, depending on the lens and filter combination. It was critical that the gallium infrared lens not become damaged by the weld spatter.

3.7.3 Emissivity Measurements

The emissivity measurements are critical in obtaining a true temperature from the infrared camera. The emissivity measurements were obtained using a MiKron MQ 3600 Quantum II Laser Pyrometer. This device measures the intensity of a laser at either 0.9 μm or 1.55 μm as it is reflected off a surface of interest. The emissivity is calculated as the ratio of the initial and returning intensities. The temperature is determined by the Planck equation, shown in equation 3.1. The data is obtained in real time through Microsoft Hyperterminal. The

communication parameters in Hyperterminal must be set to BAUD 9600, DATA BITS 8, STOP BITS 1 and PARITY NONE.

$$T = \frac{h_P c}{\lambda k_B}\left[\ln\left(\frac{\varepsilon}{M}+1\right)\right]^{-1} \tag{3.1}$$

The emissivity pyrometer was positioned at the same location as the infrared camera, as shown in Figure 3.7. The orientation of the emissivity probe was identical to that of the infrared camera; however, the probe was located 1 m away from the substrate surface to ensure the image was in focus. Measurements of the emissivity of the surface were collected over for the entire duration of the deposition of the coating, including arc initiation and extinguishing.

3.8 Plasma Arc Images

The plasma arc runs were recorded using a Sony DXC-390 1/3-type three-chip CCD digital camera with 770 (horizontal) by 500 (vertical) effective picture elements operating at 30 frames per second with a shutter speed of 1/4000. The filter pack included one polarizing filter, three ND4 and one ND2 neutral density filters, and a P-452 protective lens. The positioning of the apparatus is shown in Figure 3.14; the camera position was held constant and the welding direction was modified such that front and side views could be obtained.

The plasma arc images were captured for autogeneous runs, powder with matrix only and powder with matrix and carbide. Standard runs were obtained as well as increases in current to 150A, plasma gas to 4 lpm and travel speeds to 7.62 mm/s.

The images were analyzed using MATLAB image analysis toolbox programming language. The code is located in Appendix C. The program turned the colour image to grayscale and sought the location of the maximum intensity. The size of the plasma arc was also measured from the data.

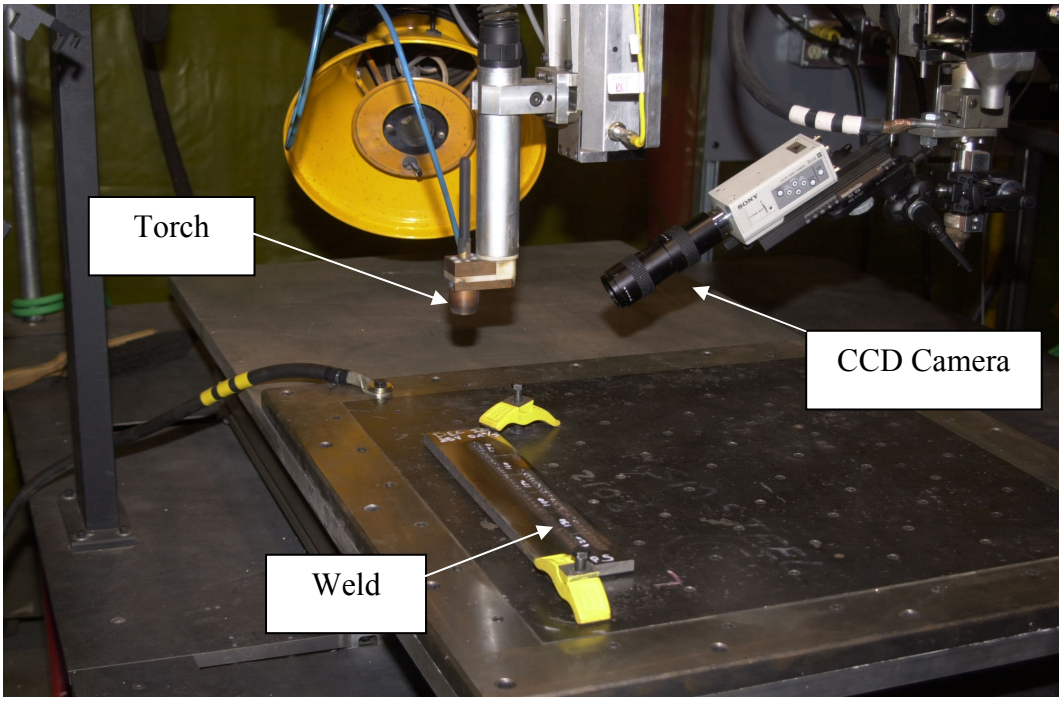

Figure 3.14: Experimental setup for plasma arc image acquisition

3.9 Scanning Electron Microscopy

The coatings were also examined using scanning electron microscopy (SEM). The metallographically prepared deposits were coated in an ultra-thin layer of gold, deposited by low vacuum sputtering. This layer was added to prevent the buildup of static electric fields on the specimen due to the electron irradiation required during imaging. In addition, the gold coating improves surface conductivity allowing for an improvement in imaging contrast. Semi-quantitative elemental analysis was performed using energy dispersive x-ray (EDX) techniques of points, lines and areas.

There were two SEM-EDX systems used to visualize the powders and coating as well as quantify the elements. The primary system consisted of a Hitachi S-2700 Scanning Electron Microscope equipped with a PGT (Princeton Gamma-Tech) IMIX digital imaging system and a PGT PRISM IG (Intrinsic Germanium) detector for Energy Dispersive X-Ray Analysis. The Backscattered Electron

Detector is comprised of a GW Electronics System with 47 four quadrant solid state backscattered electron detectors. The accelerating voltage used for capturing images and performing EDX analysis was 20 kV. The second system was a Hitachi S3400N scanning electron microscope at an accelerating voltage of 20kV. The elements present in the coating were detected by an Oxford INCAx Sight 7490 EDX detector. Boron could not be detected and carbon could not be quantified using EDX due to low fluorescence yield, overlap of peaks and high mass absorption near the surface.

3.10 Abrasion Resistance Testing

ASTM G65 Dry Sand/Rubber Wheel Tests [ASTMG65] were performed to measure the coatings performance in terms of the particle size, particle fraction and particle shape. The test load was 30 lb and the sand type was 50/70 silica flowing at a rate of 240 g/min. Two tests of 6000 revolutions were performed; the second was repeated over the first wear scar. The wheel diameter was 9 inches.

4 Experimental Results and Discussion

The results of the experimental study of the homogeneity of the coatings are presented and discussed. In order to understand the factors which contribute to inhomogeneity, the extent of the problem was initially established.

The degree of inhomogeneity in the wear resistant coatings was quantified, using the image analysis technique described in Section 3.5, under a variety of deposition conditions. The parameters explored were current, voltage, plasma gas flow rate, shielding gas flow rate, carrier gas flow rate, travel speed and volume fraction of carbide. The intent of this study was to discover the parameters which correlated with changes in inhomogeneity.

Images of the plasma arc were captured during the welding process to quantify the change in shape of the arc with the addition of the powder. The position of the powder particles was tracked and the particle velocity was estimated. This work yielded a greater understanding of the heat input of the welding arc in PTAW compared to GTAW.

Infrared thermography was used to measure the temperature of the surface of the deposit during the welding process. The relationship between operational parameter, surface temperature and homogeneity was investigated. In order to obtain a true temperature measurement, the emissivity of the deposit was measured using laser reflectometry. The emissivity was a function of temperature over the melting region of the MMC. The liquidus and solidus of the matrix were measured using differential scanning calorimetry. The measured temperature was adjusted using a correction algorithm. The temperature measurements allowed an understanding of the relationship between welding temperature, homogeneity and the process conditions.

The effect of heat input on the metallurgy of the coating was investigated by scanning electron microscopy. Both angular monolithic carbides and spherical eutectic carbides were studied. The degree of tungsten carbide dissolution was explored to understand the effects of welding temperature on coating properties other than inhomogeneity.

The wear resistance of the angular and spherical carbide MMC coatings was measured using ASTM G65 abrasion tests. This test is the industrial standard used to quantify improvements in coating design.

4.1 Quantification of WC Distribution

Coatings were deposited using PTAW under a variety of conditions: current, voltage, plasma gas flow rate, shielding gas flow rate, carrier gas flow rate, travel speed and volume fraction of carbide. The coatings were sectioned and observed under an optical microscope. The amount of WC in the deposit was measured using image analysis as a function of the coating thickness. It was hoped that the operating parameters that contributed to a more homogeneous coating would be revealed.

4.1.1 Benchmark of Homogeneity

To establish a benchmark, six coatings were deposited under standard operating conditions (Table 3.4), with an initial carbide volume fraction of 50 vol% WC. These conditions were previously established for the MMC as they yielded a visually acceptable coating that adhered to the substrate. The results for the benchmark test are shown in Figure 4.1 and a random selection of three of the corresponding metallurgical cross sections are shown in Figure 4.2. The depth is measured from the surface of the deposit (0%) to the substrate (100%). The error bars are the standard deviation of multiple measurements made within a coating image. The points represent the average values at each location in the depth of

the coating for each test. The black line is the average carbide amount based on the six tests.

Upon inspection of the optical micrographs (Figure 4.2), the three images appear very similar. There is a region at the surface depleted of carbide. The amount of carbide increases suddenly around 15% of the depth of the surface. There are small regions void of carbide, randomly distributed throughout the coating. The carbide appears to be more densely packed near the substrate surface. The average carbide volume fraction presented in Figure 4.1 matches the profile shown in the optical images.

However, Figure 4.1 shows that there exists a high degree of variation of the volume of carbide both within the entire sample and between each sample. At each depth position, the average amount of carbide measured over 3 images varied up to 25%, as shown by the different marker styles. The error bars for each test were typically around 10%. Hence, the carbide amount at any depth ranged between 25 to 50% of the average measurement. This indicated that a high degree of variation is inherent to the process itself, even when all parameters are held constant. The largest area of variation occurs when the depth is up to 30% from the surface. The variation is a result of the presence of the random void regions, which can be contributed to the loose packing and settling characteristics of the carbide. However, the average trend does match the images very well and can be used for further comparison and analysis.

The average overall carbide volume fraction over the entire deposit for the benchmark tests was calculated from the images to be 38 ± 3 vol% WC. The standard deviation within each sample was 17 ± 2 vol% when taking 20 horizontal slices. This measurement shows that the variation between samples is small, even though the variation within a particular sample is large. Reporting the average carbide volume fraction gives a measure of the actual amount of carbide in the sample. The size of the standard deviation of a sample indicates the degree

of carbide settling. That is, the larger the standard deviation, the larger the region of carbide depletion at the surface.

The actual volume fraction of carbide in the premixed commercial MMC was reported to be a nominal 50 vol% WC. Typically, a 6 to 10 kg bottle of premixed MMC is remixed by hand for up to 15 minutes prior to being poured into the hopper. This is to ensure an even distribution of carbide as settling may have occurred during shipment or over time. The benchmark study revealed that the volume fraction of carbide was 38 vol% WC, which is significantly lower than that reported by the manufacturer. There are several reasons that the measured carbide fraction was lower. The supplier may have made an error due to poor quality control. Since the carbide is exposed to high temperatures of the plasma, the tungsten carbide particle may experience some degree of dissolution in the melt. The carbide is also traveling at a high velocity through the plasma, so it has the potential to deflect off the surface of the substrate if the powder stream is wider than the molten weld bead. In terms of the error in the quantification method itself, it is accurate to 2-3 %. The size of the particles in the image analysis program could be varied by one pixel radius, which resulted in a 2-3 % change in total carbide concentration. In all cases, the best match of the digitized image to the original image was manually chosen. This method was proven accurate though analysis of 10, 20, 30, 40 and 50 vol% controlled mixtures.

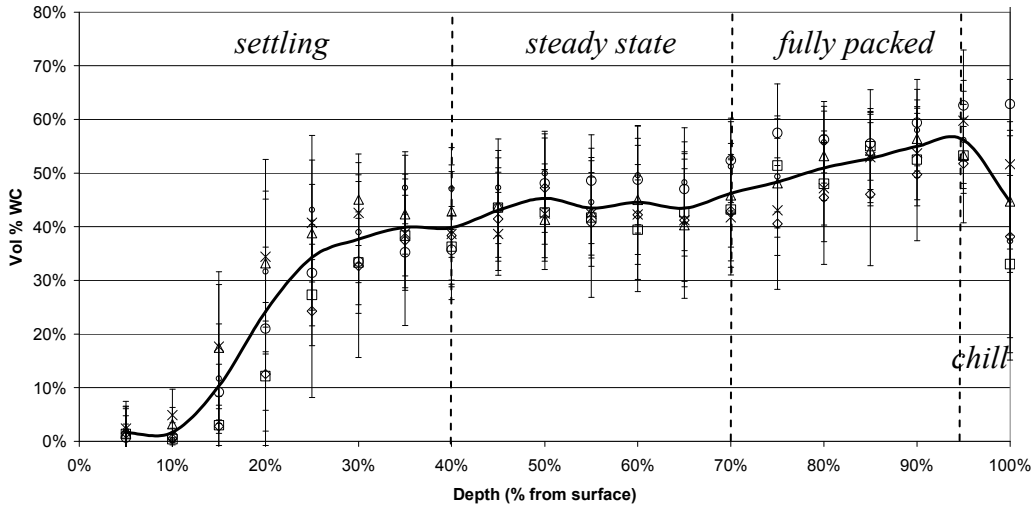

Figure 4.1: Distribution of tungsten carbides to establish a benchmark homogeneity profile. Deposited under standard operating conditions (130 A, 23 V, plasma gas 2 lpm, carrier gas 1.4 lpm, shielding gas 9 lpm, travel speed 3.81 mm/s).

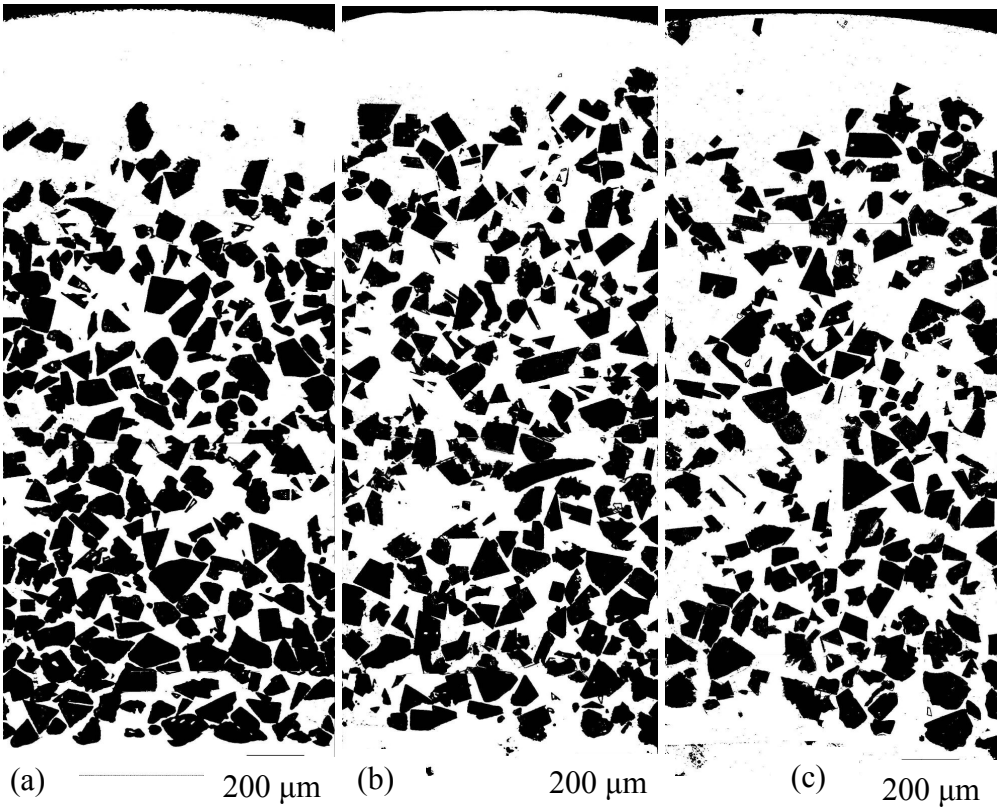

Figure 4.2: Three examples of the cross section of deposits from benchmark tests.

Upon inspection of the average carbide profile (black line in Figure 4.1), the volume fraction of carbide is initially close to zero and increased to 40v% between 10 and 35% of the depth. This region is where the majority of the settling of the carbide occurs. From 35 to 70% of the depth, the carbide level remains relatively constant at 40v%. Another increase in carbide fraction is experienced from 70 to 95% of the depth up to a value of 55v% WC. This was the carbide volume fraction calculated during the loose packing study in section 3.1.2, and can be considered the fully packed region. Near the substrate (95 to 100% depth), a small decrease in carbide fraction is exhibited. The slight decrease in carbide at the chill regime to 50 vol% WC can be attributed to the fact that the MMC solidifies immediately upon contact with the substrate. The carbide has no opportunity to settle or accumulate since there is no liquid.

In summary, this figure shows that there are four regions of settling:

- the settling regime (0-40% depth);
- the steady state regime (40-70% depth);
- the fully packed regime (70-95% depth), and;
- the chill regime (95-100% depth).

The average carbide volume fractions in the each of the regimes for the benchmark study are listed in Table 4.1. The error reported is the average of the standard deviation from each sample. The volume fraction of carbide in the settling region was measured to be 21 ± 17 vol% WC. Not only is this value far below the nominal carbide volume fraction of 50 vol%, but the distribution is very large. This is due to the fact that the amount of carbide increases from zero to approximately 40 vol% WC over the settling region. The distribution will always be large when a high degree of particle settling occurs.

The average carbide level in the steady state region is 44 ± 2 vol% WC and 52 ± 3 vol% WC for the fully packed region. The amount of carbide in the steady state

region is statistically lower than that of the fully packed regime, since the error bars do not overlap in any case. This can be attributed to [DAV1996]:

1. The increased weight of the carbide in the deposit column compresses the lower carbides closer together;
2. The total thickness of the coating is gradually developed as the powder is deposited. The initial layer is thin and the carbides are able to achieve a fully packed deposit. As the deposit increases in thickness, there is more time required for the carbides to settle through the settling region and reach and/or apply pressure to the steady state and lower regions before the matrix solidifies.

Table 4.1: Carbide volume fraction for each regime of the benchmark tests

Regime	***Carbide volume fraction***
Settling	21 ± 17 %
Steady State	44 ± 2 %
Fully Packed	52 ± 3 %
Chill	50 ± 8 %

The goal to obtain an ideal coating would be to have the carbide fraction at all four regimes to be equal. In the case of a 50 vol% WC MMC, each regime would report 50 vol% WC from the image analysis measurements.

4.1.2 Effect of operational parameters on homogeneity

The following figures illustrate the carbide distribution over the experimental conditions tested: current (A), plasma gas (PG), carrier gas (CG), shielding gas (SG), travel speed (TS), voltage (V) and multipass (2 pass/3 pass). The 50 vol% sample is one where the amount of WC was mixed in house to equal 50 vol% WC. There are a select few operational parameters which yield an improvement in homogeneity; however, the large error bars shown in each figure make it difficult to confidently define relationships between operating parameter and improvement in homogeneity.

Lowering the current to 110A (Figure 4.3) has the most significant effect on the homogeneity when only considering the adjustment of operating parameters.

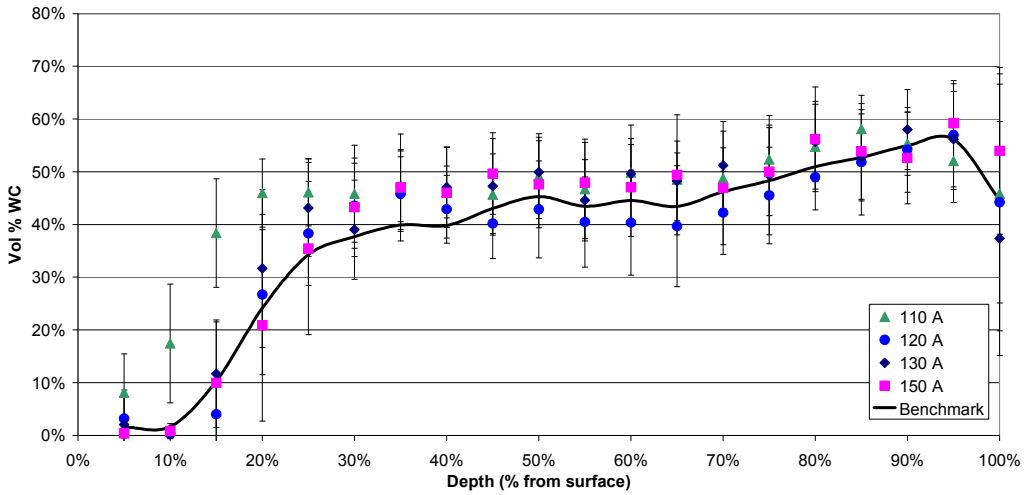

Figure 4.3: Longitudinal WC distribution over depth for current values of 110A to 150A

In the 0-20% depth region, the 110A experiment yields carbide homogeneity greater than the benchmark. The error bars do not overlap that of the other tests, so it can be concluded that the 110A condition yields a smaller settling region. Currents of 120A to 150A all performed similarly in the 0-20% depth region. Lowering the current to a critical value can result in an improvement of homogeneity. In the case of this material system, the critical current is 110A. As the current is lowered, the heat input of the arc decreases. The decrease in heat input results in a lower temperature of the molten metal. The time to solidification would be faster and less settling of the carbide would be permitted.

A small improvement is shown with a decrease in plasma gas flow to 1 lpm (PG1) from a benchmark (Figure 4.4) in the settling region. The average homogeneity in this area is superior by up to 10%v WC with when the plasma gas flow is 1 lpm (PG1) instead of 2 (PG2) to 4 lpm (PG4). There is no difference in the homogeneity in the settling region with plasma gas flows greater than 2 lpm (PG2). Reducing the gas flow has two effects on the process – it changes both the

temperature and velocity profile of the arc. When increasing the plasma gas, the enthalpy of the arc increases, thus increasing the convective portion of the heat input of the arc. A model by Wilden et al. [WIL2006] predicted that the peak temperature of the plasma arc decreases with increasing plasma gas flow. Their work theorized that since the arc power is constant (current and voltage are constant) but the gas flow increases, the arc energy density decreases because a larger volume of gas is being heated. As the enthalpy increases, the temperature gradient near the surface increases resulting in higher heat transfer. This results in more heat being added to the substrate region. Finally, the higher the plasma velocity, the faster the particle velocity and lower the time the particles are exposed to the hot plasma. Thus, the temperature of the particles is expected to be reduced and a minor increase in temperature occurs with increasing plasma gas flow. This reduces the time for solidification compared to the standard condition and less carbide settling occurs.

There is no trend with the carrier gas flow experiment, as both lowering (1.0 lpm – 1.0CG) and raising (2.0 lpm 2.0CG) the carrier gas result in improved homogeneity (Figure 4.5) compared to the benchmark. The range of carrier gas explored could have had little effect on the actual amount of powder transported.

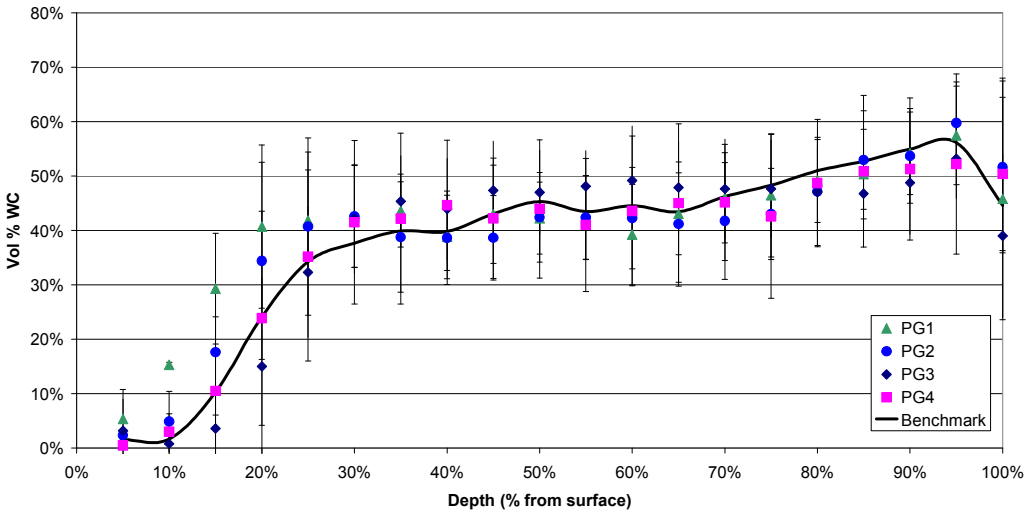

Figure 4.4: Longitudinal WC distribution over depth for plasma gas flow rate values of 1 lpm to 4 lpm

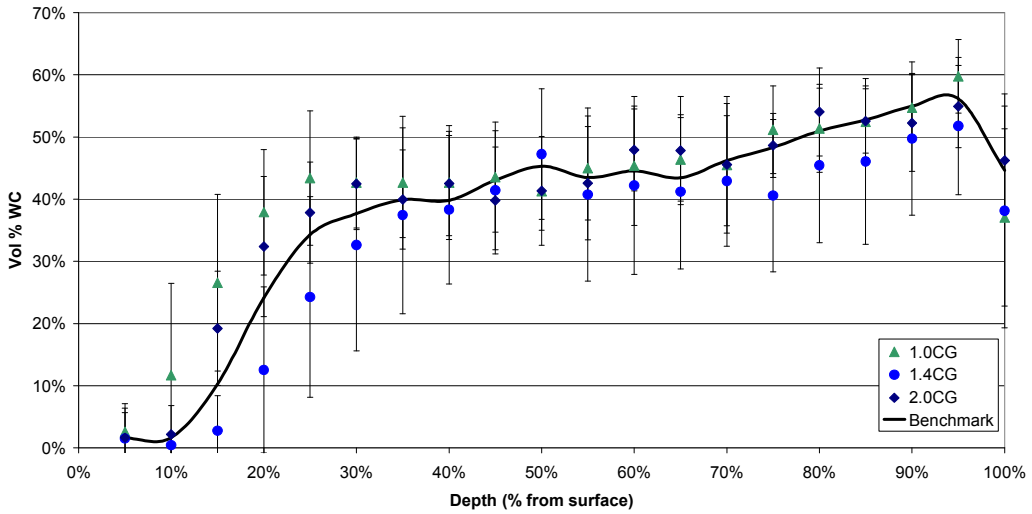

Figure 4.5: Longitudinal WC distribution over depth for carrier gas flow rate values of 1 lpm to 2 lpm

Results similar to those found with the carrier gas were discovered also with changes in shielding gas and voltage. The average of the lowest setting, a shielding gas rate of 7 lpm (7SG), yielded an improvement in homogeneity (Figure 4.6) when compared to the benchmark. However, the trend was not consistent. A higher shielding rate did not necessarily result in inferior homogeneity. Decreasing the voltage to 20V resulted in poorer homogeneity (Figure 4.7) when compared to the benchmark. There was no improvement in homogeneity compared to the benchmark when the voltage was increased to 24.5V. The variations in homogeneity seen in the voltage experiment could simply be a result of the inherent variability of the deposition process as established in the benchmark study (Figure 4.1). The range of voltages examined may have been too small in order to change the heat input of the arc sufficiently to see differences in particle homogeneity. The heat input of the arc is a product of the current and voltage. The ranges the current and voltage can be adjusted and still obtain a good coating are up to 80 A or up to 5 V. The current controls the arc heat input much more than the voltage.

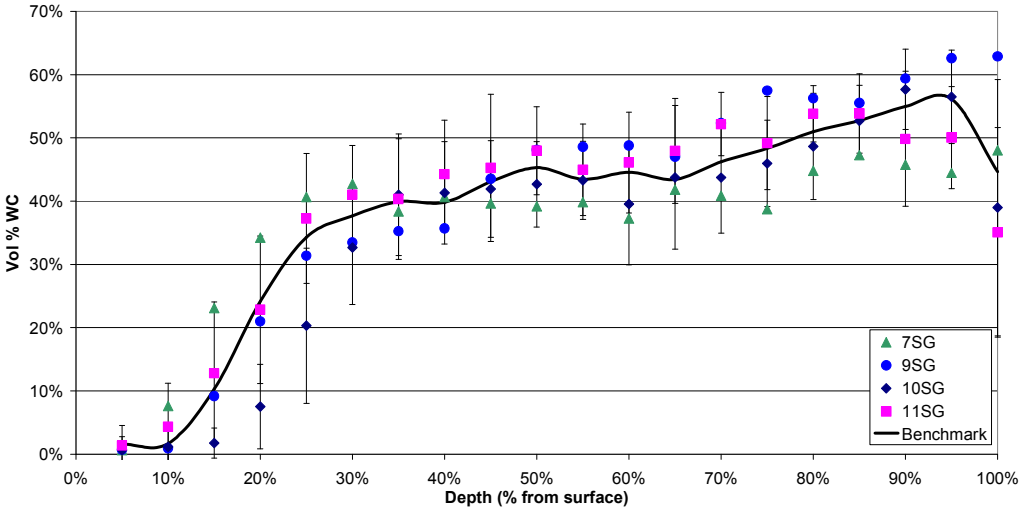

Figure 4.6: Longitudinal WC distribution over depth for shielding gas flow rate values of 7 lpm to 11 lpm

Interestingly, increasing the travel speed resulted in no improvement in homogeneity in the settling regime (Figure 4.8); the repeatability was far superior to those measured for the benchmark. Increasing the travel speed results in a thinner coating, as the powder is deposited over a larger region. Less heat is being transferred into the coating which is thinner, so solidification would occur quickly and there would not be sufficient time for settling of the carbides. A higher travel speed should result in a more homogeneous coating [AND2003]; however, this is not seen in these results. The homogeneity measured for the travel speed experiments is lower than the benchmark in all three cases. The error bars of the data include the benchmark, concluding that there is no statistical difference between the travel speed experiments and the benchmark study. Since the range of the benchmark study was shown to be large, differences in homogeneity would be difficult to measure due to the inherent variability of the process. The range of travel speeds tested may not be large enough to yield adequate sensitivity in the homogeneity of the coating.

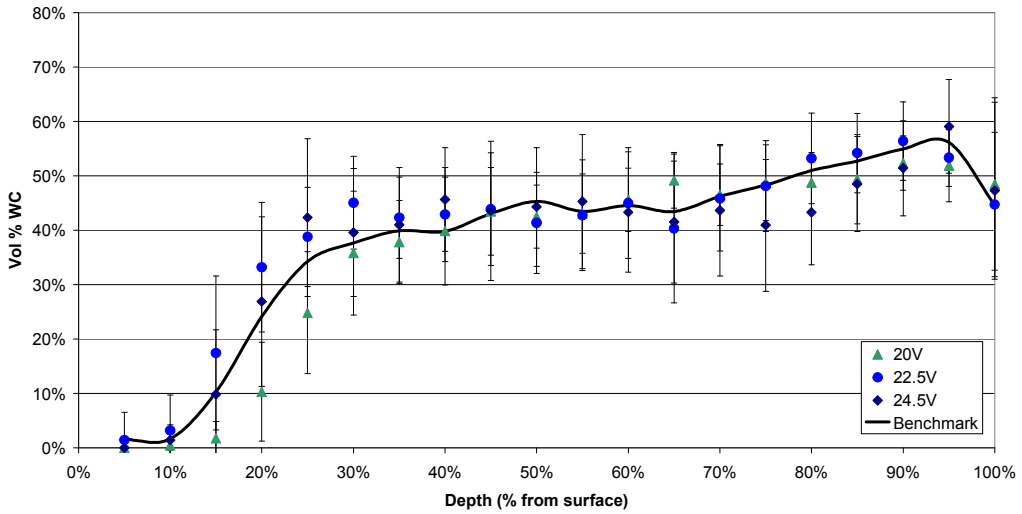

Figure 4.7: Longitudinal WC distribution over depth for voltage values of 20 V to 24.5 V

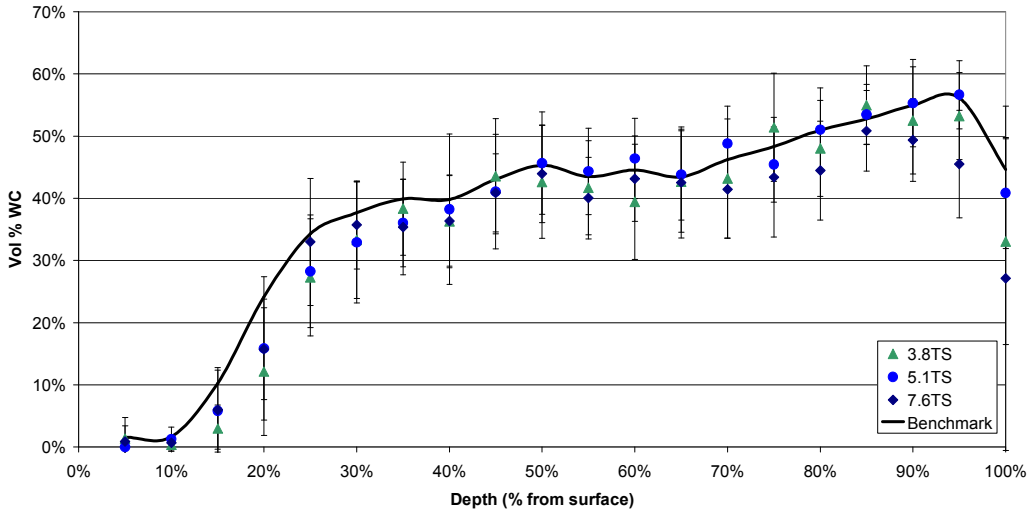

Figure 4.8: Longitudinal WC distribution over depth for travel speed values of 3.8 mm/s to 7.6 mm/s.

In Figure 4.3 to Figure 4.8, the carbide settling profiles are similar and follow that of the benchmark study. At the surface, there is a region void of carbide. The volume fraction of carbide increases quickly from zero to approximately 40 vol% at the depth increases to 40% from the surface. This region accounts for the majority of the settling of the carbide. The two plateaus are also apparent in the figures: the first one (the steady state region) occurs from 40 to 70% of the depth

and the second one which contains more carbide occurs from 70 to 95% of the depth (fully packed region). A decrease in carbide is seen at the coating/substrate interface. The average results are consistent and the trend is clear and repeatable, even though the error within a sample is large.

The 50 vol% WC, double and triple pass stringers (Figure 4.9) show superior homogeneity. The amount of carbide throughout the depth is almost constant. The four regimes are difficult to distinguish. Only in the top 5% of the depth is the amount of carbide reduced. The double and triple pass stringers are virtually identical in their homogeneity.

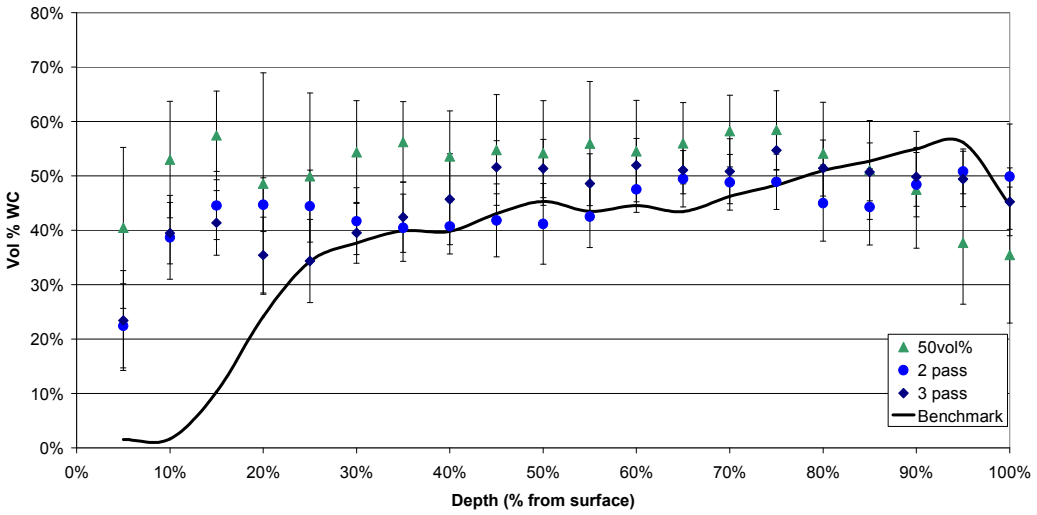

Figure 4.9: Longitudinal WC distribution over depth for total WC fraction of 50%, and double and triple pass stringers

The 50 vol% WC condition shows the most homogeneous cross section, as well as the highest amount of carbide overall – it is consistently just over 50 vol%. The amount of homogeneity in the steady state and fully packed regimes for the double and triple pass tests fluctuate around 45 vol% WC. This indicated that the actual amount of carbide in the MMC was suspected to be lower than what was reported by the manufacturer at 50 vol%.

The amount of carbide in the settling regime was compared over the parameters tested to reveal the degree of settling, shown in Figure 4.10. The benchmark study revealed a carbide volume fraction of 21 ± 17 vol% WC over the same region. There are few improvements in coating homogeneity made when changing operational parameter within error. The condition that showed a significant improvement in homogeneity was the 50 vol% WC, double pass and triple pass tests. Small improvements are made with decreasing the current to 110A, lowering the plasma gas to 1 lpm (PG1), and reducing the carrier gas to 1 lpm (1.0CG). These results will be discussed further.

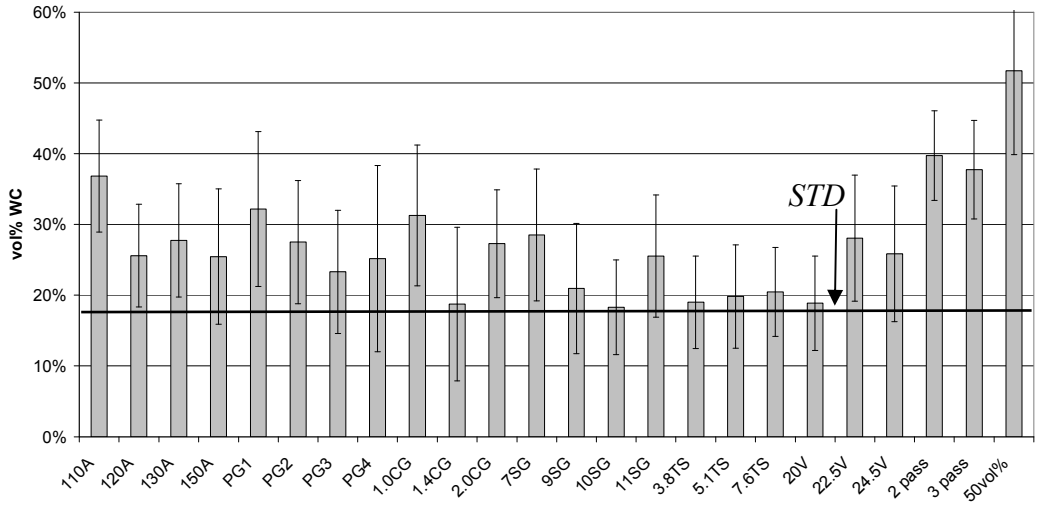

Figure 4.10: Average WC found in the settling region (0 to 40% of the depth) for all conditions tested. The standard (STD) conditions yielded a carbide volume fraction of 21±17 v%WC (black line).

4.1.3 Effect of Carbide Volume Fraction on Homogeneity

Coatings with carbide volume fractions of 10, 20, 30, 40 and 50 vol% WC were deposited under standard conditions. The cross sections are shown in Figure 4.11. It is clearly shown that the size of the steady state and fully packed region increases with carbide fraction. The profile of the volume fraction of carbide along the depth of the deposited is shown in Figure 4.12. At 40 vol% WC, the

coating is almost homogeneous through the thickness. When the carbide amount reached 50 vol%, the coating is fully homogeneous.

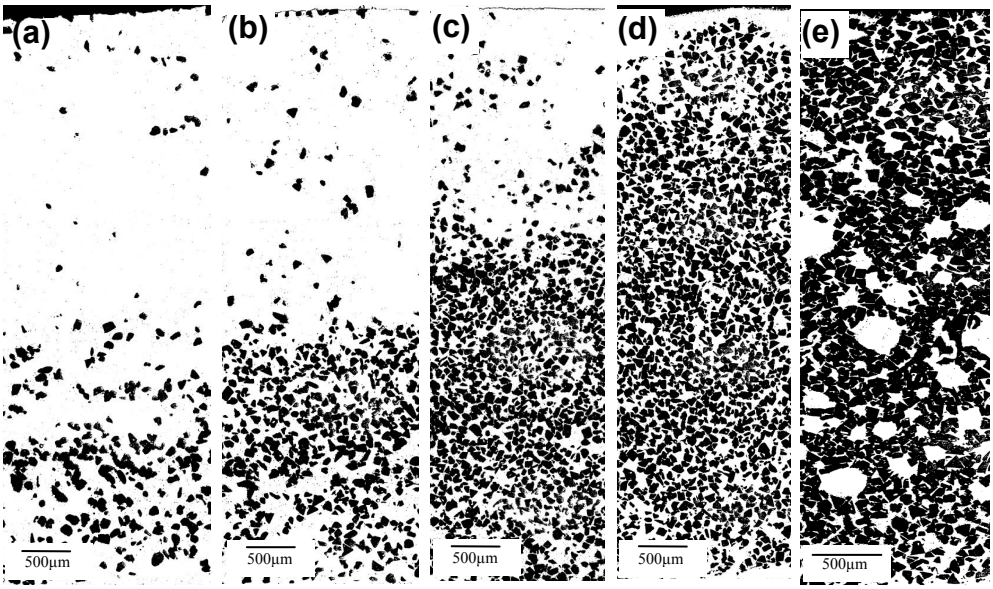

Figure 4.11: Micrographs of carbide volume ratios of (a) 10, (b) 20, (c) 30, (d) 40 and (e) 50 vol% deposited under standard conditions.

The amount of carbide measured in the settling region was compared against the total carbide measured in the section. There is a strong trend, seen in Figure 4.13 that shows that the coating homogeneity is directly linked to the amount of carbide in the powder. The dashed line indicates ideal homogeneity; the carbide distribution is even, considering the amount of carbide present in the initial mix. This suggests that the volume fraction of tungsten carbide in the MMC is more important in obtaining a homogeneous coating than changing operating parameters. This conclusion is reached by knowing the packing characteristics of the carbides in order to obtain the ideal volume fraction of carbides in the initial powder mix. It can be confirmed that the ideal volume fraction to obtain uniform homogeneity for this MMC approaches 50 vol% WC.

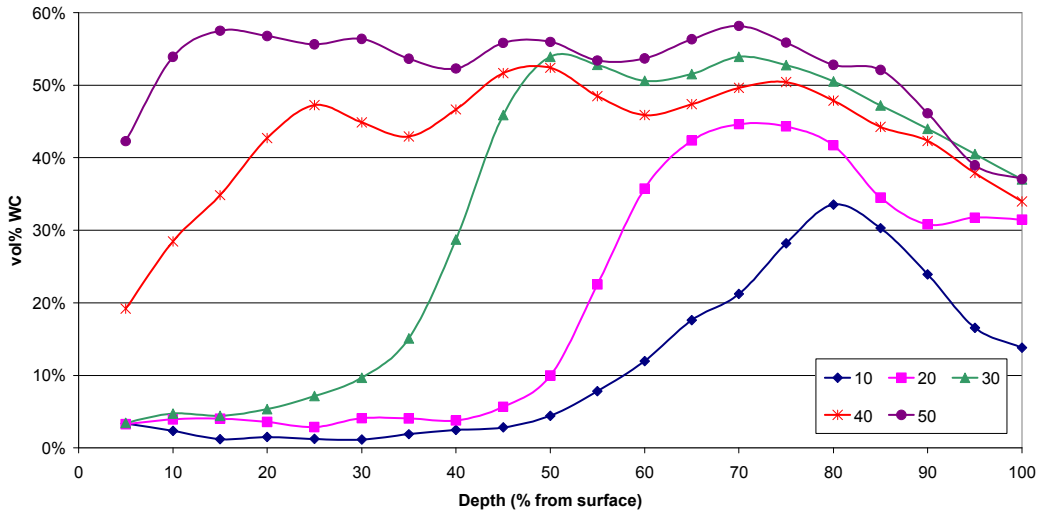

Figure 4.12: WC distribution for carbide mixes ranging from 10-50 vol% WC.

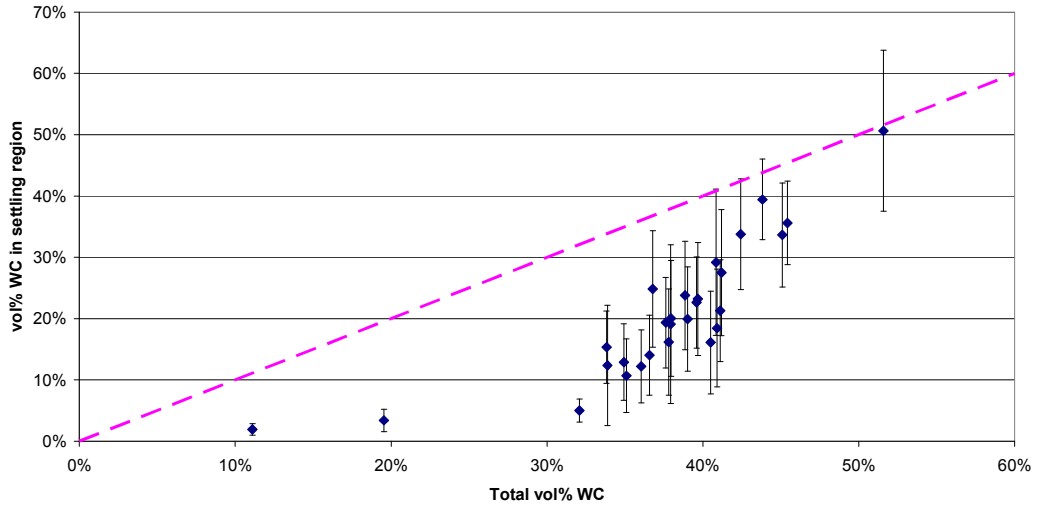

Figure 4.13: Volume fraction of carbide in settling region compared to total carbide in entire deposit. The pink line is ideal homogeneity.

It is imperative to note that the bulk of the tests (those with carbide fractions of 35-45 v% WC) were produced from the same batch of powder and the same hopper. The powder specifications state that the amount of carbide was 50 vol% WC; clearly that amount was not obtained. At approximately $100/kg, approximately $10/kg was paid for carbide not received. Either more stringent

manufacturing methods or an alternative powder delivery method are required, to ensure a consistent matrix-carbide ratio. A dual hopper system where the matrix and carbide powders are separate and are mixed just before entering the nozzle could be developed.

4.1.4 Summary

The homogeneity of the carbide in the deposit was quantified as a function of the deposit depth. A typical profile has four distinct regions: settling, steady-state, fully packed and chill. The profile of a standard coating was not homogeneous. Several key operating parameters were adjusted to determine if improvements in homogeneity could be made. A small improvement in homogeneity of the settling region was made with an increase in current and a decrease in plasma gas flow. A significant improvement was made by doubling and tripling the deposit thickness. The deposit was completely homogeneous when the volume fraction of carbide exceeded 50 vol% WC.

In order to predict the homogeneity of the coating, a combined settling and solidification model was developed and will be presented in Chapter 5. To verify the model, both the carbide homogeneity and the cooling thermal profile of the deposit are required. This section has quantified the carbide homogeneity. The next section presents the thermal measurements made of the deposit by infrared thermography.

4.2 Thermal Measurements of the Deposit

In order to obtain thermal measurements of the deposit, both contact and non-contact methods were investigated. An instrumented substrate was not feasible due to electrical interference with the arc. Non-contact methods were pursued and infrared thermography was selected to obtain real-time image sequences of the deposit during processing. Several cameras were investigated and the results

of the cameras are presented. In order to acquire a real temperature from the infrared camera, both the emissivity and the melting range of the MMC were measured. The emissivity was measured during welding by laser reflectometry and was a function of temperature. The liquidus and solidus of the MMC were measured using differential scanning calorimetry. The temperature data was collected under the same conditions explored in the previous section. Correlations between temperature, processing condition and homogeneity are presented.

4.2.1 Contact Methods

Thermocouples were not appropriate for this type of measurement, as they could not measure the surface temperature. It was not safe to immerse a thermocouple under the arc into the welding pool while the arc was ignited. Only the substrate temperature could be estimated. Unfortunately, the K-type and B-type thermocouples were not able to measure a real temperature of the substrate during the welding process. The ceramic sheath around the B-type thermocouple kept cracking and shorting out the thermocouple. The temperature range detected by a B-type thermocouple was up to 1800°C. The thermocouple directly under the welding path (placed 1 mm under the surface) reported a temperature of less than 225°C. This was not possible as the thermocouple was fused to the substrate, thus the temperature recorded by the thermocouple should have been around 1600°C. The K-type thermocouples, capable of measuring temperatures between -200°C to 1350°C, also reported a temperature of less than 225°C. The thermocouples experienced significant interference with arc voltage. The incoming voltage signal from the thermocouples was depressed upon ignition of the pilot arc and again with the transferred arc. Hence, only non-contact methods were pursued.

4.2.2 Initial Infrared Imaging Results

Infrared cameras were used to collect thermal data of the weld from both the side and rear face of the weld. The emissivity programmed in the camera was held at 1, to facilitate subsequent postprocessing.

Upon inspection of the thermal images shown for an autogeneous weld (Figure 4.14) and for a deposited coating (Figure 4.15), the arc is indeed visible. Both figures show an image of the arc on next to an image captured after the arc is immediately extinguished (arc off). It is not possible to determine where the boundary between the plasma arc ends and the surface of the weld begins. The long wavelength camera was chosen so that the arc would not be visible in the image. The welding arc (argon plasma) emits radiation at wavelengths up to 1.6μm. There are no reports of any spectral activity in argon above 2μm, which made the long wavelength cameras ideal for measuring the surface temperatures of coatings during welding as the arc would be invisible.

Two other phenomena are revealed when comparing the two figures: there is a significant amount of reflection due to the plasma arc, and the coating appears to be much colder than the substrate. Due to the high heat input of the plasma arc, it cannot be expected that there would be a temperature gradient of ~400°C between the surface and coating in less than the coating width of 5 mm.

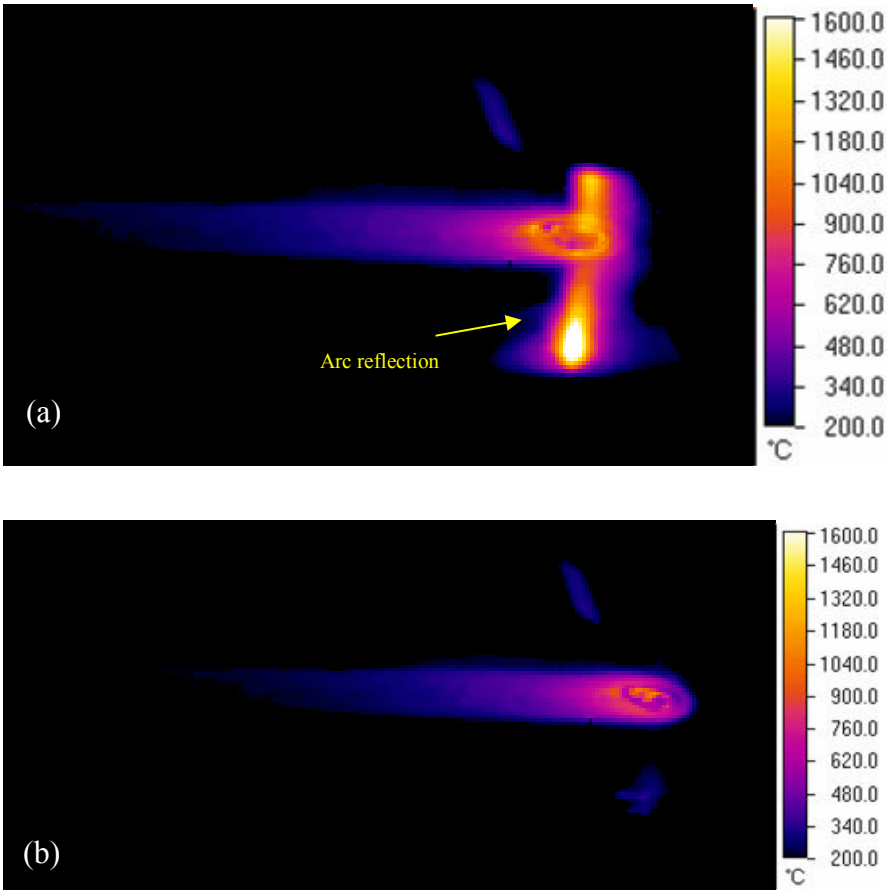

Figure 4.14: MiKron 7600Pro thermal image, side view, standard autogeneous welding conditions and emissivity set at 1: a) arc on, b) arc off.

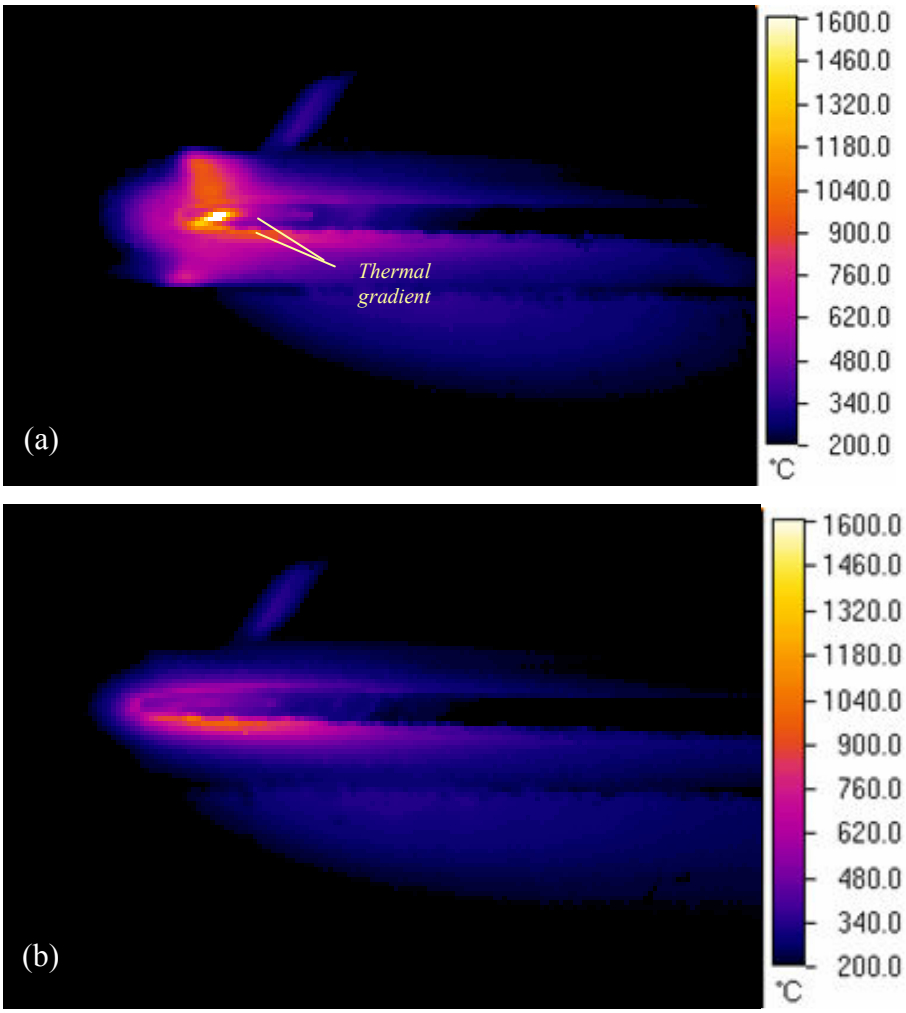

Figure 4.15: MiKron 7600Pro thermal image, side view, deposition under standard welding conditions and emissivity set at 1: (a) arc on, (b) arc off.

4.2.3 Plasma Arc Reflection and Image Artifacts

When viewing the infrared images recorded by the MiKron 7600Pro for both autogeneous and deposit coating conditions, a bright spot is visible on the surface, as shown in Figure 4.14 and Figure 4.15. This bright spot moves around over the surface of the molten area due to the convection in the pool. The presence of the arc visible to the camera also causes a significant amount of reflection, seen as the bright yellow spot in the side view. The reflection of the plasma arc for the autogeneous image occurs primarily on the substrate; however, the reflection of the arc when the powder is injected occurs on the molten surface of the coating.

It was initially difficult to distinguish the arc from the weld pool from certain angles, which led to the measurement of the arc temperature rather than the temperature of the weld pool. At an angle of 45°C to the back of the welding direction (Figure 4.16), the plasma arc reflection is reduced significantly; however, the pool itself cannot be resolved from the arc. The image is enlarged and cropped to show reduction of arc reflection, but there is no distinction between the arc and the coating surface at the hottest area of the coating. The image resolution appears degraded because the image is enlarged. Thus, real-time temperature of the coating while being deposited cannot be measured using this technology. Measurements of the surface including interference from the arc reflection are obtained instead.

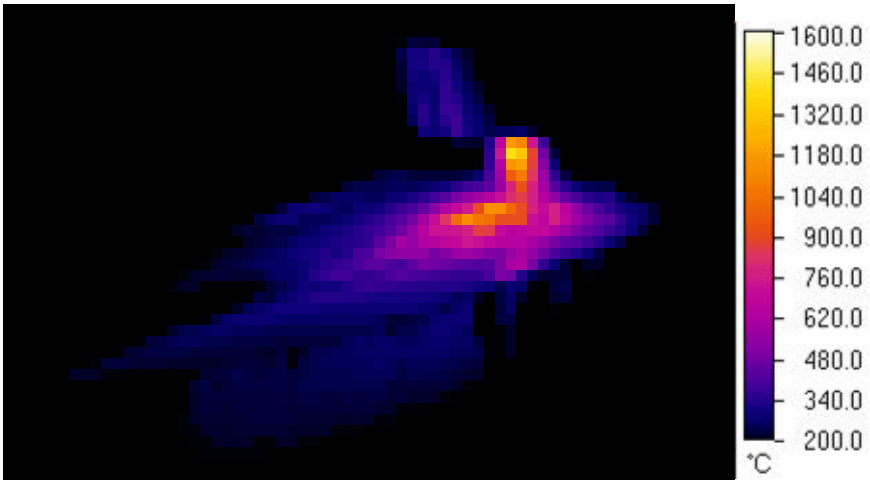

Figure 4.16: MiKron 7600Pro thermal image taken from a 45° angle at a distance of 2m, deposition is under standard conditions.

The best position to capture thermal data was from the rear view as the image of the surface of the coating and substrate were enhanced. A sample of this view is shown in Figure 4.17, which is deposited under standard conditions. A striking result emerges, the presence of an inverted pitchfork shape, or 'M' is seen where the arc meets the substrate surface. The typical teardrop thermal footprint is not apparent (as shown in Figure 4.14). In contrast to thermal weld pool models of PTAW shown by Goldak et al. [GOL1986], Ravichandran [RAV2001] and Chu and Lian [CHU2004], it is shown here that PTAW with powder results in a very

different thermal pattern than autogeneous PTAW. The sides of the coating appear cooler than the centre and surrounding portion under the nozzle. Altering the shielding gases did not change the shape of the cooling zone. An autogeneous weld was laid with the cooling gas on, but with no powder, to determine if carrier gas had a cooling effect. Shown in Figure 4.18, the classical teardrop thermal footprint is seen – the same that is seen with the typical autogeneous run (Figure 4.14). Note that the stand off distance has drastically reduced compared that shown in Figure 4.14. The carrier gas does not contribute to the cooling of the sides and surface.

The width of the heat affected zone in the substrate is much larger in the PTAW runs with powder injected than those of the autogeneous runs. This is likely a result of the insulating effects of the coating.

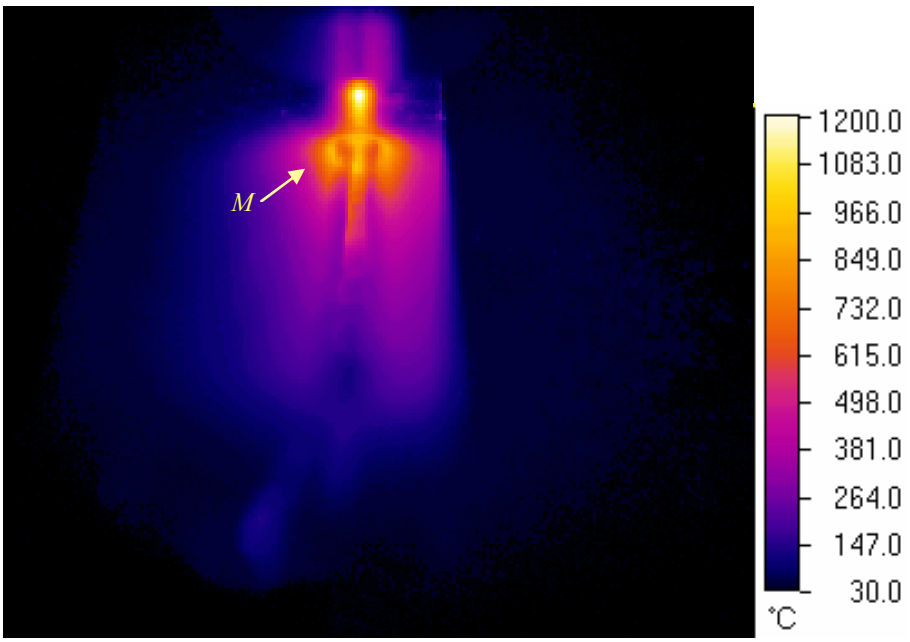

Figure 4.17: MiKron 7600Pro thermal image, back view, deposition under standard welding conditions and emissivity of 1.

A timed sequence of the arc being extinguished was examined. The time between images is approximately 0.1 s. Shown in Figure 4.19, the arc is completely on (a), partially extinguished (b) and completely extinguished (c). As the arc

extinguishes, the intensity of the arc reduces and disappears, but the centerline intensity (centre of the 'M') also disappears. Thus, the 'hot' line down the centre of the coating is simply the reflection of the arc along the surface. The annular hot area surrounding the beginning of the coating is also a reflection; that of the hot nozzle.

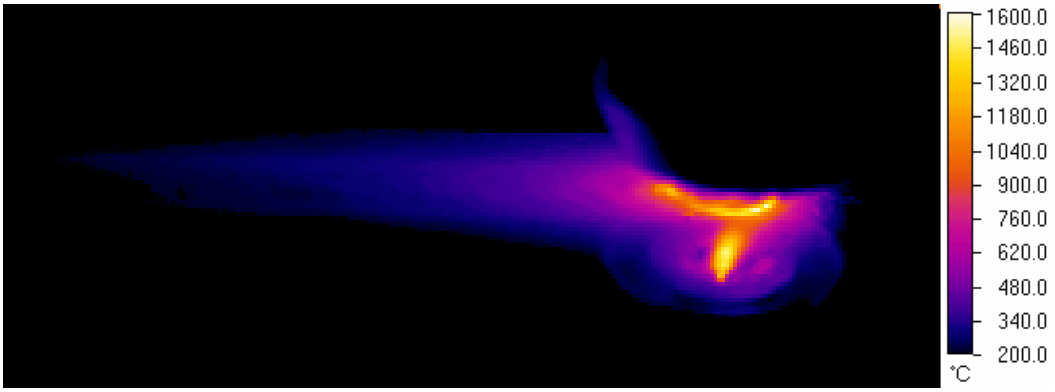

Figure 4.18: MiKron 7600Pro thermal image, side view, standard autogeneous welding conditions but the carrier gas is on (no powder injected) and emissivity of 1.

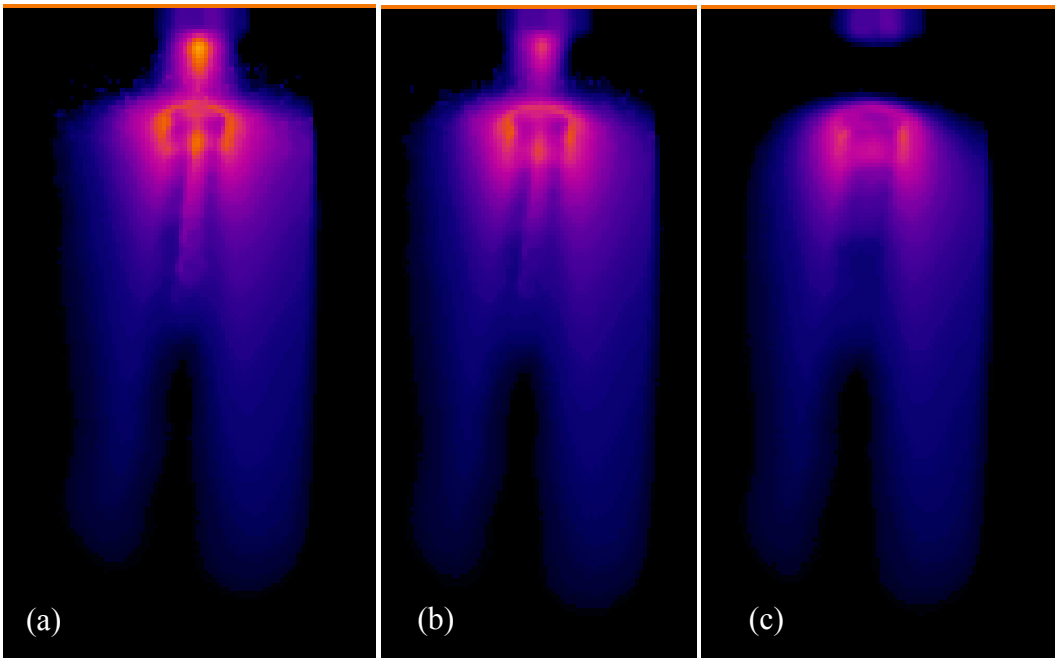

Figure 4.19: MiKron 7600Pro thermal image, back view, deposition under standard welding conditions and emissivity set to 1: (a) arc on, (b) arc starting to extinguish, (c) arc fully extinguished.

The enhanced resolution of the P620 camera is shown in Figure 4.20. These images were instrumental in confirming the reason behind the 'M' shaped thermal profile recorded by the 7600Pro. This camera revealed that the lower resolution of the 7600Pro was the main cause that had led to some erroneous conclusions about the cooling profile of the weld (compare Figure 4.17 to Figure 4.20). While the differences in the image when the arc is on or off are visible with the 7600Pro, the details due to the increased resolution are dramatic. It is apparent that the hot region down the centre (middle leg of the M) is a reflection artifact and not a real hot spot.

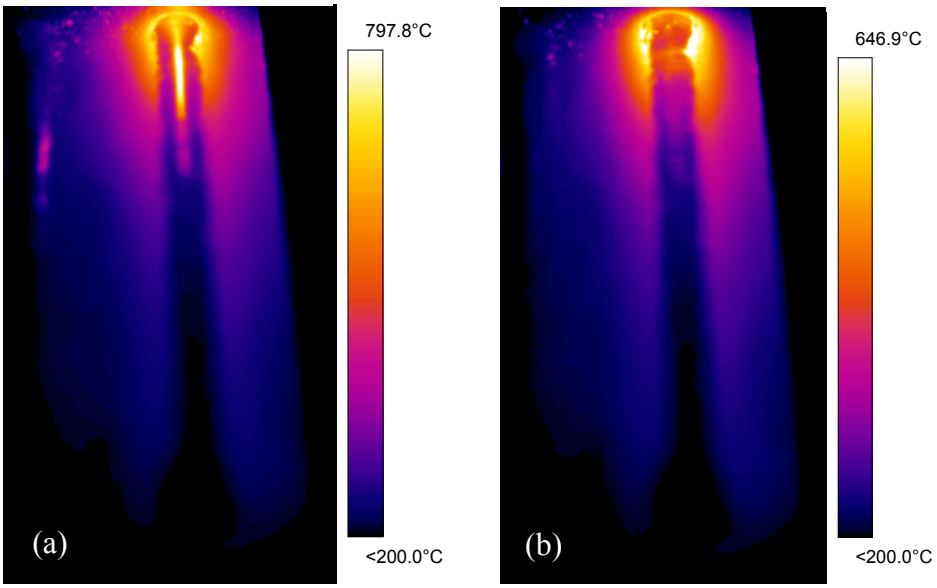

Figure 4.20: FLIR P620 thermal image of the rear view of the weld, standard deposition conditions, with the (a) arc on and (b) arc off.

Further examinations of the images in Figure 4.20 are of interest. The coating (which is the darker region down the middle appears to be cooler than the substrate. The large apparent difference in temperatures of the substrate and coating is attributed to the difference in emissivity between the coating and substrate. As discussed previously, emissivity is a function of temperature, material and surface conditions. The coating is a NiCrBSi with WC particles and is visually more lustrous than the steel surface. The region underneath the nozzle

is also liquid, thus altering the emissivity values. However, a significant contribution to the difference in emissivity is that the coating is hemispherical whereas the substrate is flat. To obtain true temperature values, the emissivity of the surface must be known and the data corrected to account for this difference.

The thermal images from the front view of the weld are shown in Figure 4.21 as standard deposited welds with the arc on and with the arc extinguished. The temperature of the coating can be resolved with the arc off; however, the camera lens requires protection due to the weld splatter, which is prominent to the front of the weld. The cost of the lens is approximately $5000US, so it must be properly protected from damage. Options for lens protection included a special cover plate at a cost of $1000US per use, or covering the lens with kitchen grade food plastic wrap. Unfortunately, both lens covers alter the transmission of the infrared waves, the effect of which is unknown. Thermal imaging from the front view was not pursued.

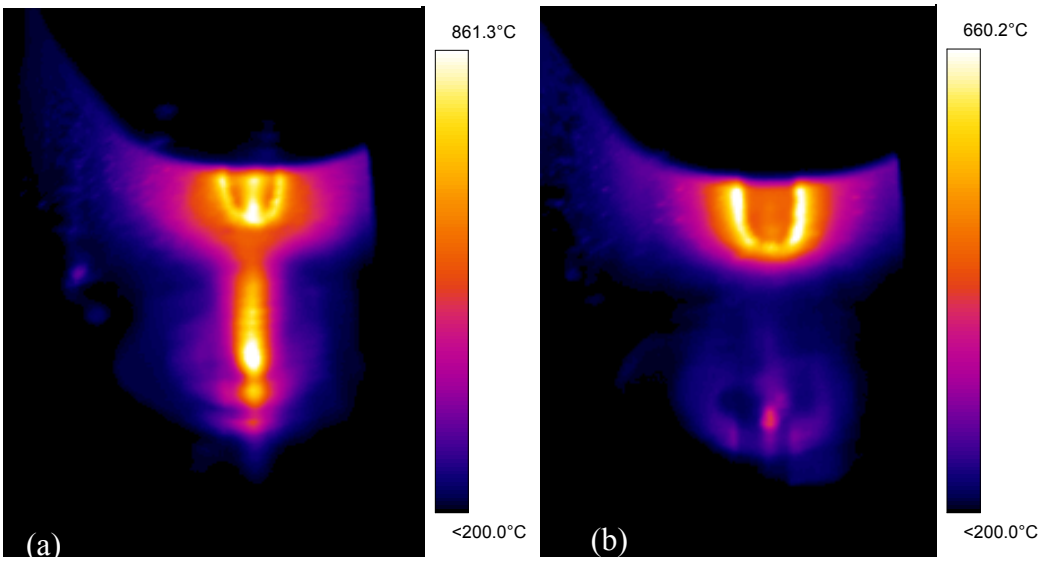

Figure 4.21: FLIR P620 thermal image of the front view of the weld, standard deposition conditions, with the arc on (a) and arc off (b).

The M9103 is designed for high temperature IR measurements, used primarily in steelmaking applications. The advantage of this camera is that emissivity is more

stable at near IR wavelengths, and the sensitivity of the camera at this wavelength measuring high temperatures is orders of magnitude greater than the 7600Pro and P620. However, since the camera captures IR of the same wavelength that the arc is most intense, the image is completely saturated with the arc. This is shown in Figure 4.22. The arc interferes with the entire image despite the high resolution of the camera. The other problem with this camera is that it cannot measure temperatures below 650°C, which makes focusing of the object difficult before welding is initiated.

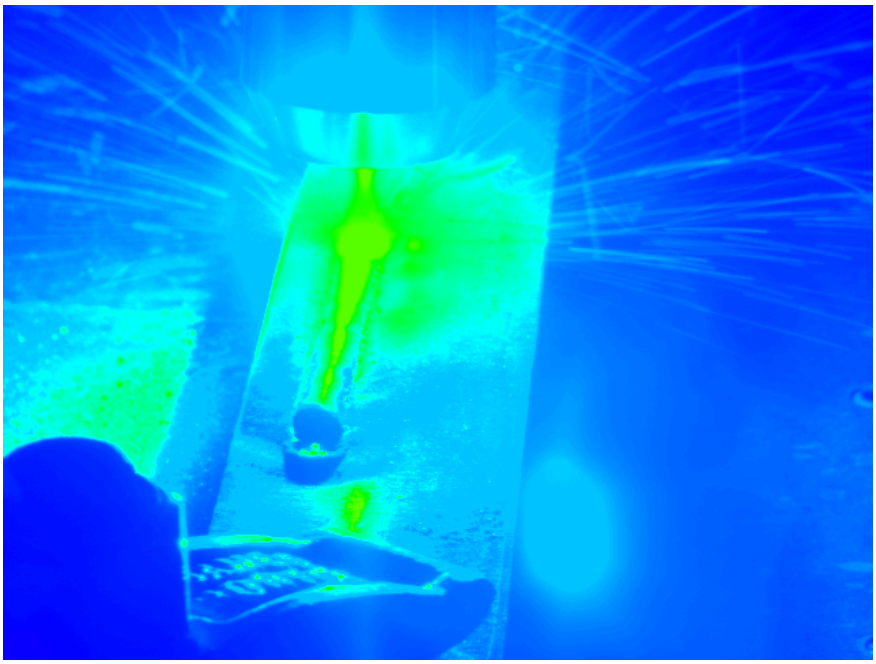

Figure 4.22: MiKron M9103 themal image of weld, standard deposition conditions, rear view.

The filtering lens (1.06-1.08μm) was applied in order to address the saturation. The filter restricts temperature measurement to less than 1500°C and the only component that was visible in the image is the arc and either the reflection on the surface or the location on the welded coating that is 1500°C (Figure 4.23). There was not sufficient temperature variation to identify the coating or substrate. In addition, the melting temperatures of the MMC are far below this temperature, solidification profiles would not be obtained with the use of the filtering lens.

Since the arc was still visible with the filter, it brings into question the validity of the argon I spectrum for this application. Either the atomic spectrum varies at elevated temperatures, or the small additions of iron or nickel vapours in the argon plasma cause a shift from the reported spectra. In other research, problems with accurately measuring the arc length by sensing the arc light in the ultraviolet range [LI2001] were attributed to the realization that the arc light consists of continuum and spectral lines of different elements in the arc column, namely that of the substrate.

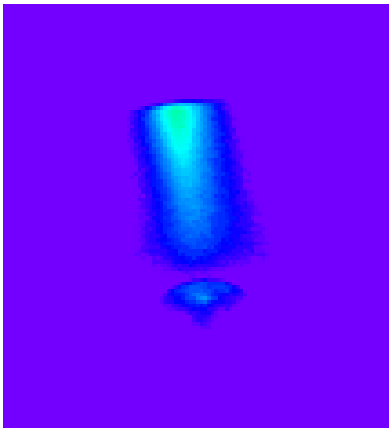

Figure 4.23: MiKron M9103 thermal image of weld, standard deposition conditions, rear view, with filtering lens.

The images reveal that none of the cameras can measure the temperature of the weld pool under the arc, either because of the argon interference or the reflection of the arc. Filters were not able to address these issues. The most feasible way to collect temperature measurements with the current equipment was immediately after the arc was extinguished. The methodology of taking temperature measurements of the weld pool under these conditions is presented in the next section.

However, infrared thermography technology could be instrumental in measuring the heat affected zone of welding, as the emissivity would be constant and there

would be no interference with the reflection of the arc. Figure 4.24 shows with exceptional clarity the profile of the arc and the thermal profile of the substrate.

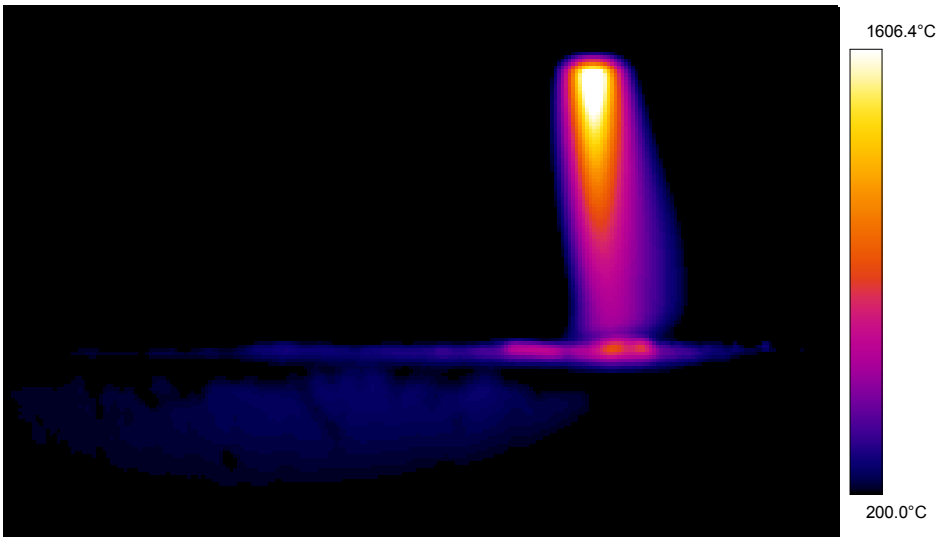

Figure 4.24: FLIR P620 camera, autogeneous weld, side profile, showing the arc profile and the thermal profile of the substrate.

4.2.4 Thermal Data

The temperatures of the coating were collected only when the arc was fully extinguished, due to the interference with the welding arc. The maximum temperature of the deposit was measured within a 3x3 pixel square at the end of the deposit directly underneath the arc. A cooling profile of the region of interest is shown with the infrared images superimposed in Figure 4.25. When the arc was on, the temperature was constant around 900°C (Tavg_arc on). The arc was extinguished resulting in a rapid drop in temperature, Tavg_drop. The temperature then increases slightly to Tavg_inc. This is believed to be due to the change in emissivity over the phase change. The dependence of an accurate emissivity value in order to obtain a real temperature result is also seen with the P620, illustrated in Figure 4.26.

The coating temperatures for the remainder of this work were collected using the Mikron 7600Pro for a variety of operating parameters. Shown in Figure 4.27, are the Tavg_drop for the parameters tested, collected with an emissivity of 1. The label indicates which parameter was changed; all other parameters remain at standard operating conditions.

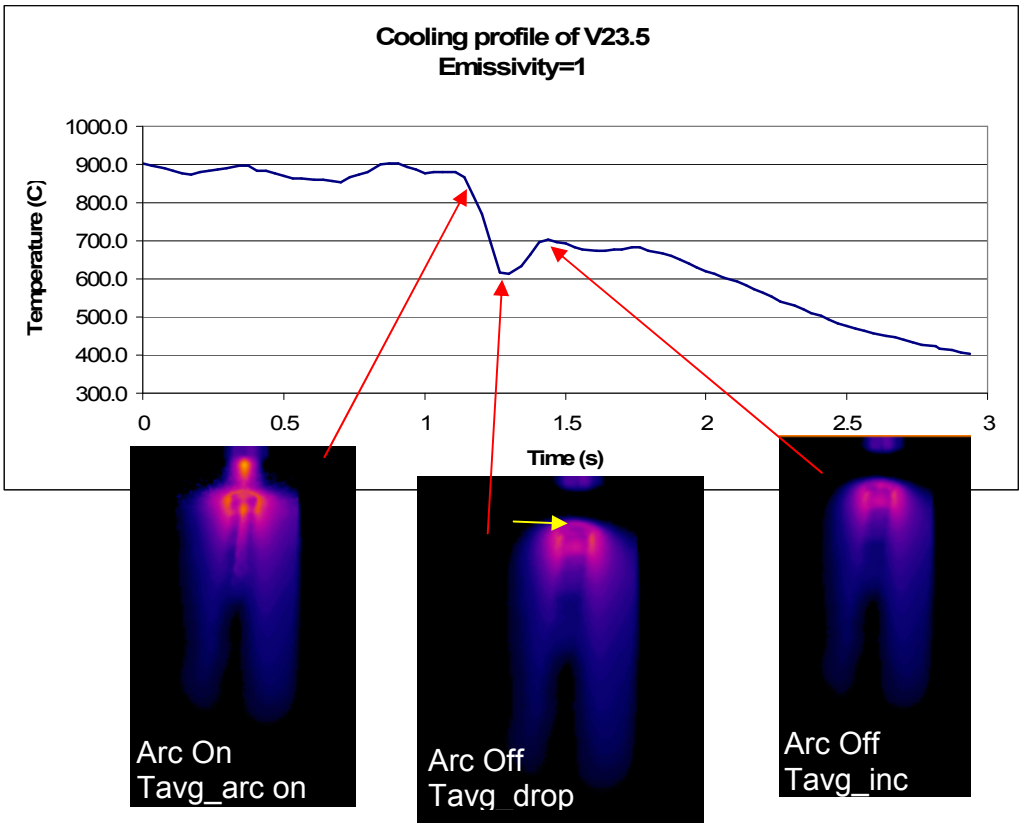

Figure 4.25: Temperature profile at arc-off collected by the Mikron 7600Pro camera. The yellow arrow shows the region where the temperature is recorded for all cases.

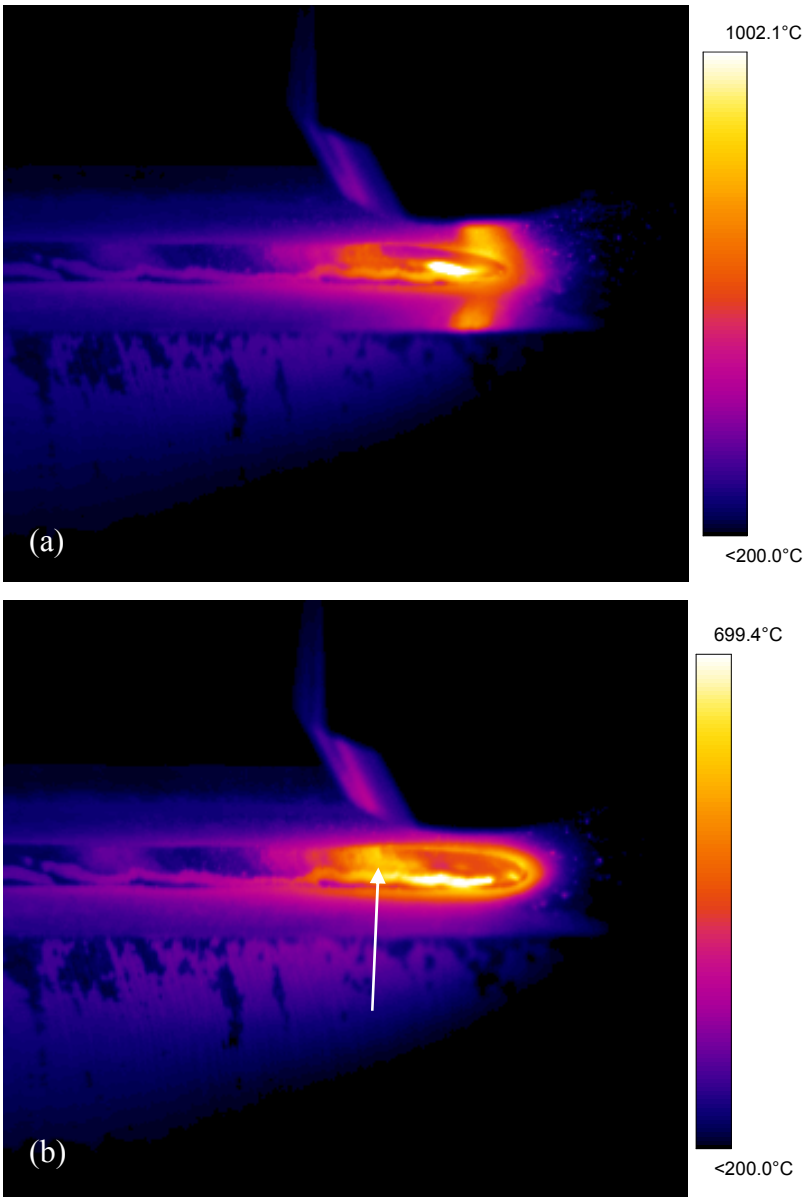

Figure 4.26: FLIR P620 thermal image of the side view of the weld, standard deposition conditions, with the arc on (a) and arc off (b). The effect of emissivity on apparent temperature as the coating solidifies is highlighted (arrow).

Each condition was repeated in triplicate; the error bars indicate the standard deviation of the three runs. These temperatures are significantly below that of the melting range of the alloy and are clearly not valid. The true emissivity of the coating is not 1, and as such, the temperatures are required to be corrected with the proper emissivity as well as to account for their change in emissivity over the

phase change. The temperatures do follow a general trend though, such as the higher the arc enthalpy, the higher the surface temperature of the coating. For example, as the current and voltage increase, more heat is being put into the weld and the temperature increases. However, the temperature of the weld is not between 550°C and 700°C as the melting point of the alloy was specified by the manufacturer as 1050°C; these are extremely underestimated values. Clearly the emissivity of the deposit is different from that of the substrate and is likely to change with temperature as it solidifies. A method was established to correct the temperatures obtained by the IR camera. The temperatures obtained by the IR camera with an emissivity of 1 were modified with the algorithm discussed in further sections.

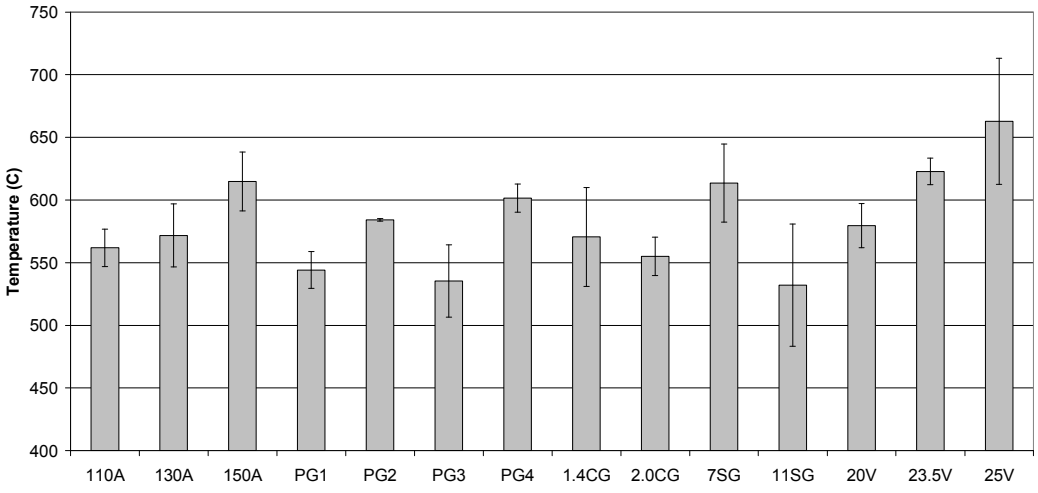

Figure 4.27: Surface temperatures of coatings under various operating parameters, with no post-processing. Measurements were taken using the Mikron 7600Pro using an emissivity value of 1.

4.3 Correction Algorithm for Infrared Thermography

The temperatures acquired of the surface of the deposit by infrared thermography were not correct. To obtain a true temperature, the emissivity of the surface must be known. There are no reported emissivity values for this material at elevated temperatures. Hence, the emissivity was measured using a laser reflectometer.

The liquidus and solidus of the MMC was measured using differential scanning calorimetery in order to corroborate the corrected temperatures. If the corrected temperatures of the liquid weld pool were above the solidus, the algorithm was logical.

The correction algorithm obtained the real temperatures by utilizing the emissivity and intensity measurements through an iterative approach.

4.3.1 Emissivity

The literature notes differences in emissivity between the liquid and solid phase of a material. In addition, the surface of the liquid can be highly reflective as discussed earlier. The laser pyrometer was used to make accurate emissivity measurements of the surface as soon as the arc is extinguished. Both the position and the angle of the laser pyrometers were identical to those used for the infrared camera.

The temperatures recorded by the infrared cameras were not real temperatures. They must be corrected with the appropriate emissivity value – the ratio of the radiative intensity reflected compared to a blackbody at the same temperature. Emissivity varies with material, phase, wavelength, surface condition and temperature. It should be noted that emissivity is not temperature dependent for all materials and is more dependent on the atomic structure of the metal. As the metal is heated, electrons become more excited. This does not occur exclusively at one independent temperature, but over a range.

The emissivity of the coating surface measured by laser pyrometry during welding is shown in Figure 4.28. Multiple runs were measured in order to capture the temperature as the coating was deposited and heated as well as during the cooling period when the arc was extinguished. The value of emissivity is nominally 0.8 at the low temperature range and falls to nominally 0.2 as the material is heated. The transition occurs between 900°C and 1200°C. The

emissivity increases to a value of 0.7 when cooling. The fact that the emissivity did not return to its original value of 0.8-0.9 could be a result of an oxide or carbon debris present on the surface after cooling. Although these emissivities were measured at a wavelength of 1.55 μm, and hence not exactly the same values as they would be with the higher wavelength of infrared cameras Alpha or Beta, they are similar to values reported for Ni in literature. The emissivity of molten nickel is given as 0.340 by Ratanapupech and Bautista [RAT1981] and 0.15 by Rulison and Rhim [RUL1995]. At a wavelength of 2μm, the emissivity of nickel at 1100°C increased from 0.2 to 0.6 as it oxidized, reported by Fan et al. [FAN2003]. Since there is little documentation regarding the emissivities of metals at high temperatures and during liquid states, a comparison of the emissivities of similar metals is required.

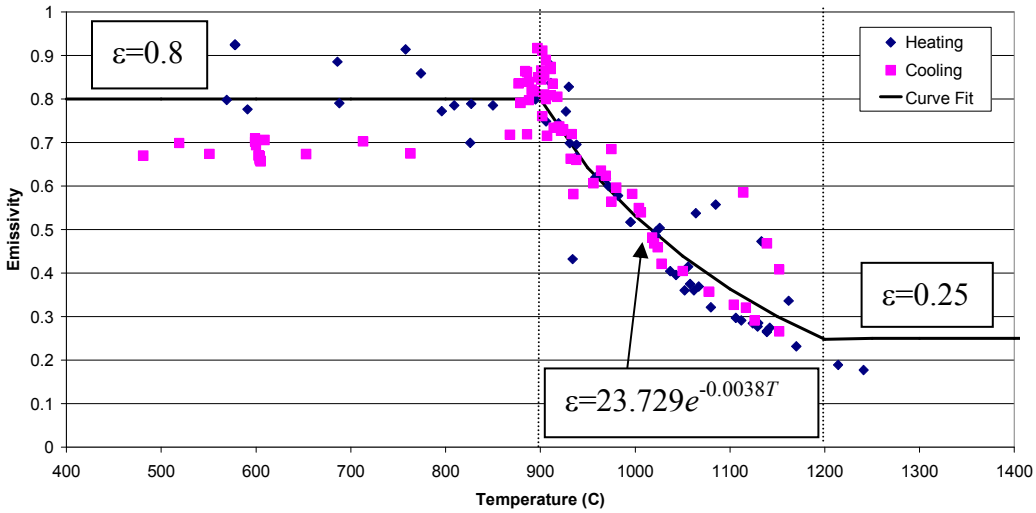

Figure 4.28: Emissivity of NiCrBSi and WC powder deposited during PTAW, measured at a wavelength of 1.55 μm. The camera captured the signal from the rear view. This figure also shows the reversibility of emissivity with temperature.

The spectral emittance of nickel in air is reported up to its melting point. Shown in Figure 4.29 is the normal spectral emittance of nickel (TOU1970). It is obvious that there is no standard value and emissivity is highly dependent on the surface conditions and environment. The lower values were measured in a

vacuum or in an inert environment, whereas the higher values were measured in air. The reported emissity values around 0.85 were from a polished Ni specimen, whereas the emissivity values around 0.6 were from an as received specimen. The measurements taken for this study were not measured in a vacuum or in a controlled environment. It can be concluded that the variation in emissivity under temperatures of 900°C are a direct result of the surface condition.

Measurements of oxidized metals are most prevalent in the literature. A reported emissivity value of liquid mild steel is 0.28 [OME2007] and 0.34 for liquid nickel [RAT1981], and published emissivities of oxidized steel as 0.80 and oxidized 80Ni-20Cr as 0.89 [OME2007]. Ganz et al. [GAN1998] found that the emissivity of a nickel-based alloy (Inconel 617) at a temperature of 1073K was held between at 0.84 and 0.88 at wavelengths of 2 to 6 μm. Since the reported emissivity of similar materials are comparable to the experimental results, the experimental emissivity values are valid.

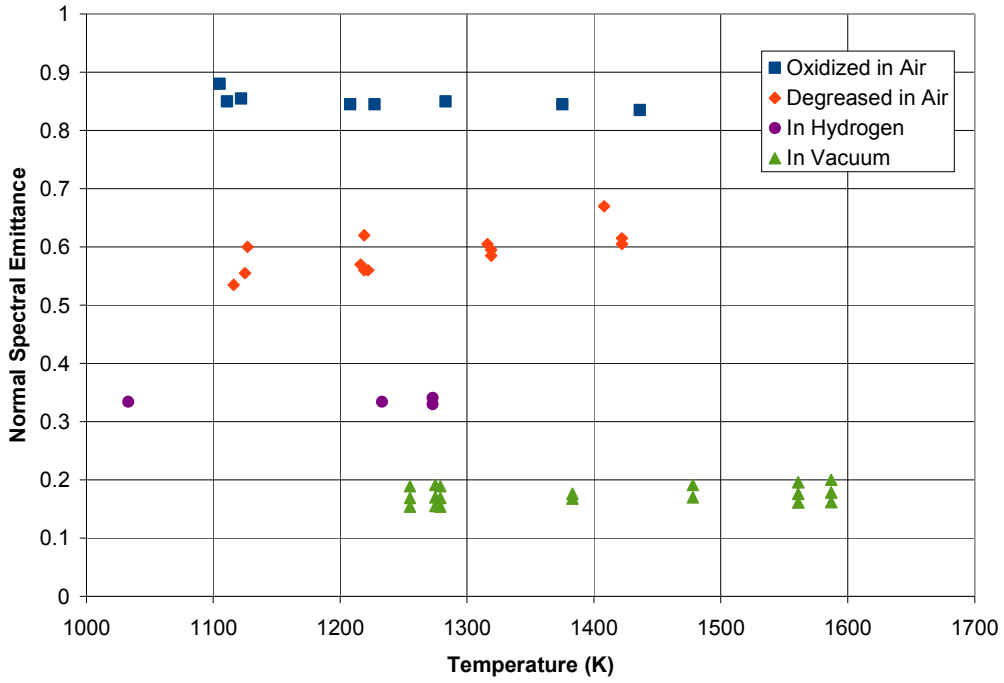

Figure 4.29: Normal spectral emittance of nickel [modified from TOU1970].

The emissivity increases with temperature to approximately 0.2 from 0.8 and returns back towards its initial value when cooling. The relationships between temperature and intensity for the infrared camera can now be calculated by including the relationship of emissivity with temperature as shown in equation 4.1. This equation is an exponential curve fit of the data in Figure 4.28 by calculating the least squares fit of the equation $y=de^{bx}$. The R-squared value, determined from a transformed regression model, was 0.83.

$$\varepsilon = \begin{pmatrix} 0.8 \\ 23.729e^{-0.0038T} \\ 0.25 \end{pmatrix} if \begin{matrix} T < 900^{\circ}C \\ 900^{\circ}C \le T \le 1300^{\circ}C \\ T > 1300^{\circ}C \end{matrix} \quad (4.1)$$

There is a small segment during the initial heating and cooling phase that does not fit the regression where the temperature is between 1050°C to 1150°C. These results were collected immediately when the deposition started and the width of the weld bead was smaller than the spot size of the probe. Thus, emissivity data was collected from the steel substrate as well as the coating.

4.3.2 Differential Scanning Calorimetry Results

The only thermal data reported about NiCrBSi is that the melting point is 1050°C, so it was critical that the solidus and liquidus were evaluated by high temperature differential scanning calorimetry (DSC). This would ensure that the temperatures measured by the infrared camera were in line with the melting temperatures of the alloy.

The DSC measured that the melting of the NiCrBSi powder itself was initiated at 1012°C (liquidus) and peaked at 1036°C (solidus), shown in Figure 4.30. The heat of fusion was measured at 79.4 J/g. When WC was added (Figure 4.31), a small endothermic peak was detected prior to melting with an extrapolated onset temperature of 974°C and a peak area of 0.84 J/g. The melting of the combined powder started at 1008°C and peaked at 1030 °C. The heat of fusion was

measured to be 38.1 J/g. There were no peaks with the carbide alone (Figure 4.32). Thus, the small endothermic peak is likely a result of a formation of the η phase, which occurs at temperatures greater than 900°C and was identified as Ni_2W_4C [LIA1997].

The DSC results confirm that the measured temperatures of 550°C to 700°C obtained with the infrared cameras were incorrect. In addition, the drop in emissivity coincides with the phase change measured by the DSC. For this particular alloy, the change in emissivity occurs over a range larger than its liquidus to solidus region.

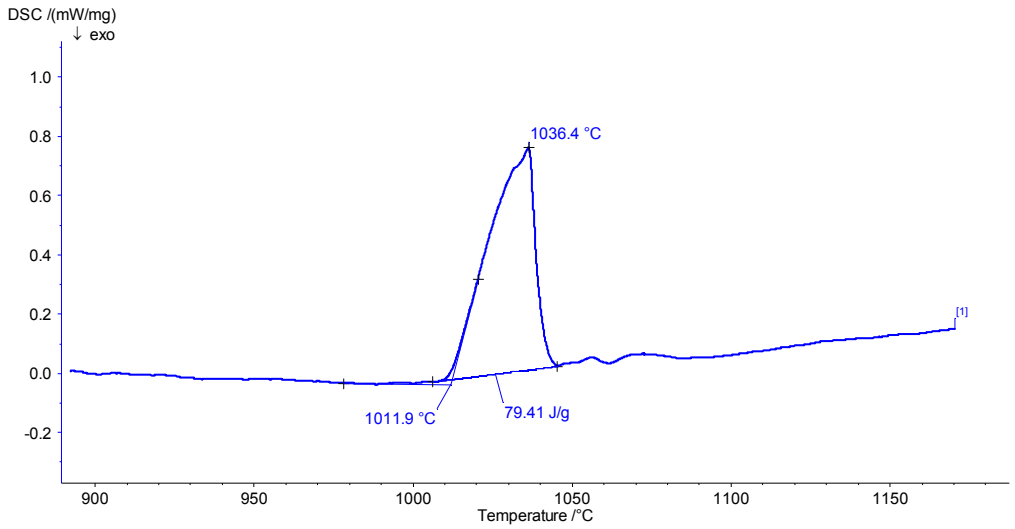

Figure 4.30: Differential scanning calorimetry results for NiCrBSi powder

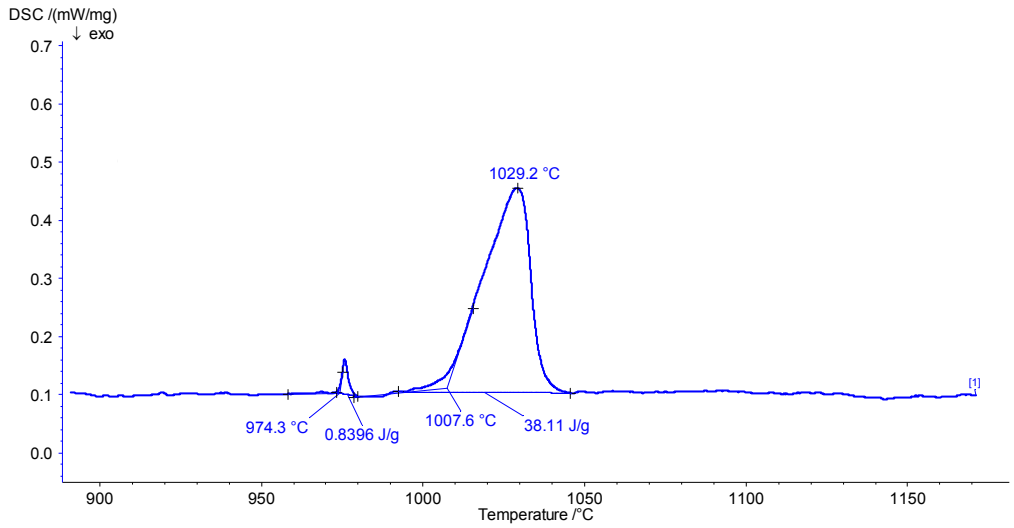

Figure 4.31: Differential scanning calorimetry results for NiCrBSi + 50vol% WC

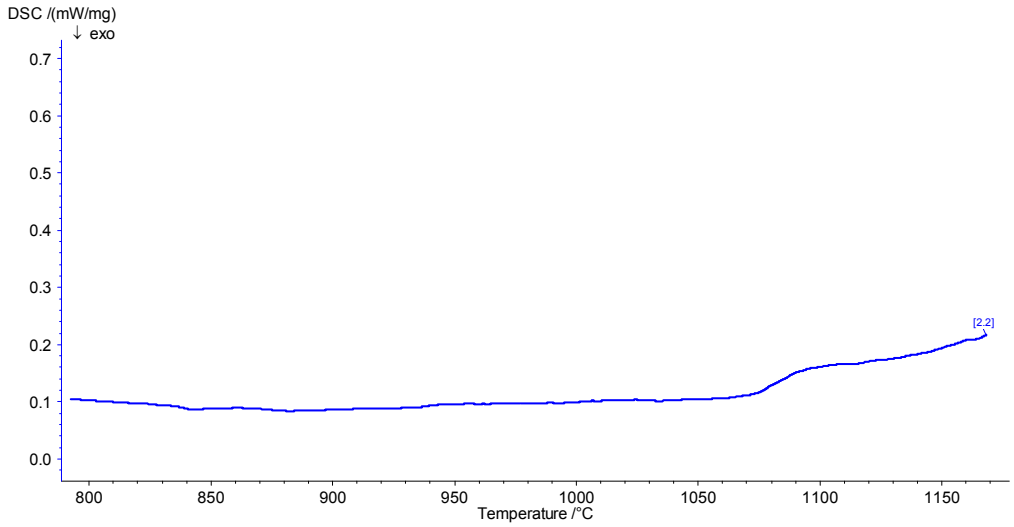

Figure 4.32: Differential scanning calorimetry results for WC

4.3.3 Correction Algorithm

The temperatures measured by the infrared camera were acquired with an emissivity value of 1. It was found that the emissivity of the deposit ranged from 0.2 to 0.7 as it cooled. To obtain true temperature values, the emissivity of the

surface must be used to correct the infrared temperature data. A correction algorithm was developed because the emissivity was not constant.

The relationship between the measured surface temperature when the emissivity was 1 and the exitance energy (intensity) was determined by integrating Wien-Planck's equation (Equation 2.11) over the wavelength region of interest (8-14 µm) for a variety of emissivity values. This was computed using MiKron's intensity calculator program, MBRC. The relationship between temperature and intensity was fit to a power equation of the form $y=dx^b$ using a least square fit methodology. The relationship between intensity and temperature in the wavelength region of 8-14 µm and 600 to 1800 °C is shown in Figure 4.33 for five different emissivity values.

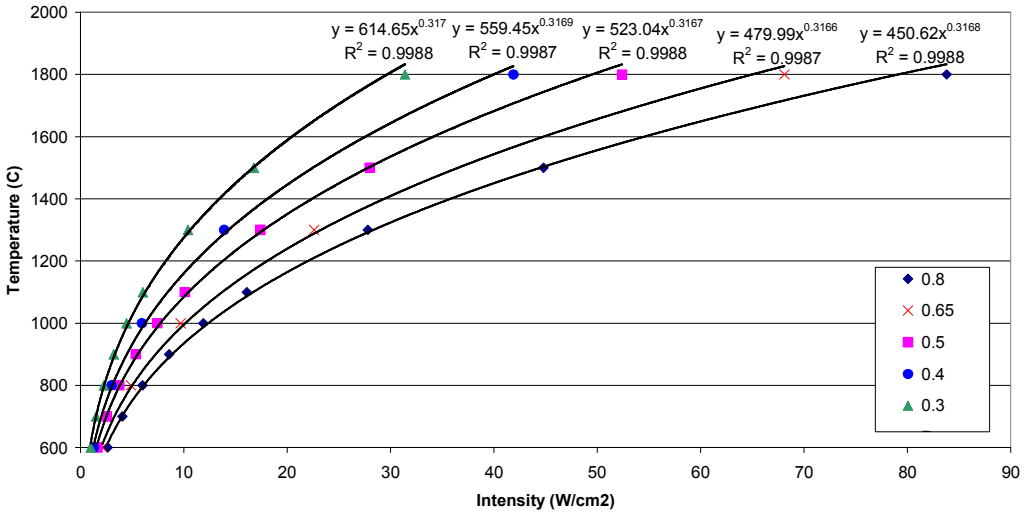

Figure 4.33: Relationship between intensity and temperature for emissivities ranging from 0.8 to 0.3 over a wavelength region of 8-14 µm.

Since emissivity also plays an important role in the relationship between temperature and intensity, a power equation was fit between emissivity and the *d* coefficient, the pre-exponent from Figure 4.33. The power relationship between *d* and emissivity is shown in Figure 4.34 and the final relationship is shown in equation 4.2.

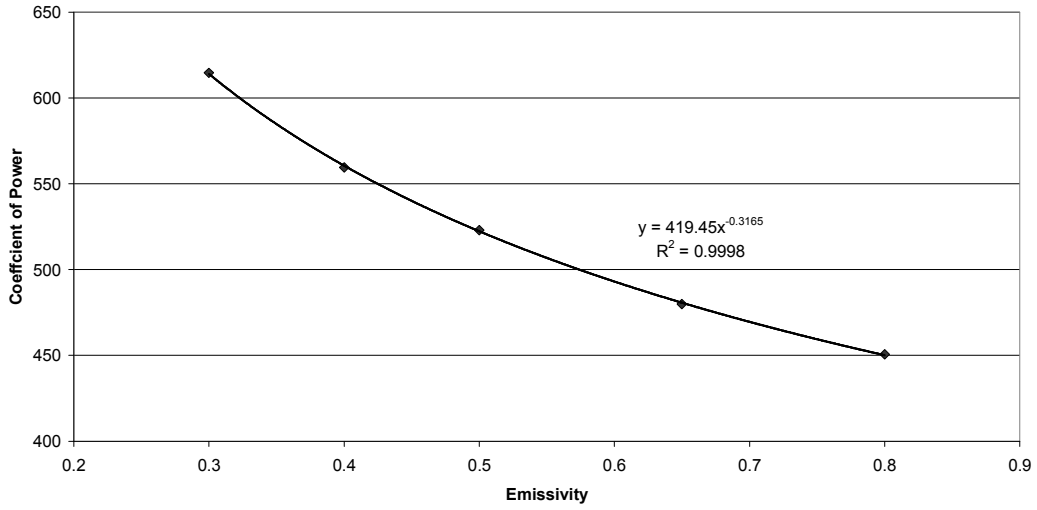

Figure 4.34: Relationship between emissivity and pre-exponent coefficients from the equations shown in Figure 4.33.

$$T = 419.5\varepsilon^{-0.3165} M^{0.3168} \tag{4.2}$$

A graphical representation of the conversion between the infrared temperatures collected by the camera (with an emissivity of 1) and the corrected temperature (with the experimental emissivity values) is shown in Figure 4.35. The temperature recorded by the infrared camera increases from 400°C to 800°C when the MMC is heated in its solid state. The actual emissivity of the solid is between 0.7 and 0.9. The corrected temperatures during the same heating region increase from 500°C to 1000°C. During the transition between solid and liquid, the effective emissivity decreases from 0.8 to a value between 0.2 to 0.4. The infrared camera records a decrease in surface temperature between 800°C to 500°C, however, after the correction is applied with an appropriate emissivity, the corrected temperature in the same regime increases from 900°C to 1200°C. When the MMC is completely liquid - at approximately 1200°C, the emissivity is constant at 0.2 to 0.4 and both the infrared temperature and corrected temperature increase. When the appropriate emissivity is applied, a continuous increase in temperature occurs as the material is heated from 500°C to 1500°C. The error associated with emissivity is large in this region, as small changes in emissivity

yield large changes in corrected temperature. The correction algorithm utilizes a range of effective emissivity values in the solid and liquid region since a more rigorous investigation of emissivity at the liquidus and solidus is required. The laser reflectometry was able to measure the emissivity change over the transformation and was not sensitive at temperatures outside of that region.

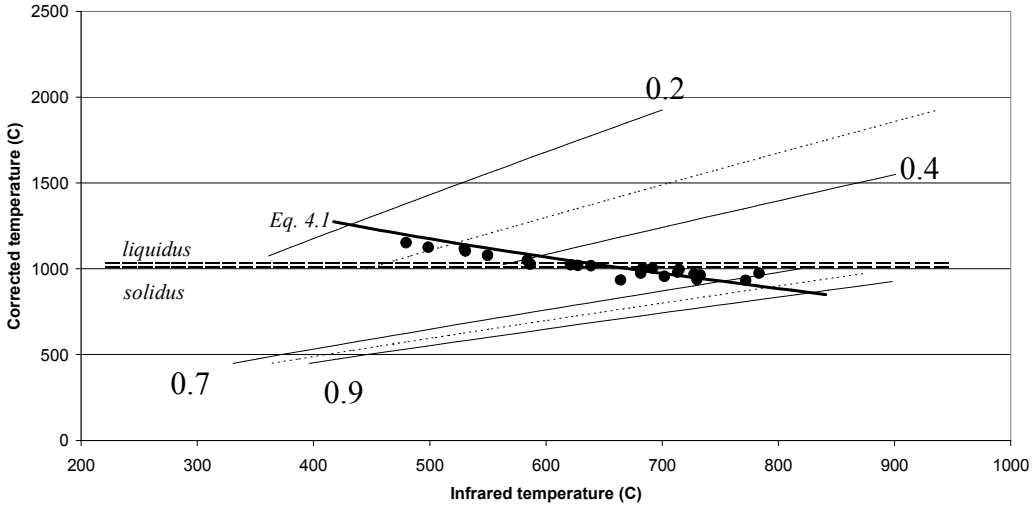

Figure 4.35: Conversion between infrared temperature (emissivity =1) and corrected emissivity. The emissivity of the MMC is a function of temperature and will decrease from 0.8 to 0.2 over the melting region.

The temperature results from Figure 4.27 were corrected using an iterative approach presented in the flow chart shown in Figure 4.36. The temperature reported by the infrared camera at an emissivity of one ($T_{\varepsilon=1}$) is applied to the Wien-Planck equation (Equation 2.11) to obtain the intensity value of the blackbody (M_{bb}). An emissivity value is guessed (ε_j) and the real intensity of the object is calculated (M_j). The real temperature of the object (T_j) is calculated based on equation 4.2 (the relationship between temperature, intensity and emissivity for the long wavelength camera). To determine if the guessed emissivity is correct, the emissivity of the new temperature (ε_{j+1}) is calculated according to equation 4.1 (the experimental relationship between emissivity and temperature). If the difference between the guessed emissivity (ε_j) and the calculated emissivity (ε_{j+1}) is greater than 0.001, then the calculated emissivity

(ε_{j+1}) becomes the new guess emissivity (ε_j). A new intensity is calculated (M_j) based on the new guess emissivity (ε_j) and the procedure is repeated. If convergence is achieved, the solution for the actual temperature and emissivity is obtained.

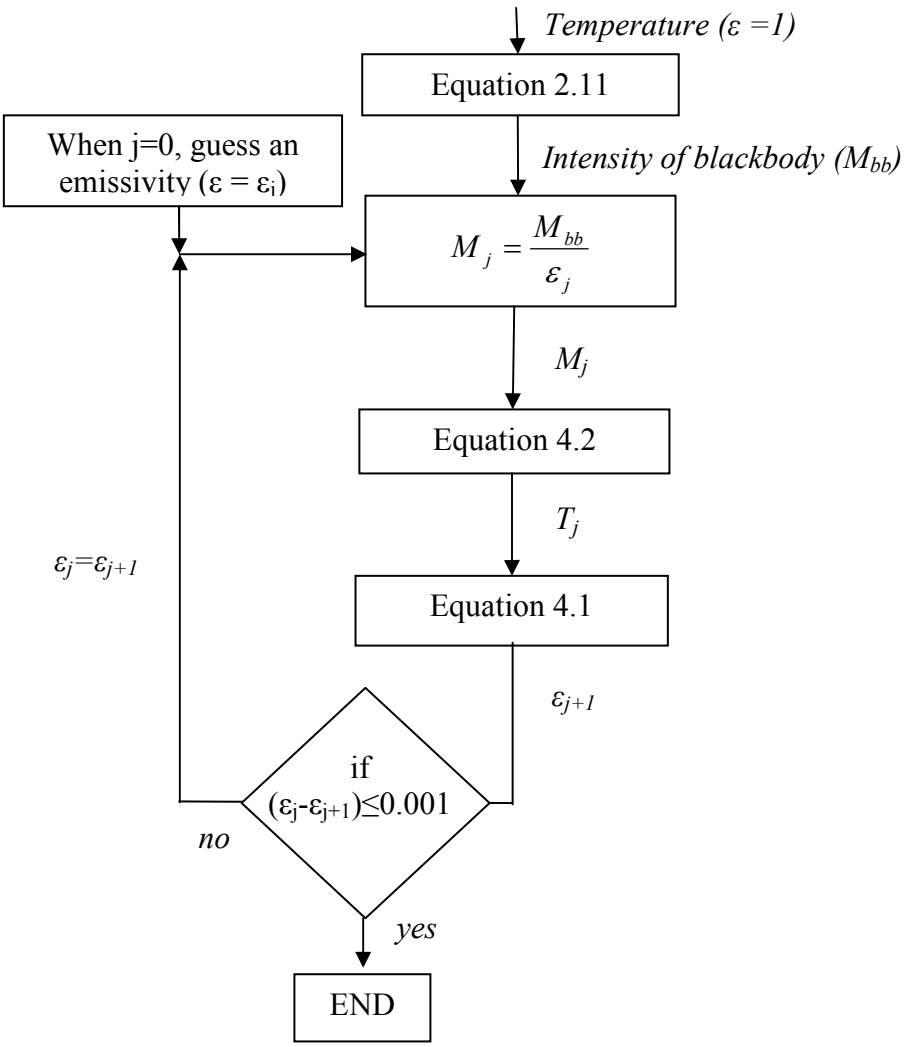

Figure 4.36: Flowchart of temperature correction algorithm.

The corrected temperatures are shown in Figure 4.37. They are significantly higher than the temperatures recorded with an emissivity of 1. The melting range of the MMC is between 1012°C and 1036°C. All the corrected temperatures are within or exceed this range within error. This concludes that the correction

algorithm presented is accurate and is able to calculate the absolute temperature of the MMC as it solidifies by infrared thermography. The corrected temperature results indicate the following trends in the PTAW process. As current increases from *110A* to *150A* and voltage increase from *20V* to *25V*, the weld pool temperature increases. The heat input of the arc is increased as the current or voltage rises, thus the surface temperature rises accordingly.

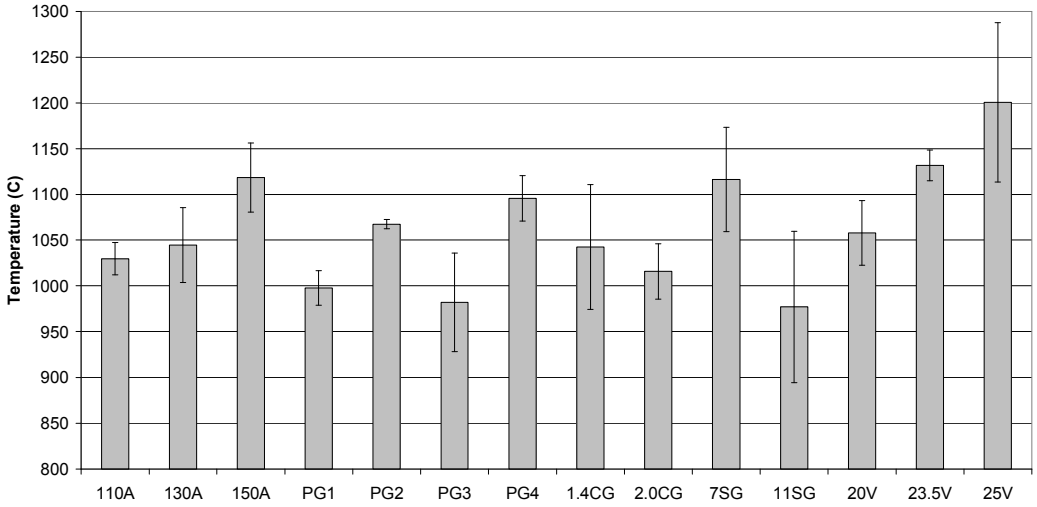

Figure 4.37: Surface temperatures of coatings under various operating parameters. The temperatures have been corrected to account for their accurate emissivities. The error bars are the variation between experiments.

When the shielding gas is increased from 7 lpm (7SG) to 11 lpm (11SG), the weld pool temperature decreases. Increasing shielding gas flow rate results in faster cooling of the surface of the deposit. On the other hand, increasing the plasma gas from 1 lpm (PG1) to 4 lpm (PG4) has little effect on the weld pool temperature. When increasing the plasma gas, the enthalpy of the arc increases, thus increasing the convective portion of the heat input of the arc. A model by Wilden et al. [WIL2006] predicted that the peak temperature of the plasma arc actually decreases with plasma gas flow. Since the arc power is constant (current and voltage are constant) but the gas flow increases, the arc energy density decreases because a larger volume of gas is being heated. As the enthalpy increases, the temperature gradient near the surface increases resulting in a higher

heat transfer. This results in more heat being added to the substrate region. Finally, the faster plasma velocity increases the particle velocity and reduces the time the particles are exposed to the hot plasma. Thus, the temperature of the particles is reduced and a minor increase in temperature is measured with increasing plasma gas flow.

There is a very small change in temperature with increasing the carrier gas from 1.4 lpm (1.4CG) to 2.0 lpm (2.0CG). An increase in carrier gas results in an increase in powder feed to the nozzle. The extra powder mass would require more heat in order for melting to occur and would be deposited at a lower temperature than the lower carrier gas case.

The temperatures measured from the cooling profile of the deposit after the arc was extinguished (Figure 4.25) were subjected to the correction algorithm, shown in Figure 4.38. Without the correction algorithm (black continuous line), the temperature increases from 500°C to 600°C in half a second. The temperature increase slows dramatically at around 610°C. A rapid increase to approximately 620°C occurs followed by a slow cooling period to 200°C. This figure highlights that without the correction algorithm, the temperature increases during solidification and does not reach the actual liquidus, but a temperature of approximately 620°C. To show continuous cooling of the surface, the correction algorithm was applied to the infrared temperature data. The algorithm was applied in the reverse time steps, from 4.5 s to 0 s. An emissivity of 0.7 was applied to the solid region to obtain a real temperature. The coating is deemed a solid after 2s on Figure 4.25 and 1 s on Figure 4.38. The first second of the temperature data obtained in Figure 4.25 was omitted as the arc was on and the arc interference was too severe to obtain a reliable temperature. The measured effective emissivities were applied to the mushy zone region (the region between the solidus and the liquidus). A linear approximation of the change in emissivity between the mushy zone and the solid was required to make the temperature continuous. This occurred between 700°C and 1012°C. Further experiments to

better quantify the change in emissivity at the solidus region are required to facilitate a convergent continuous temperature solution.

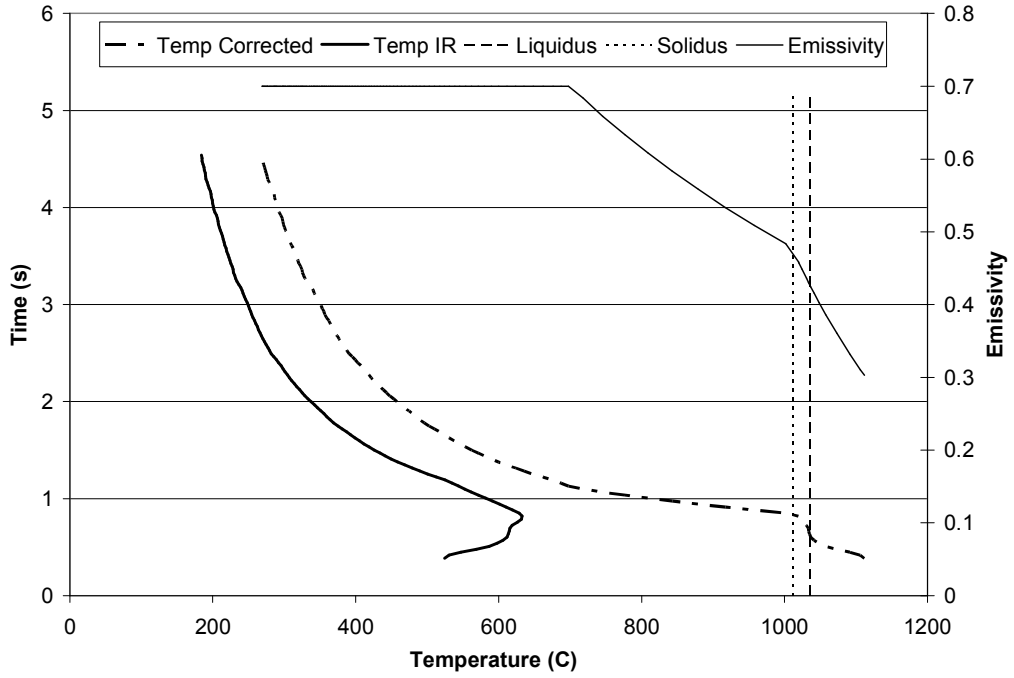

Figure 4.38: Correction algorithm applied to the temperature cooling profile of the deposit after the arc is extinguished.

The well known heat input (Q) equation, shown in Equation 2.2, is often used as it simplifies the variables which contribute to the heat in the weld to the current (I), voltage (V) and travel speed (v). The thermal data collected using the infrared cameras indicates that this relationship is not suitable for calculating the heat input for a complex welding process such as PTAW with powder deposition. The equation does not consider the complex interdependence of the effects of the plasma and shielding gases on the heat input, as clearly they have an effect on the resultant temperature of the surface. It is recommended that the use of this equation be limited to simple welding situations only.

4.3.4 Correlation between Infrared Temperatures and Measured Homogeneity

The temperature of the pool at arc off (Tavg_drop) has a weak correlation with the amount of carbide in the settling region (Figure 4.39). The corrected temperature at arc off for each of the process experiments was compared to the carbide amount in the settling region. A higher amount of carbide in the settling region results in a more homogeneous coating. A subtle trend can be identified that lowering the temperature results in a more homogeneous coating. However, the variability is too great to make a definitive conclusion.

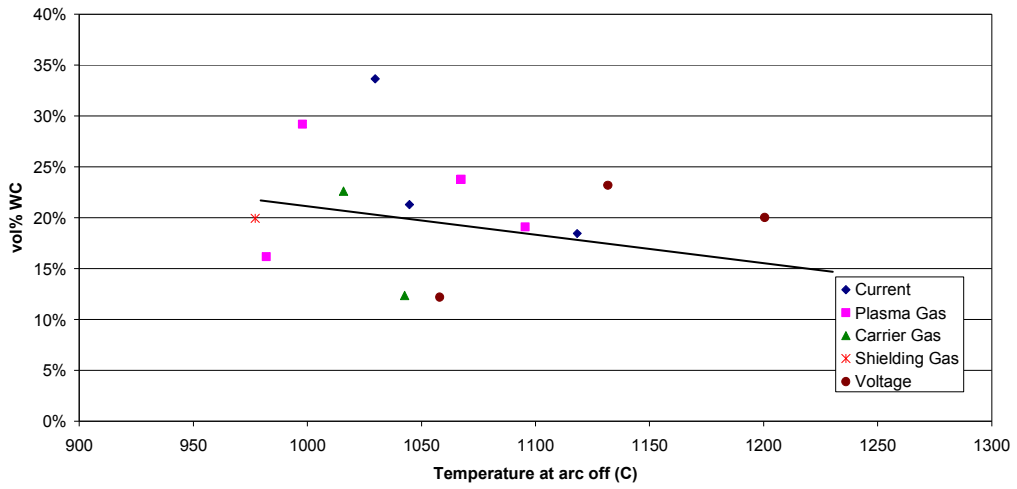

Figure 4.39: Relationship between arc off temperature and WC amount in the settling region of the deposit.

4.3.5 Summary

Infrared thermal images of plasma transferred arc welded coatings were collected. A higher resolution camera is required to capture the images as significant detail is lost with poorer resolution images that will result in misinterpretation of the image since the region of interest for this application is very small. The argon plasma arc, although not purported to be visible in wavelength ranges greater than 2 μm, is visible with both the long wavelength and short wavelength cameras. The interference of the arc and reflection on the surface make it impossible to

measure the surface temperature of the coating while the arc is on. The temperature can only be collected once the arc is extinguished. The classical tear drop shape of the weld pool with and without powder feed is not apparent in the infrared images. This is attributed to the high reflectivity of the liquid pool and the high variability of the effective emissivity of the alloy with temperature.

The emissivity of the surface plays a significant role in obtaining the correct temperature of the coating. The emissivity was found to decrease as the temperature increased between 900 to 1300 °C. The temperature was corrected using the measured emissivities and were within the melting temperatures of the alloy as determined by calorimetric studies of the alloy powder.

Using corrected emissivities, the effect of various process variables on the temperature of the PTAW deposit were determined. Increasing current and voltage resulted in an increase in the temperature of the deposit, as predicted. The shielding gas acts to cool the surface of the deposit, therefore, increasing the shielding gas decreases the surface temperature. Increasing the plasma gas resulted in a slight increase in surface temperature. This is a result of higher enthalpy transfer to the substrate rather than the coating. There was little change in temperature when increasing the carrier gas flow rate.

A thermal profile of the deposit as it was cooling was obtained. This profile is required to validate the temperature output of the combined settling and solidification model presented in Chapter 5.

In the next section, images of the plasma arc itself were captured using digital video cameras under various processing conditions. The analysis of these images provided an estimation of the initial and boundary conditions of the combined settling and solidification model. In addition, the results of the analysis highlight the differences in the shape and brightness of the plasma arc due to the presence

of the powder compared to an autogenous arc. This information is not found in the literature.

4.4 Plasma Arc Imaging

To further develop the boundary conditions and initial conditions required for the model, images of the plasma arc were captured by both regular and high speed cameras. For example, very little has been explored in the literature on the effect of carrier gas flow on the shape of the plasma arc. The images of the arc provide several initial and boundary conditions needed for the model, such as the initial particle velocity.

4.4.1 Arc Shape

An image of the plasma arc under various operating conditions was captured using a digital video camera with a pack of neutral density filters, as described in section 3.8. Since the arc temperature itself cannot be measured, as it had been modeled to be from 18000 to 30000 K by Jonsson et al. [JON1994], the intensity can be quantified. It should be noted that the intensity is a relative value and not absolute. The intensity (or brightness) of the plasma arc is related to the temperature of the plasma [OLS1963]. A model was developed that was able to correlate welding parameters with the arc light radiation (LI2000). Shown in Figure 4.40 is the plasma arc for a standard autogeneous weld. Several predicted features are apparent:

- the typical bell shape for a welding arc [NES1962] [RYK1974] [MCK1986] [ZHU1995] [FUD1997]and as a Gaussian distribution [PAV1969],
- the collimated core found in PTAW [COU1993] [AIT1998],
- the substrate is melted, the surface is depressed and the humping phenomenon is apparent [MEN1999].

However, when powder is applied, the arc shape changes significantly, as is shown in Figure 4.43. Compared to the autogenous case, the arc is no longer bell

shaped or symmetrical and the core is not as apparent. The plasma arc is less bright and less intense. Adding powder reduces the temperature of the arc from the autogeneous case, as the powder absorbs heat from the arc. Very little of the substrate is melted, as no depression of the surface is visible.

When increasing the plasma gas, the collimated core becomes larger and brighter – thus the temperature of the arc increases (Figure 4.42). The enthalpy of the arc increases directionally, thus increasing the convective portion of the heat input of the arc. These images confirm the Fluent derived model by Wilden et al. [WIL2006]. As the plasma gas increases, the arc will become more collimated and the gas velocity will increase. However, that model predicted that the peak temperature actually decreases with plasma gas flow. Since the arc power is constant but the gas flow increases, the arc energy density decreases because a larger volume of gas is being heated. As the axial enthalpy increases, the temperature gradient near the surface increases resulting in a higher heat transfer. Finally, the faster plasma velocity increases the particle velocity and reduces the time the particles are exposed to the hot plasma. Thus, the temperature of the particles would be reduced.

As the current increases, the intensity of the entire image increases, thus the enthalpy of the arc increases (Figure 4.43). The temperature of the arc would increase when increasing arc power; that is by increasing either current or voltage. The intensity of the entire arc will increase and thus the temperature gradient near the surface of the substrate. This will result in a hotter surface temperature and reduce the solidification rate of the deposit, thus allowing for a greater degree of settling.

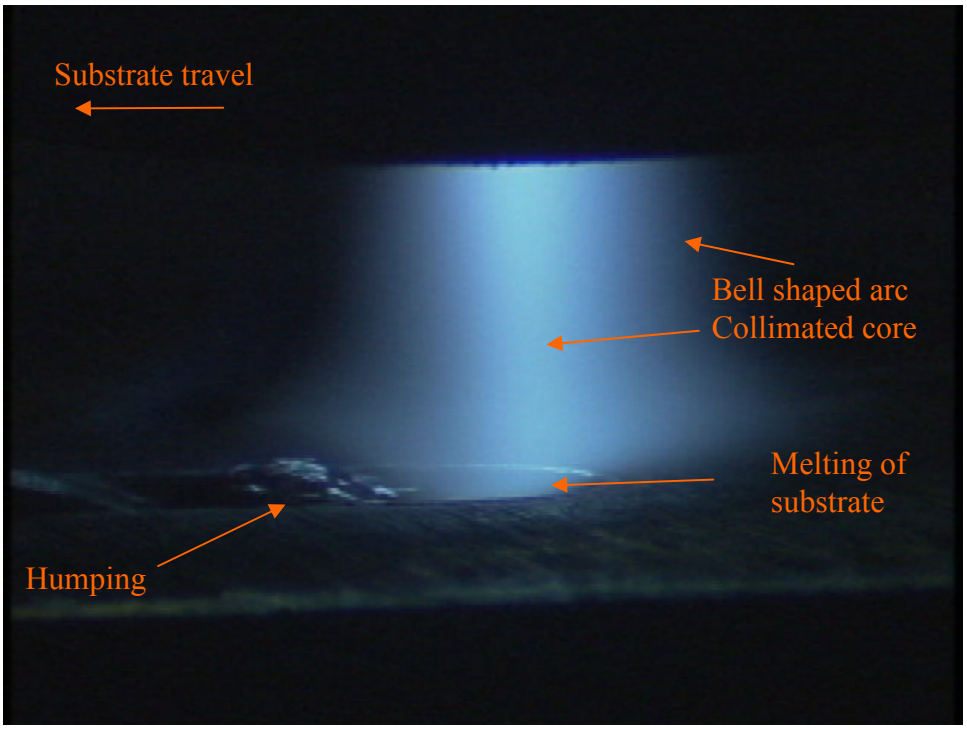

Figure 4.40: Image of plasma arc of a standard autogeneous weld

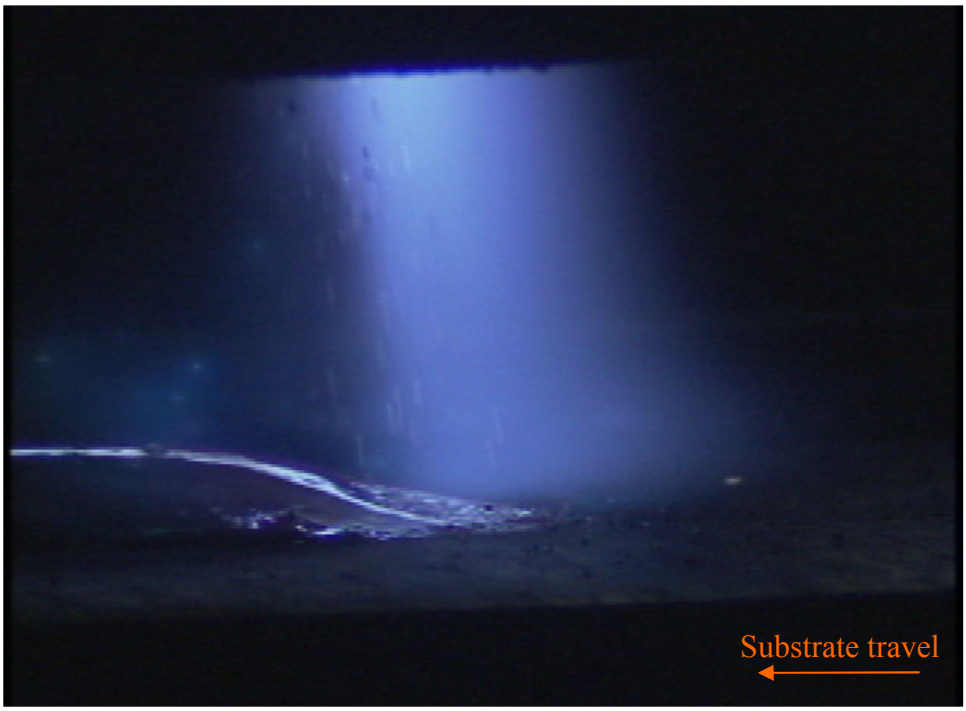

Figure 4.41: Image of plasma arc with NiCrBSi +WC powder addition, under standard conditions.

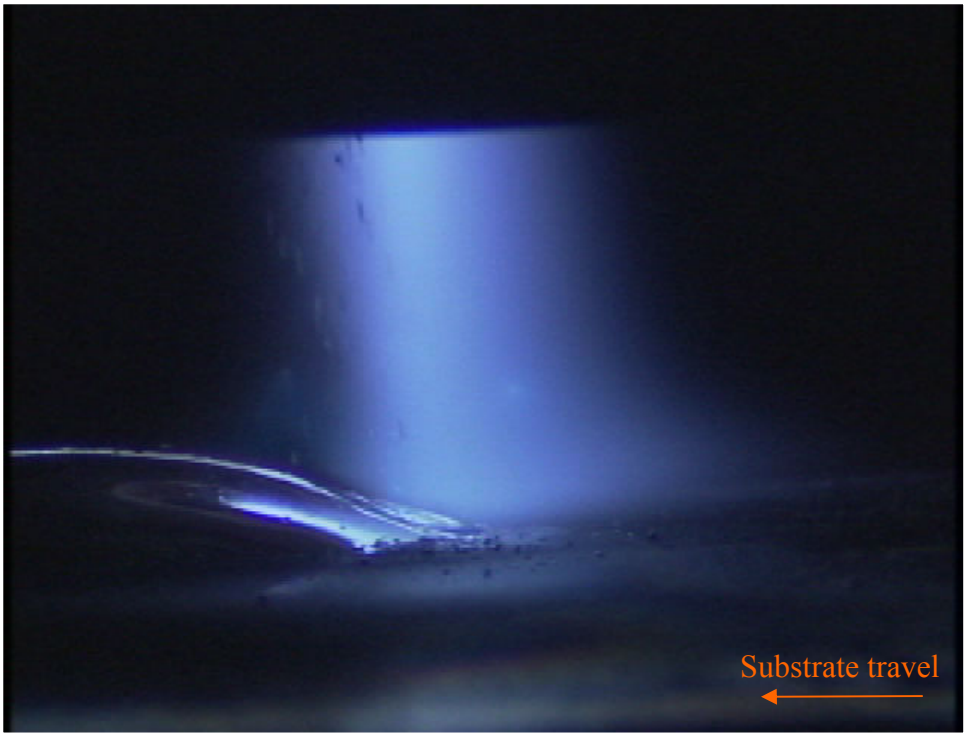

Figure 4.42: Image of plasma arc with NiCrBSi +WC powder addition, and increased plasma gas flow rate.

Figure 4.43: Image of plasma arc with NiCrBSi +WC powder addition, and increased current.

The plasma arc images were analyzed using image analysis in MATLAB. The images were modified to a 256 bit gray scale image. The position and magnitude of the maximum pixel gray scale value was recorded. Shown in Figure 4.44 is the difference in the skew of the collimated plasma core. The red line in Figure 4.44 is the position of the maximum intensity of the core as a function of the height of the plasma arc for an autogeneous weld. The green line shows the position of the core when NiCrBSi-WC powder is added to the trailing side of the arc. The resulting effect is to push the core forwards. The figure also reveals that the height of the arc is greater with the addition of powder.

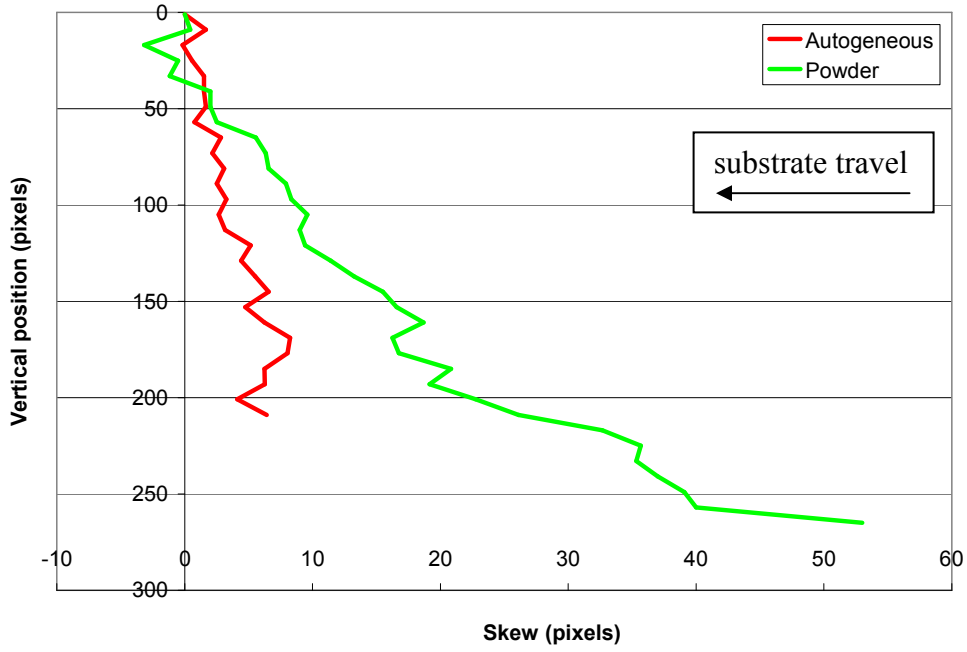

Figure 4.44: Average skew of intensity value of collimated core of the plasma arc under autogeneous conditions (Auto) and with powder addition (NiWC).

The length of the arc is quantified over all the arcs tested and is shown in Figure 4.45, where the labels represent the parameter that was varied. The operational parameters for both the autogeneous and Ni-WC arcs are identical, except that there is carrier gas flow of 1.4 lpm and powder for the Ni-WC case. The values tested for each operational paramters are listed in Table 4.2. The travel speed is different for the autogeneous and powder cases to ensure a constant voltage. The

addition of the powder significantly increases the length of the arc. Although the voltage recorded is the same for all the experiments (23.5 V), the distance between the back of the nozzle and the coating surface would be less than the distance from the front of the nozzle to the steel substrate. This difference would have a profound effect on arc physics. An asymmetric voltage drop would have two effects. Firstly, electrons are accelerated by the voltage drop between the cathode and anode. A greater voltage drop would act to increase the velocity of the electrons, thus increasing the heat input at the anode. The heat input is increased at the front of the arc, resulting in more melting of the substrate and increasing dilution. Secondly, the current density would not be symmetrical forcing the magnetic field to skew. The plasma jets would be pushed not towards the surface of the anode, but back towards the powder. The molten powder being deposited on the surface experienced a swirling effect, visible in video recordings of the welding process; the flow pattern was circular from the substrate towards the surface of the coating. This is the same direction that the skewed plasma jets are forced to travel due to the asymmetry of the arc.

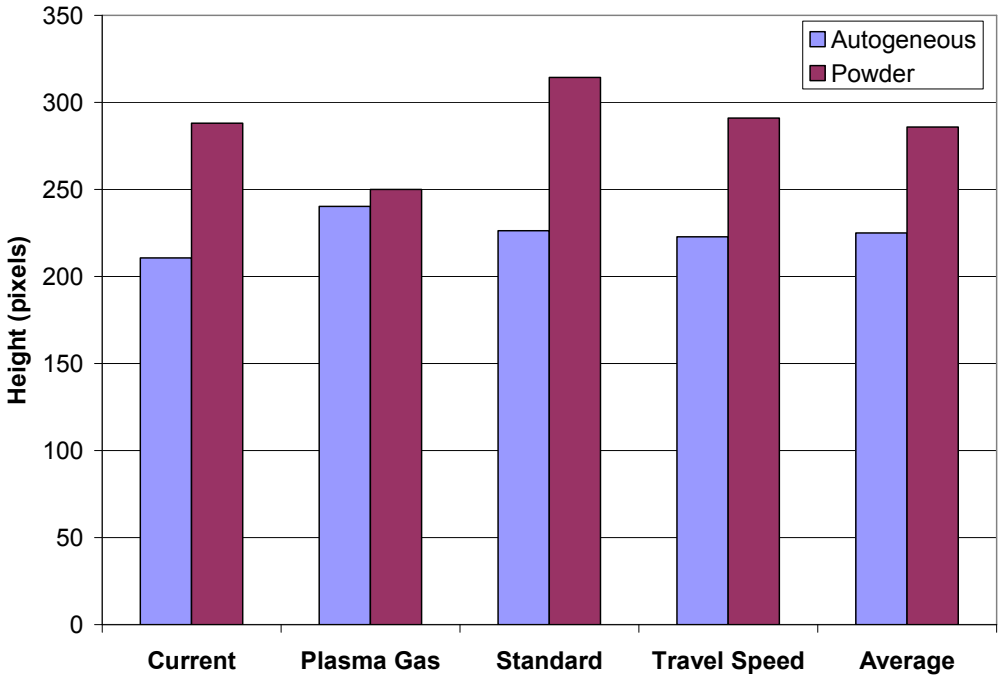

Figure 4.45: Arc height (in pixels) of autogeneous arcs and powder added arcs and changes due to increase in operating variables.

Table 4.2: Range of operational paramters tested for plasma arc imaging. The voltage was held constant at 23.5V.

Parameters	*Standard*	*Increase*
Current	130 A	150 A
Plasma Gas	2 lpm	4 lpm
Travel Speed	2.5 mm/s	5.1 mm/s

Another interesting result was the position of the maximum intensity of the core between the nozzle and the surface of the deposit (not the substrate). Shown in Figure 4.46 are the profiles of arc intensity when increasing current, plasma gas flow and travel speed compared to the standard condition for both autogeneous and Ni-WC powder welds. The intensity for the standard condition for the autogeneous run drops 25 grey scale values, where the Ni-WC run drops 50 grey scale values. Since intensity is a function of heat input of the arc, the Ni-WC arc contains less enthalpy than the autogeneous arc. This is because enthalpy is transferred to the powder as the powder is injected at room temperature and there is a large temperature gradient between the powder and the arc.

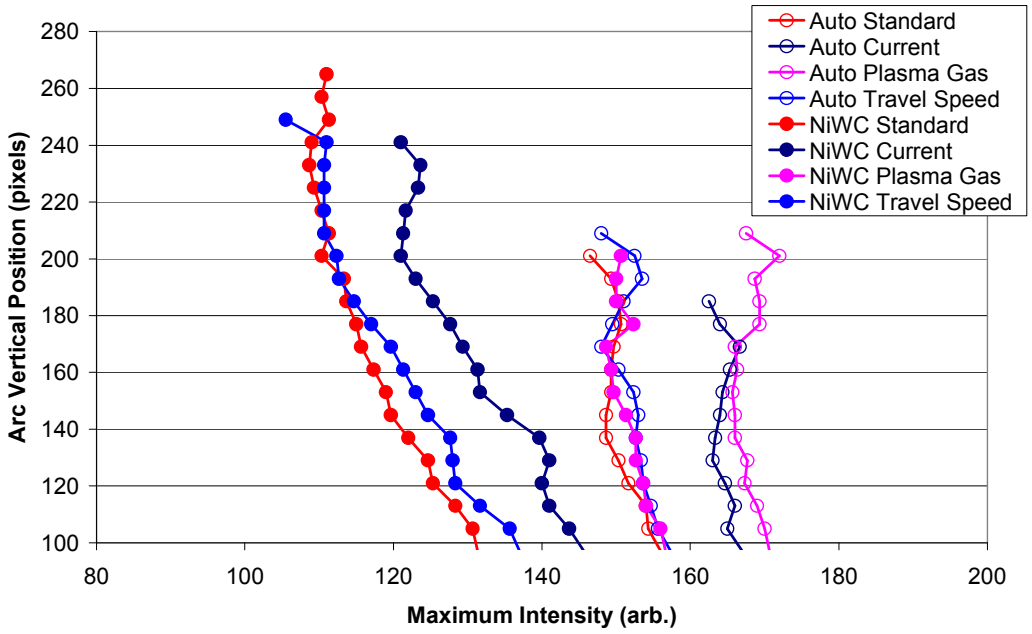

Figure 4.46: Profile of maximum intensity of arcs

Considering now only the autogeneous arcs, increasing the current and plasma gas flow increases the intensity of the arc similarly. The plasma gas profile is slightly

higher than the current profile thus, the plasma gas arc is slightly hotter than the current arc up to the top of the coating, which are both hotter than the standard arc. Increasing the travel speed has no effect on the arc intensity compared to the standard arc.

When the powder is injected into the arc, the intensity of the arc is lower than the autogeneous arcs. Increasing the plasma gas flow with the addition of powder increases the intensity to that of an autogeneous arc. A moderate increase in intensity is found with an increase in current. There is a negligible improvement in intensity for increases in travel speed. The maximum intensity difference between autogeneous and powder added arcs is 50 values with increases in current. This difference drops with increases in plasma gas flow rate to 25 values. The increase in directional enthalpy for the plasma gas increase must compensate for the powder injection in the core.

Finally, the arc is brighter in the autogeneous images, which confirms the results found with the plasma arc images: the autogeneous welding arcs are hotter than the arcs when powder is introduced. The temperature of the arc when the powder is included is less than that of the autogeneous arc. This is a result of the heat transferred to the powder from the arc in order to melt the powder.

The images were also used to provide guidance to the heat input boundary conditions. This topic will be further explored in Chapter 5.

4.4.2 Particle Velocity

The position of individual particles was tracked over a short sequence captured during the deposition process. Shown in Figure 4.47 is the position of a particle over 16 frames, identified as the red marker. The camera was acquiring an image at a rate of 2000 frames per second. Fifteen particles were tracked at various distances from the arc. The velocity of the particles is shown as a function of the y-position in Figure 4.48. The y-position is the displacement from the nozzle to

the substrate surface. The particle is accelerated from a velocity of 0.6-1.0 m/s to a velocity of 1.0-2.3 m/s along its trajectory. The difference in particle velocity can be attributed to the differences in particle mass and the proximity of the particle to the core of the plasma arc due to the three-dimensionality of the powder flow. Based on the data shown in Figure 4.48, the initial particle velocity at the surface of the deposit can be assumed to be 1.5 m/s.

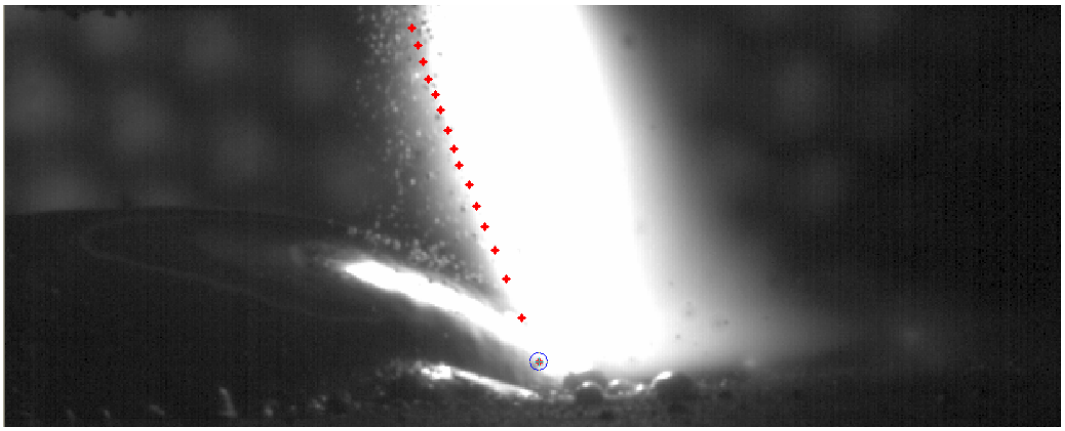

Figure 4.47: Tracking of a single particle in the plasma over a series of images during deposition

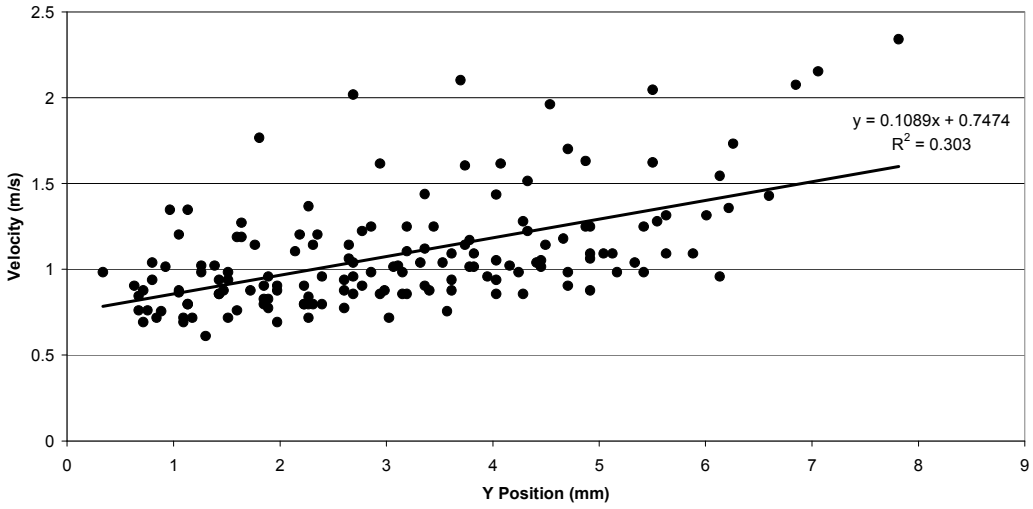

Figure 4.48: Velocity of 15 particles as a function of distance from the nozzle.

4.5 Microstructural Characterization of the Deposit

The microstructure of the coatings was examined using both optical and scanning electron microscopy. The changes in microstructure due to changing processing conditions and carbide type were investigated.

The components of the matrix alone were investigated and consisted of a primary Ni dendrite with a multi-phase interdendritic region. As the amount of heat input increased (or cooling rate decreased), the volume fraction of the interdendritic region surpassed that of the primary dendrite.

The addition of WC to the matrix caused a dramatic change in microstructure. There is sufficient heat to partially dissolve the carbide such that free tungsten and carbon are available to react with the matrix. Tungsten is found in solid solution in the matrix dendrites, as well as a major constituent in the complex carbides. The morphology of the carbides changes with the heat input from thread-like to dendritic to needle-like.

The amount of WC dissolved gives insight into the temperature of the arc to which the powders are exposed. Tungsten is ideal for analysis using SEM and EDX techniques due to its high atomic number, and small interaction volume. The very bright areas in the images in the backscatter electron mode make it easy to locate the regions rich in tungsten. The interaction volume of tungsten is also significantly smaller than the spot size, which makes the resolution of areas with tungsten good in both imaging and x-ray modes.

Finally, the degradation of spherical eutectic tungsten carbide particles was investigated. The carbides contained free tungsten and/or carbon, which allowed for a significant amount of degradation of the carbide.

4.5.1 Matrix Microstructure

The matrix was deposited under two heat input conditions, 120A and 170A, in order to determine effects of heat on the microstructure. All other conditions were held constant. The images were taken near the surface and in the center of the coating. All samples are etched with a modified Murakami's reagent to delineate phases.

The microstructure of the matrix consists of a primary dendritic structure with an interdendritic phase, observed in Figure 4.49a. A black phase is seen within the interdendritic phase (δ). With higher current, the heat input increases resulting in a lower cooling rate. This results in a larger primary dendrite size (Figure 4.49b). A component located within the interdendritic phase – the dark phase (δ), has a higher distribution at the higher current. Measured using threshold histrogram image analysis techniques, the amount of δ increases from 2.5% to 4.6% as the current is increased from 120 A to 170A. This is indicative of more coarsening and is consistent with lower cooling rates.

The secondary electron (SE) mode in Figure 4.50 shows that the interdendritic region has been etched more than the dendrite. The microstructure present is a dendritic phase, surrounded by a multi-phase interdendritic region as well as dispersed black phases. Referring to Figure 4.50 (BSE) and Table 4.3, the primary dendrite (1) is composed of Ni, Si and Cr. There are two phases identified interdendritically: a phase composed of primarily Ni (2a), and another with a composition similar to that of the primary dendrite (2b). The dark phase (3), referred as δ in the optical images, is high in Cr and is likely a chromium carbide.

The microstructure is more ordered in the centre of the coating and the differences between the primary dendrite and the multi-component interdendritic are apparent. Shown in Figure 4.51, the primary dendrite (1) is larger. This is indicative of slower cooling rates; as the cooling rate decreases, there is more time

permitted for dendrite growth [FLE1974]. The components of the interdendritic can be identified. Consulting with Table 4.4, the eutectic (2a and 2b) appears in the interdendritic, of compositions primarily of Ni (2a) and the other similar to that of the primary dendrite (2b). The chromium phase (3) is globular rather than acicular and is present within the interdendritic. It appears that the growth of (2b) is a result of loss of the purer Ni phase (2a).

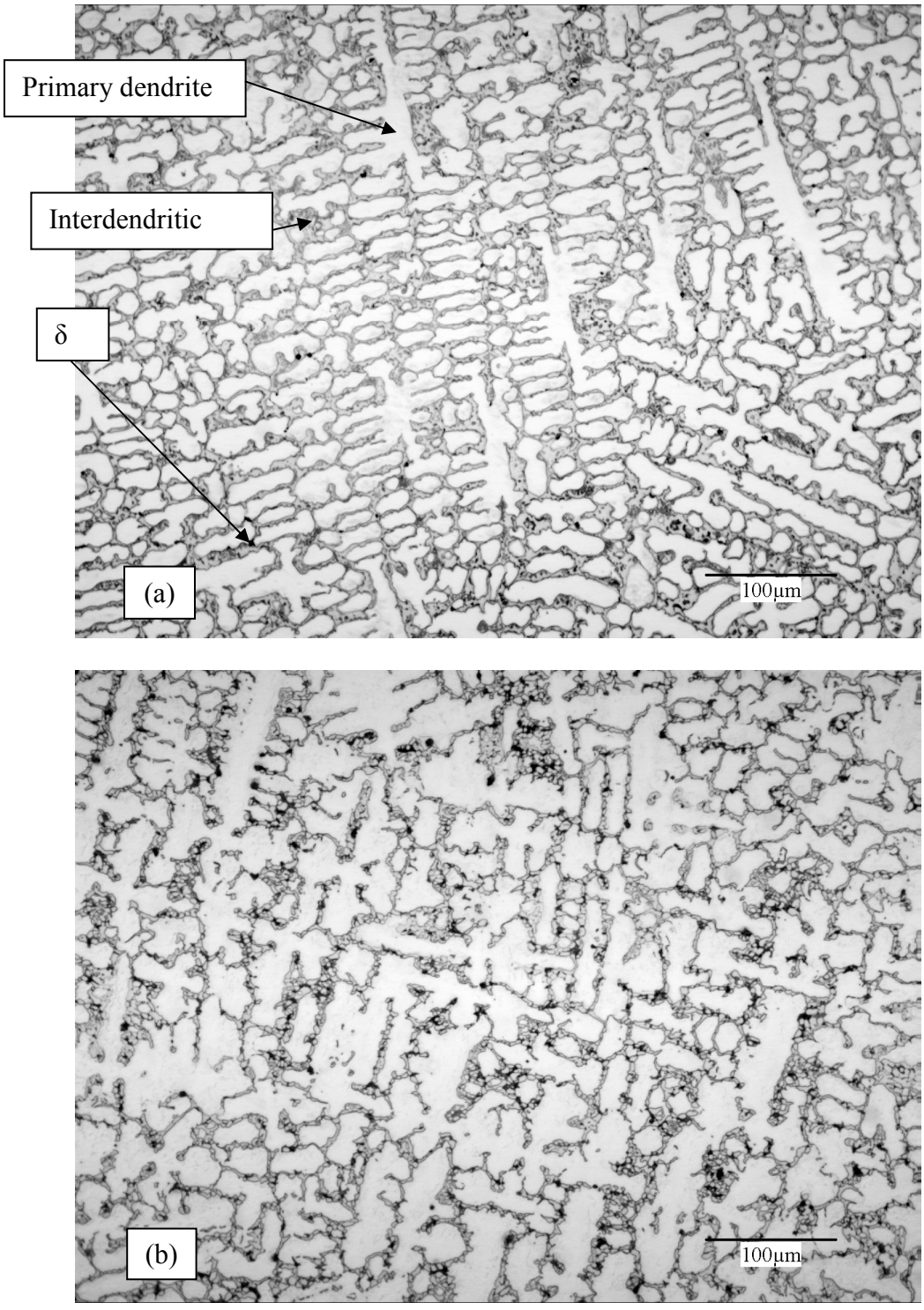

Figure 4.49: Optical microscopy of matrix only powder A using a current of (a) 120 A and (b) 170 A.

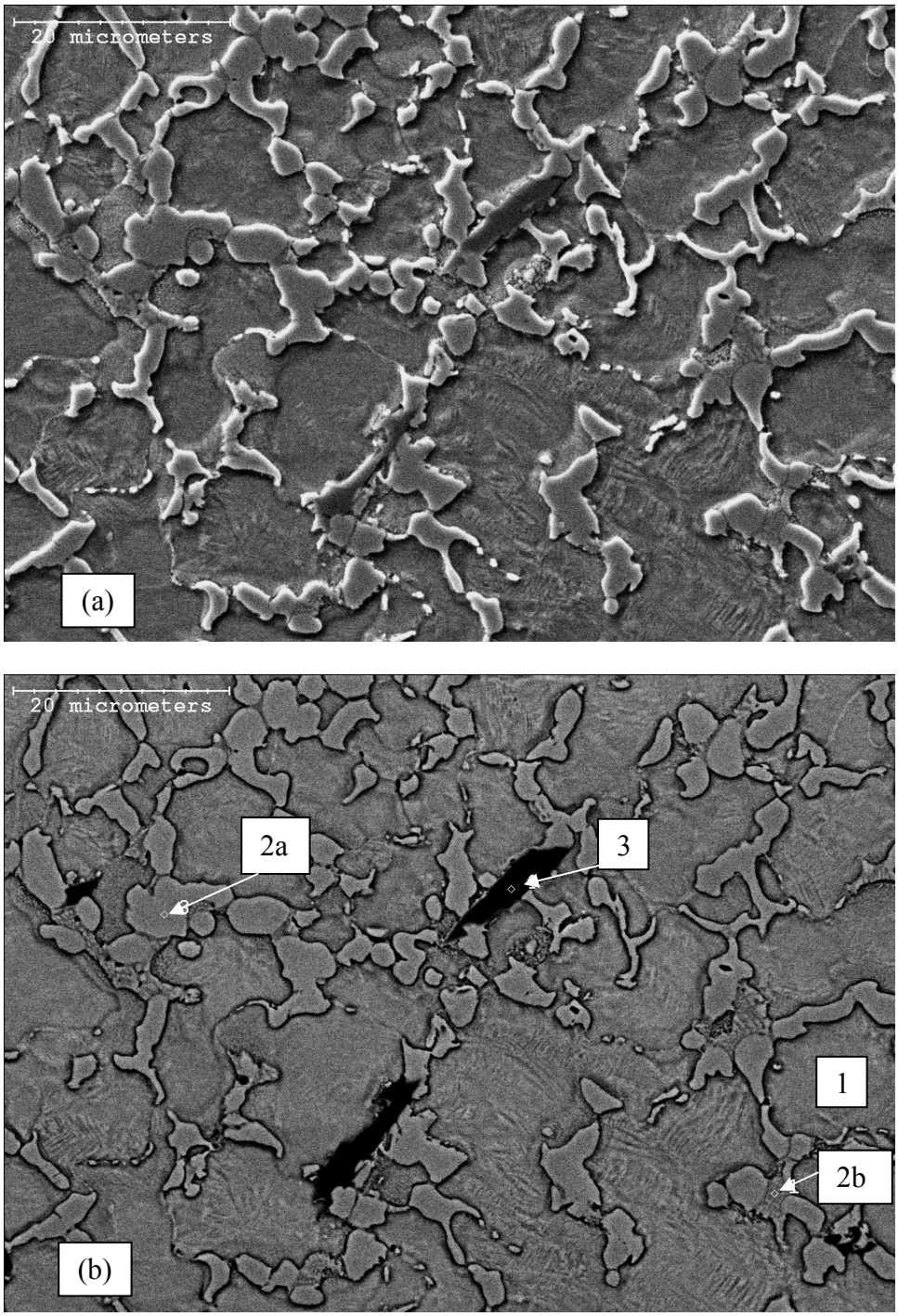

Figure 4.50: Microstructure of matrix near top surface in SE (a) and BSE (b) modes at 120 A.

Table 4.3: EDX results of points indicated on Figure 4.50. Composition is in at%.

Element	***1***	***2a***	***2b***	***3***
Si	4.3	-	8.2	-
Cr	6.2	4.4	2.3	**87.8**
Fe	1.7	0.9	0.5	0.5
Ni	**87.9**	**94.7**	**88.7**	11.7
P	-	-	0.4	-

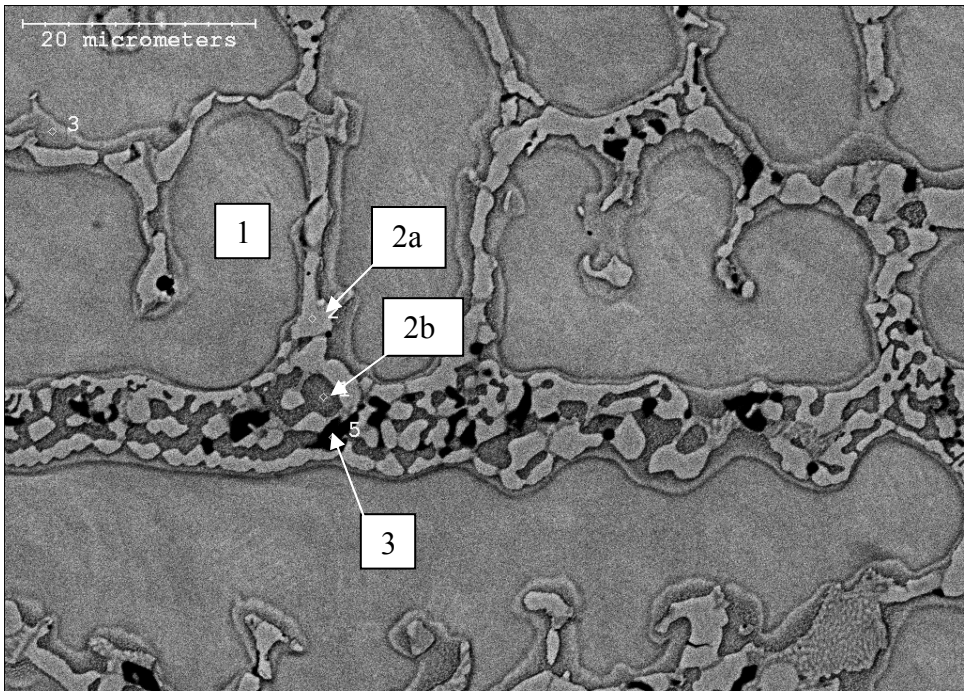

Figure 4.51: Microstructure of matrix powder A in the centre of the coating in BSE mode at 120 A.

Table 4.4: EDX results of points indicated in Figure 4.51

Element	**1**	**2a**	**2b**	**3**
Si	2.5	-	6.2	-
Cr	6.6	3.6	4.1	**81.9**
Fe	2.7	1.4	2.1	0.7
Ni	**88.2**	**94.9**	**87.6**	17.4

The microstructure of the matrix is coarsened when deposited with a higher current (Figure 4.52). The heat applied has a significant effect on the phase distribution, which could have a result in the performance of the coating. The size of the primary dendrite phase (1) is at least double that found in the lower heat input coating (Figure 4.50). There are 4 components to the interdendritic region (elements listed in Table 4.5): a primarily Ni phase (2a), a phase similar in composition to the primary dendrite (2b), a fine mixture of 2a and 2b (2c) and a Cr phase (3). These phases are similar to the results found in the center of the low heat input coating.

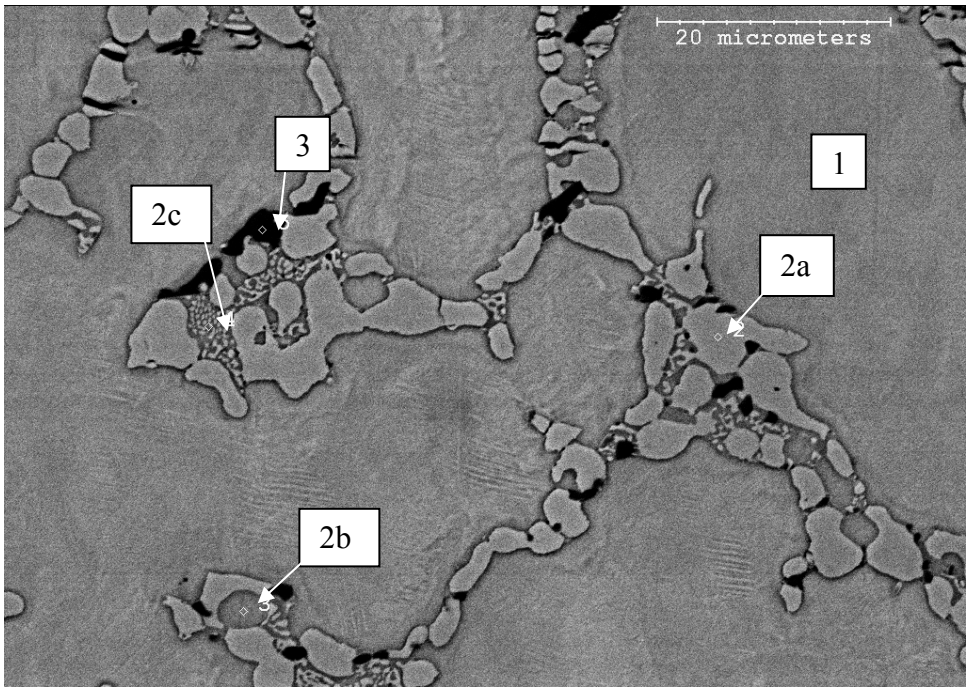

Figure 4.52: Microstructure of matrix powder A near surface viewed in BSE mode, deposited at a current of 170 A.

Table 4.5: EDX results of surface of high heat input coating of points indicated in Figure 4.52.

Element	***1***	***2a***	***2b***	***2c***	***3***
Si	2.3	-	4.8	8.4	-
Cr	5.9	4.1	4.0	2.5	**95.2**
Fe	9.3	4.9	8.0	3.4	1.1
Ni	**82.5**	**91.0**	**83.2**	**85.7**	3.7

In the center of the high heat input coating, the interdendritic structure dominates (Figure 4.53). Referring to Table 4.6, the phase compositions are very similar to those from the surface of the coating. The primary dendrite remains rich in Ni (1). The interdendritic matrix consists of a phase primarily composed of Ni (2a), a phase similar to the primary dendrite (2b), the mixture of the two (2c) and the Cr phase (3). The mixture appears very clearly as a eutectic. The primary dendrite (1) is more globular in shape, and the eutectic appears to compromise more of the volume. The eutectic microstructure is prominent (2c); both phases 2a and 2b are now very apparent as the components of the eutectic. This is characteristic of slower cooling rates where equilibrium microstructures can evolve. It is likely that the toughness of the interdendritic structure is less than the primary dendrite and this could lead to unpredictable spalling of the coating.

Increasing the current when depositing the matrix powder resulted in:

- an increase in the fraction of interdendritic phase;
- an increase in the size and amount of Cr carbides;
- a coarsening of the primary dendrite phase; and,
- an increase in the size of the eutectic phase within the interdendritic.

This analysis revealed that the microstructure of the matrix is highly sensitive on the amount of heat applied during deposition. As cooling rates decrease, the interlamellar spacing of the eutectic increases.

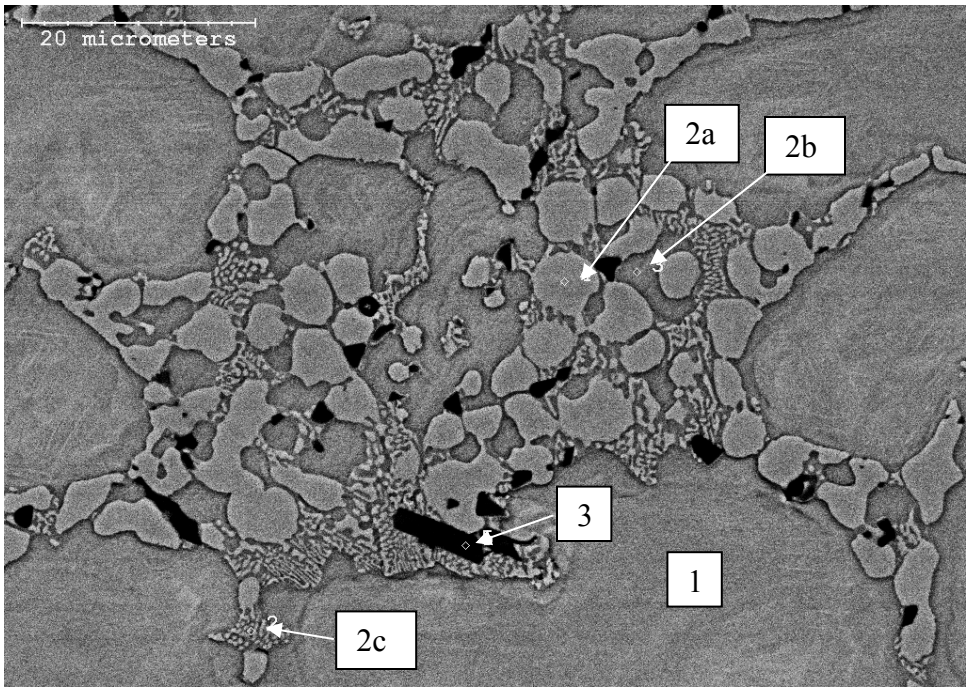

Figure 4.53: Microstructure of matrix Powder A near centre of coating taken in BSE mode, deposited at a current of 170 A.

Table 4.6: EDX results of the centre of the high heat input coating.

Element	***1***	***2a***	***2b***	***2c***	***3***
Si	3.2	-	4.6	5.5	-
Cr	6.2	4.0	4.7	3.3	**91.8**
Fe	9.9	5.4	8.3	4.2	1.1
Ni	**80.6**	**90.6**	**82.4**	**87.0**	6.7
S	-	-	-	-	0.4

4.5.2 MMC Microstructure

The macrocrystalline WC was added to the matrix powder and deposited under standard conditions. The effect on the microstructure with the addition of the carbide was examined. The coatings investigated were:

- standard commercial mix (50 vol% WC nominal) – single pass;
- standard commercial mix (50 vol% WC nominal) – double pass
- standard commercial mix (50 vol% WC nominal) – triple pass
- 50 vol% WC mixed with matrix powder (fully packed) – single pass.

Shown in Figure 4.54 are images of the four coatings taken by optical microscopy. Both the standard (a) and fully packed angular (b) WC mixtures are fully homogeneous throughout the thickness of the deposit. Image analysis of the coating revealed that there was slightly more tungsten carbide in the fully packed mixture than the standard mixture (>3 vol%). This can also be seen in the image as the carbides are packed closer together and there are circular regions void of carbide. This seems to occur when the carbide volume fraction is equal or greater than 65w%. The kinetics of the formation of the denuded carbide zones is currently not fully understood.

The inhomogeneous distribution of WC particles was observed in the multi-pass specimen. More settling occurred with 2 passes (c) and 3 passes (d) than a single pass due to the extra heat input. The morphology of the matrix is not observed in these images as they were not etched.

To understand the phase structure of the coating, SEM analysis was required, as the microstructure was indistinguishable using optical microscopy.

4.5.2.1 SEM and EDX Results

All images were taken from backscattered electron (BSE) modes as more phase information was revealed. Image contrast increases with atomic number, and since W is present in large quantities, it was easy to identify phases that contain W due to the increase in brightness. All EDX information was taken with a spot size of 1 μm. The analysis is semi-quantitative due to the surface not being perfectly flat and the presence of the light elements carbon and boron. The compositional data is presented in atomic percent.

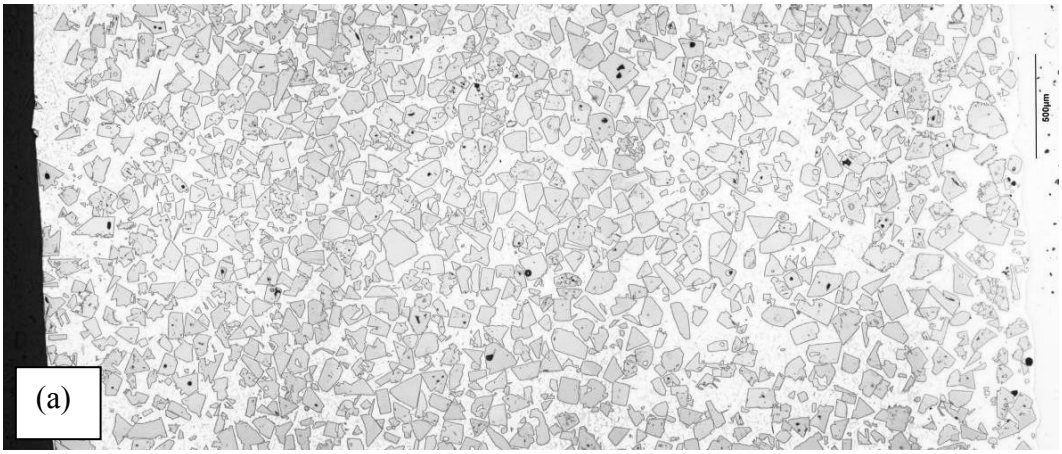
(a)
500µm

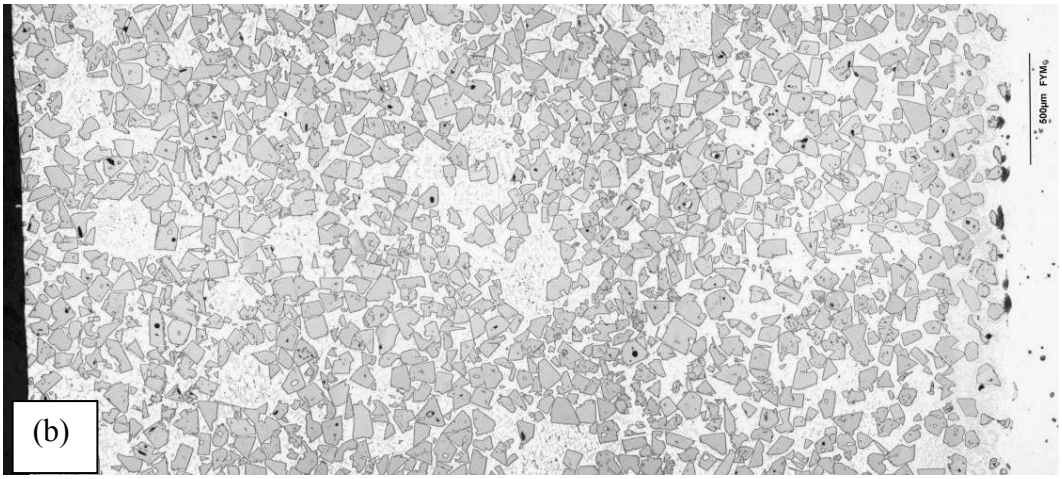
(b)
500µm FYM6

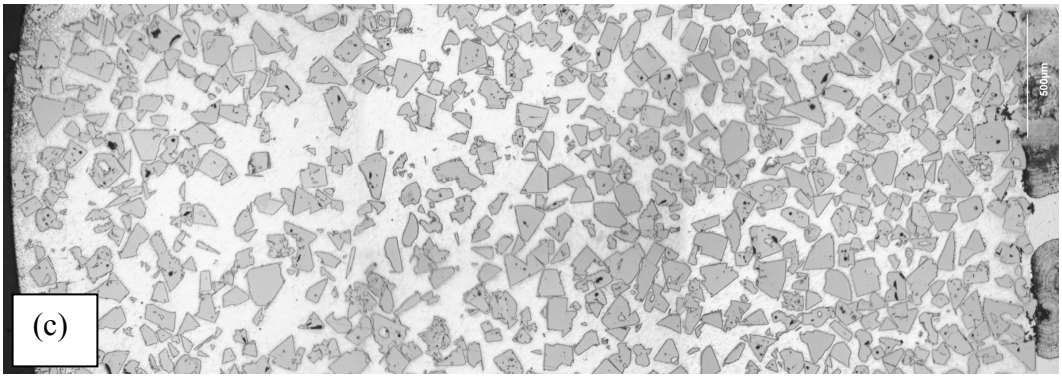
(c)
500µm

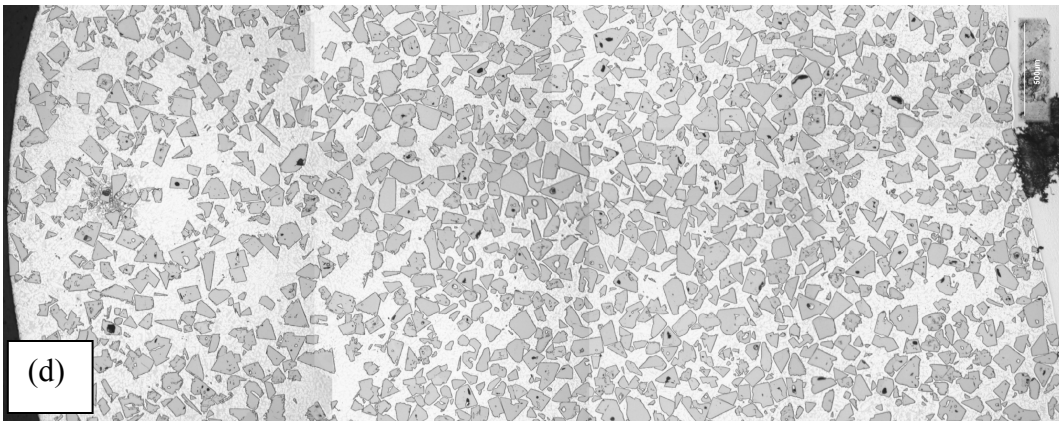

Figure 4.54: Optical metallograph of cross section of (a) standard commercial mixture, (b) fully packed macrocrystalline WC single pass, (c) fully packed macrocrystalline WC double pass, and (d) fully packed macrocrystalline WC triple pass. Top of overlay is on left edge.

4.5.2.1.1 Fully packed (50 vol% WC with matrix powder)

The fully packed specimen did show a homogeneous distribution of WC particles throughout the coating, shown in Figure 4.54b. However, circular zones denuded of primary WC particles were present. Shown in Figure 4.55 is a BSE image of the denuded zones. Due to the significant atomic number contrast between the WC particles and the Ni-alloy matrix, it is easy to determine the areas where W is present. In Figure 4.55, small white phases are dispersed throughout the circular denuded regions.

The two regions of interest are the phases in the denuded regions and between the primary WC particles elsewhere in the coating. The primary WC particles in Figure 4.56 are coarse and there are small particles distributed in a smearing fashion around the particles. This unidirectional smearing is due to the cutting of the diamond saw. The WC particles are very hard and are prone to fracturing. It can be seen that there are two matrix phases: A and B. EDX results indicate that the A phase is mainly Ni, and the B phase contains higher levels of W, Cr and Si, shown in Table 4.7. The presence of W in solution of the gray Ni-phase increases the average atomic number of the phase and hence the brightness. The

morphology found with the matrix only in terms of the dendritic and interdendritic phases are not seen with the addition of WC particles.

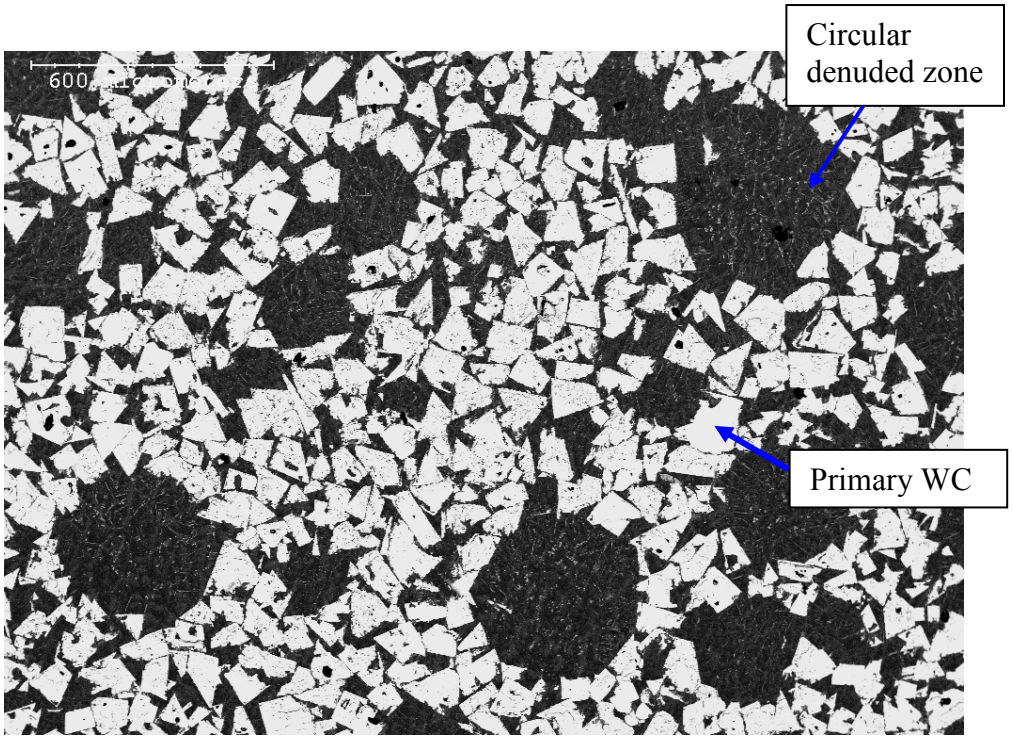

Figure 4.55: BSE images of MMC containing 50 vol% WC and matrix powder.

Inspection of the inter-particle matrix reveals the presence of complex phases. Their morphology is either thread-like or granular, shown in Figure 4.56. The thread-like phases (4) have a complex composition such as $(W,Cr_2,Ni)_xC_y$, based on the EDX results (Table 4.7). Their brightness is less than the primary WC particles, but greater than the matrix – a direct result of the W content of the complex carbide. The particle size is approximately 1.5 μm wide and ranges from 10-20 μm long. There appears to be some branching of the carbide. The small granular particles (5) are around 1 μm in diameter and have the composition ratio $(W,Cr,Ni_2)_xC_y$. There is also Nb and Ti found in these carbides, which is a result of mixing with the steel substrate since no Nb or Ti is found in the powder itself. The other phase of interest (6), is very bright and is very high in Ni and W.

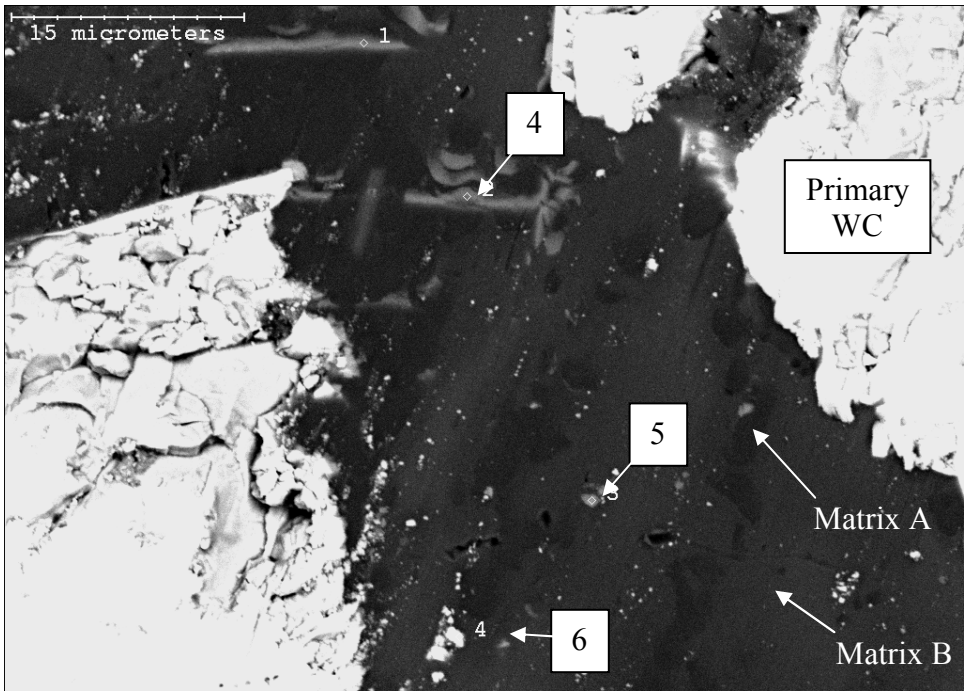

Figure 4.56: Primary WC particles and matrix between particles

Table 4.7: EDX results of matrix and complex carbides in Figure 4.56.

Element	***Matrix A***	***Matrix B***	***4***	***5***	***6***
Si	1.6	3.4	4.7	6.9	11.8
W	0.4	3.4	**21.5**	**21.5**	**45.0**
Cr	2.6	5.0	**48.8**	**22.3**	1.8
Fe	1.1	1.9	0.9	1.0	1.1
Ni	**94.4**	**86.3**	24.1	**39.2**	**40.2**
Ti	-	-	-	7.3	-
Nb	-	-	-	1.9	-

The circular regions denuded of primary carbide are not empty space, but a mixture of matrix and complex carbide phases. Figure 4.57a shows a high density of the complex carbide within the denuded region, which is homogeneously distributed with a random orientation. A magnified view (Figure 4.57b) shows the presence of the thread-like carbide, with composition shown in

Table 4.8. The carbides (7-10) are all (W,Ni,Cr) carbides of similar composition. Phase 7 and 9 are the brightest and largest in the image, composed primarily of Ni and Cr. It appears like the core of the complex carbide may have a higher W content than the branches. Phase 8 is less bright than Phase 7, due to the higher amounts of Ni and less W, thus a lower average atomic number. The angular particle, Phase 10, is composed almost equally of Ni, Cr and W. The one difference between the thread-like phase in the inter-particle matrix and those in the denuded region is that the carbides located in the denuded region are much brighter. This phase is also larger than those found in the inter-particle matrix, measuring approximately 2 μm in width. The brighter particles have a higher percentage of W, which is a direct result of the higher average atomic number of the phase. The matrix is still the two phases: A, near pure Ni phase, and B, the (W,Cr,Si) Ni phase.

The shape of the circular denuded zones being spherical indicates that they were formed above the deposit. The typical size of the denuded zone is 150 to 400 μm, significantly larger than the size of the matrix powder (63 to 180 μm). The denuded regions only occur with high volume fractions of WC. These regions are prone to removal during a G65 wear abrasion test. A theory regarding the presence and formation of the denuded zones lies in the particle kinetics in the plasma. The carbides particles are heated to high temperatures, beyond the melting point of the carbide. Since the temperature of the plasma is in excess of 10 000 K, it is feasible that some of the carbide vaporizes. The W vapour diffuses into the Ni droplets, along with the C. The Ni droplets may coalesce, forming these spheres and the complex carbide needles precipitate within. The spheres enter the deposit as a mushy phase and retain their spherical shape as they solidify in the coating. Since only one manufacturer of macrocrystalline carbide was used, it is conceivable that the manufacturing process is such that the carbides are not entirely stable at high temperatures. A review of the stability of various carbide types and manufacturers at high temperatures should be conducted.

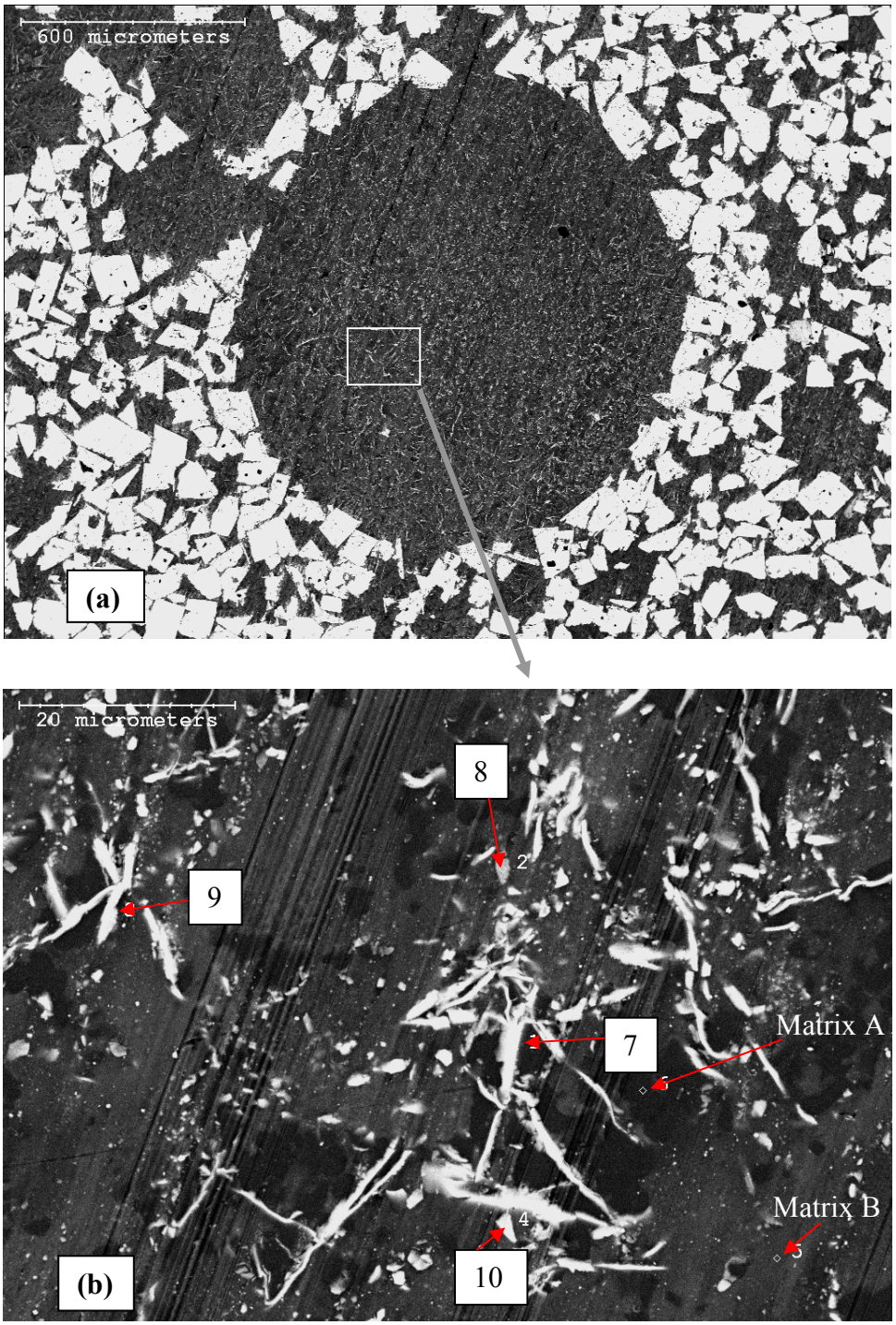

Figure 4.57: Circular denuded region microstructure (a) and magnification of phases located within region (b).

Table 4.8: EDX results of phases in void microstructure shown in Figure 4.57.

Element	***7***	***8***	***9***	***10***	***Matrix A***	***Matrix B***
Si	9.6	5.0	7.7	6.8	0.3	3.8
W	**39.4**	16.2	**31.4**	**27.4**	1.0	3.0
Cr	**28.8**	**27.1**	**35.6**	**29.7**	2.6	4.2
Fe	0.7	1.6	1.2	1.3	0.8	2.0
Ni	16.6	**50.1**	**24.1**	**34.7**	**95.4**	**87.0**
Ti	4.7	-	-	-	-	-

To identify the thread-like and granular phases as carbides, the sample was etched with a modified Murakami's solution, which acts to remove carbides. The sample was also polished to better delineate the Ni alloy phases. Shown in Figure 4.58a, there are no longer bright areas within the denuded sections and a eutectic structure is apparent. A magnified view of the denuded region (Figure 4.58b) reveals five structures: a needle carbide, a granular carbide, a bright dendrite (C), a light gray interdendritic (D), and a dark gray interdendritic (E).

The composition of the matrix in all three regions is similar to that of Matrix B. The bright core dendrite is the Ni-based alloy with high W and Cr, shown in Table 4.9. The difference between the two interdendritic phases is that the darker one has less W and more Si. After the primary dendrite solidified, the interdendritic liquid partitioned into a tungsten rich alloy (brighter) and a silicon rich alloy (darker). The composition of the needle carbide has a high amount of interference from the matrix, since the carbide was etched and effectively removed.

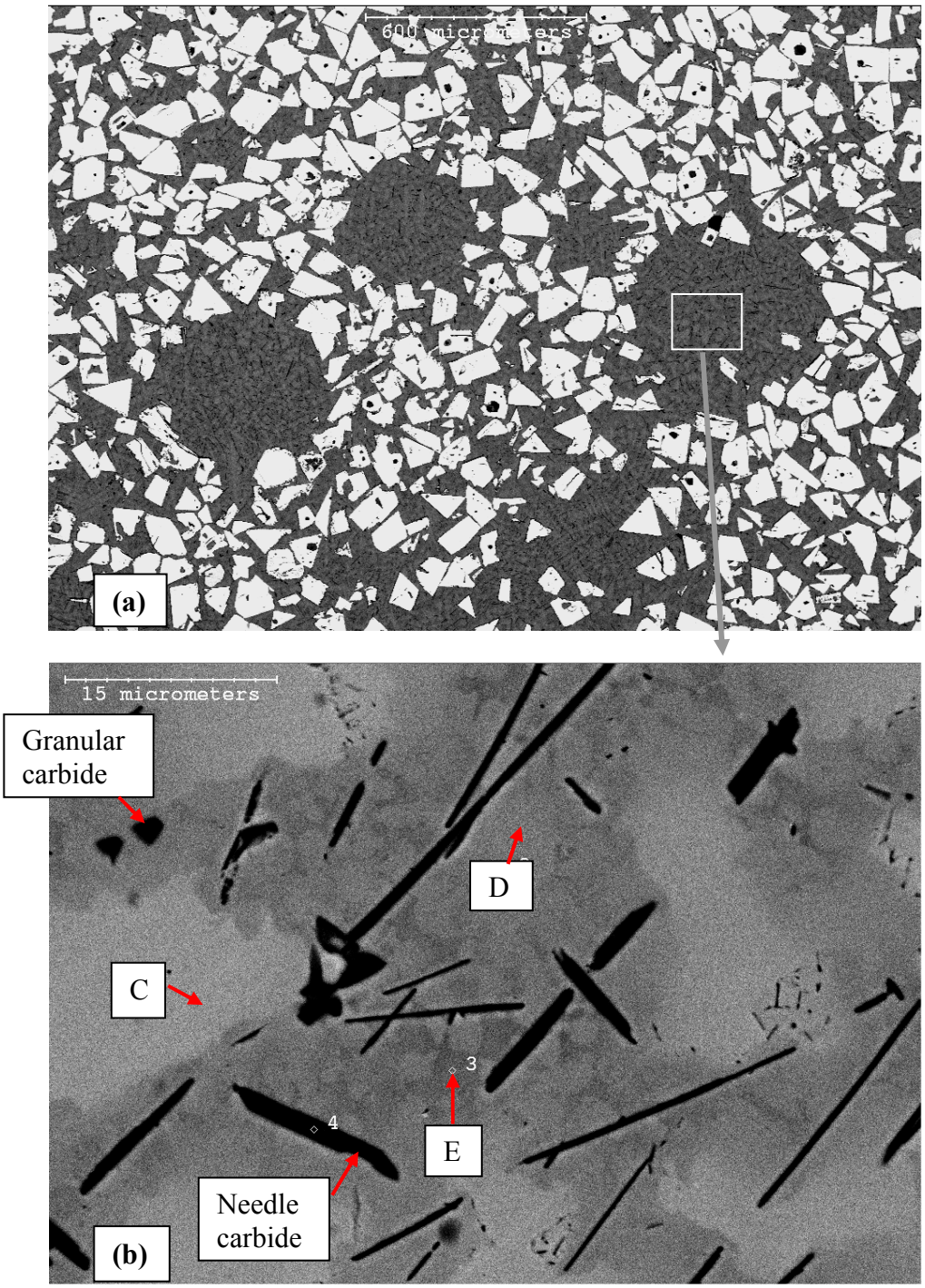

Figure 4.58: Fully packed sample etched with modified Murakami's reagent: full view of denuded region (a), and close-up of matrix and carbides (b).

Table 4.9: EDX results of matrix in denuded region of a polished/etched fully packed MMC.

Element	*C*	*D*	*E*
Si	3.3	4.4	6.6
W	3.1	1.4	0.7
Cr	5.2	3.9	2.4
Fe	2.2	1.8	1.4
Ni	86.3	88.5	88.9
Ti	-	-	-

4.5.2.1.2 Standard Commercial Mix (Single and Multi-pass Coatings)

The microscopy of the coatings produced with the standard commercial mix are very different than those with the mixed 50 vol% WC powder. In addition, the secondary carbides produced on the double passes are vastly different than those found with a single pass. In the fully packed single pass, as shown in the previous section, the secondary carbides were present in both between the primary WC and within the circular denuded zones and had a thread-like morphology.

In the single pass coating with the commercial mix, the region depleted of WC particles is located on the exterior of the coating, where the highest cooling rates occur. In BSE mode (Figure 4.59a), it can be seen that there is a fine distribution of bright particles in the matrix that was not observed with optical microscopy (Figure 4.54c). This phase is concentrated along the periphery, but is also found surrounding the WC particles to a small degree. A magnified view (Figure 4.59b) shows the highly dendritic structure of the secondary phase. It is composed of a gray matrix (12) and a bright 2-phase cored dendrite (11,13).

Referring to Table 4.10, the core (11) of the secondary phase is high in W and contains Cr in a W_2Cr ratio. The surrounding gray zone (12) contains equivalent amounts of W and Cr. The matrix phase is Ni-based (Matrix), but also contains a large amount of Fe. The black worm-like phase was not identified.

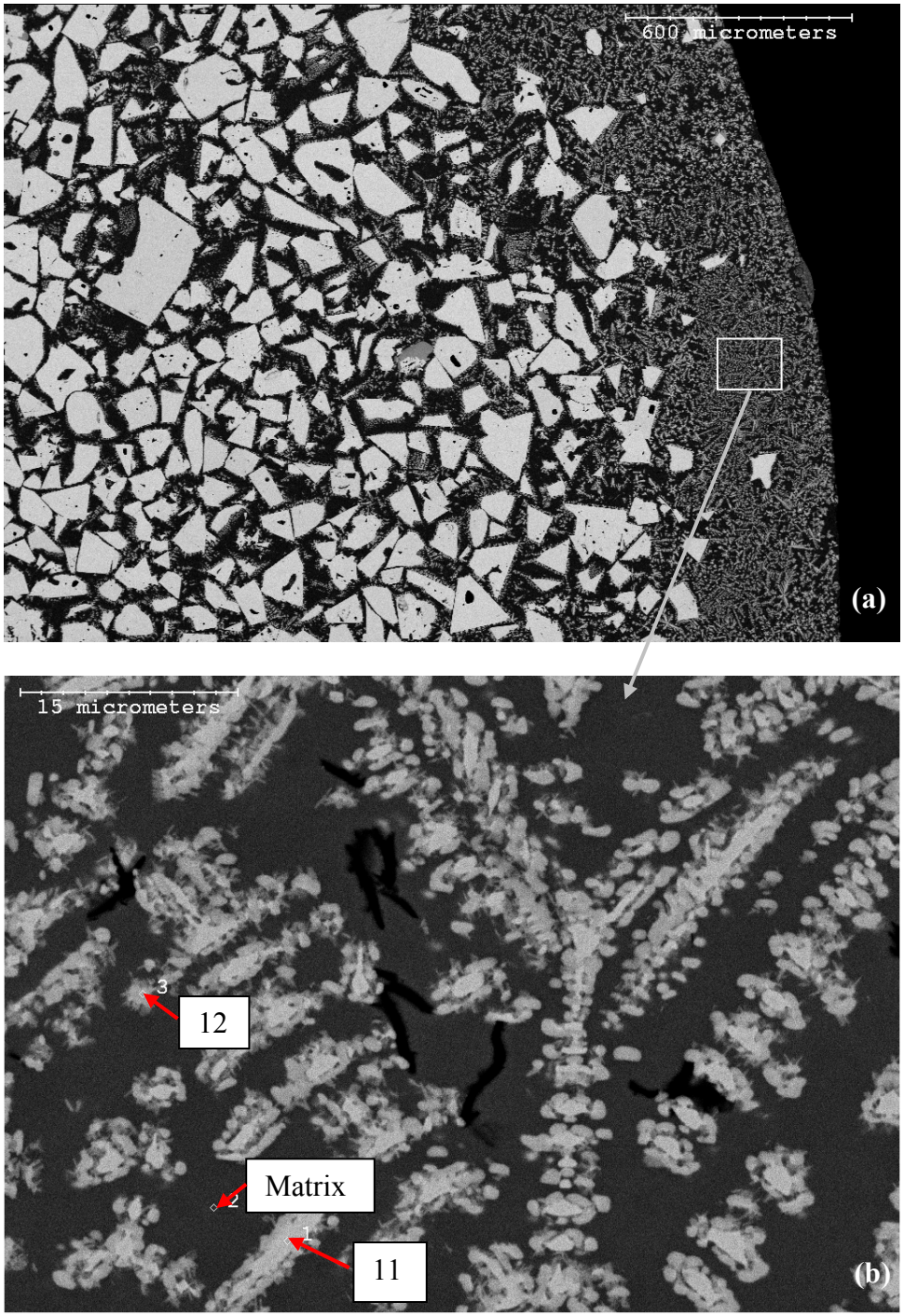

Figure 4.59: Single pass coating with inhomogeneous distribution of WC and fine particles on periphery (a) and magnified view of secondary phase (b).

Table 4.10: EDX results of single pass secondary phase shown in Figure 4.59

Element	***11***	***12***	***Matrix***
Si	7.7	4.1	4.5
W	**50.0**	**40.0**	0.3
Cr	**28.3**	**40.0**	2.7
Fe	5.0	6.0	**22.6**
Ni	9.0	9.8	**69.9**

Further into the matrix where the WC particles are more densely packed, the secondary phase is found surrounding the primary WC particles, shown in Figure 4.60a. The morphology of the secondary phase is dendritic similar to that found near the surface. They are most prominent on the borders of the primary WC (Figure 4.60b), which display a high degree of cleavage, likely due to melting or degradation of the primary WC particle. The EDX analysis (Table 4.11) revealed that the constituents of the microstructure were the primary WC, the cored secondary carbide (13, 14, 15) and the Ni matrix (Matrix). It should be noted that W and Si share identical x-ray peaks and can interfere with each other. This explains the presence of Si in the primary WC. There are small compositional changes between the layers of the cored secondary carbide. As the secondary carbide appears less bright, the amount of W in the phase decreases.

The morphology of the carbide present on the surface of the multiple pass coating is needle-like instead of dendritic, shown in Figure 4.61a. The primary WC particles found near the surface exhibit a high degree of melting as shown in the cleavage surrounding the carbide (Figure 4.61b). The acicular secondary carbides are randomly oriented.

A magnified view of the secondary acicular phase is shown in Figure 4.62. The EDX analysis (Table 4.12) revealed that the needles (16 and 17) are high in W and Cr, with compositions similar to the dendritic carbide shown in Figure 4.60. The secondary acicular carbide contains a very high amount of W, in the ratio W_3Cr. The matrix is similar in composition as previously reported; Ni-based with

some Fe. The duller secondary carbide phase (16) is either a coring of the brighter secondary carbide phase (17), or is the brighter phase appearing from beneath the surface. It is likely revealing information from below the surface, due to the high amount of Ni found from the EDX results.

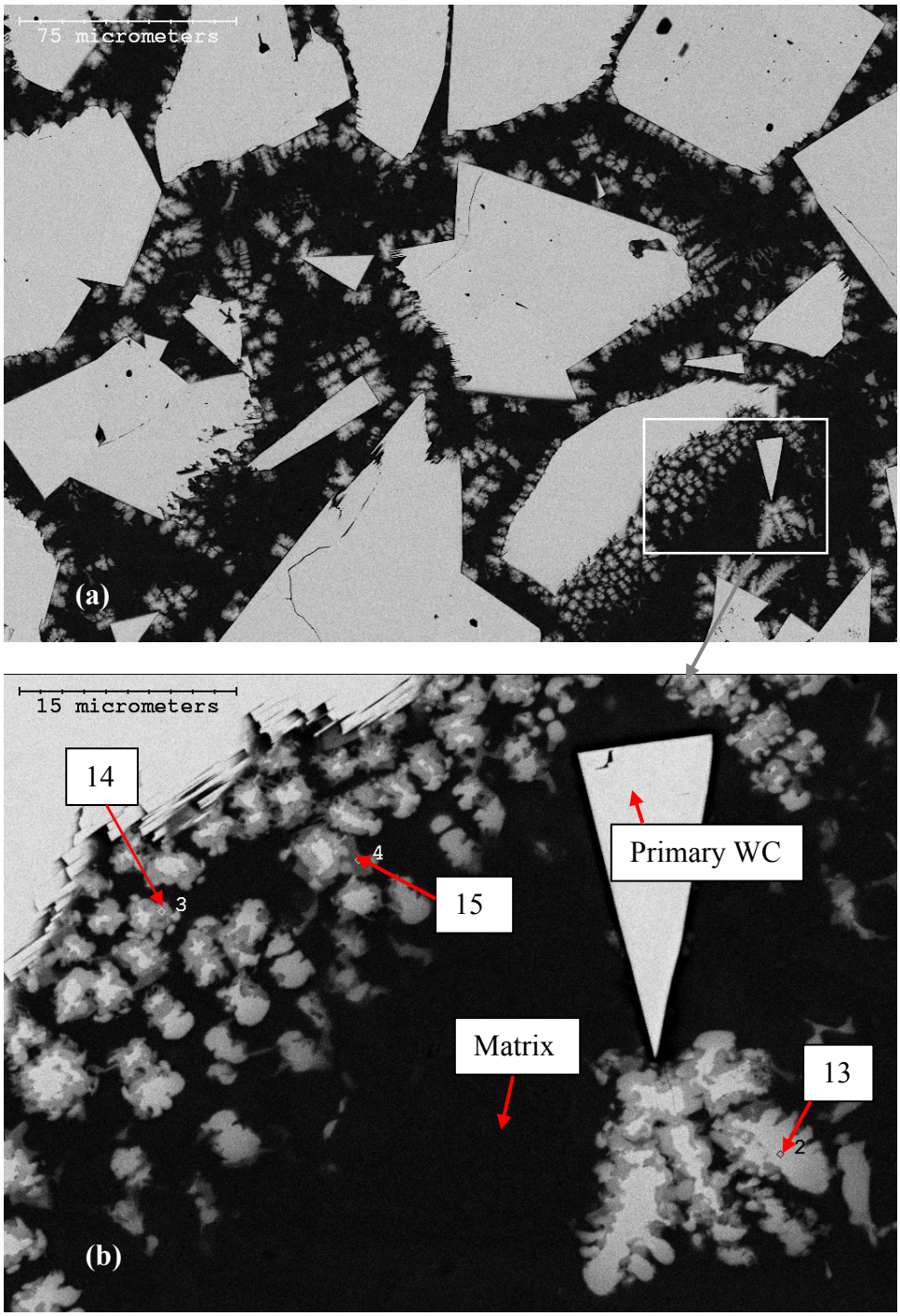

Figure 4.60: BSE image of secondary phase surrounding primary WC particles in single pass coating (a), magnified view (b)

Table 4.11: EDX results of secondary phase surrounding primary WC particles in single pass coating

Element	***Primary WC***	***13***	***14***	***15***	***Matrix***
Si	14.0	4.1	3.4	1.0	3.4
W	**76.4**	**36.3**	**31.6**	16.3	0.4
Cr	3.3	**48.3**	**52.1**	**48.6**	2.9
Fe	2.0	4.9	6.1	18.4	**22.5**
Ni	4.2	6.4	7.0	15.7	**70.8**

An interesting phenomenon is the evolution of the morphology of the secondary carbide; from acicular on the surface to dendritic further into the centre of the coating, shown in Figure 4.63. It appears that a higher cooling rate near the surface yields acicular secondary carbides.

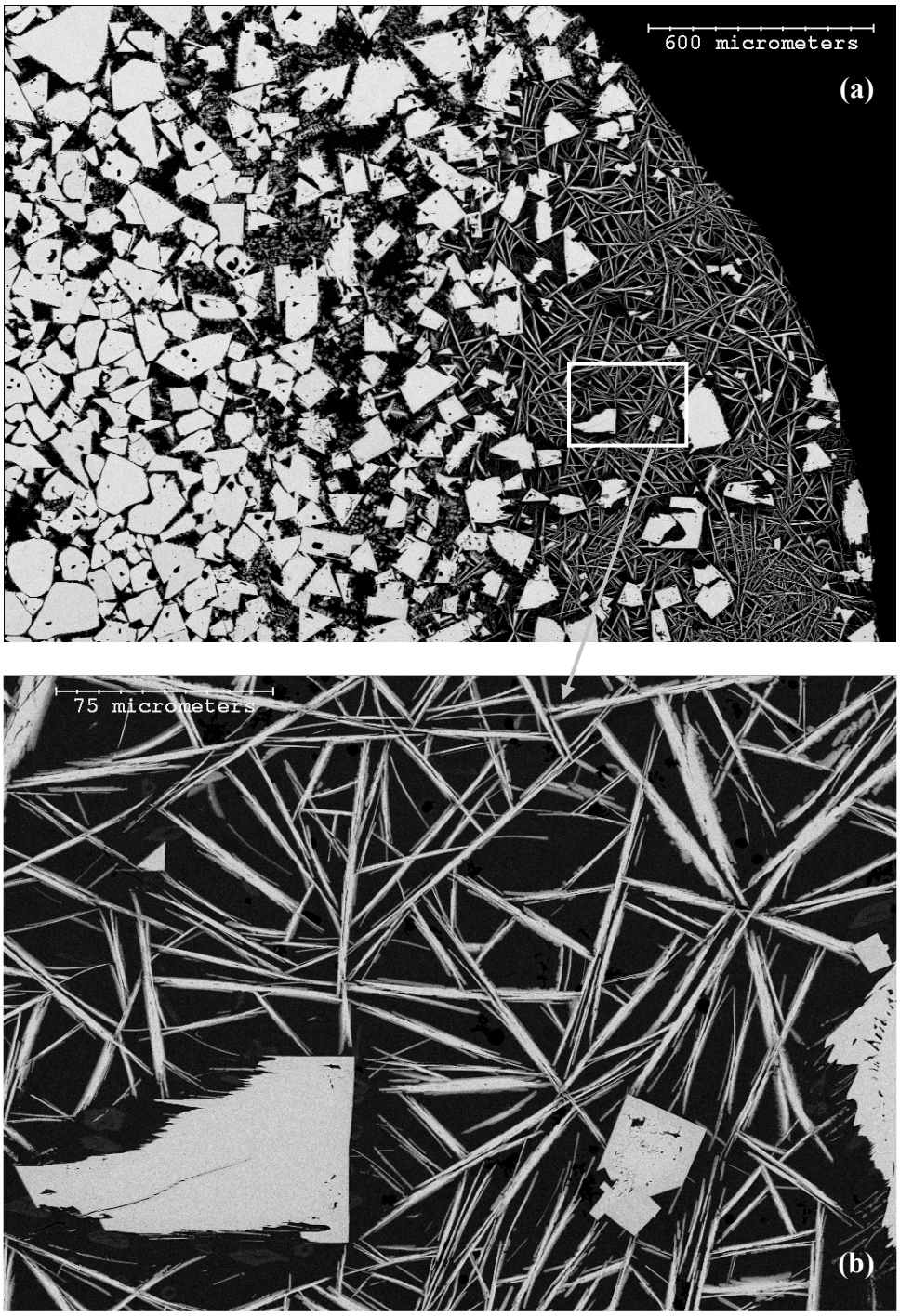

Figure 4.61: BSE image of surface of multiple pass coating, showing acicular secondary carbides at the surface (a) and dissolution of primary WC particles with acicular secondary phase (b)

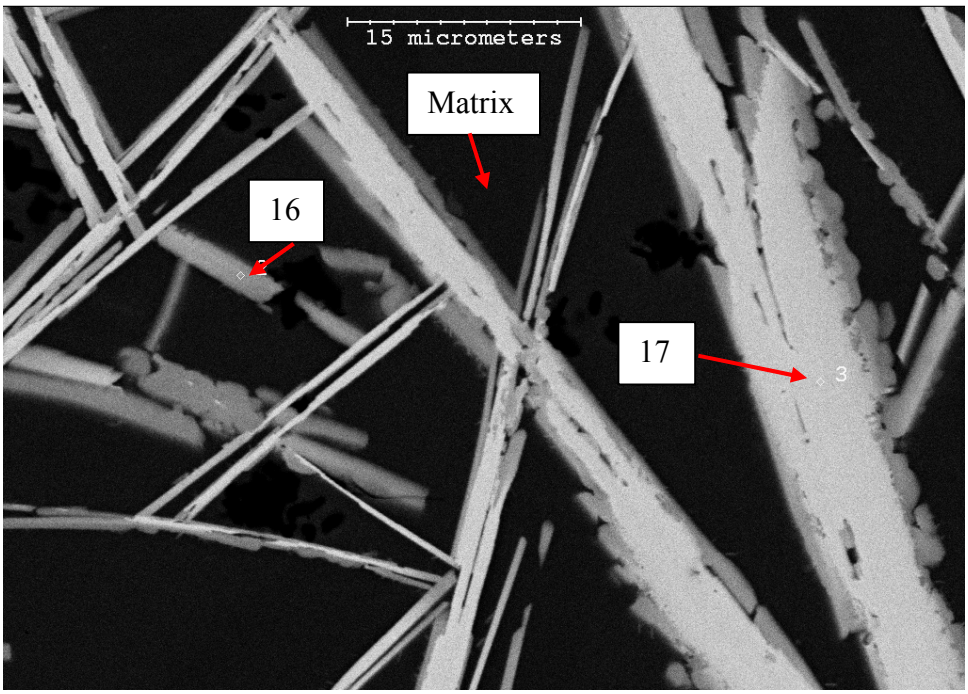

Figure 4.62: Magnified view of secondary acicular carbide phase found in multiple pass coating

Table 4.12: EDX results of needle-like phase found on periphery of dual pass coating

Element	***Matrix***	***16***	***17***
Si	5.0	6.4	9.9
W	1.0	**35.6**	**61.3**
Cr	3.0	**44.1**	**21.2**
Fe	10.3	2.9	2.3
Ni	**80.7**	10.9	5.3

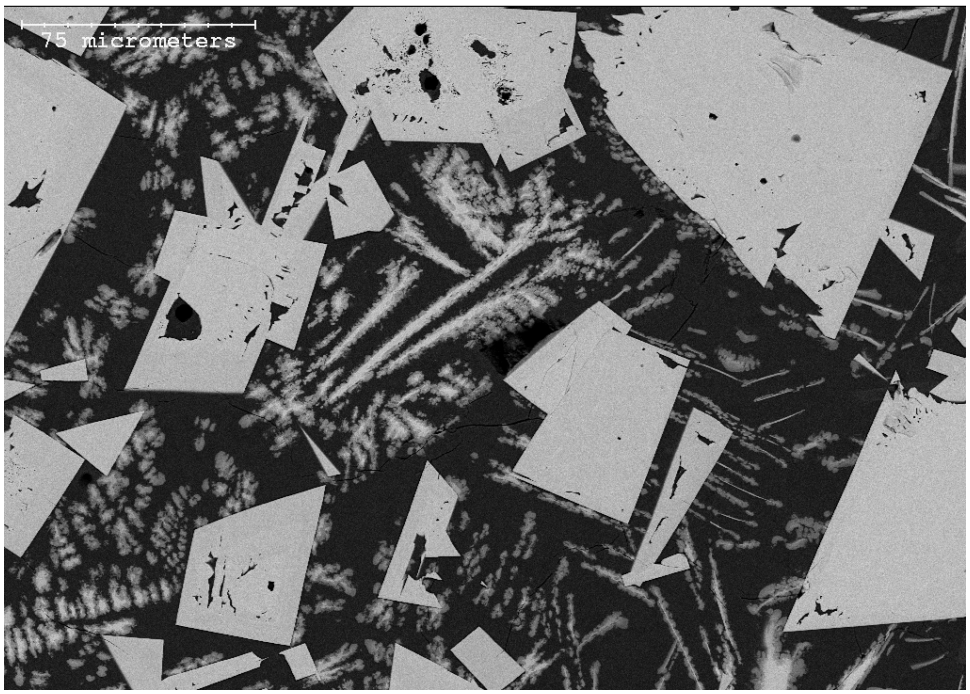

Figure 4.63: BSE image of change in morphology of secondary phase from acicular on surface to dendritic surrounding WC particles further into the matrix

4.5.3 Phase Evolution

The matrix only coatings consists of a primary Ni dendrite with an interdendritic microstructure composed of a near pure Ni phase, a Ni rich solution of Fe and Si, a eutectic of the two and chromium carbide, as described in section 4.5.1 - Matrix Microstructure. The relative amounts of each phase are dependent on the cooling rate: the slower the cooling rate, the more interdendritic phase and eutectic are present.

The addition of WC alters the microstructure dramatically, shown in section 4.5.2 - MMC Microstructure. The reinforcing particle experiences some dissolution and reacts with the matrix. The unique microstructure of the matrix only coatings is not identified with the addition of WC. The matrix remains dendritic, but each phase is a solid solution of Si, W, Cr, and Fe with the balance Ni. No eutectic microstructure is apparent and the delineation between phases is often difficult. This indicates that the cooling rate was higher than the matrix alone. The heat

sink in these composite coatings is a result of WC – it has a low latent heat, and a higher thermal conductivity. The low latent heat will result in dissolution of the particle and the presence of W in solution.

The formation of the tungsten-based carbides is a function of the heat input and the amount of W present. When there is less free tungsten, the carbides are thread-like with 20-30 at% W or block-like with up to 40 at% W. Characterization of the chromium-based precipitates indicated that the blocky types are chromium borides and the needle like types are chromium carbides [DAS2005]. The surface of the deposit was found to be primarily needle shaped chromium carbides, whereas further into the centre of the coating both bulky globular and needle shaped chromium carbides as well as irregular eutectic chromium borides were present [SUD2008]. Chromium is also present with W as a major component, usually in the same amount. With an increase in WC (from 50 wt% to 65 wt%), the morphology of the secondary complex carbide alters significantly. The carbide has an increase in W to 50 at%, with the balance mostly of Cr, and is present in the denuded zones and directly surrounding the original WC particle. The most significant difference is that the carbide becomes dendritic in shape and forms in layers. The layered effect of this type of secondary carbide may be a result of re-melting of the complex carbide during the zig-zag deposition pattern with re-solidification of the exterior of the carbide with a slightly different composition. With a second pass, the carbides must again experience at least partial solubility in the melted zone. The morphology of the high W carbide (up to 60 at%) is needle like, situated only on the periphery of the coating. This area experiences the highest rate of cooling. Further into the coating, the dendrite-like carbides are present around the original carbides. Thus, as time permits, the carbide will prefer a rounder dendritic shape.

The issue with this analysis is that exact phases were not determined due to the solubility of all the elements in each other. A pseudo-ternary diagram of the Fe-W-C system is shown in Figure 4.64. A carbide of composition Fe_3W_3C is formed in the range of tungsten possibly present in the liquid. Ni and Cr behave

similarly to Fe when in solution with W and C, as shown in previous literature [POS1986]. It is probable that a complex carbide in the M_6C notation is produced, but cannot be confirmed without further analysis. Shown in Figure 4.65 is the ternary diagram of Cr-W-C. At high W and Cr concentrations, a variety of complex carbides are formed.

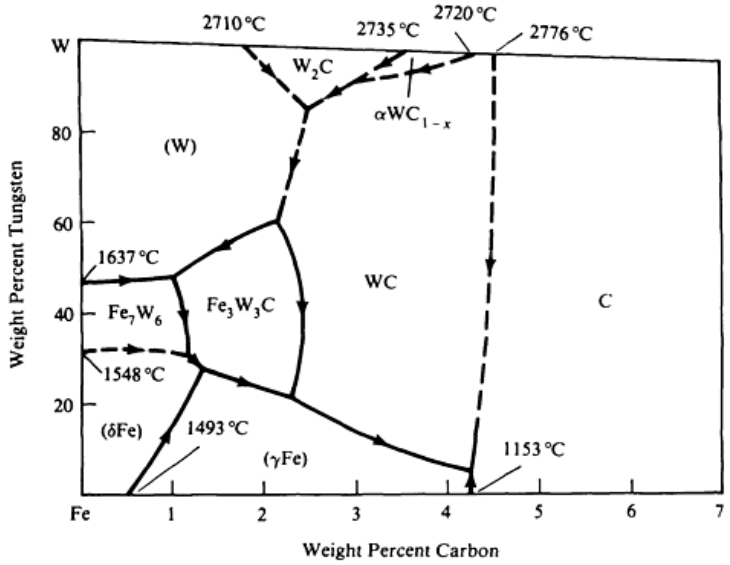

Figure 4.64: Pseudo-ternary diagram of Fe-W-C system [BAK1992]

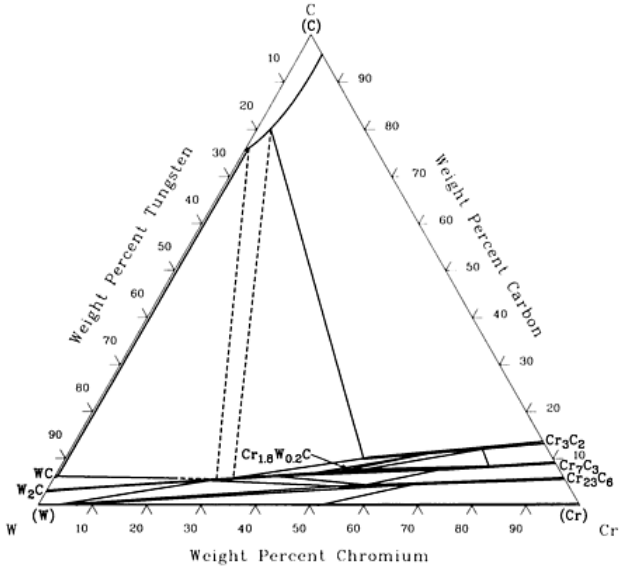

Figure 4.65: Ternary diagram of Cr-W-C system [BAK1992]

4.5.4 Effect of Operating Parameters on Carbide Morphology

It was seen that the morphology of the secondary carbide was acicular on the surface and dendritic further into the centre. The difference in cooling rate was thought to be the contributing factor to the shape of the secondary carbide. The morphology of the coatings deposited under lower and higher temperatures was examined. The lowest temperature coating was deposited under 110A and reached 1029°C and the highest temperature at 25V and 1200°C. The measured carbide fraction of the two samples are 45 vol% WC and 38 vol% WC, respectively. The temperatures were measured using infrared thermography and are corrected with the appropriate emissivity.

Shown in Figure 4.66, the surface of both overlays is heavily distributed with two types of a bright secondary carbide based phase. It was previously shown that any phase that appeared bright in the SEM was tungsten-based. The primary tungsten carbide is seen as the large angular phases. Since the higher temperature sample had a lower overall carbide volume fraction, the size of the denuded zone of primary carbide on the surface is larger. A magnified view (Figure 4.67) identifies the secondary phases more clearly. The smaller lath-like and starburst carbides (18) are tungsten and chromium based phases, shown from EDX results in Table 4.13. Deeper into the overlay, there is a bright feathery phase surrounding the primary carbide (19). The feathery phase is composed mainly of Fe and Ni, with a small amount of W. There are significantly more of the lath-like and feathery phases in the higher temperature overlay.

Further into the overlay, no difference in the metallography of coatings between the low and high temperature coatings. However, the morphology is very different than that found at the surface. Shown in Figure 4.68, there is a primary Ni phase, with a complex interdendritic phase with very different amounts of W present. However, the primary elements are Ni, Fe and W. The different cooling rates at the surface and substrate produce a distinctly different microstructure. A higher temperature results in more tungsten based phases being present in the

matrix region due to increased dissolution of the primary WC particles. There is no tungsten in the NiCrBSi powder before it is deposited, hence, the primary WC is degrading and reacting with the matrix to form a variety of secondary phases. This microstructure was called a herringbone structure [ZHA2006], produced by higher heat contents which allow more time for WC to react with the matrix. Elemental mapping showed the florets or herringbone phases to contain chromium and boron [GUR2007]. The effect of these phases on coating performance is unknown, but may contribute to the premature deterioration of the coatings [COC1997].

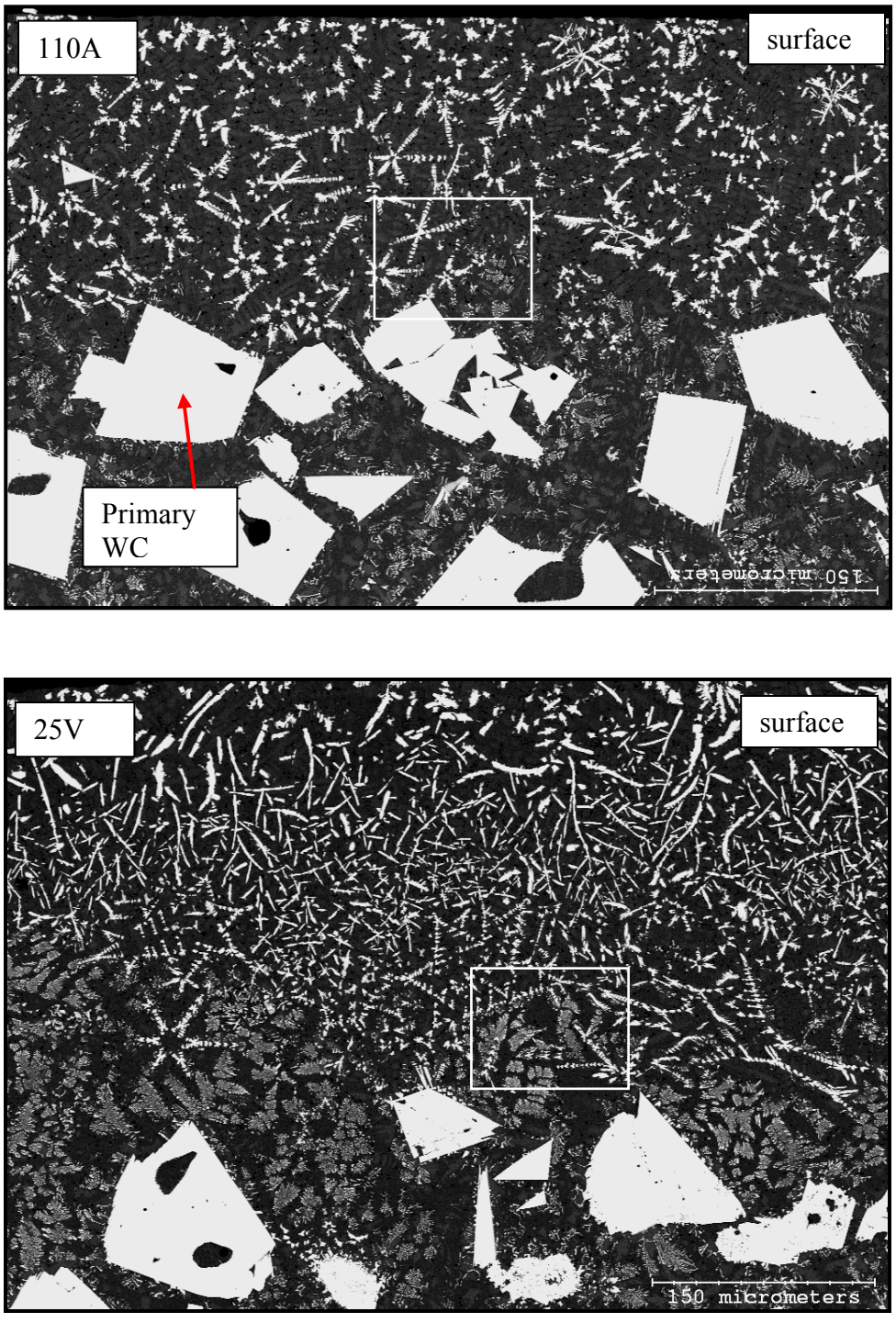

Figure 4.66: SEM image of cross section of coating near the surface deposited at low temperature (110A) and high temperature (25V), 200x. The white boxes are the areas magnified in Figure 4.67

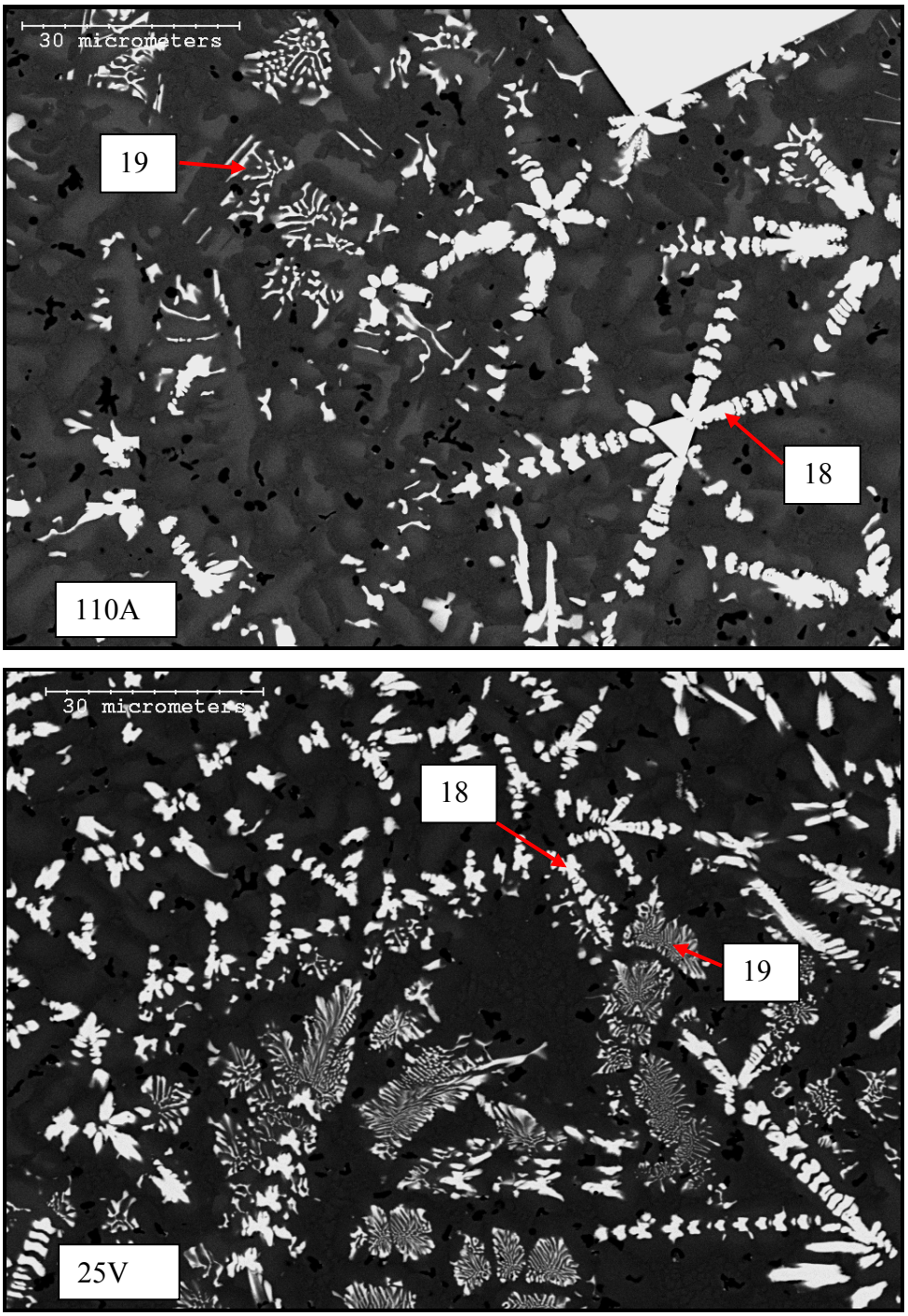

Figure 4.67: SEM image of cross section of coatings deposited at low temperature (110A) and high temperature (25V) near the surface, 1000x.

Table 4.13: EDX results of secondary phases found near surface of low and high temperature coatings (from Figure 4.67)

Element	***18***	***19***
Si	3.9	3.9
W	**59.8**	9.6
Cr	**18.0**	4.6
Fe	9.5	**25.9**
Ni	8.2	**55.6**

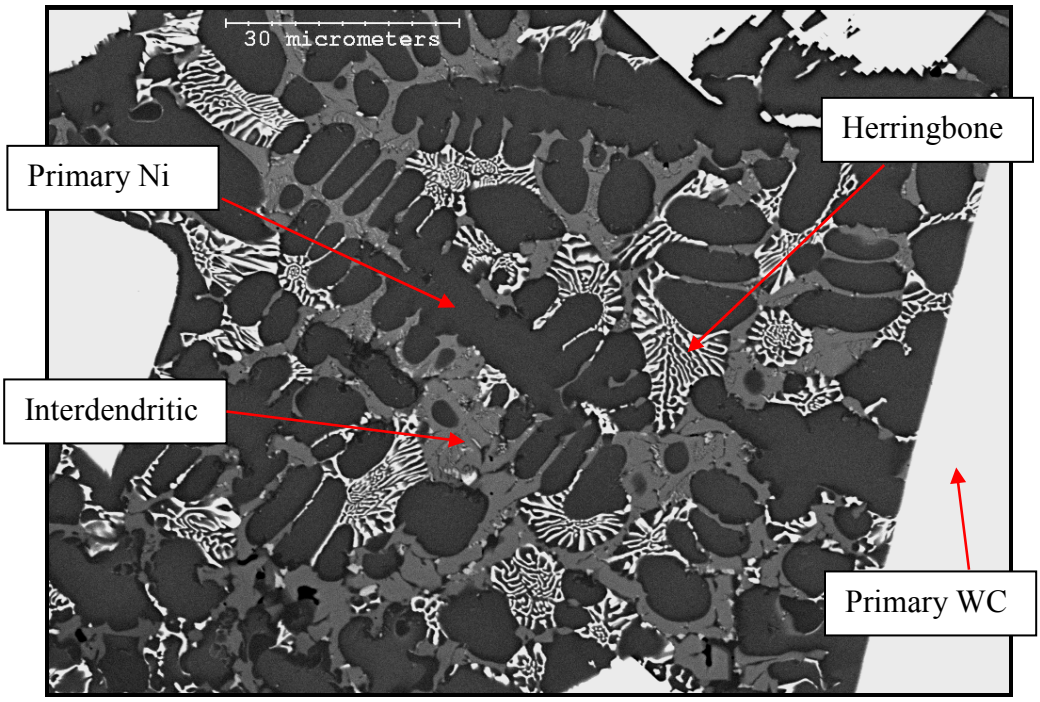

Figure 4.68: SEM backscattered electron image of coatings at low temperature (110A) near substrate interface, 1000x.

4.5.5 Effect of WC Amount on Morphology of Complex Carbide

It was shown in that the amount of carbide was the key factor in achieved a homogeneous coating (Figure 4.13). This section compares coatings deposited from the standard commercial powder. Although this powder had a nominal 50 vol% WC, image analysis results revealed that there was a significant reduction in actual carbide volume fraction. The images analyzed below which have a small variation in WC amount (34 vol% versus 41 vol%), but were deposited under

identical heat input conditions. The incidence of the lath like secondary carbides and the (Ni,Fe,W) herringbone regions was examined. At the surface of the coatings (Figure 4.69), a higher WC volume fraction results in a finer distribution of lath like secondary carbides in the settling region and more herringbone between the primary carbides. At the substrate/coating interface, there is considerably more of the herringbone phase with the higher WC volume fraction, and the image shows an increase in the brightness of the herringbone phase between the primary tungsten carbides (Figure 4.70). At a higher magnification, Figure 4.71 shows that the herringbone phase nearly comprises the entire matrix. Also shown in this image is the extent of degradation the primary tungsten carbide. As the volume fraction of WC increases, the higher the amount of W and C able to dissolve and reprecipitate in the matrix. Although both samples were deposited under the same conditions, a finer structure is related to a faster cooling rate. Since WC has a higher thermal conductivity than the matrix, increasing the volume fraction of carbide acts to increase the cooling rate.

The effect of the dissolved tungsten in the matrix on overlay performance has not been identified in the literature. The standard abrasion test (ASTM G-65) should not be the only qualifying test. It is recommended that studies be carried out on the impact strength, corrosion resistance and fracture toughness of the matrix as a function of dissolved tungsten. These initial studies may lead to further analysis of the WC-NiCrBSi system and reveal alternate material solutions for other applications.

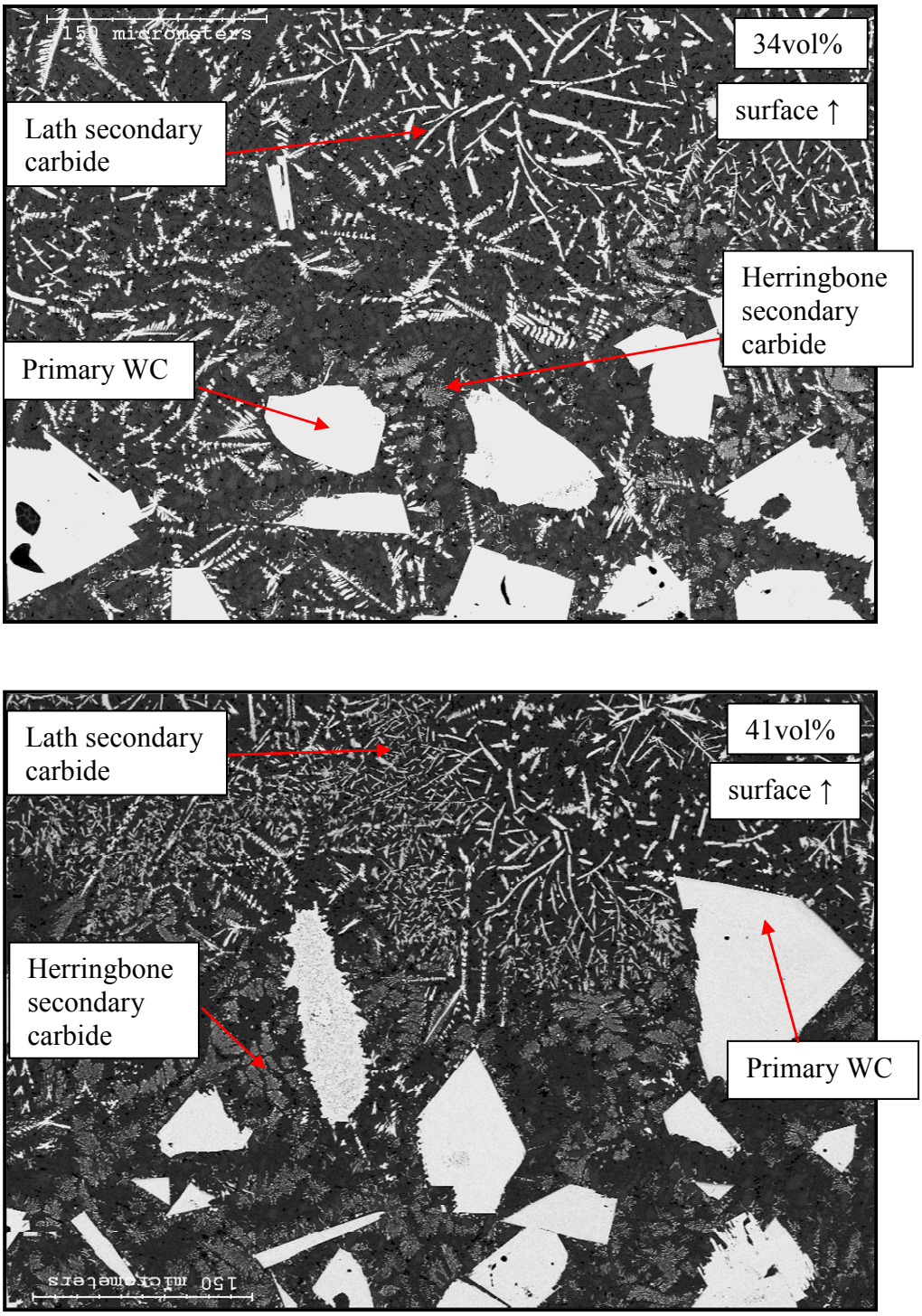

Figure 4.69: SEM backscattered electron image of cross section of coating near surface at low (34 vol%) and high (41 vol%) WC volume fractions, 200x.

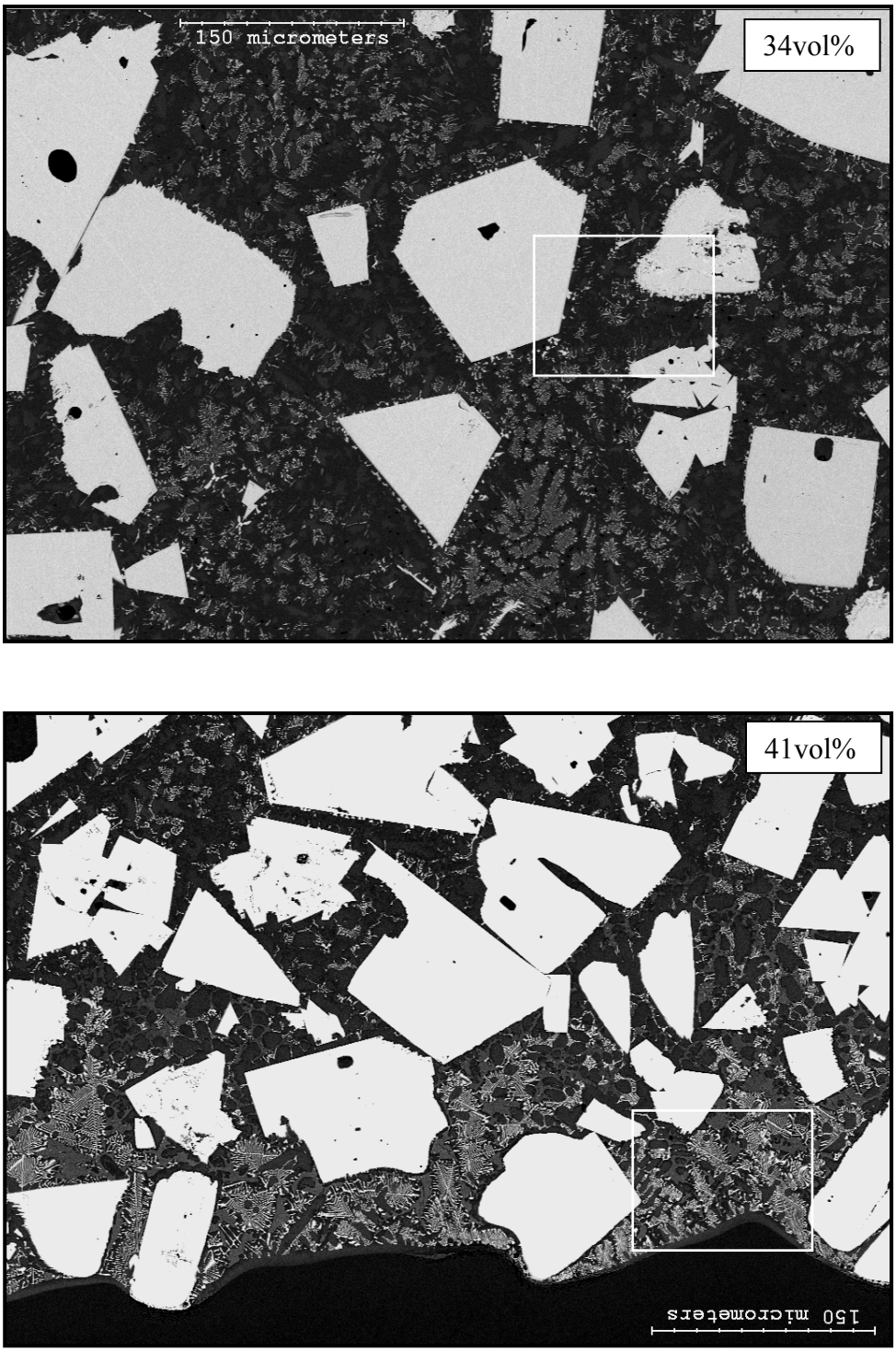

Figure 4.70: SEM backscattered electron image of cross section of coating taken near substrate/coating interface at low (34v%) and high (41v%) WC volume fractions, 200x. The white squares are magnified in the following figure.

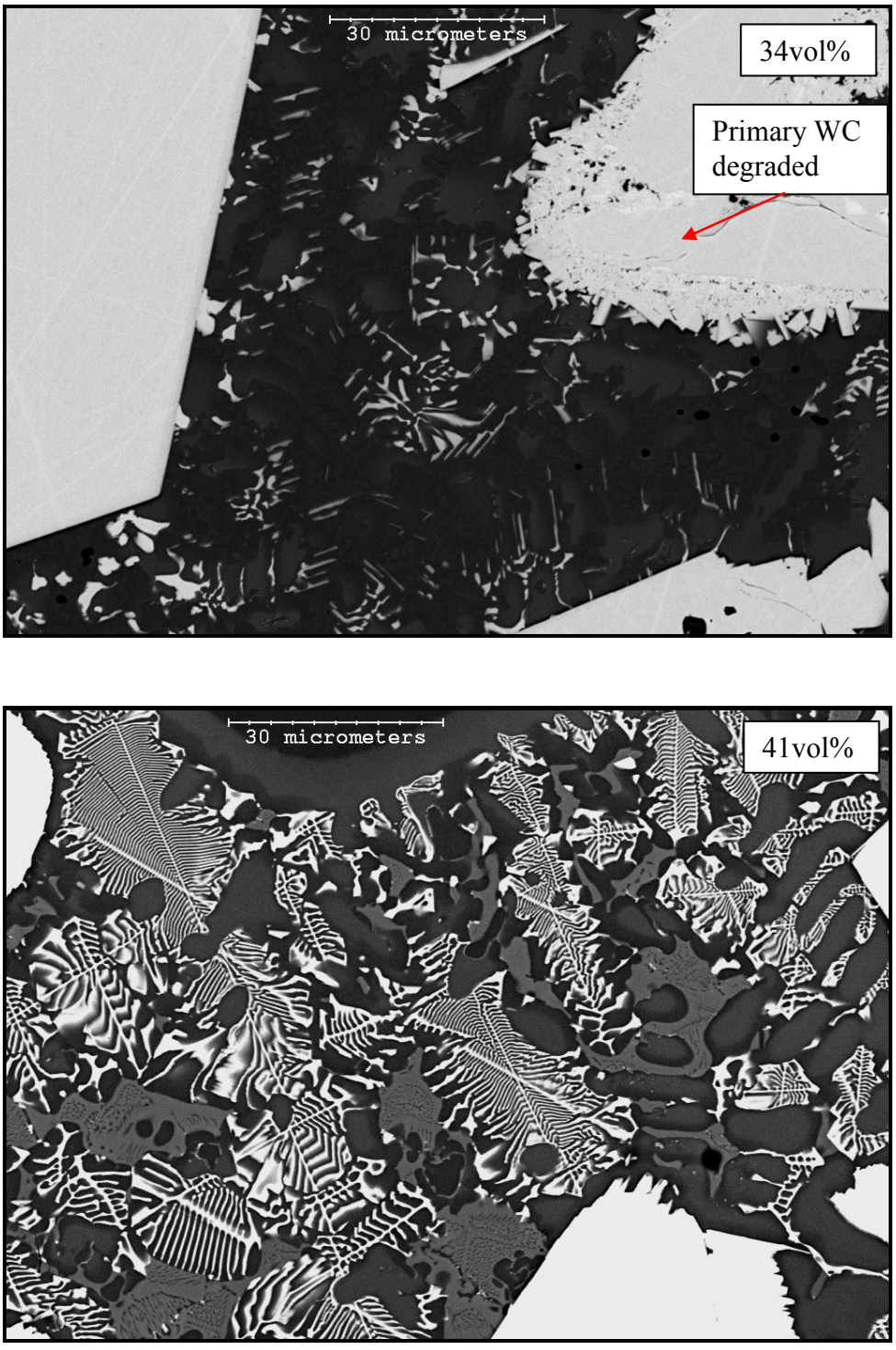

Figure 4.71: High magnification image of cross section of coating taken near the subtrate/coating interface by SEM backscattered electron mode, at low (34v%) and high (41v%) WC volume fractions, 1000x.

4.5.6 Metallographical Analysis of Spherical WC/W_2C Powders

The weldability and carbide morphology of eutectic spherical tungsten carbide powders was examined.

An EDX scan and x-ray diffraction analysis was performed on the spherical particles in order to determine the composition in wt% (Table 3.3) and the phase constituents. The EDX scan revealed that the only elements detected were tungsten and carbon. There was twice as much carbon in the RPS powder than the PS powder.

The x-ray diffraction analysis revealed that the powders were not purely eutectic in composition (Figure 3.2). Although they both contained WC and W_2C, the PS sample contained free carbon and tungsten and the RPS sample contained free carbon.

The spherical powders are significantly different than the monolithic angular powders in terms of phases and elemental analysis. Presented below is a metallographical analysis of the spherical eutectic tungsten carbide-containing overlays.

4.5.6.1 Optical microscopy of eutectic carbide MMC coatings

Optical images of the cross section of the coatings are presented in Figure 4.72. The random packing factor of the spherical carbide was determined to be 60 vol% (73wt%), and the cross section of the fully packed spherical PS powder is shown in Figure 4.72a. Although the weight percent of carbide in the coating is higher than with angular particles, and the particles appear to be homogeneously distributed through the coating thickness, there are a significant number of voids in the regions and a high degree of carbide dissolution. It is difficult to distinguish individual carbides. There are only a few carbides that maintain their original morphology. Reducing the amount of carbide from 73wt% to 40wt% (Figure 4.72b) resulted in less degradation of the carbide; however, the coating is

not homogeneous. There are also some regions were porosity is evolving. Porosity tends to occur with the presence of free carbon in the carbides. When the carbides are heated, the carbon reacts with the small amount of dissolved oxygen in the nickel matrix to form CO gas [KRI1968] [BRO1981], which is not able to make it to the surface before solidification occurs.

The spherical RPS powder experienced the least amount of degradation and porosity (Figure 4.72c) but the distribution of particles in the coating is inhomogeneous. It appears that the PS powder is not suitable for deposition by PTAW due to the free carbon and tungsten.

A closer examination of the degradation of the fully packed spherical PS sample is shown in Figure 4.73. There are 4 types of carbides present:

- fully degraded – only 'feathers' present (A),
- degraded but shape intact (B),
- partially degraded (C),
- unreacted (D).

The fully degraded and partially degraded carbides are shown in greater detail in Figure 4.74. The boundary between the reacted and unreacted carbide is evident. It was not expected that such a severe level of primary carbide degradation would occur with PTA processing of the spherical PS carbide product. The presence of free tungsten appears to render the carbide highly unstable when exposed to the high temperatures of PTAW.

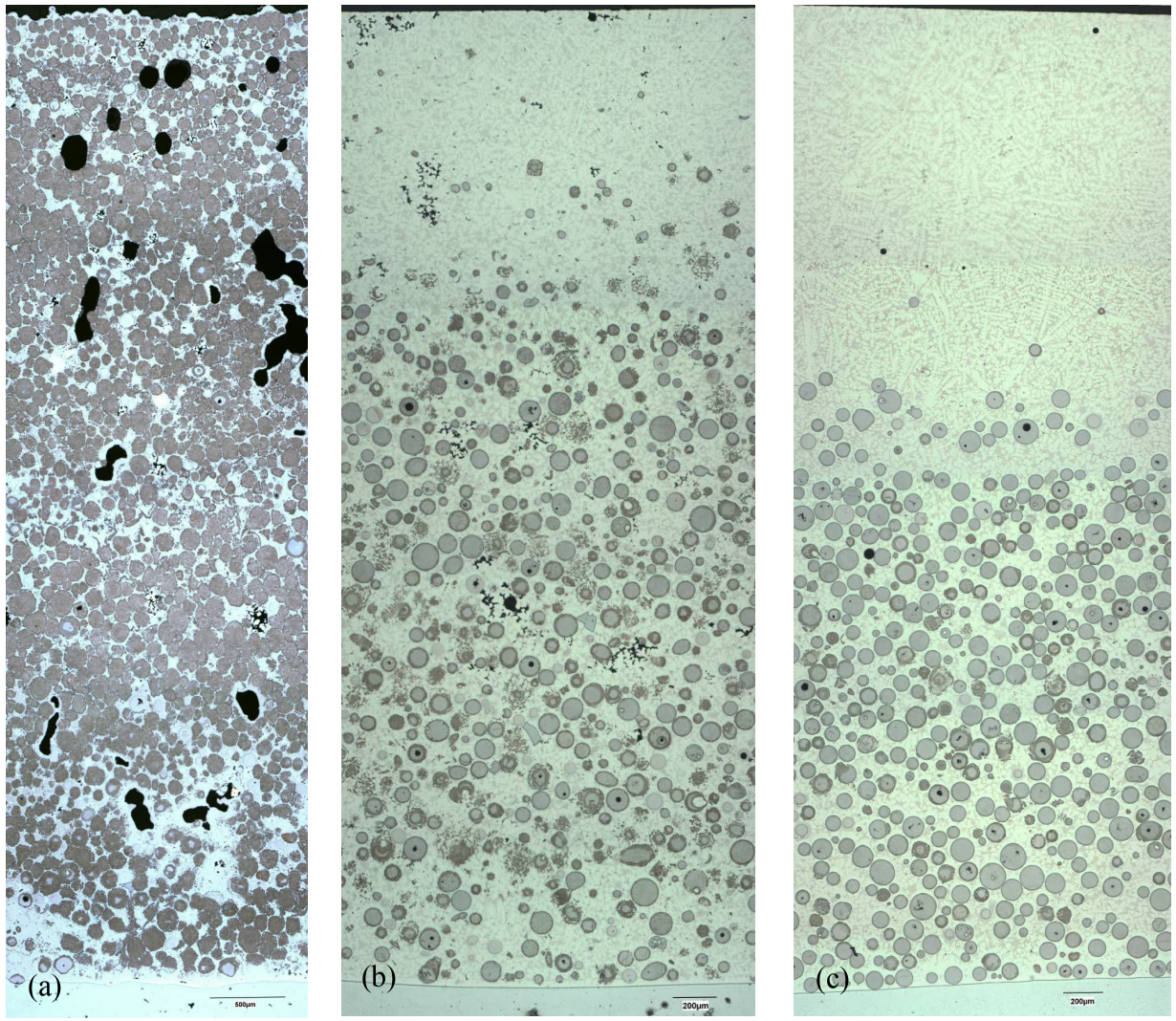

Figure 4.72: Spherical WC/W_2C mixtures (a) 73wt% spherical PS, (b) 40wt% spherical PS and (c) 40wt% spherical RPS.

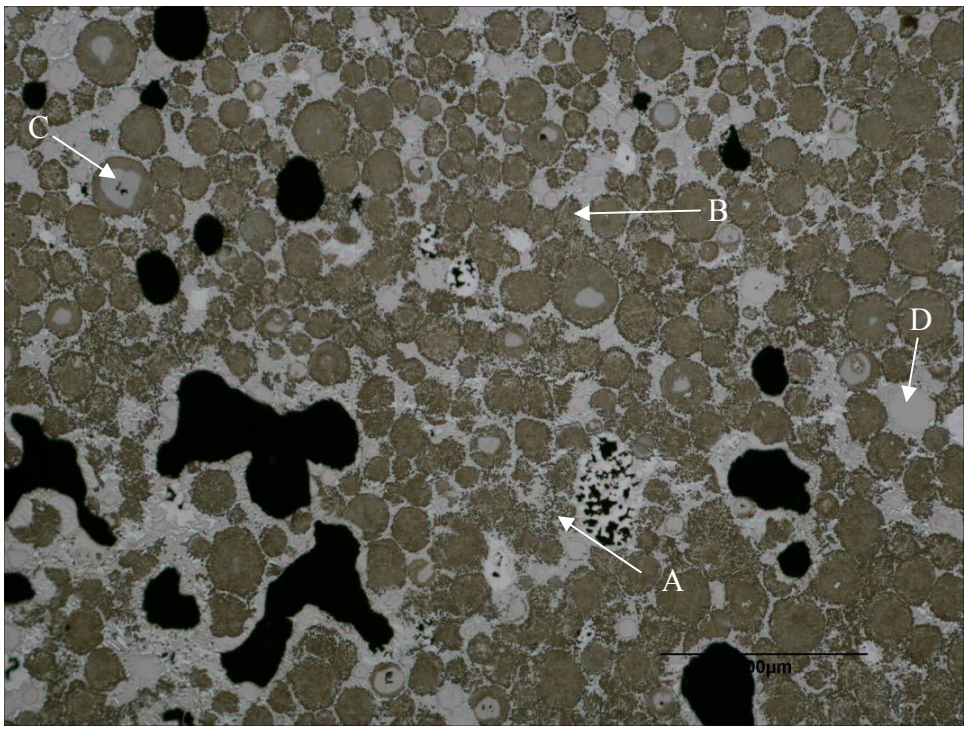

Figure 4.73: Optical metallograph of fully packed spherical PS tungsten carbide, x50.

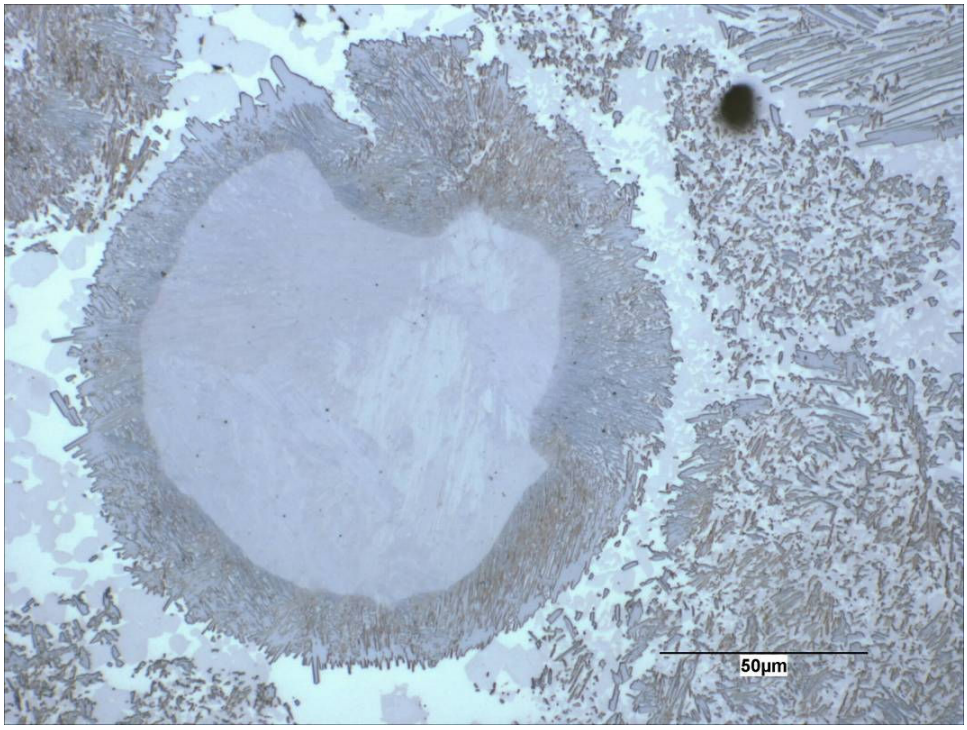

Figure 4.74: Degradation of fully packed spherical PS tungsten carbide, 500x.

4.5.6.2 Scanning Electron Microscopy of Eutectic Carbide MMC Coatings

Scanning electron microscopy and EDX was performed to identify the constituents of the degraded carbide. The image evaluated is shown in Figure 4.75. The primary carbide itself has three distinct regions which appear eutectic, identified as Spectrum 1, 2 and 3. Surrounding the carbide is a angular phase which appears to be a product of primary carbide degradation. The amount of tungsten and carbon in each of the three areas of the primary carbide are summarized in Table 4.14. All three areas are very similar in terms of elemental analysis. The amount of tungsten and carbon in the three regions are very similar, thus indicating that carbon has not diffused towards the outside of the particle. However, the actual phase present is unknown and may be different from region to region. Stoichiometrically, the phase present could be W_2C, as there are twice as many tungsten atoms as carbon atoms. However, when comparing the results of this EDX scan to that of the carbide before deposition, the amount of carbon has decreased from 4.5 wt% to approximately 3.2 wt%. This decrease in carbon can be a result of the excess free carbon in the powder which is sublimated upon heating. The porosity is likely a result of the free carbon sublimation.

A line scan of the region shown in Figure 4.75 reveals the relative amounts of carbon, tungsten, nickel and iron through the primary carbide (Figure 4.76). The region which was scanned is shown with the yellow line. The elements identified are colour coded: the carbon is red, tungsten is green, nickel is blue and iron is purple. The amount of carbon does not fluctuate over the entire scan. The amount of tungsten is relatively constant, except decreases at the surface of the carbide and is almost not present in the black nickel rich matrix. The other component found at the surface of the carbide is nickel and iron. It appears that there is a reaction between the carbide surface and the metal matrix. The amount of iron is high in the matrix.

An area elemental map was conducted of a fully and partially degraded carbide, shown in Figure 4.77. The region scanned, highlighted by the pink rectangle,

includes secondary carbides identified by the long rectangular phase, in the matrix and surrounding the primary carbide. The elements mapped were nickel, chromium, iron and tungsten and their respective maps are shown in Figure 4.78. The nickel is not present in any considerable amount in the primary partially degraded carbide. It is primarily found in the matrix phase (black). Chromium is not preferentially found in any particular region. The iron is found only in the matrix and not in the carbides. The primary carbide (large sphere) is exclusively tungsten. Tungsten is also found in the secondary carbides, wherever the matrix is not located.

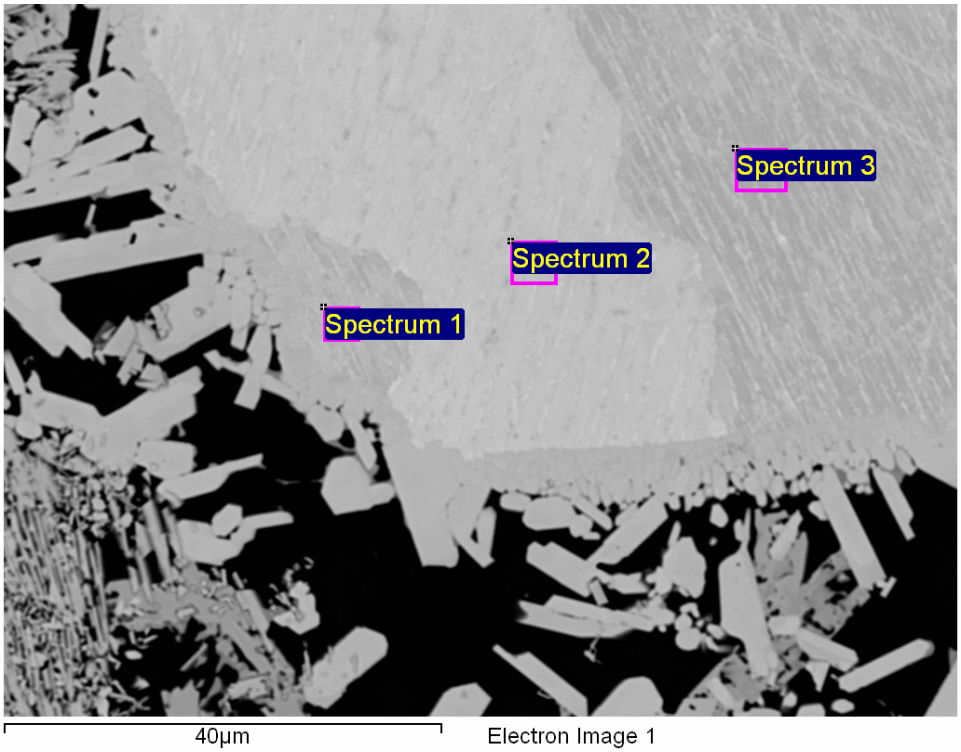

Figure 4.75: SEM image of partially degraded spherical PS carbide, 1500x.

Table 4.14: EDX semi-quantitative analysis of elements scanned in spectra from Figure 4.75.

Element	***1***	***2***	***3***
C (at%/*wt%*)	31/*2.9*	36/*3.5*	34/*3.2*
W (at%/*wt%*)	69/*97.1*	64/*96.5*	66/*96.8*

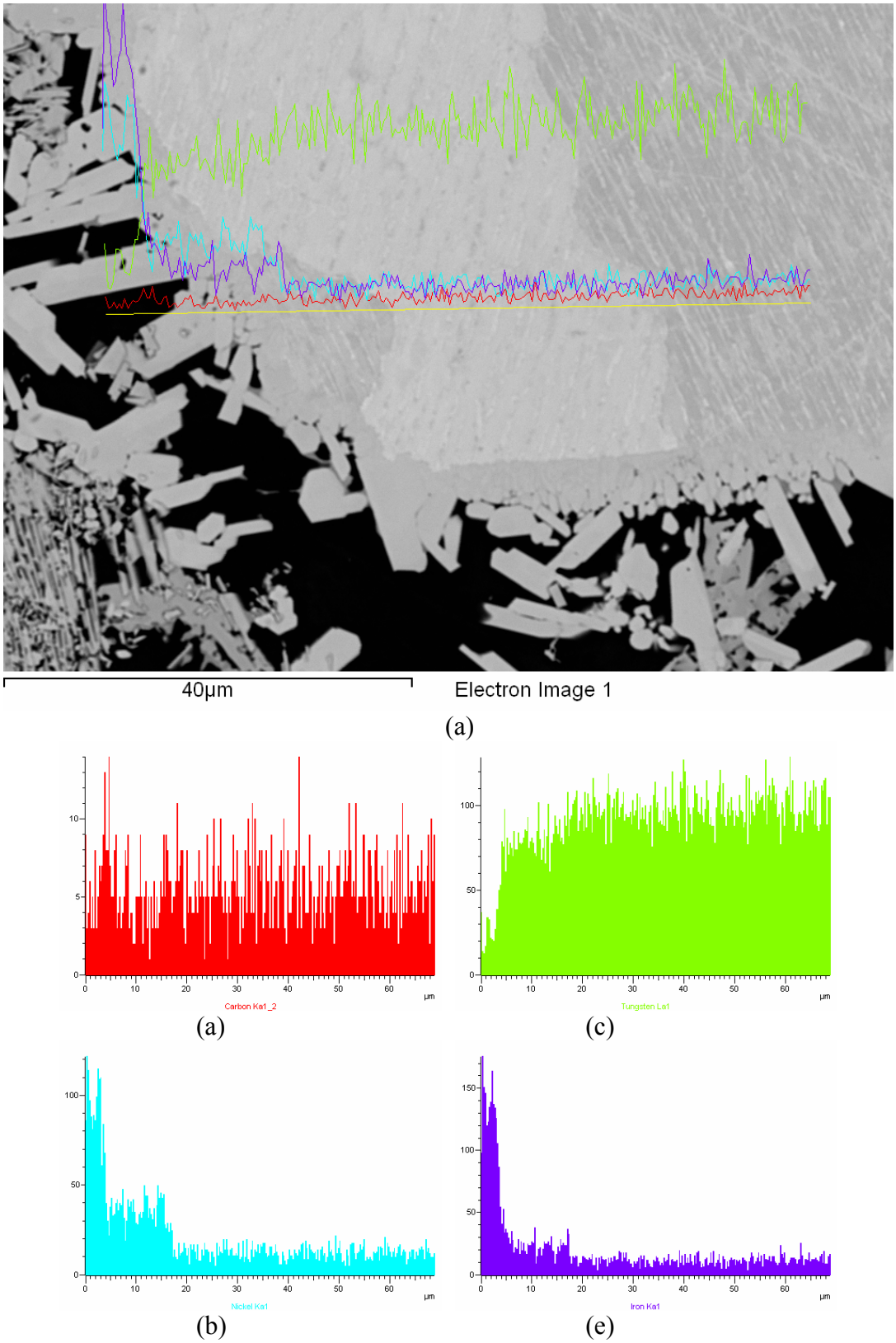

Figure 4.76: (a) Line scan of degraded tungsten carbide, revealing relative amounts of (b) carbon, (c) tungsten, (d) nickel and (e) iron.

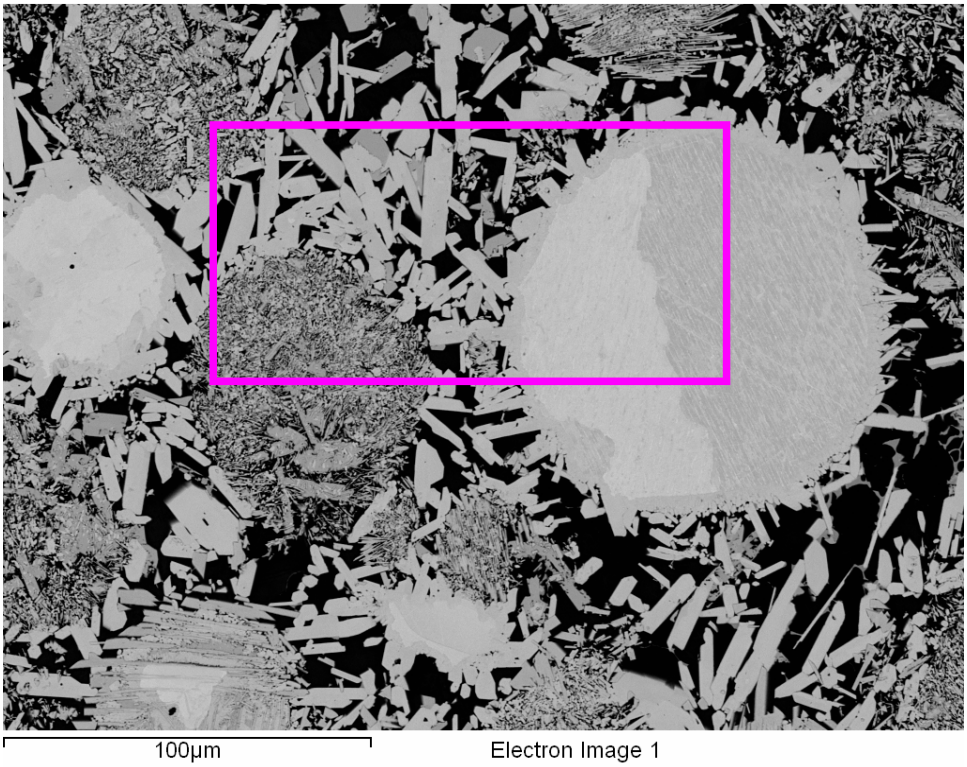

Figure 4.77: SEM micrograph of partially and fully degraded primary tungsten carbides, 500x. An elemental area scan was conducted in the highlighted region.

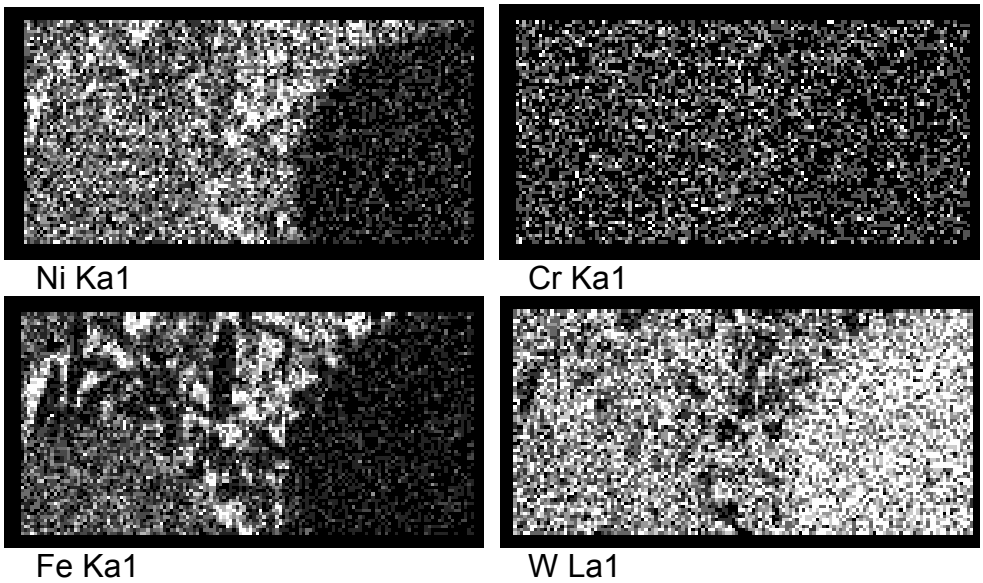

Figure 4.78: Area scan of degraded tungsten carbide and surrounding matrix to reveal relative amounts of nickel, chromium, iron and tungsten – from Figure 4.77.

The scanning electron microscopy did not reveal a reason for the mechanism of primary carbide degradation. Tungsten is not diffusing towards the surface the primary carbide but these spherical carbide particles are not stable when processed by PTAW. It was stated in Section 2.4.2.1.1 that the eutectic decomposes to W and WC at 1250°C. This was seen with this work. Eutectic carbides are not stable when deposited by PTAW. The secondary carbides formed are tungsten based and originate from the surface of the primary carbide.

4.6 Abrasion Wear Results

Abrasion wear tests were performed on coatings deposited under several operating conditions, as well as coatings with different carbide types. The G65 test simulates the abrasive wear the coatings experience in service. Typical mass losses for commercial tungsten carbide coatings are 0.1 g for the first 6000 revolutions and less than 0.05 g for subsequent revolutions [AND1998].

It was shown that improvements in homogeneity were achieved with increases in current. Four deposits were laid with an initial volume fraction of carbide of 30 vol%. A standard coating was deposited, followed by a decrease in current to 110A, a decrease in voltage to 20V and a decrease in plasma gas flow rate to 2 lpm. Each change in parameter was independent of the other – that is, only one change occurred and all other remained at standard deposition conditions. The homogeneity profiles are shown in Figure 4.79. For a coating with 30 vol% WC, the amount of carbide in the settling region increased from 22 vol% to 32 vol% when the current was decreased from 130A to 110A. Both decreasing voltage and plasma gas flow rate yielded no improvement in homogeneity.

The small increase in homogeneity in the settling region due to a decrease in current resulted in a small decrease in mass loss in the first 6000 revolutions, but no difference in the second 6000 revolutions (Figure 4.80). This would be expected, since the first test removes most of the settling region. If more carbide is present in the settling region, there will be less mass lost as the carbide is resistant to this type of

abrasion. After the settling region is removed, the volume fraction of carbide is equal in all the samples at 40 vol% WC. The mass loss is thus equal for all the samples. When the plasma gas flow was decreased, the amount of carbide in the settling region decreased to 12 vol%. This resulted in an increase in mass loss on the first abrasion scar.

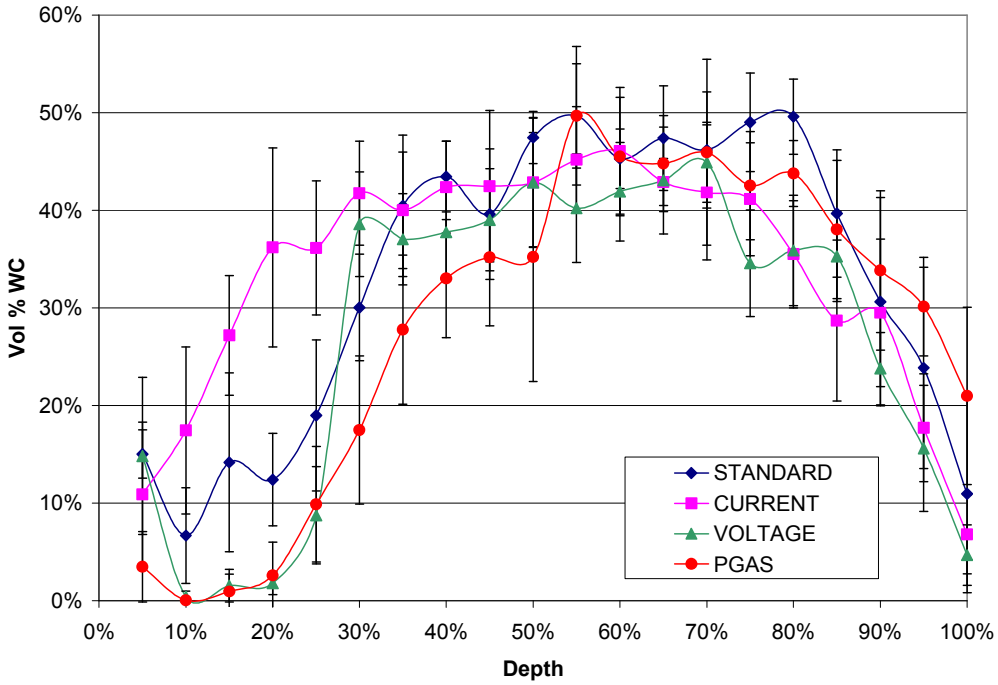

Figure 4.79: Homogeneity profile of coatings deposited under various conditions with constant volume fraction of WC powder (30 vol%).

The G65 abrasion wear results for the differences in carbide type/shape, shown in Figure 4.81, indicate that the spherical carbides are not comparable to the monolithic angular WC samples. The wear abrasion of the spherical carbide coatings is up to 5 times as high as the standard industrial coating. Both the standard mixture and fully packed coatings meet the typical results. The coating was deposited at the fully packed ratio of carbide at 50 vol%. The amount of carbide in the standard coating was reported to be 50 vol% based on the supplier information.

The fully packed coating performed more consistently between tests and had a lower initial mass loss for the first pass. Since there was less WC in the standard coating,

there is a larger settling region at the surface void of WC particles. The wear of first test of the standard coupon is measuring mostly the resistance of the matrix itself. After the initial settled region is removed, the wear of the standard and fully packed coatings are similar. Since there is slightly more WC in the fully packed sample, the mass loss is slightly less.

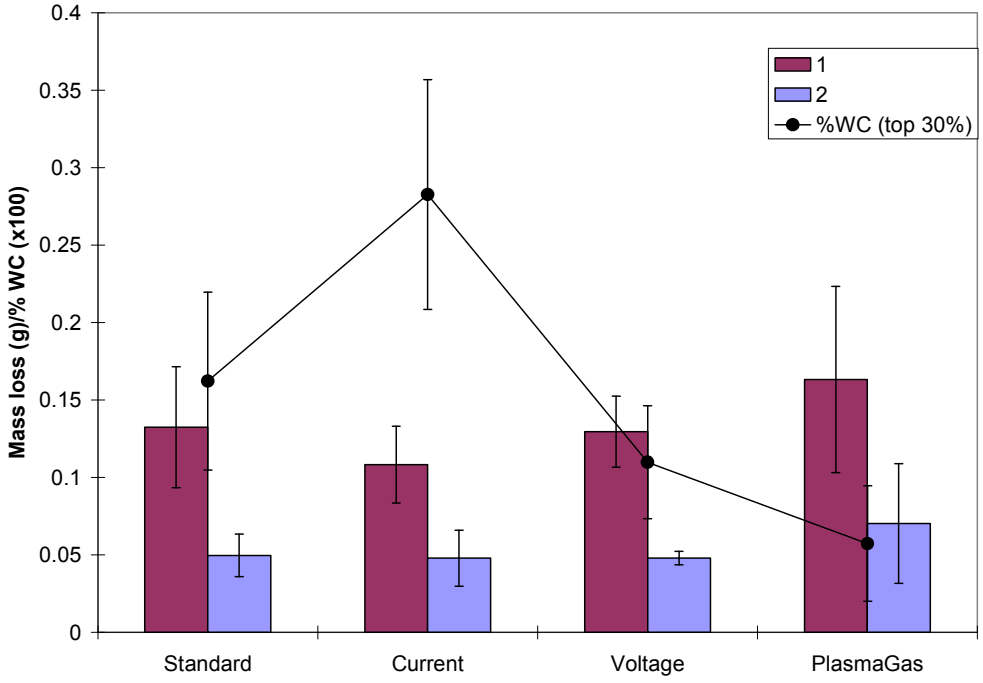

Figure 4.80: ASTM G65 abrasion wear results for a NiCrBSi-WC MMC, containing 30 vol%WC, deposited under various operating conditions. Each condition was increased according to the test matrix.

The spherical tungsten carbide coatings did not perform well. The fully packed PS coating (73 wt%) resulted in a mass loss twice as great as the monolithic coatings. The reason for the poor performance was shown in the optical micrograph of the sample, which large voids between particles and a significant amount of degradation of the particles, which is prevalent in eutectic types of carbide. These two factors contribute to the reduced wear performance. When the amount of carbide was decreased, there was less carbide at the surface, resulting in higher mass losses for the first test. Although more of the matrix was removed for the 40 w% coatings for the

first test due to the higher degree of carbide settling, the PS and RPS carbide coatings were still susceptible to a significant amount of mass loss. The wear abrasion results indicate that fully homogeneous coatings, with no voids, perform optimally. The size of the spherical and monolithic carbides were similar.

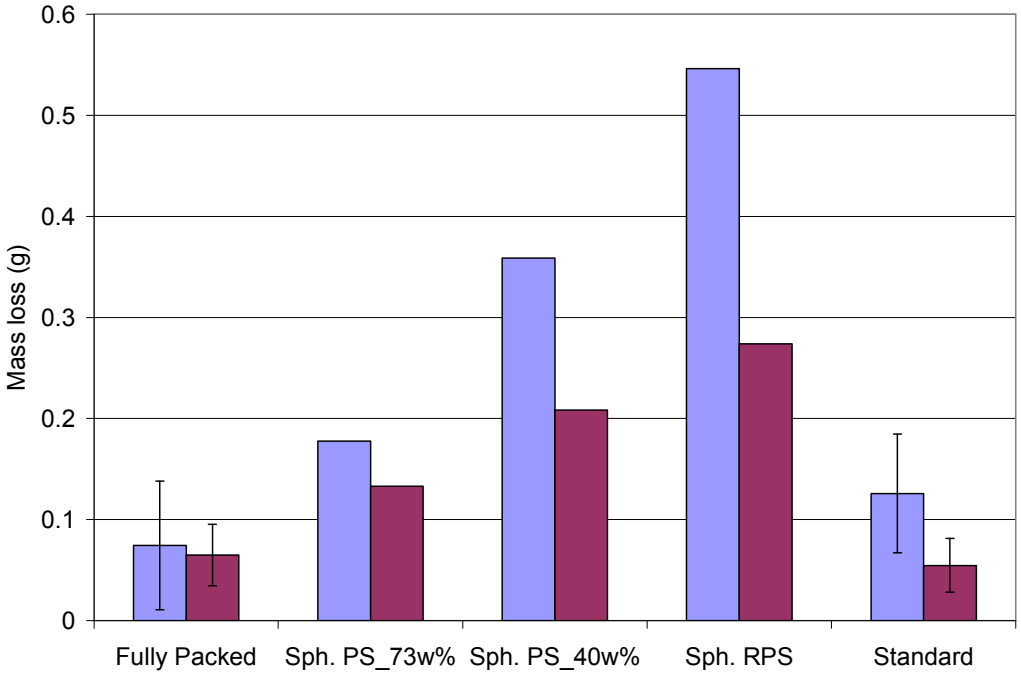

Figure 4.81: ASTM G65 abrasion wear test results. The first bar (blue) is the first set of 6000 revolutions and the second bar (fuchsia) is the second set of 6000 revolutions applied to the same wear scar.

4.7 Summary

The degree of inhomogeneity in the wear resistant coatings was quantified using image analysis. Very little difference in the homogeneity profile existed when changing the operational parameters. The volume fraction of carbide was the most significant factor in obtaining a homogeneous coating. Lowering the current made a modest improvement in homogeneity.

Images of the plasma arc were captured during the welding process to quantify the change in shape of the arc with the addition of the powder. The particle velocity was estimated through particle tracking to be between 1.5 and 2.0 m/s. This work yielded a greater understanding of the heat input of the welding arc in PTAW compared to GTAW, as it was shown that the arc is no longer axisymmetric with the addition of powder. The arc brightness is reduced with the addition of powder. The brightness of the arc intensified with increasing current and plasma gas flow. It was concluded that the arc brightness is a measure of arc heat input and arc temperature.

Infrared thermography was used to measure the temperature of the surface of the deposit during the welding process. To acquire a true temperature, the emissivity of the materials must be known. The emissivity of the deposit was measured using laser reflectometry and was found to decrease from 0.8 to 0.2 as the temperature increased from 900°C to 1200°C. A correction algorithm was applied to calculate the actual temperature of the surface of the deposit. The corrected temperature did increase as the heat input of the weld increased.

The effect of heat input on the metallurgy of the coating was investigated by scanning electron microscopy. The degree of tungsten carbide dissolution was explored and it was found that the primary tungsten carbide experienced some dissolution and reaction with the matrix to produce a secondary tungsten based carbide. The type of secondary carbide produced was a function of heat input and amount of primary carbide present.

The wear resistance of the coatings was measured using ASTM G65 abrasion tests. It was found that the wear resistance of the coating is directly proportional to the amount of carbide present. The spherical coatings performed poorly – a direct result of the severe degradation experienced by the carbides.

In the next chapter, a model will be developed which will predict the temperature of the coating as it solidifies and the resulting homogeneity of the carbide within the coating. The temperatures measured using infrared thermography and the settling profiles of the carbide quantified using image analysis are the validation tools for the model.

5 Solidification and Particle Settling Model

This section describes the modeling effort for the solidification and particle settling of MMC powder as it is deposited onto a substrate by PTAW. Although it was shown that significant variability was found within the tested operation windows in terms of coating homogeneity and surface temperature, the fundamental model presented agrees well with the experimental results. This is an achievement considering the fundamental approach taken to construct a model of a complex process.

A schematic of the process is shown in Figure 5.1. There are four regions which are included in the model:

1. The plasma arc;
2. The shielding gas;
3. The coating and substrate, and
4. The surrounding environment.

The modeling efforts made in each of the regions are described in the following sections.

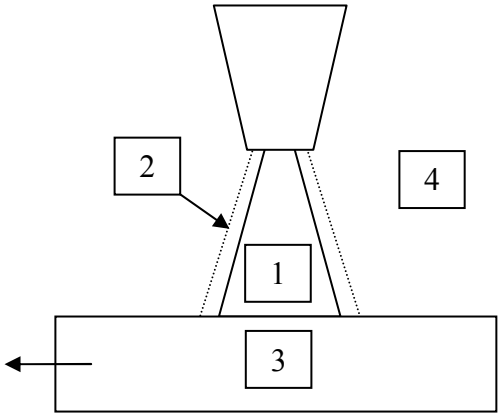

Figure 5.1: Schematic of regions modeled in PTA process.

5.1 Thermal Solidification Component of the Model

The deposition of the coating was modeled as a 1-dimensional heat transfer problem. The general heat conduction equation for a 1D problem is defined in equation 5.1. Symbol definitions are listed in the legend. There were two stages to the model, represented at region 3 from Figure 5.1: depositing the droplets of Ni and WC onto the surface followed by cooling of both the deposit and substrate. The steel substrate is 1 cm in thickness and is present before mass is added. During the first stage, the powder is added at a constant temperature and rate. The powder is added until the thickness of the deposit is obtained, after which the heat input of the arc is terminated and both the substrate and deposit cool. A schematic of the problem in the three stages is shown in Figure 5.2.

$$\frac{\partial T}{\partial t} = \alpha \frac{\partial^2 T}{\partial x^2}$$
$$\alpha = \frac{k}{\rho c_p} \tag{5.1}$$

The boundary condition on the $n=1$ node is a constant temperature of T_{sub}. The initial condition is T_{sub} at all substrate nodes. The substrate is divided into nodes of equal size to the weld nodes. The powder is added at a constant temperature, such that the initial condition of each new node added is T_i. No distinction is made between the temperatures of the Ni and WC particles, which will be discussed in section 5.1.2.2. The boundary conditions along the travel direction of the weld will be discussed in the section dealing with assumptions (section 5.3).

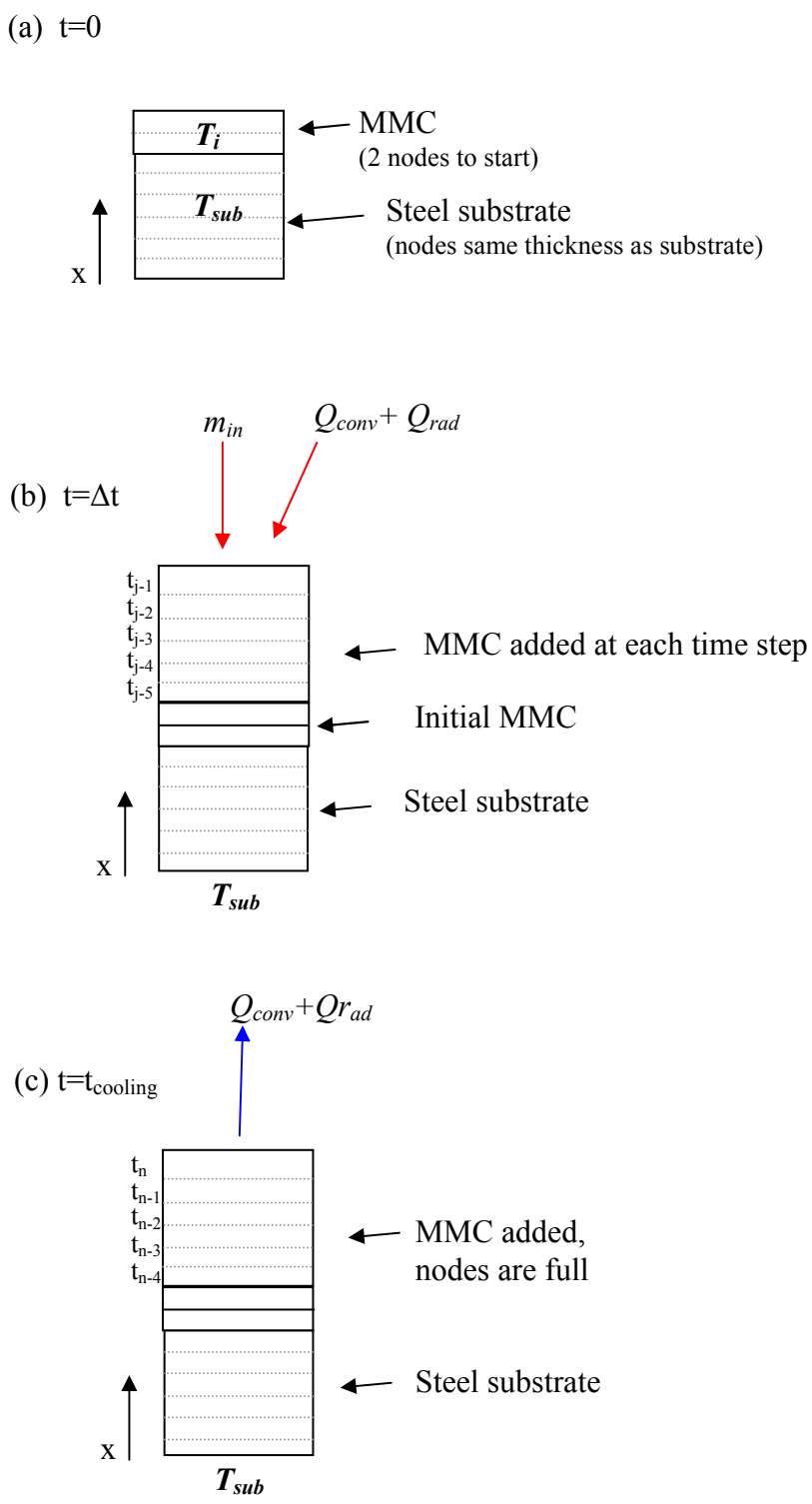

Figure 5.2: Schematic of thermal solidification model, initial conditions (a), during node filling (b) and upon cooling of the deposit and substrate (c).

The n^{th} node is subject to a constant heat flux boundary condition, shown in equation 5.2. The heat transfer coefficient, h, changes during the process. Referring to Figure 5.1, there are three distinct modes: when the plasma arc is on (1), when the plasma arc is extinguished and the shielding gas is still active (2), and when all gases are off and the surface is subjected to air cooling (4). A full analysis of the development of the heat transfer coefficients follows.

$$\left.\frac{dT}{dx}\right|_{x=n} = -\frac{h}{k_{x=n}}\left(T_{x=n} - T_{\infty}\right) \tag{5.2}$$

5.1.1 Development of the Heat Transfer Coefficient

The development of the heat transfer coefficient for each mode will be investigated independently. Firstly, the effects of the plasma gas will be explored, followed by the shielding gas and finally with ambient air. These regions are shown in Figure 5.1 as 1, 2 and 4, respectively.

5.1.1.1 Plasma Gas Heat Transfer Coefficient

The plasma gas region is located in Figure 5.1 as location 1. In order to calculate the heat transfer coefficient of the plasma gas, an estimation of the temperature and velocity of the gas is required. The arc is modeled as a fluid with constant temperature and velocity.

The estimation of the plasma velocity was complex as the literature does not agree. The velocity of the plasma gas could be estimated according to equation 5.3 [XIB1998]. Shown in Figure 5.3, is the velocity of the plasma gas as a function of radial distance and current. The properties of argon at high temperatures are found in Appendix B. The current (I) was 130A, with a r_* of 0.005 m, which is the radial distance in which 95% of the plasma heat is concentrated. The magnetic permeability (ω) of argon plasma is $4\pi \times 10^{-7}$ H/m. The velocity of the plasma decreases as the distance from the centre increases. At a distance of 4 mm (0.004 m) from the centre of the plasma, the velocity of the

plasma at a temperature of 10 000K is 12 m/s. A change in current from 110A to 150A will result in an increase in plasma velocity of 10 m/s to 14 m/s at a temperature of 10 000K (Figure 5.4).

$$V_{\infty}(r) = \frac{\sqrt{30\omega}I}{6\pi r_{*}\sqrt{\rho_{\infty}}}\sqrt{\left(1 - \frac{12r^{2}}{5r_{*}^{2}} + \frac{9r^{4}}{5r_{*}^{4}} - \frac{2r^{6}}{5r_{*}^{6}}\right)} \tag{5.3}$$

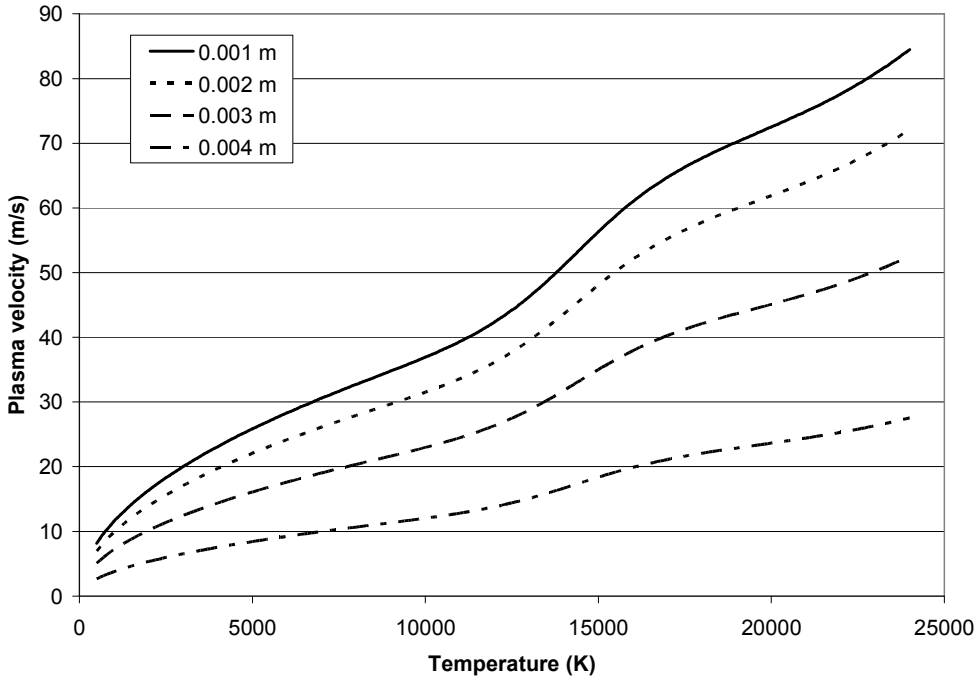

Figure 5.3: Estimation of plasma velocity, as a distance from the centre ranging from 0.001 m to 0.004 m.

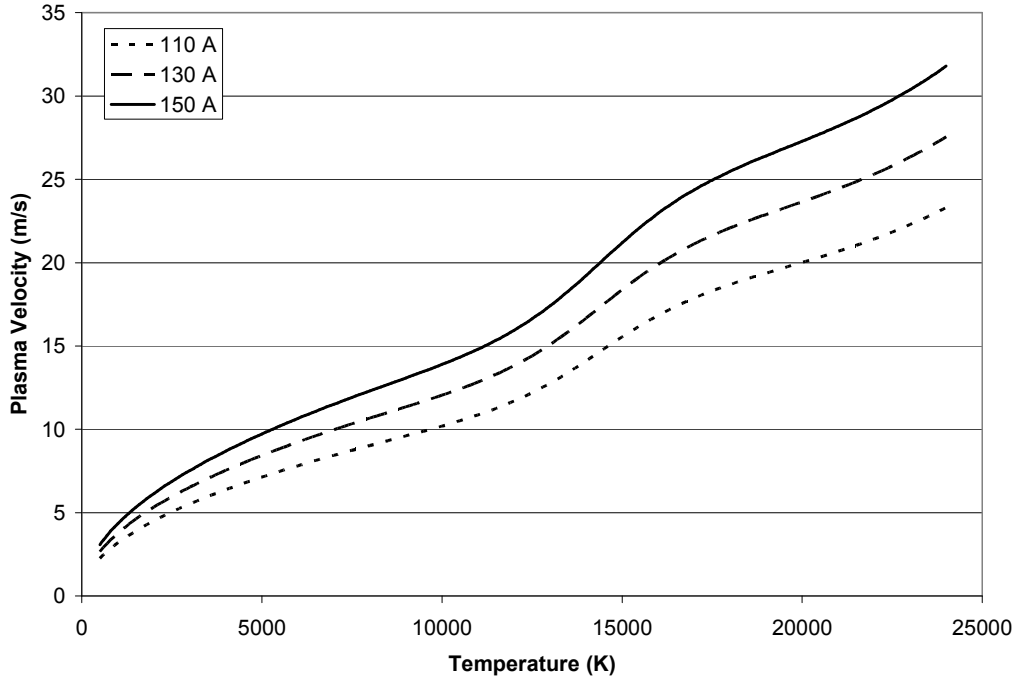

Figure 5.4: Estimation of plasma velocity, with current ranging from 110A to 150A.

Similar results were reported by Wilden et al. [WIL2006], who modeled the gas flow behaviour of a PTAW argon plasma and obtained a maximum centre velocity of 13 m/s with a plasma gas flow of 5 lpm and a power of 4.0 kW. Lancaster [LAN1986] estimates the velocity of an argon plasma by the product of a constant and the current. The value of the constant was 0.25 [KIM2003], resulting in a plasma velocity of 32.5 m/s for a current of 130A. However, Aithal et al. [AIT1998], predicted a streamwise (axial) velocity dropping from 1000 m/s at the nozzle to zero at a distance 9 mm away. Radial components were also investigated. At a distance of 4 mm from the centre, the plasma velocity does not exceed 50 m/s in the first 8 mm. The axial plasma velocity decreases from 300 m/s at the centre of the plasma to approximately 50 m/s at the edge of the collimated region, at a current of 200 A [CHO1990]. Tanaka et al. [TAN1999] assumed the gas velocity for a GTAW arc was 300 m/s and 50 m/s for currents of 150 A and 50 A, respectively.

The methodology to calculate the velocity and temperature of the arc in plasma arc welding [MET1975] was duplicated with the operating parameters of this experiment. The resulting temperature and gas velocities are shown in Figure 5.5. For a standard current of 130A, the average temperature is 13 000 K and the gas velocity is 185 m/s.

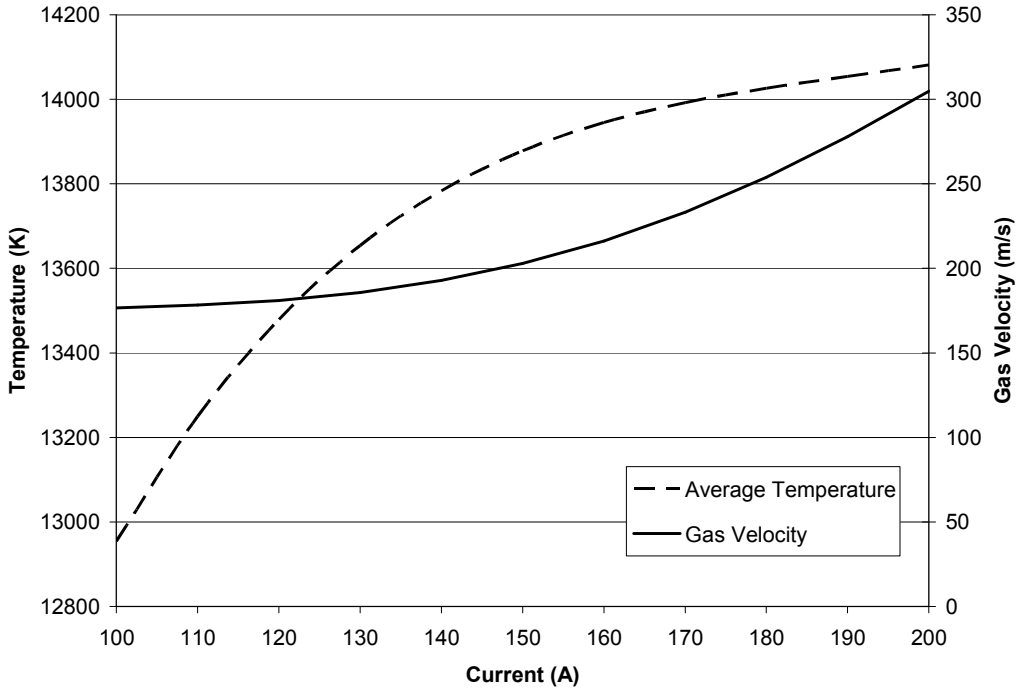

Figure 5.5: Gas velocity and temperature of a plasma arc in welding.

Another study [OGA1996] examined the heat transfer experimentally and theoretically of an impinging plasma jet at atmospheric pressure on a wall. A cylindrical thermal probe measured the plasma temperature and velocity. It was concluded that the heat transfer coefficient needed a correction factor of up to 2 as the temperature exceeded 10 000 K. The velocity of the plasma attained 100 m/s at a distance 1.5 mm away from the nozzle. Fast Fourier transforms were used to characterize the amplitudes and phase angles of images of the plasma jet in order to estimate the plasma velocity [SIN2000]. The experiments show that the plasma velocity profile for an arc with a current of 100 A and a gas flow rate of

20 lpm ranged between 150 m/s in the centre of the arc to 50 m/s 2.0 mm out in the radial direction.

It is clear that there exists a significant difference in the plasma gas velocities reported in literature. For the purposes of this study, gas velocities up to 200 m/s will be considered to determine its sensitivity on the plasma gas heat transfer coefficient. This will be discussed later in this section.

The Reynolds number (equation 5.4) of the argon fluid was calculated over a range of temperatures and velocities, shown in Figure 5.6. The diameter (d_p) or characteristic length (L) for the problem is 5 mm – the width of the stringer bead of coating. For a plasma velocity of 10 m/s, the Reynolds number does not exceed 20. As the velocity increases and the temperature decreases, the Reynolds number increases. Reynolds numbers below 2000 indicate laminar flow that is calm and regular [INC1996]. For all reasonable plasma velocities, the Reynolds number is within the laminar region. It is logical that the flow be laminar since the kinematic viscosity of hot argon gas is very high compared to ambient air – approximately 270 times. The higher the kinematic viscosity, the more difficult it is to 'move' the fluid.

$$\mathrm{Re} = \frac{U\rho d_p}{\mu_f} = \frac{U\rho L}{\mu_f} = \frac{UL}{\upsilon_f} \tag{5.4}$$

The temperature of the plasma arc is reported more consistently in the literature. According to the few PTAW models, the temperature range is listed in Table 5.1. The temperature range is defined as the centerline temperature outside the nozzle and the temperature on the edge of the collimated zone. The average temperature at the edge of the collimated zone for the three references is 8 333K. The powder is injected into the plasma at the edge of the collimated zone, so a temperature of 8 000 K was used as a standard plasma temperature for the model presented in this work.

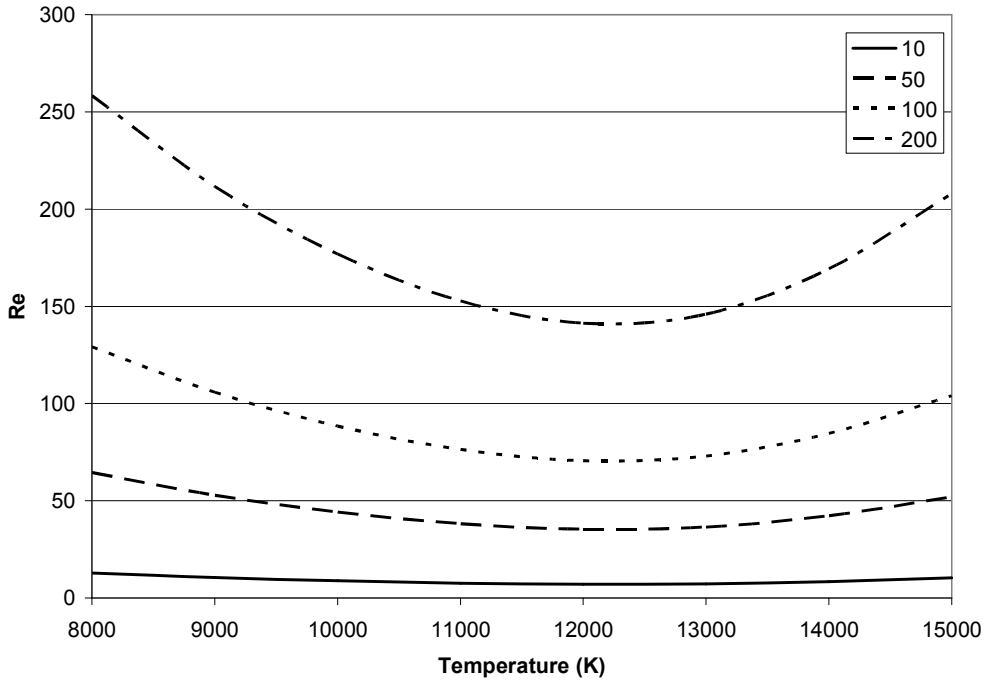

Figure 5.6: Reynolds number of argon plasma fluid with velocities ranging from 10 m/s to 200 m/s

Table 5.1: Plasma transferred arc predicted temperature ranges

Source	*Temperature Range*
FUD1997	17 000 K to 11 000 K
AIT1998	20 000 K to 8 000 K
WIL2006	14 000 K to 6 000 K
CHO1990	21 000 K to 11 000 K

As shown, the plasma is laminar and reaches temperatures in the order of 10 000 K. Other free-burning plasma arcs have also been modeled as laminar flow [COU1993]. The heat transfer coefficient for laminar flow over a horizontal flat surface is shown with equation 5.5, valid for Pr>0.6. The associated Prandtl (Pr) numbers for the same fluid averages to 0.61 (Appendix B – Figure 1e). The Prandtl number is a dimensionless number approximating the ratio of kinematic viscosity and thermal diffusivity, shown in equation 5.6.

$$h = 0.332\,\mathrm{Re}^{1/2}\,\mathrm{Pr}^{1/3}\,\frac{k}{L} \tag{5.5}$$

$$\mathrm{Pr} = \frac{\mu_f c_{p,f}}{k_f} \tag{5.6}$$

The values of *h* from equation 5.5 are shown in Figure 5.7 for argon plasma with a temperature of 500 to 13 000 K and for ambient air. The heat transfer coefficient significantly increases as the temperature increases from 8 000 K to 13 000 K. At a gas velocity of 100 m/s, the heat transfer coefficient increases from 164 to 1015 W/m^{2}K. This considerable increase is a result of the polynomial argon properties. As the temperature of the argon gas lowers to near ambient (500 K), the heat transfer coefficient reduces to less than 200 W/m^{2}K. The heat transfer coefficients for ambient air (blue line) are similar to an argon plasma operating at a temperature between 9 000 K and 10 000 K. This is because air is less viscous than argon.

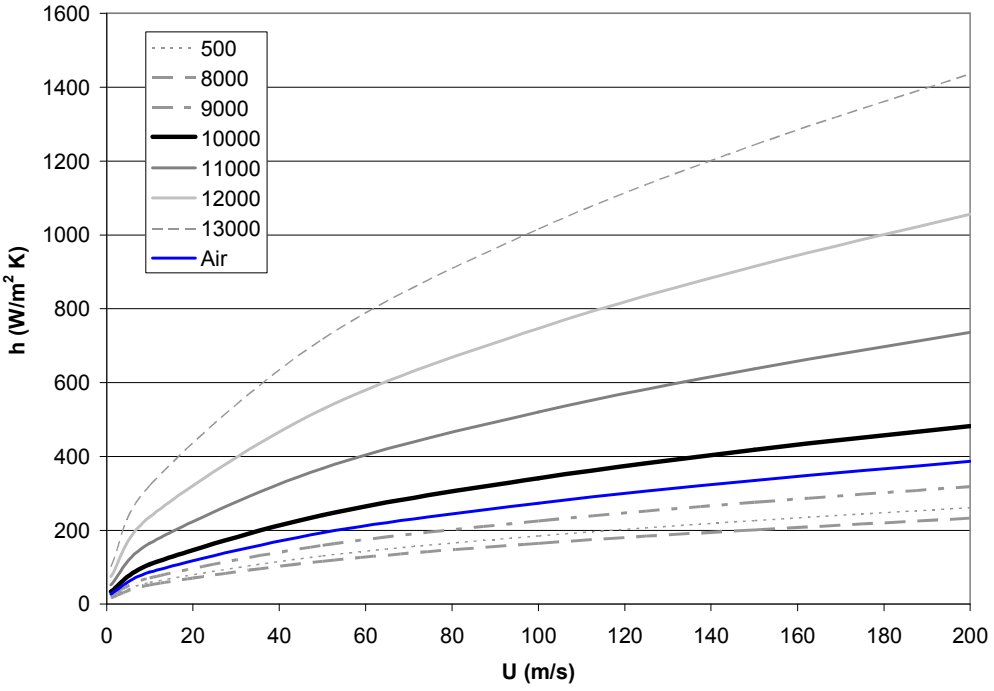

Figure 5.7: Heat transfer coefficient for a laminar argon plasma (temperatures ranging from 500 K to 13 000 K) and ambient air, following equation 5.5

However, the plasma gas emulates a single impinging jet rather than laminar flow parallel to a flat plate. The heat transfer coefficient of a single unconfined impinging jet for argon over the same temperature range and for ambient air was calculated. The correlations for the heat transfer coefficient and the corresponding Nusselt number are shown in equation 5.7 for the heat transfer coefficient for a single round free surface jet impinging on a surface [BEJ2003]. These correlations are best suited for 1000<Re<51 000. Although values of Reynolds numbers were not obtained in the suitable range, the corresponding heat transfer coefficients were sought. The values of the coefficients are m=0.5, n=0.532, C_1=0.516 and C_2=0.491. The dimensions for Reynolds number are D_i for the diameter of the jet near the substrate and L_h is the length of the impingement region. For this study, D_i is 0.004 m and L_h is 0.005 m. This was measured from the plasma images in the previous chapter. At a plasma velocity of 100 m/s, the heat transfer coefficient increases from 764 to 4729 W/m^{2}K over the plasma temperatures of 8000 to 13000K, respectively (Figure 5.8). This is a significant increase from the laminar problem and likely represents the heat transfer coefficient more appropriately.

$$
\begin{aligned}
h &= \frac{NuD_i}{k} \\
\frac{\overline{Nu}}{\mathrm{Pr}^{0.4}} &= C_1\,\mathrm{Re}_{D_i}^{m}\,\frac{L_h}{D_i}\,A_r + C_2\,\mathrm{Re}_{L_*}^{n}\,\frac{L_h}{L_*}\left(1 - A_r\right) \\
A_r &= \frac{\pi D_i^2}{4L_h^2} \\
L_* &= \frac{0.5\left(\sqrt{2}L_h - D_i\right) + 0.5\left(L_h - D_i\right)}{2}
\end{aligned}
\qquad (5.7)
$$

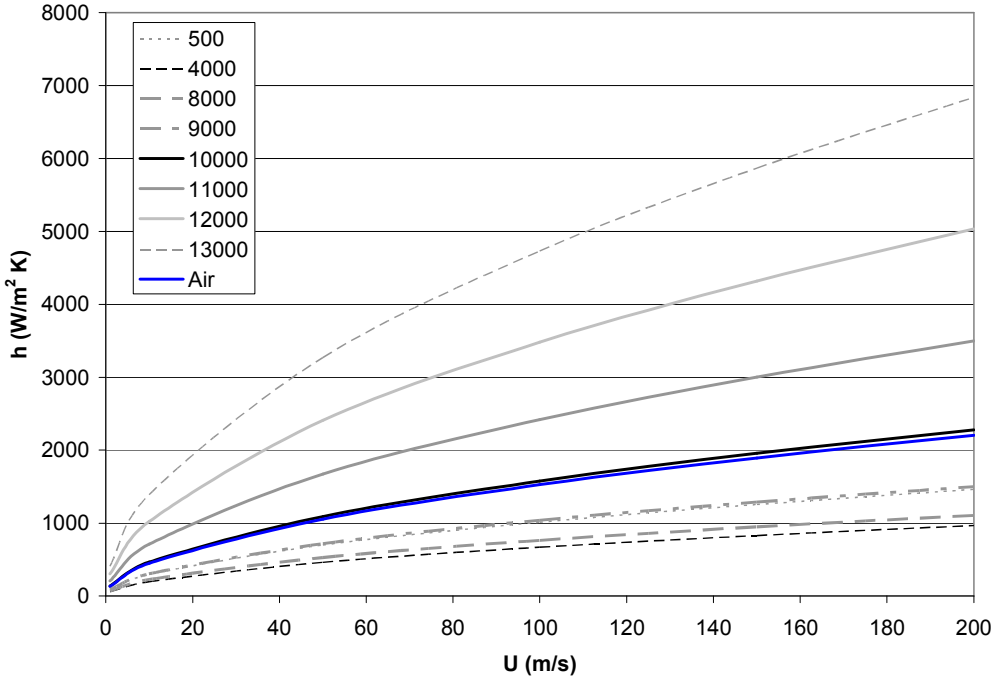

Figure 5.8: Heat transfer coefficient for a single impinging jet of argon plasma or ambient air, following equation 5.7

Another correlation for the heat transfer coefficient for a laminar vertically impinging jet [GOR1961] is shown in equation 5.8, where L is stand-off distance and Re is calculated at the jet exit. The results are shown in Figure 5.9. At a plasma velocity of 100 m/s, the heat transfer coefficient of a plasma between 8 000 and 13 000 K would be 4 000 to 25 000 W/m^{2}K. Following the assumptions of some studies where the plasma gas velocity was between 10 to 50 m/s (Figure 5.10), the corresponding heat transfer coefficients would be in the range of 400 to 8 000 W/m^{2}K.

$$h_c = 13\,\mathrm{Re}^{0.5}\,\mathrm{Pr}^{0.33}\,\frac{k_{plasma}}{L} \tag{5.8}$$

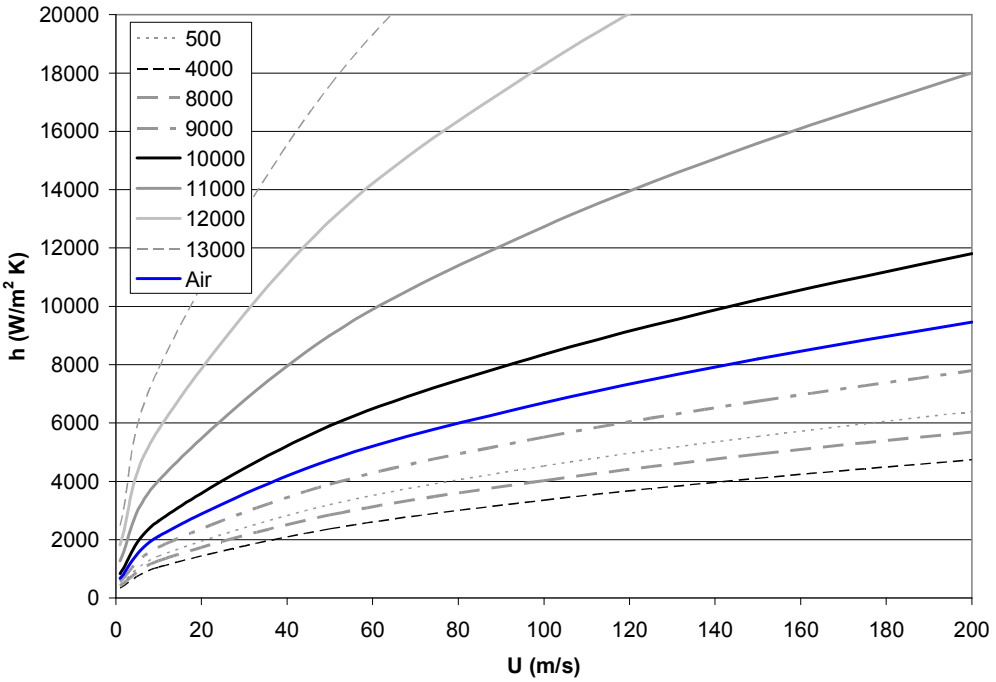

Figure 5.9: Heat transfer coefficient for a single laminar impinging jet of argon plasma or ambient air, following equation 5.8

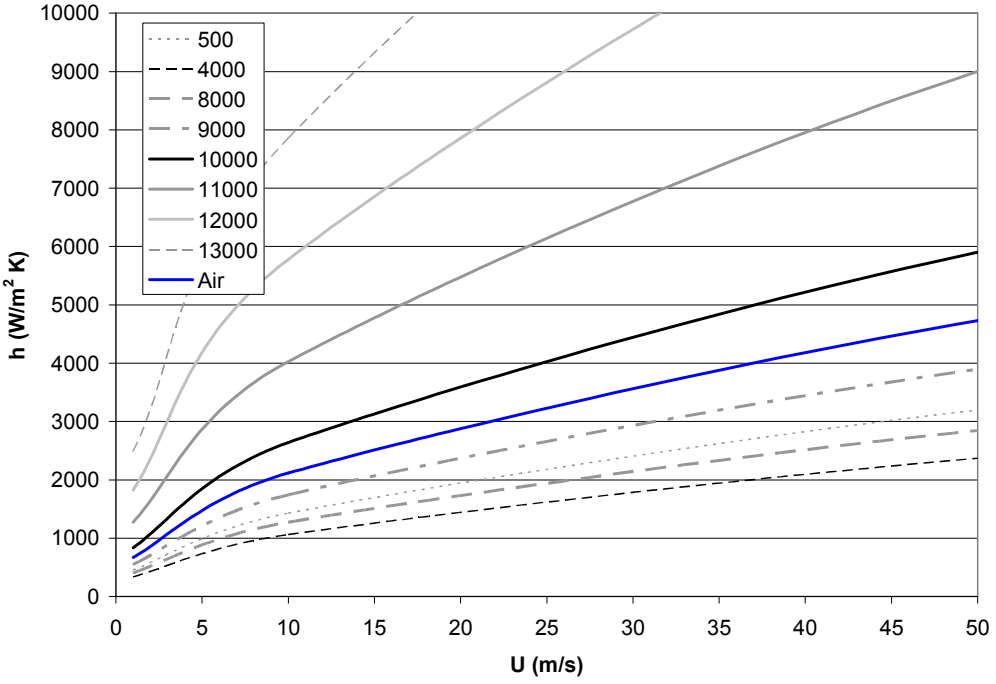

Figure 5.10: Heat transfer coefficient for a single laminar impinging jet of argon plasma or ambient air, following equation 5.8, showing detail at lower velocities.

The values of heat transfer coefficient and the resultant velocity are summarized in Table 5.2 for temperature ranges between 8 000 and 10 000 K. The range of plausible standard heat transfer coefficient for the plasma arc while initiated in the model presented in this work was 1100 to 2900 W/m^2K. This was based on the range of average heat transfer coefficient for a plasma traveling at velocities from 10-100 m/s between 8 000 and 10 000 K.

Table 5.2: Summary of heat transfer coefficients for an argon plasma arc.

Condition	*Velocity (m/s)*	*h (W/m^2K)*
laminar flat plate	100	164 - 341
	10-50	52 - 241
impinging jet	100	764 - 1576
	10-50	224 - 1090
laminar jet	100	4025 - 8346
	10-50	1272 - 5900

5.1.1.2 Shielding Gas Heat Transfer Coefficient

The shielding gas is an annulus surrounding the collimated plasma arc, shown in Figure 5.1 in region 2. Its purpose is to provide an inert environment for the liquid metal, assist in collimating the arc and provide cooling to the weld. The inlet temperature of the shielding gas is around 298 K, however, the proximity to the plasma arc heats the shielding gas. The temperature of the side of the arc was approximated to 8 000 K. Taking the average of the two temperatures, the shielding gas temperature can be estimated at 4 000 K. The duration of contact with the shielding gas is dependent on the travel speed of the torch and the flow rate of the gas. For a torch travel speed of 3.81 mm/s, a 5 mm length of material will be contacted by shielding gas for 1.3 s. Thus, the shielding gas heat transfer coefficient was applied for 1.3 s.

The dimensions of the annulus were an outer diameter of 0.02 m and an inner diameter of 0.018 m, resulting in a surface area of 6.0E-05 m^2. With a gas flow rate of 10 lpm, the gas velocity was 3 m/s. The relationship between Reynolds number with plasma velocity and temperature is shown in Figure 5.11. It can be seen that as the temperature increases, the Reynolds number decreases; as the temperature of the plasma decreases, the flow becomes less laminar.

The heat transfer coefficient for argon at 4000 K traveling at 3 m/s over a flat plate as laminar flow is 30 W/m^2K (Figure 5.7). The heat transfer coefficient for a laminar horizontal plate was studied further in terms of the fluid velocity and temperature. If the Prandtl number is much less than one, the heat transfer coefficient takes on the form shown in equation 5.9 [INC1996] rather than equation 5.5.

$$h = 0.565\,\mathrm{Re}^{1/2}\,\mathrm{Pr}^{1/2}\,\frac{k}{L} \tag{5.9}$$

The solutions of heat transfer coefficient are shown in Figure 5.12 for both Pr near 1 and Pr<<1. This figure shows that the heat transfer coefficient does not exceed 300 W/m^2K when the fluid temperature is below 8 000 K. There is little difference between the solutions due to Pr. At 10 000 K to 15 000 K, there heat transfer coefficients for Pr<<1 are significantly larger than the solutions when Pr is near 1. However, the Pr in this region is near one and equation 5.9 is not applicable. As the temperature increases to 20 000 K, the Pr drops significantly, however, there is little deviation between the two solutions, except when the temperature is around 15 000 K. With laminar flow, in the temperature ranges expected in the shielding gas region (between 298 K and 8 000 K), the heat transfer coefficient cannot exceed 300 W/m^2K.

Heat transfer coefficient values of 30 and 300 W/m^{2}K underestimate the degree of heat transfer in this dynamic process and it was hypothesized that the flow was likely not completely laminar.

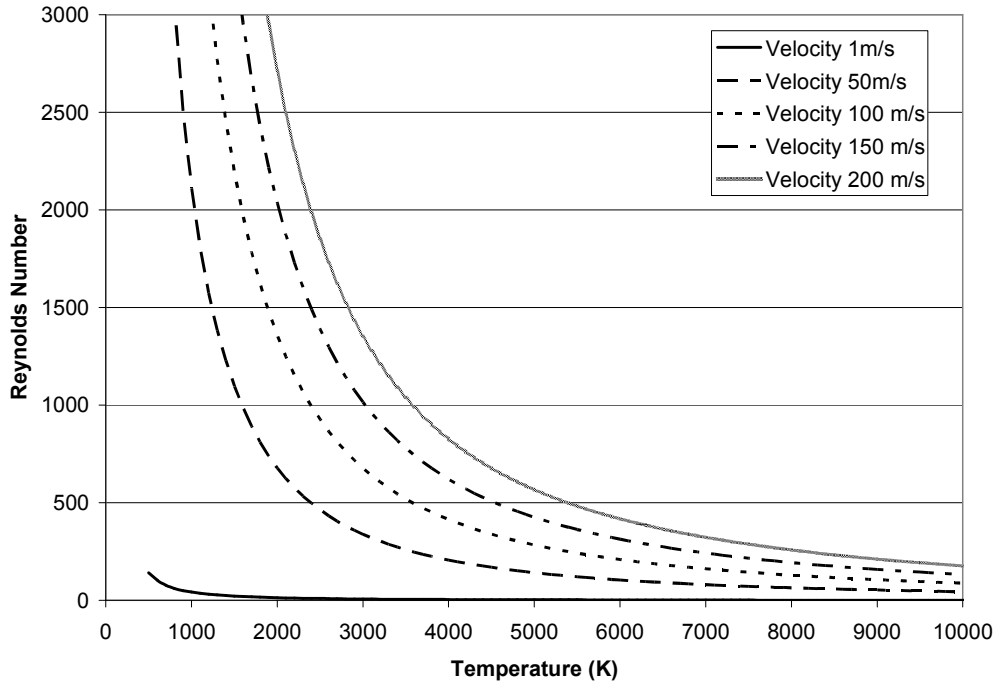

Figure 5.11: Reynolds number of shielding gas

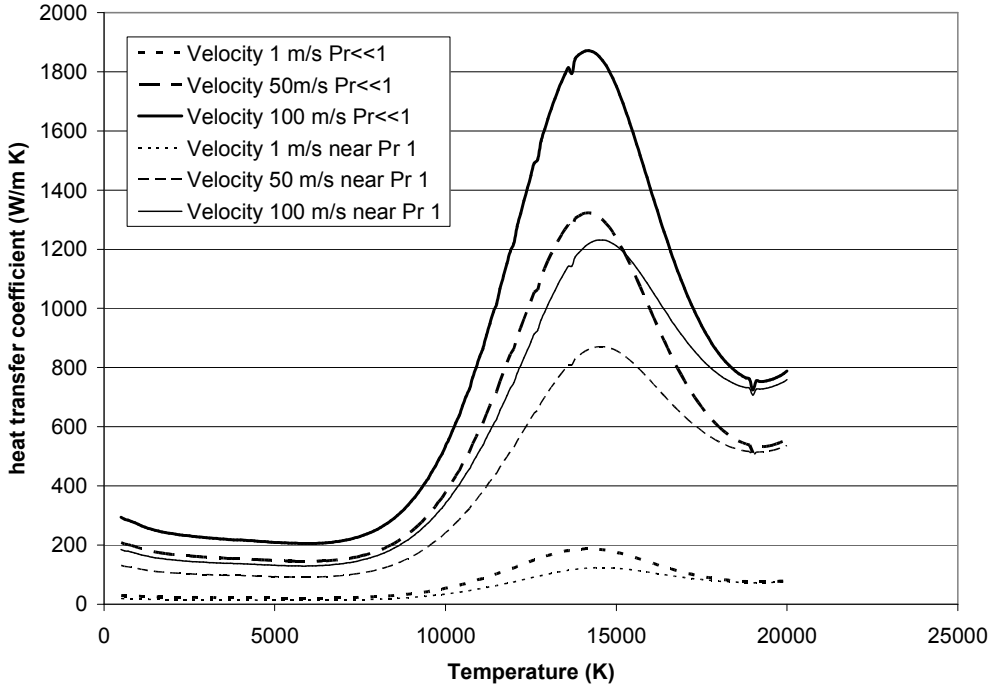

Figure 5.12: Heat transfer coefficient for shielding gas for Pr <<1 and Pr near 1, laminar flow on a horizontal plate

Revisiting the impinging jet scenario from Figure 5.8, the heat transfer coefficient for argon gas at 4 000 K lies between 57 and 967 W/m^{2}K. The heat transfer coefficient is higher for argon temperatures of 500 K, due to the polynomial temperature dependent properties. The values for the heat transfer coefficient for a laminar impinging jet of argon at 4 000 K are 331 to 2300 W/m^{2}K for gas velocities up to 50 m/s. Higher heat transfer coefficients can be obtained using an impinging jet approach. The range of heat transfer coefficients based on an average of all the methods for gas velocities up to 50 m/s applicable for the shielding gas is between 200 and 1600 W/m^{2}K.

5.1.1.3 Ambient Air Heat Transfer Coefficient

When the arc and shielding gas are extinguished, the surface is subjected to still air at room temperature or cooling by the fume hood (region 4 in Figure 5.1). Both scenarios were considered to investigate the probable range of heat transfer coefficients. The relationship for the heat transfer coefficient of still air on a

horizontal plate is shown in equations 5.10 to 5.12 [INC1996] and graphically in Figure 5.13. The Rayleigh number, *Ra*, is a dimensionless number which represents the ratio of buoyancy to viscous forces of the fluid. For this problem the Rayleigh number is between 10^4 and 10^7. The range of heat transfer coefficients for still air over a flat plate, where the characteristic length is 0.005 m, is between 3 and 14 W/m^{2}K for ($T_{surface}$-T_∞) between 1 and 1000 K. The fluid properties change for every ($T_{surface}$-T_∞), since the properties are based on the average temperature, T_f. However, for air at 300K, the kinematic viscosity is 1.59E-5 m^2/s and the thermal diffusivity is 2.25E-5 m^2/s. The heat transfer coefficient will decrease as cooling progresses.

$$Nu_L = \frac{hL}{k} \tag{5.10}$$

$$Nu_L = 0.54 Ra_L^{\frac{1}{4}} \quad (10^4 \le Ra_L \le 10^7) \tag{5.11}$$

$$Ra_L = \frac{g(T_{surface} - T_\infty)L^3}{\upsilon \alpha T_f} \tag{5.12}$$

If the air has a velocity component due to draughts induced by the fume hood or due to the shielding gases displacing the air, the heat transfer coefficients follow the laminar cooling on a horizontal plate and are shown in Figure 5.7. The fume hood suction is located parallel to the substrate, so the flow of air is also parallel over the plate. Air is represented by the blue line, and has a range of heat transfer coefficients between 27 and 387 W/m^{2}K for velocities between 1 and 200 m/s. The higher values of heat transfer coefficient are due to the lower kinematic viscosity of air compared to argon.

The fume hood draws welding fumes at a flow rate between 17 and 25.5 cubic meters per minute [AME2007]. With a distance to the source of 0.3 m, and a face diameter of 0.2 m, the air velocity is between 0.56 m/s and 0.85 m/s. The corresponding Reynolds numbers range from 81 to 121, which indicate laminar

flow. The heat transfer coefficient equations assuming laminar flow on a flat plate are within the range of 26 and 33 W/m^2K.

Therefore, for convection over a flat horizontal plate in PTAW conditions, the cooling gas can result in natural or laminar convection with corresponding heat transfer coefficient ranging from 3 to 400 W/m^2K. Subsequently analysis will show that the deposit cooling is not sensitive to the value chosen for the heat transfer coefficient.

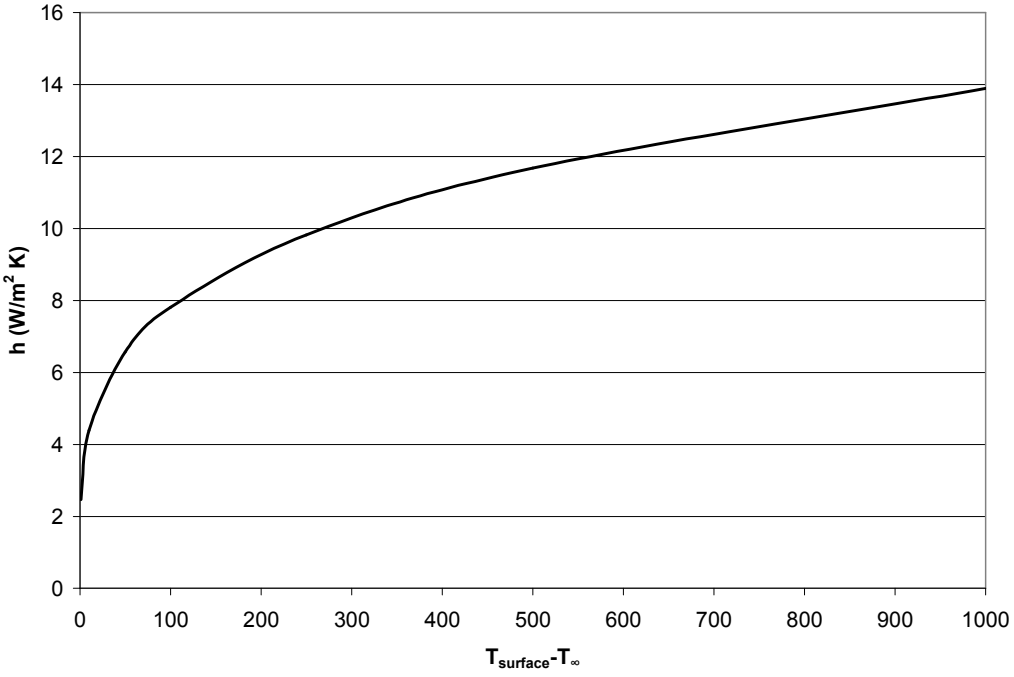

Figure 5.13: Heat transfer coefficient for still air over a horizontal plate

5.1.2 Temperature of Incoming Particles

The incoming temperature of the nickel matrix and tungsten carbide particles is required for the model. The particles are carried from the hopper to the nozzle by an argon carrier gas. The two powder ports in the nozzle are located 45° from the trailing edge. The powder is heated and accelerated by the plasma and deposited on the substrate surface. To estimate the temperature of the particle as they are

deposited on the surface, a model of a single particle (both nickel and tungsten carbide) heated by a plasma fluid was developed.

A significant amount of research has been conducted to calculate the temperature and velocity the particles achieve during thermal spraying. The same modeling methodology can be applied to plasma arc welding to estimate the amount of heat absorbed by the particles from the arc. The difference in the physics between plasma spraying and plasma arc welding is the distance traveled by the particle, the delivery position of the particles into the plasma and the plasma temperatures and velocities.

The Biot number of the particle was calculated to determine if the particle was heated uniformly without temperature gradients. A simple 1-D heat conduction model was developed to track the temperature and velocity as the particle exited the nozzle and was deposited onto the surface. The distance between the torch and the substrate is less than 10 mm.

5.1.2.1 Biot Number of Powder

The Biot number (*Bi*) is a dimensionless number used in transient heat transfer calculations, and is the ratio of the resistance to conduction within the body (internal) to the resistance to convection across the fluid boundary across the body (external). The Biot number is defined in equation 5.13, where h is the heat transfer coefficient, L is the characteristic length and k is the thermal conductivity.

$$Bi = \frac{hL}{k} \tag{5.13}$$

In this case, *Bi* is used in the heat flow model of cold Ni or WC sphere immersed in the hot arc plasma. The heat flow must pass from the hot plasma to the surface of the sphere, and then into the sphere itself. If the thermal resistance within the

sphere is much less than the resistance to convection, $Bi<<1$ [INC1996]. As such, temperature gradients within the body can be neglected.

To calculate Bi, the heat transfer coefficient must be known (equation 5.14). The Nusselt number, Nu, for a particle heated in a plasma is shown in equation 5.15 [LEE1985] [WAN1999]. The variable properties of the plasma due to large temperature and velocity gradients and noncontinuum effects are addressed in f_{prop} (equation 5.16) and f_{Kn} (equation 5.17). The plasma properties are determined at temperatures in the bulk of the fluid near the particle, w, at the particle surface, s, or the film temperature, f, which is the average of the bulk and surface temperatures. Additional terms can be added to address changes in viscosity, density and heat capacity [LEW1973] [FIS1979] [CHE1982]. Non-continuum effects due to the plasma have been found to be important for particles less than 20 μm [CHE1983].

$$h = \frac{k_f Nu}{d} \tag{5.14}$$

$$Nu = \left(2 + 0.6\,\mathrm{Re}^{\frac{1}{2}}\,\mathrm{Pr}^{\frac{1}{3}}\right)\left(\frac{c_{p_k}}{c_{p_w}}\right)^{0.38} {f_{prop}}^{0.6} f_{Kn} \tag{5.15}$$

$$f_{prop} = \frac{\rho_p \mu_p}{\rho_w \mu_w} \tag{5.16}$$

$$f_{Kn} = \left[1 + \left(\frac{2-a}{a}\right)\left(\frac{\chi_w}{1+\chi_w}\right)\frac{4}{\mathrm{Pr}_w} Kn^*\right]^{-1} \tag{5.17}$$

$$\text{where } Kn^* = \frac{\mathrm{Pr}_w}{\rho_w \upsilon_w r_p}\frac{k_f}{c_{p,f}}$$

$$\text{where } \upsilon_w = \left(\frac{8\Re \tilde{T}_w}{\pi W}\right)^{1/2}$$

Shown in Figure 5.14 are *Bi* for Ni and WC spheres in a hot plasma. The simulation was conducted for a plasma velocity of 200 m/s and the particles velocity of 2 m/s. The plasma velocity of 200 m/s was chosen since it was the upper limit. Since *Bi* for the both the WC and the Ni particles is less than 0.1 for all diameters, the heating of the powders can be modeled by the lumped sum capacitance model.

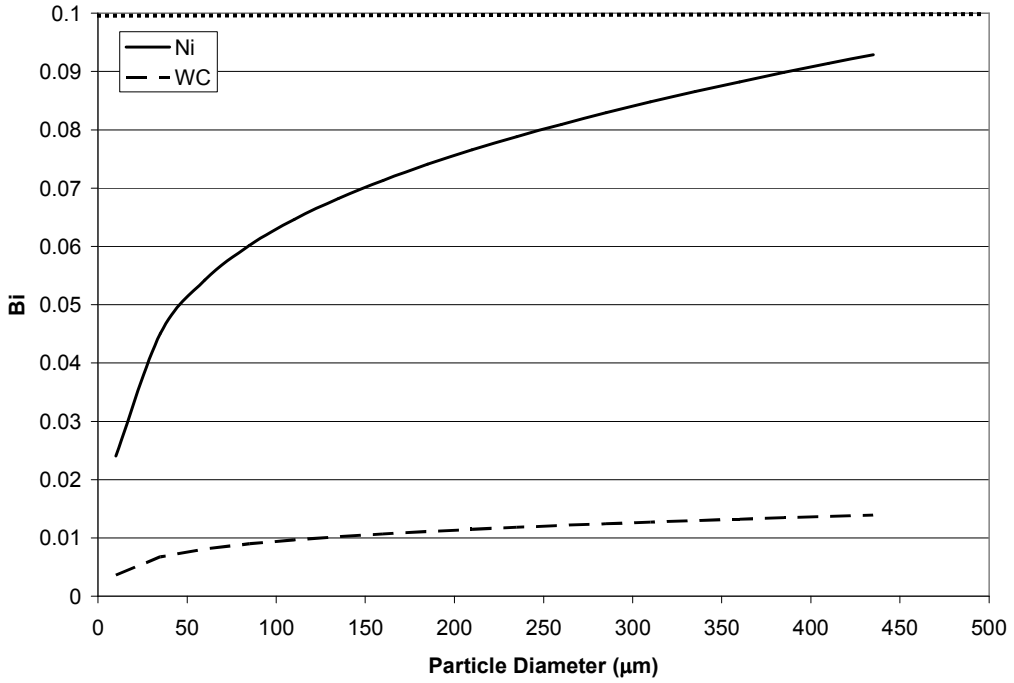

Figure 5.14: Biot number for powder spheres travelling at 2 m/s in a 200 m/s hot plasma. The dotted line indicates the maximum Biot number such that thermal gradients do not occur within the powder (Bi=0.1).

5.1.2.2 Temperature and Velocity Model of Powder Particles

The heat conduction within a single spherical particle given convective and radiative heat transfer from the plasma has been well developed. The interface between the solid and liquid boundaries was monitored as well as the vapourization and evaporation boundaries [LEE1985]. Further advances were focused on more efficient numerical solution techniques (polynomials [LEE1988], finite volume [WU1991], CFD software using LAVA code for

plasma flame simulation [WAN1998]), the effect of a continuous stream of particles [VER1998] rather than a single particle, the array of phase change paths of the particle [WAN1999], the effect of carrier gas flows [AHM2001] [FAU2004], and the effect of non-spherical particles [WEN2003] [XU2003]. Validation of these models occurred by thermocouple instrumentation of the substrate, evaluating the splat morphology, and tracking the particle trajectory through the plasma plume.

A 1-D heat conduction analysis of the particles was modeled considering the convective heat flux input described in equation 5.18. The heat transfer coefficient follows equations 5.14 through 5.17. A schematic of the problem is shown in Figure 5.15. Latent heat evolution is considered in the same method as that described in section 5.1.3. Evaporative and radiative losses of the particle were not included.

$$\dot{Q}_{plasma} = 4\pi r_p^2 h\left(T_w - T_s\right) \tag{5.18}$$

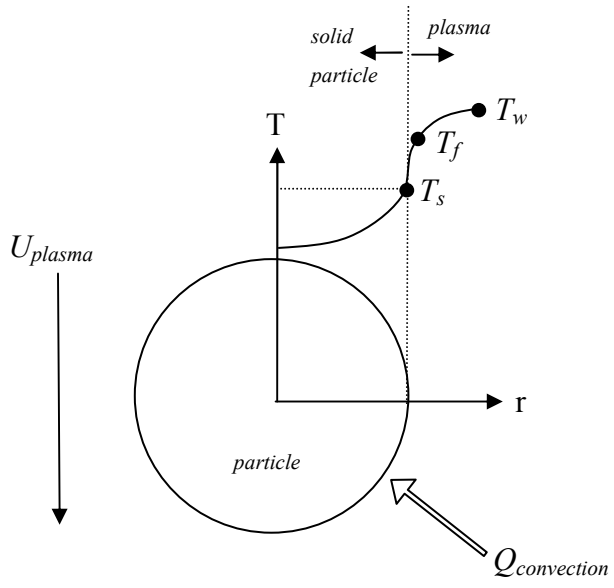

Figure 5.15: Schematic of particle heating and dynamics model

Shown in Figure 5.16 are the thermal histories for both Ni and WC particles with a radius of 150 μm. The Ni and WC particles reach their melting points in 0.003s and 0.006s, respectively. The Ni particle reaches the substrate/overlay surface, which is located a maximum of 0.01 m away, in less than 0.0055 s, however, the WC particle, due to its large density, takes over 0.006 s. It can inferred that it is highly probable that WC experiences some melting (melting point - 2870°C) when exposed to the hot plasma since the temperature of the particle just exceeds the melting point before its impact with the substrate. At 0.01 m, the temperature of the Ni and WC particles are 2600 K and 3300 K, respectively. Thus, an incoming temperature in the range of 2600 to 3300 K would be appropriate. At 150 A, the surface of a GTAW weld was reported to be between 2 500 and 3 000 K at the centre [JON1994].

Referring to Figure 5.17, in 0.006 s (the average time required for a particle to travel 0.01 m – the maximum distance between the nozzle and substrate) the velocity of the Ni and WC particles are 3.14 m/s and 2.14 m/s. According to the plasma tracking imagery, the average particle velocity measured was 2 m/s. This experimental result validates this model.

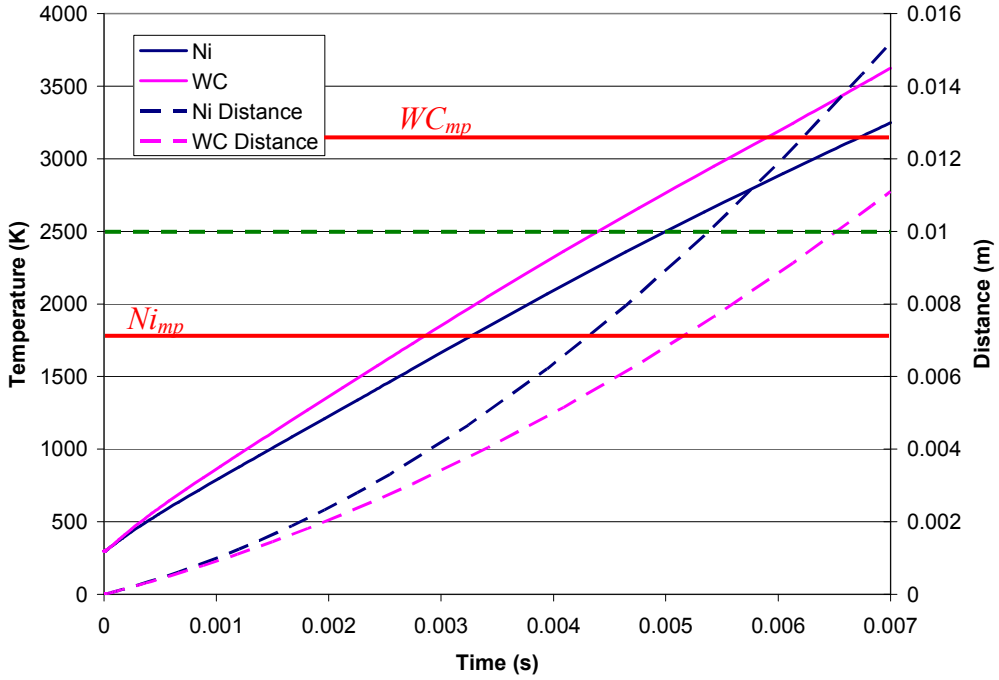

Figure 5.16: Temperature of Ni and WC particles as they travel from the nozzle to the substrate (max. 0.01 m – green broken line). The melting points of the individual powders are marked in red.

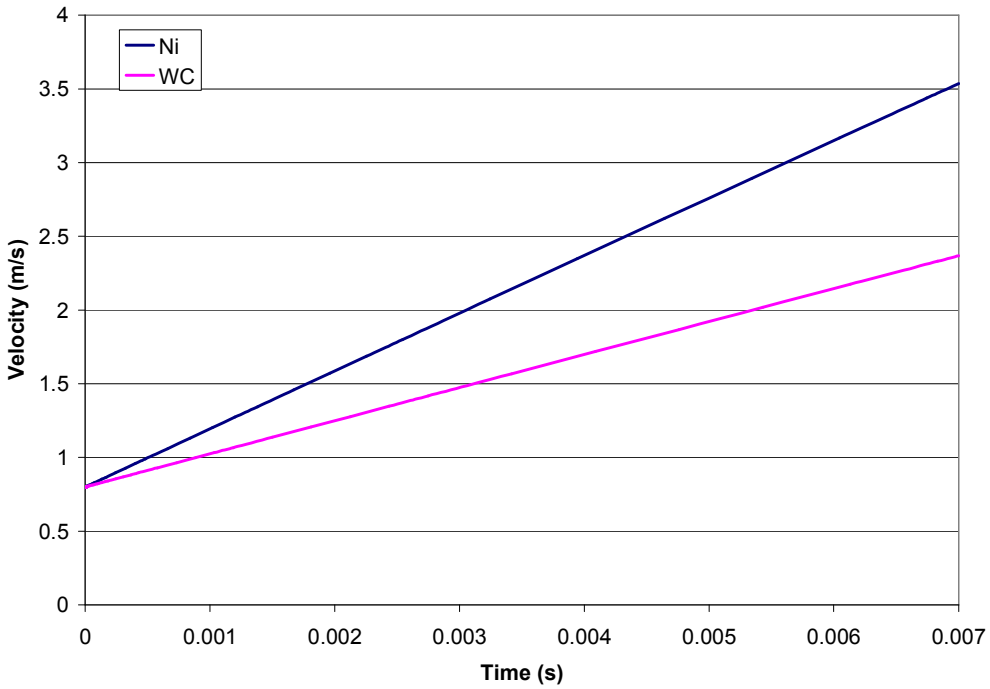

Figure 5.17: Particle dynamics of 150 µm spherical Ni and WC powders.

5.1.3 Implementation of Phase Change

It was shown that the nickel powder exceeded its liquidus temperature. To account for the phase change of the nickel matrix, an enthalpy model was considered. The phase change was modeled linearly from the solidus (T_{sol}) to the liquidus (T_{liq}), a schematic shown in Figure 5.18. The melting temperatures of the alloy were measured using differential scanning calorimetry and were found to be 1012°C (T_{sol}) and 1036°C (T_{liq}). The fraction of liquidus was calculated between T_{sol} and T_{liq} according to equation 5.19.

The latent heat (Λ) of the matrix alone was measured by differential scanning calorimetry to be 79410 J/kg. With the addition of 50 v% WC, the measured latent heat was reduced to 38100 J/kg. A linear interpolation was established to correct for the latent heat when the volume fraction of carbide was within the range of zero to 50 percent.

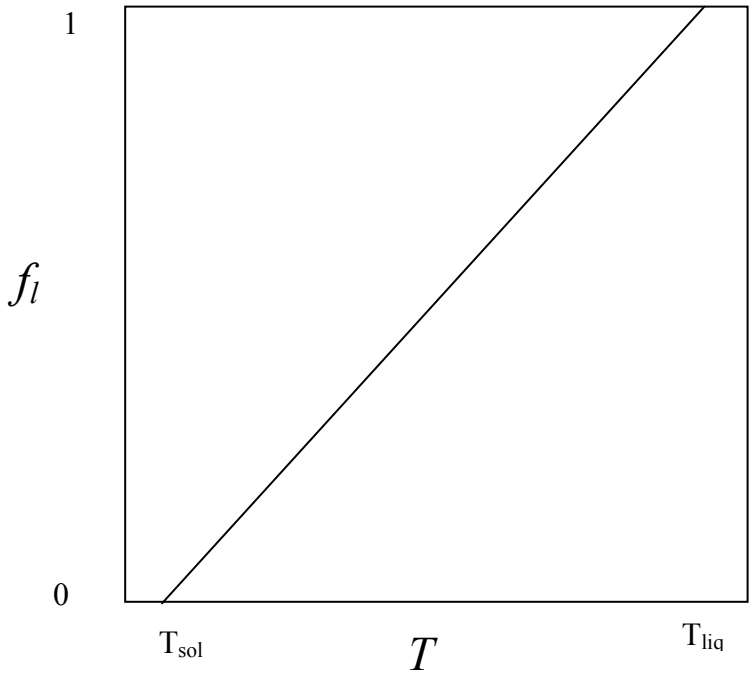

Figure 5.18: Linearization of phase change regime

$$f_l = \frac{1}{T_{liq} - T_{sol}} T - \frac{T_{sol}}{T_{liq} - T_{sol}} \tag{5.19}$$

The phase change term is added onto the general heat conduction equation as follows (equation 5.20). This set of differential equations was solved when the temperature of the cell was between the liquidus and solidus.

$$\begin{aligned} &\frac{\partial T}{\partial t} + \frac{\Lambda}{c_p}\frac{\partial f_l}{\partial t} = \alpha \frac{\partial^2 T}{\partial x^2} \\ &\frac{\partial T}{\partial t} = \frac{\alpha}{(1 + \frac{f_l \Lambda}{(T_{liq} - T_{sol})c_p})} \frac{\partial^2 T}{\partial x^2} \end{aligned} \tag{5.20}$$

5.2 Settling Component of the Model

Single particle settling of a WC sphere in liquid Ni with no solidification was investigated in the Stokes' regime. This analysis determined the time required to obtain terminal velocity of the WC particle; if the time was very small, the settling model could be simplified to include only terminal velocity. The effect of the velocity of the liquid on the particle kinetics was also investigated.

The problem was modeled by balancing the forces on a single sphere accelerating though a liquid, described in Section 2.5. The forces considered were gravity, buoyancy, drag and added mass. The result is a set of differential equations (equation 5.21 [GUT1975]), which when solved track the velocity and position of the sphere moving through the liquid. The initial conditions are $t=0$, $z=0$, $U=U_0$.

$$\begin{aligned} &\frac{dU}{dt} = \frac{-(1-\gamma)g}{\gamma + C_A} - \frac{3C_D U|U|}{4d(\gamma + C_A)} \\ &\frac{dz}{dt} = U \end{aligned} \tag{5.21}$$

where $\gamma = \rho_{solid}/\rho_{liquid}$.

The solutions are heavily dependent on the drag coefficient C_D. The laminar drag coefficient, $C_{D\text{-}lam}$ (equation 5.22), and alternate drag coefficient, $C_{D\text{-}alt}$ (equation 5.23), [PER2008] equations are shown. The alternate drag coefficient is applicable when the Reynolds number is between 0.1 and 1000.

$$C_{D-lam} = \frac{24}{\mathrm{Re}} \tag{5.22}$$

$$C_{D-alt} = \frac{24}{\mathrm{Re}}(1 + 0.14\,\mathrm{Re}^{0.7}) \tag{5.23}$$

The Reynolds number of the sphere moving through the liquid was calculated based on the particle diameter and the velocity of the particle. The kinematic viscosity of the liquid was 5.37E-07 m^2/s. Shown in Figure 5.19 is the relationship between Re and particle diameter. If the particle velocity is 1 m/s, the Re does not exceed 2000 and the problem is laminar. It was shown in Chapter 4 that the particle velocity in the plasma upon entering the liquid metal was up to 2 m/s. Since the particle diameter is not greater than 300 μm, the problem is laminar or semi-laminar, and the above equations are valid.

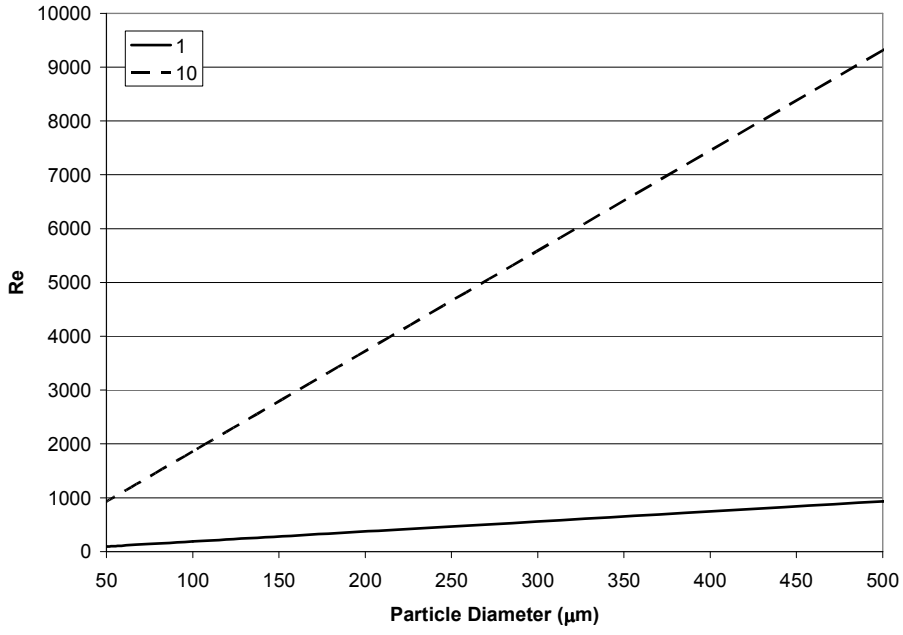

Figure 5.19: Reynolds number for a spherical particle in liquid with velocities 1 and 10 m/s

Shown in Figure 5.20 is the velocity and position of a 100 μm particle achieving its settling velocity in less than 0.02 s, with an initial velocity of 1 m/s. The density of the liquid is 7200 kg/m^3, with a constant viscosity of 10^{-3} kg/ms. The sphere reaches its terminal velocity within 0.015 s with all the forces included and a semi-laminar drag coefficient. The time increases to a maximum of 0.02 s with laminar drag behaviour. The particle settles through a 5 mm thick coating at terminal velocity in 0.32-0.41 s. The time drops to between 0.08 and 0.2 s for a 3 mm thick coating. If the particle velocity is increased to 10 m/s, the particle reaches the bottom in 0.0006 s.

Since the time to obtain terminal velocity is significantly smaller than the time to settle the thickness of the coating, it is permissible to assume that the particle velocity is its terminal velocity throughout the simulation. Adding to the model multiple particles and irregular shapes will give a better estimation of the settling characteristics of the carbide particles.

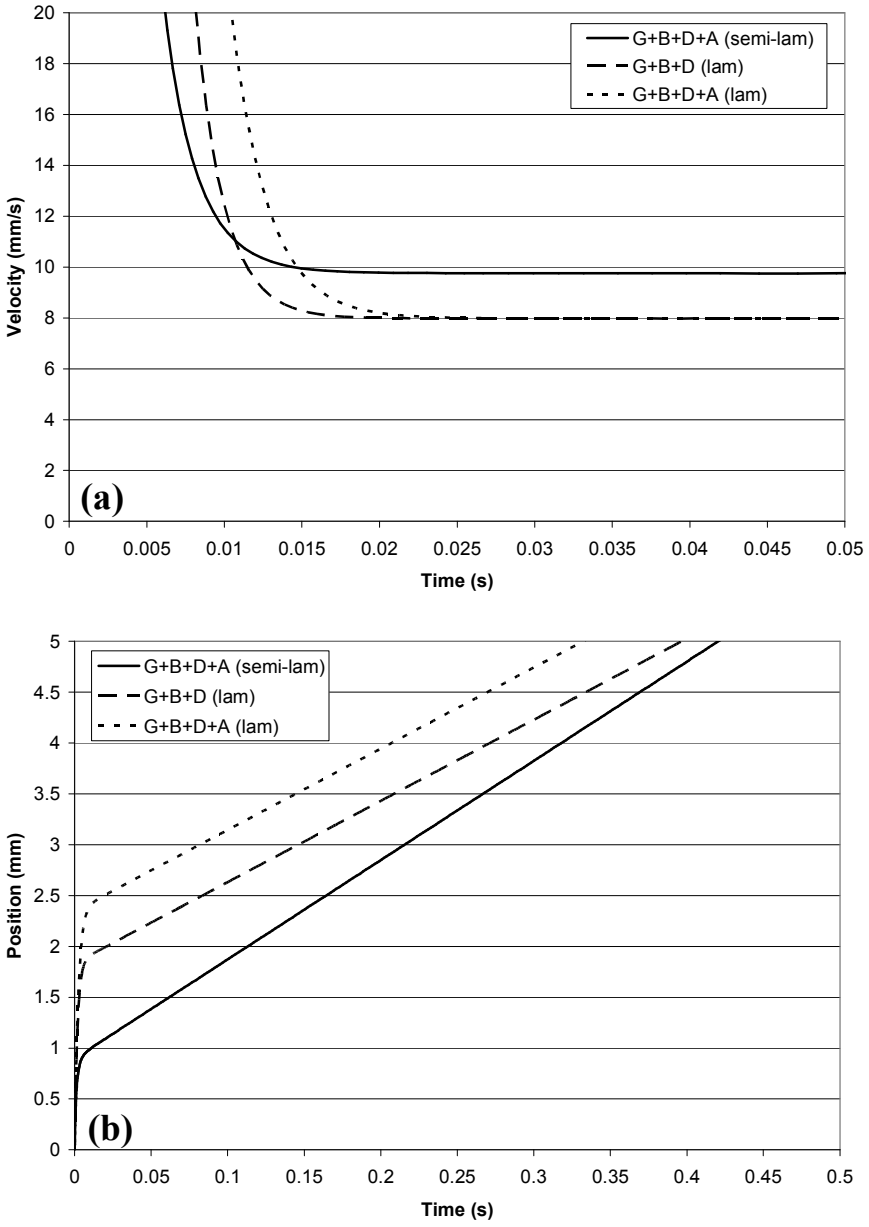

Figure 5.20: Velocity (a) and position (b) of 100 μm WC particles settling through constant viscosity, still Ni liquid. The forces acting on the particle are gravity (G), buoyancy (B), drag (D) and added mass (A). The conditions labeled (lam) are using eq. 5.22, whereas those labeled (semi-lam) are using eq. 5.23.

5.2.1.1 Particle Sphericity

Sphericity (ψ) is used to describe the shape of a particle and is defined as the ratio of the surface area of a sphere having the same volume as the particle to the

surface area of the particle (equation 5.24). The new diameter, d_*, is the particle diameter used in the applications. The average known particle diameter is d_{avg}. For a particle having the same projected area as a circle, the sphericity values are shown in Table 5.3. Tungsten carbide particles have shapes similar to a prism, such that their sphericity will be approximately 0.8. The ratio of specific surfaces is n, and is shown in Figure 5.21 as a function of average particle diameter. If d_{avg} is 150 μm, the ratio n is approximately 2.

Shown in Figure 5.22, are the d_* when n is 2 for a d_{avg} of 150 μm. Since the sphericity for a tungsten carbide is approximately 0.8, the projected particle size is around 100 μm, which is less than the actual particle size. In terms of affecting the dynamics of the problem, it was shown that there is very little change in Reynolds number at small particle diameters as the particle becomes more ellipsoidal [CAM2007]. If the Reynolds number does not change significantly, then the calculated values of particle temperature and velocity are still valid.

For a random packing fraction in the range 0.5 to 0.7, the corresponding sphericity was between 0.6 and 0.8 [YU1993]. The measured random packing fraction of the monocrystalline WC was approximately 0.55.

$$\psi = \frac{d_*}{d_{avg}} \frac{1}{n} \tag{5.24}$$

Table 5.3: Values of sphericity for equivalent sized geometric shapes [ZOU1996].

Shape	***Sphericity***
Cylinder	0.87
Hexagonal Prism	0.85
Rectangular Prism	0.79
Triangular Prism	0.72

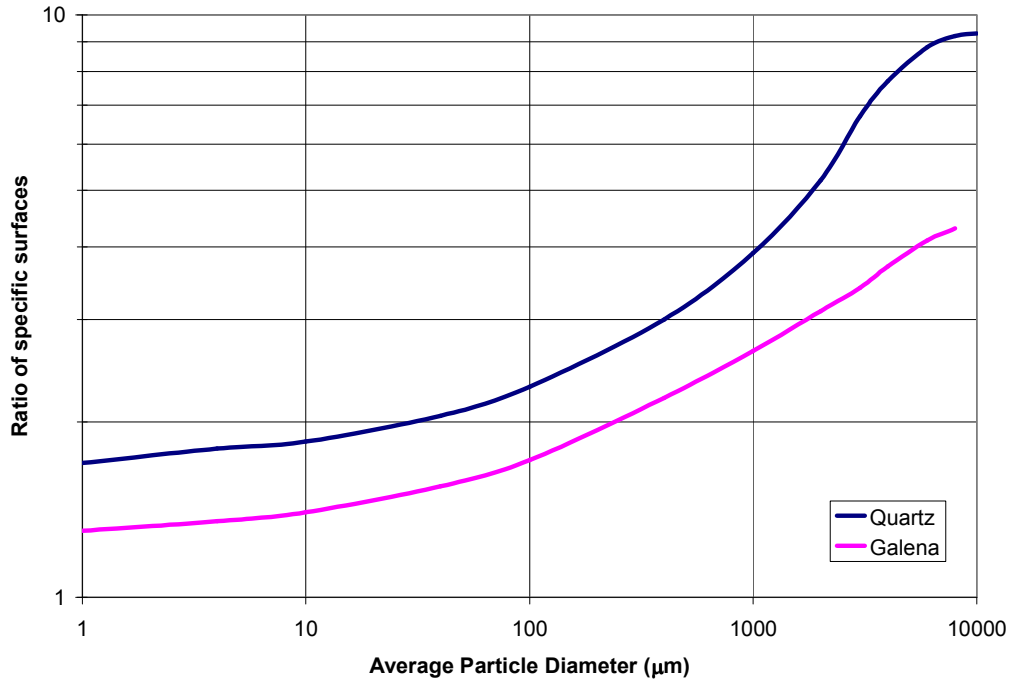

Figure 5.21: Relationship between n (ratio of specific surfaces) as a function of the average particle diameter of various minerals [BRO1950].

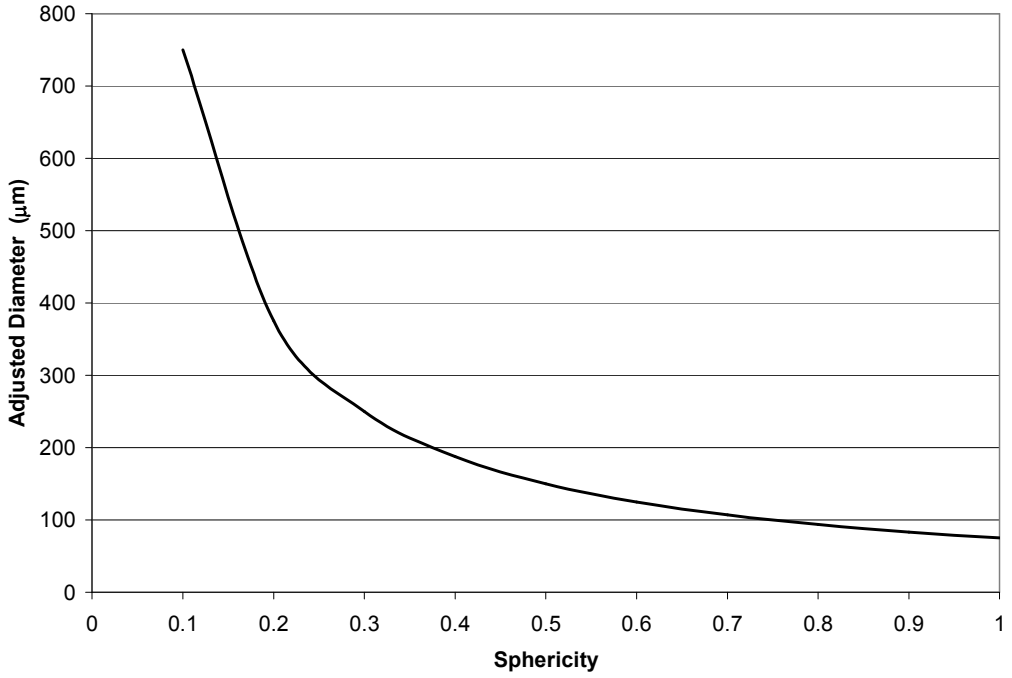

Figure 5.22: Adjusted particle diameter with changes in sphericity for ratio n=2. Initial particle size 150 µm.

5.3 Modelling Assumptions

The assumptions made in the thermal solidification and settling model are highlighted below.

1. Fluid velocity of molten metal is neglected. Fluid flow would be significant if the densities of the particles were similar. Simulations of the fluid flow in weld pools have yielded velocities of up to 3 m/s at the surface [COR1986] and go to zero in the centre. The majority of the weld pool velocity is near zero, with the exception of the surface. The particle remains at the surface for a very short period of time.
2. The deposition process has achieved steady-state. The region of interest is occurring long after arc initiation and stabilization, and the deposit bead is uniform is in width.
3. One dimensional solidification. The deposition produces heat transfer primarily through the surface of the deposit and through the substrate (in the x-direction – Figure 5.2). The Peclet (*Pe*) number [BIR1960] (the ratio of the thermal energy convected to the thermal energy conducted normal to the deposit thickness) was calculated (equation 5.25).

$$Pe = \frac{UL}{\alpha} \tag{5.25}$$

The thermal energy convected normal to the deposit thickness is essentially related to the welding velocity. The *Pe* number was considered in the y-direction (normal to the deposit thickness) as the amount of heat conducted in relation to the velocity of the welding table. If *Pe* is small ($Pe<<1$), conduction in the y-direction is dominant and a 1-D model could not be valid [RAI2007]. For this system, the table velocity was 4 mm/s and the length of the weld under the plasma arc was 10 mm. The thermal diffusivity was 1.13e-5 m^2/s, based on a mixture of 50 vol% WC in Ni at 1200 K. The corresponding *Pe* was 3.5, therefore the 1-D model is

justified. The table velocity is faster than the heat transfer down the length of the weld. Hence, $(\partial T/\partial y)=0$.

4. The liquid is in thermodynamic equilibrium due to the large thermal conductivity of the metal.
5. Particle pushing does not occur. The density of the tungsten carbide particles is twice that of the molten nickel matrix. Hence, settling of the particle occurs at a rate significantly faster than that of solidification or convection in the pool. Also, at high vol% WC, there is little mobility for the WC in the liquid nickel matrix.
6. The particles are rigid and wet the molten nickel. Any reactions between the particle and the matrix has a negligible effect on the size of the particles during settling.
7. Volume change during solidification is negligible.
8. Surface boundary conditions
    i. Powder enters at a constant temperature and feed rate (2800 K and 0.45 g/s).
    ii. Surface is heated by a combination of laminar and jet convection and radiation.
    iii. Surface is cooled by a combination of laminar and jet convection for a short period of time, followed by free convection of air and surface radiation.
9. Substrate boundary conditions
    i. The substrate starts at ambient temperature before the powder is applied.
    ii. Substrate bottom node has a constant temperature as the table is water cooled (298 K).
10. The particles are nominally spherical and uniform in dimension.
11. The terminal velocity is reached almost instantaneously, based on Stokes' Law.
12. Hindered settling is incorporated due to high concentrations of tungsten carbide.

The material properties of the nickel and tungsten carbide are thermally dependent and are listed in Appendix B.

The standard conditions are listed in Table 5.4 and the code is found in Appendix C.

Table 5.4: Standard conditions for model operation

Parameter	*Value*
Particle diameter	150 μm
Plasma temperature	8 000 K
Particle temperature	2 650 K
Substrate temperature	298 K
Powder flow rate	0.45 g/s
Deposit thickness (stringer)	3 mm
Substrate thickness	10 mm
Number of preheat steps	5
Sphericity	1
Heat transfer coefficient plasma gas	1 200 W/m K
Heat transfer coefficient shielding gas	2 000 W/m K
Heat transfer coefficient air	1 000 W/m K

5.4 Discretization of the Equations

The following section describes the discretization procedure to solve for the temperature and the carbide concentration at each node. The discrete temperatures at each node is defined by ***T(t)*** (equation 5.26) for *n* nodes. The solution for the unknown ***T(t)*** is found by discretizing the spatial derivatives using finite difference approximation.

$$\vec{T}(t) = \{T_1(t), T_2(t), T_3(t), ...T_n(t)\} \tag{5.26}$$

The parabolic partial differential equation is transformed by the method of lines into an ordinary differential equation. In the general case, when $u_i=u(x_i,t)$, the PDE is discretized to achieve the form shown in equation 5.27.

$$\frac{du_i}{dt} = f_i(\underline{u}) \tag{5.27}$$

The full set of equations for the general case is discretized following the central difference formulation, shown in equation 5.28 with the boundary conditions for the 1st (node 0) and n^{th} (node n+1) nodes included.

$$\begin{aligned} &\frac{dT_i}{dt} = \alpha \frac{T_{j+1} - 2T_j + T_{j-1}}{\Delta x^2} \\ &where \\ &T_0 = T_{sub} \\ &T_{n+1} = T_{n-1} - 2\frac{h\Delta x(T_n - T_\infty)}{k} \end{aligned} \tag{5.28}$$

5.4.1 Tracking Concentration of Carbide

For every temperature time step, the concentration of carbide in each cell was tracked. A node was applied with a known volume fraction of carbide. The Reynolds number for the cell was calculated and the terminal velocity of the single particle in the cell according to Stokes' analysis was calculated according to equation 5.29. The drag coefficient is applicable for the intermediate values of Reynolds number – between 0.1 and 1000 (equation 5.30 [GRE2008]), which are within the range calculated for this problem. The hindered settling velocity was calculated according to Equation 2.8 and 2.9. The sphericity of the particle was kept at 1. The particle velocity for a cell was averaged with the velocity of the particle in surrounding nodes. This helps prevent static piling of the particles and allows voids to form and move. The distance the carbide progressed in a time step is calculated. The number of particles that move out of the current cell and into the cell below is determined and the profile tracked. If the cell below has reached the maximum packing fraction, no particles are permitted to leave the current cell as saturation has been achieved. The maximum particle concentration in a cell was determined experimentally based on the maximum packing for a specific carbide size range, described in Chapter 4. If the temperature of the cell

was less than the solidus, the velocity of the particle was set to 1e-10 m/s (no movement was permitted).

$$U_o = \left(\frac{4}{3} \frac{(1-\gamma) g d_p}{\gamma C_d} \right)^{0.5} \tag{5.29}$$

$$C_d = \frac{24}{\mathrm{Re}} \left(1 + 0.14\,\mathrm{Re}^{0.7}\right) \tag{5.30}$$

5.4.2 Solution Methodology and Convergence

The matrix of equations was solved using MATLAB based on the *ode45* solver. The code can be found in Appendix C. This built-in solver is based on an explicit Runge-Kutta (4,5) formula, and the Dormand-Prince pair. This technique uses six function evaluations to calculate the 4th- and 5th-order accurate solutions in order to minimize error in the fifth solution. As this problem is non-stiff, the most applicable solver is *ode45*. It is the default solver in MATLAB. The *ode45* technique is a one-step solver that computes the current solution based only on the solution at the immediately preceding time step.

The default error tolerances with *ode45* are a relative error tolerance and an absolute error tolerance. The relative error tolerance applies to all components of the solution vector and is a measure of the error relative to the size of each solution component. The default corresponds to 0.1% accuracy (1e-3). The absolute error tolerances apply to each component of the solution vector, and holds a value of 1e-6.

The convergence of the model was based on a comparison of solidification time in terms of nodes, shown in Figure 5.23. The solidification time increased drastically from 10 to 20 nodes. A steady plateau is seen after 50 nodes are applied. However, the size of the cell must be equal or greater than the particle size. Figure 5.24 shows the effect of the number of nodes on the cell size. If the number of nodes exceeds 20, than the cell size is smaller than the particle size.

To ensure good convergence, the model used a value of 80 nodes for all the simulations.

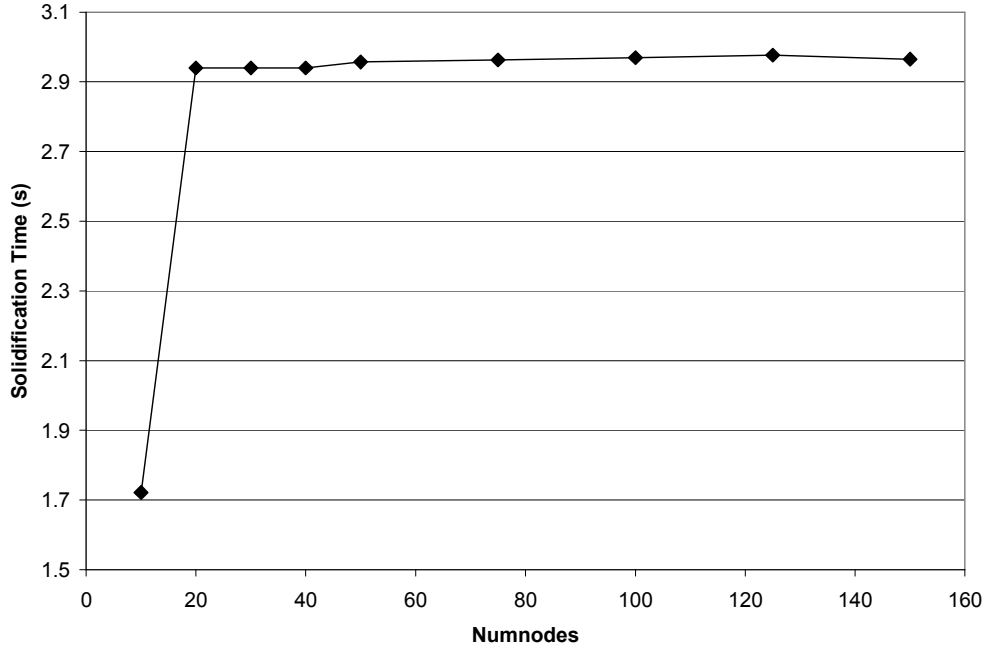

Figure 5.23: Convergence of model based on solidification time

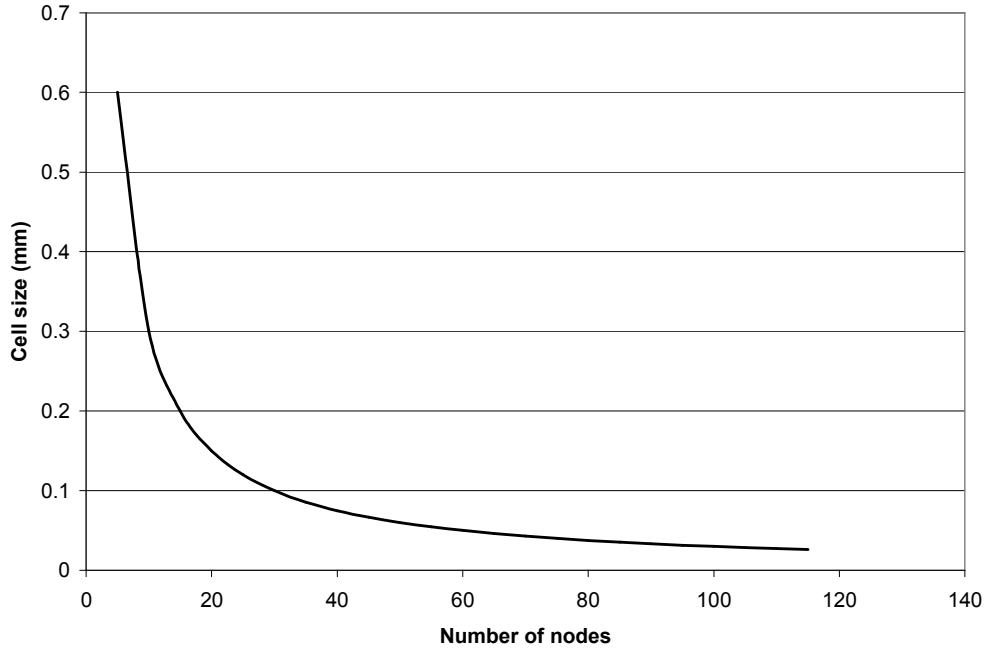

Figure 5.24: Relationship between cell size and number of nodes for a deposit thickness of 3 mm. The typical particle size is 0.15 mm.

The settling occurs at a faster rate than solidification. To accurately track the concentration changes, the settling program was run multiple times for every temperature time step. This label was named *tstepdiv* – the number of times the tracking of the concentration was called each time the temperature profile was calculated. Shown in Figure 5.25, is the convergence of the settling region for a 50 vol% WC MMC. There is little improvement in the settling profile after 100 divisions.

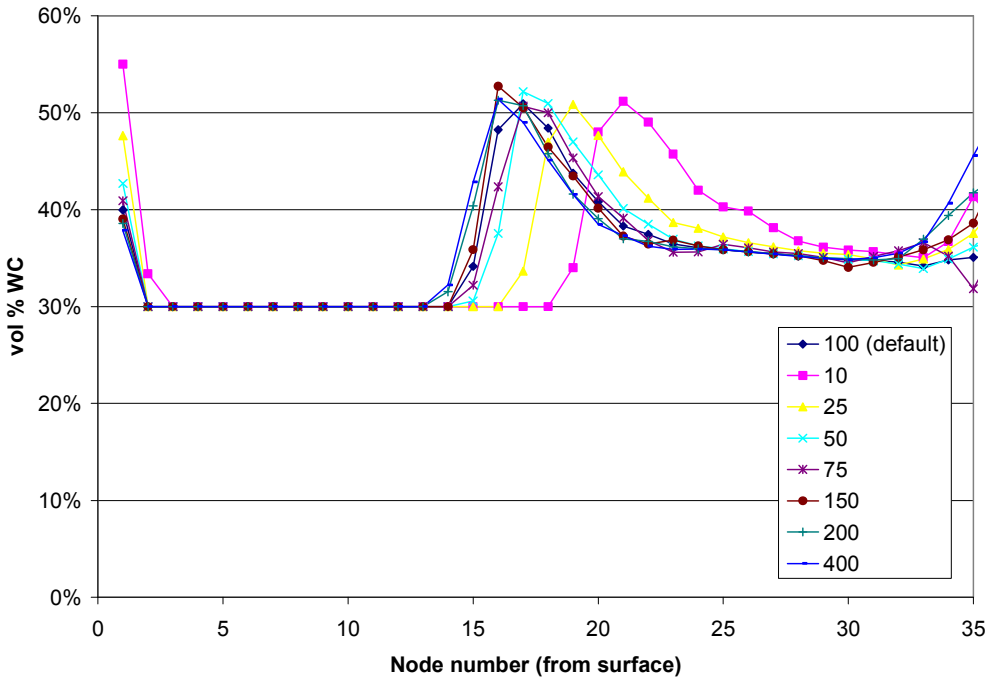

Figure 5.25: Convergence of tstepdiv as a function of the depth (number of nodes from surface) and size of the settling region.

5.5 Experimental Validation

The primary purpose of this work is to understand and predict which operating conditions yield improvements in carbide homogeneity. A significant portion of the experimental work quantified the carbide settling profiles of coatings deposited under varying conditions. One of the key experiments conducted measured the settling profile of coatings where the carbide volume fractions were increased from 10 to 50 vol% WC (Figure 4.12). The model was run under standard conditions while the initial carbide concentration was increased from 10

to 50 vol%. To validate the model, the settling profiles of the experiment should correlate well with the model output. This validation will now be presented.

5.5.1 Temperature Verification

Infrared temperature measurements of the surface of the deposit were captured during cooling and solidification of the deposit after the plasma arc was extinguished. These results further validate the model. Shown in Figure 5.26, are the experimental and predicted surface temperatures. The experimental measurements were captured only after the arc was extinguished. After the correction algorithm was applied to the raw data, the corrected temperatures (blue line, IR Temp Adj) and corresponding effective emissivities (green line, Effective Emissivity) are shown. The red line (Model surface temp) is the model prediction when the carbide concentration is 50v%, under standard modeling conditions. The pink line (Model substrate temp) is the temperature of top node of the substrate. The emissivity increases quickly while the surface is solidifying, followed by a plateau during solidification, and followed by another increase until the emissivity is constant at 0.7. The increase of emissivity from 0.47 and 0.7 is linear, as there was not sufficient experimental data to understand all the changes that occur at the solidus. A controlled experiment measuring the temperature and emissivity of the MMC would be appropriate to generate sufficient data. The collection of controlled measurements was not feasible within a welding process.

The red line is the model temperature of the top node under standard conditions. There is a small increase at the start due to the preheat phase, followed by the addition of the powder. The maximum temperature of 2 000 K of the top node corresponds to the time (0.66 s) when all the material was added. At that point, the plasma arc was effectively extinguished and cooling ensued. The first stage was cooling due to the shielding gas remaining on, after 200 time steps (approximately 1.5 s) the shielding gas was extinguished and cooling due to ambient still air and the fume hood vent continued. There is good agreement between the model and the experimental results up to the point where the coating

is solid (1.5 s). The cooling rate after this point does not match as well. The period after solidification is not critical to the model performance since no settling is occurring.

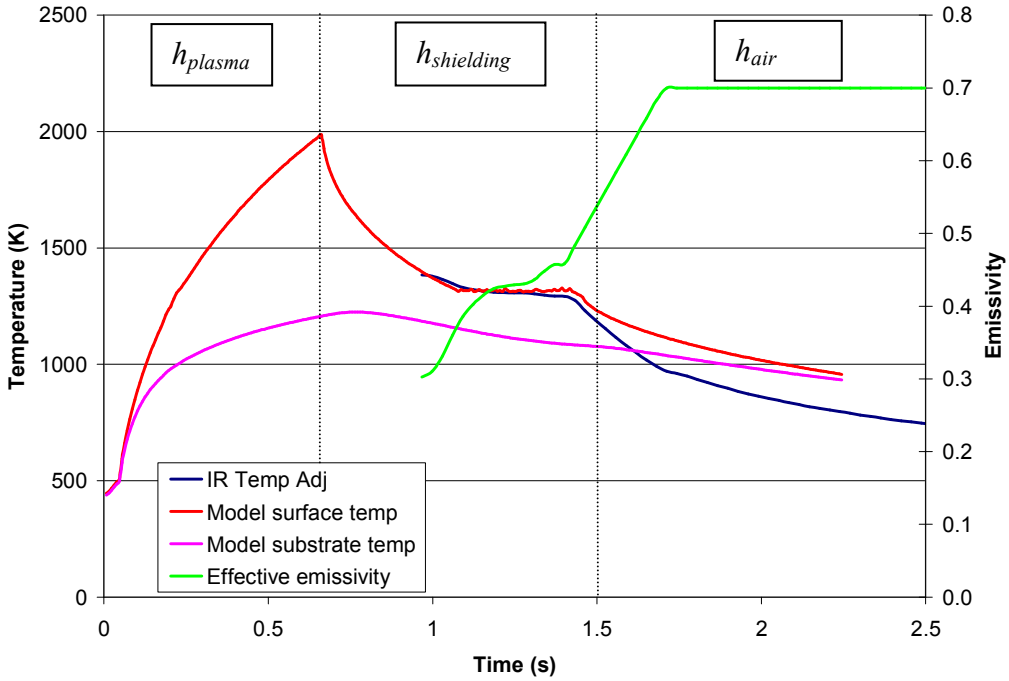

Figure 5.26: Experimental and predicted temperature results of the surface of the coating.

The temperature delta between the model and the experiment is shown in Figure 5.27. The comparison is not continuous since the temperature measurements were only collected after the arc was extinguished. The model and the experiment agree well within the shielding cooling phase. As soon as the shielding gas is switched off in the model, the error significantly increases.

The temperature of the top node of the substrate is shown in Figure 5.26 as the pink line. The temperature of the model at the substrate at the time when infrared data was collected is around 1 200 K. Shown in Figure 5.28 is an infrared image of the coating and substrate in the frame subsequent to the arc extinguishing. At the leading edge, the temperature of the steel substrate was measured using a

constant emissivity of 0.8 [OME2007]. The profile of the yellow line is shown in Figure 5.29. The maximum temperature of the substrate measured at the leading edge of the coating is 1 119 K. The maximum temperature calculated by the model is 1 224 K and is shown in the figure by the pink broken line. The predicted temperature of the top of the substrate is agrees well with the measured temperature. This also confirms that the coating freezes quickly since the substrate temperature is always less than the melting point of the matrix.

The following section will discuss the sensitivity of the operating parameters on the temperature profile and further justify the validity of the model and the choice of standard conditions.

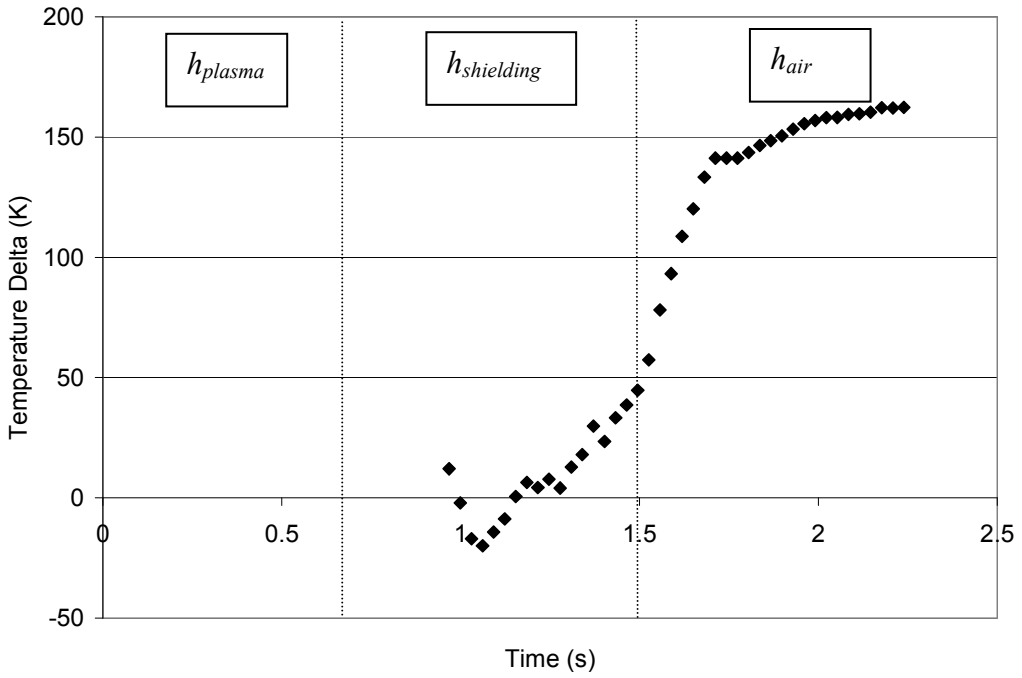

Figure 5.27: Temperature delta between model and experimental temperatures.

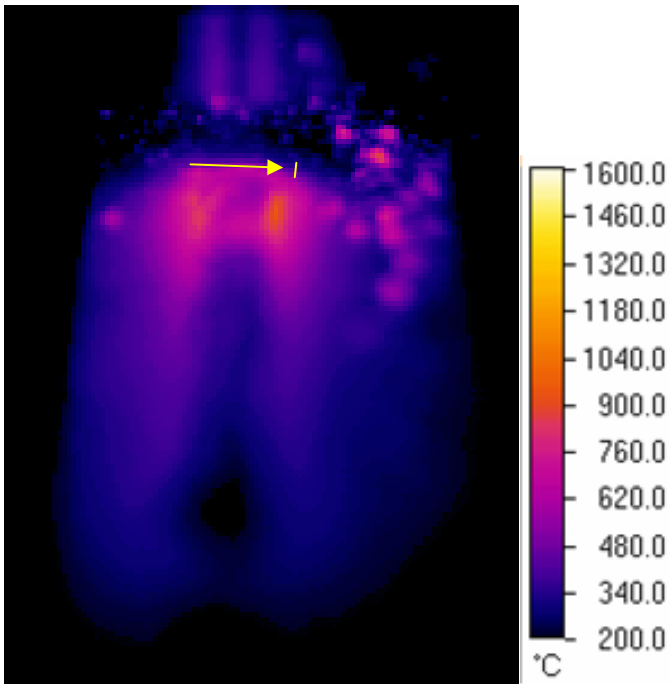

Figure 5.28: Infrared image immediately after arc is extinguished showing location of line profile of steel substrate at upper edge (6 pixels indicated by yellow arrow).

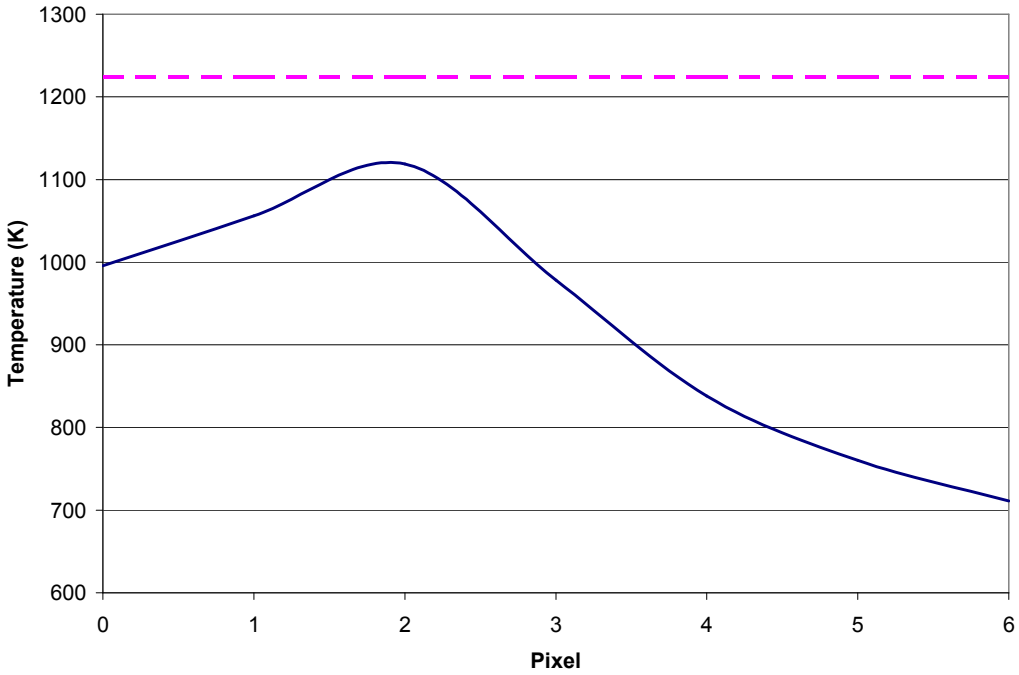

Figure 5.29: Temperature of steel substrate profile indicated in Figure 5.28

5.5.2 Sensitivity Analysis of Operating Parameters on Temperature Profile

To justify the parameters chosen for the standard conditions of the model and further validate the success of the model, a sensitivity analysis was conducted. The parameters chosen for the analysis are highlighted in Table 5.5. The range of carbide concentrations explored was from 10 to 50 vol% WC. The standard value was 50 vol% WC, since that is what is used industrially. The temperature of the plasma gas was changed by ±2 000 K. Although the models did not predict a temperature in the collimated region of 6 000 K, the particles are a stream and are subjected to a range of temperatures. The temperature of the incoming particles was adjusted by ±150 K. The range of the substrate temperature explored was 198 K to 398 K. A substrate cooled to 198 K is not industrially possible, but the effect of a cold substrate was sought. The value of the substrate thickness, powder feed rate and coating thickness was halved and doubled from the standard condition. The preheat was removed as well as extended to 100 time steps (0.75 s). The full range of the particle size was explored (50 μm to 300 μm). The sphericity was lowered from 1 (ideal sphere) to 0.6 and 0.8. A large range of heat transfer coefficients of both the plasma and shielding gases were explored.

Shown in Figure 5.30 is the variation in temperature profile with changes in carbide concentration. The bold brown broken line is the corrected infrared measurements at 50 vol% WC. The standard condition occurs with 50 vol% carbide, and matches the experiment results well. As the amount of carbide decreases, the peak temperature of the carbide decreases and the duration of the solidification plateau decreases (Table 5.6). The tungsten carbide has both a lower heat capacity and thermal conductivity than nickel. As the amount of carbide decreases, the ability for the MMC to disperse heat increases, therefore the cooling rate increases. As such, the peak temperature will be lower, as well as the time for cooling and the duration of the solidification. The maximum temperature of the surface decreased from 1986 K to 1767 K with a reduction in carbide from 50 vol% to 10 vol%. Over the same carbide range, the duration of the solidification region decreased from 0.34 s to 0.20 s.

Table 5.5: Values used for sensitivity analysis of temperature portion of the model

Mode	*Parameter*	*Standard*	*Sensitivity Limits*
Process	Plasma Gas Temperature (K)	8 000	6 000, 10 000
	Incoming Powder Temperature (K)	2 650	2 500, 2 800
	Substrate temperature (K)	298	198, 398
	Substrate thickness (m)	0.01	0.005, 0.02
	Powder feed rate (g/s)	0.45	0.225, 0.9
	Preheat steps	5	0, 25, 100
	Heat transfer coefficient (plasma)	1 200	600, 2400
	Heat transfer coefficient (shielding)	2 000	1000, 4000, 6000
Coating	Carbide concentration (%)	50	10, 20, 30, 40
	Coating thickness (m)	0.003	0.0015, 0.006
	Particle size (μm)	150	50, 300
	Sphericity	1	0.6, 0.8

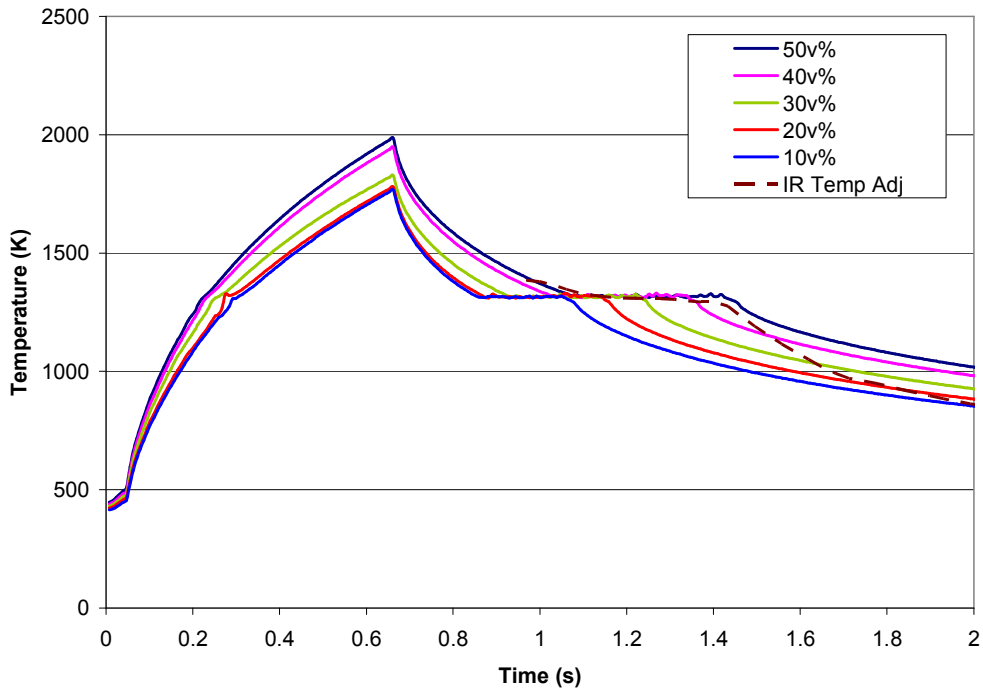

Figure 5.30: Change in temperature profile with decrease in carbide concentration. The standard condition is 50 vol% carbide.

Table 5.6: Peak temperature, corresponding time and duration of solidification for changes in carbide concentration.

Parameter	*Peak Temperature (K)*	*Corresponding Time (s)*	*Onset of solidification (s)*	*Duration of solidification (s)*
IR Temp Adj	-	-	1.09	0.31
50v%	1986	0.66	1.09	0.34
40v%	1947	0.66	1.04	0.31
30v%	1828	0.66	0.94	0.30
20v%	1780	0.66	0.87	0.28
10v%	1767	0.66	0.86	0.20

Adding more heat into the powder, either by increasing the temperature of the plasma gas or increasing the temperature of the incoming powder, increases the maximum coating temperature and the duration of the solidification time (Figure 5.31 and Table 5.7). In terms of the process, these increases can be brought about by increasing the current or voltage. It should be noted that increasing the current and voltage result in different plasma arc heat input profiles [NES1962]. Increasing the current raises the peak of the heat input distribution curve, but also widens the distribution. This will heat more of the shielding gas and the substrate. The increase in temperature of the shielding gas and substrate due to increasing the plasma gas temperature was not accounted for in the model. The higher the maximum powder temperature, the longer the time required to cool to the liquidus temperature and thus, more time is available for carbide settling. Increasing the voltage is attained by increasing the stand-off distance between the electrode and the substrate. As the distance is increased, only the peak of the heat intensity curve is increased. Thus, the heat intensity profile becomes more collimated.

As discussed in Section 4.5.1 regarding Arc Shape, the work of Wilden et al. [WIL2006] revealed that a higher plasma gas flow rate increases the gas velocity and collimation of the arc. The maximum temperature of the arc decreased, however, due to the collimation, the temperature gradient at the substrate surface increased. The model assumed that the velocity of the plasma gas was constant when the temperature increased. If the plasma gas velocity increased, then the

incoming particle velocity would also increase and the time for heating would decrease. Increasing plasma gas velocity does not have the same effect on the arc temperature and velocity as increasing arc power (current and voltage).

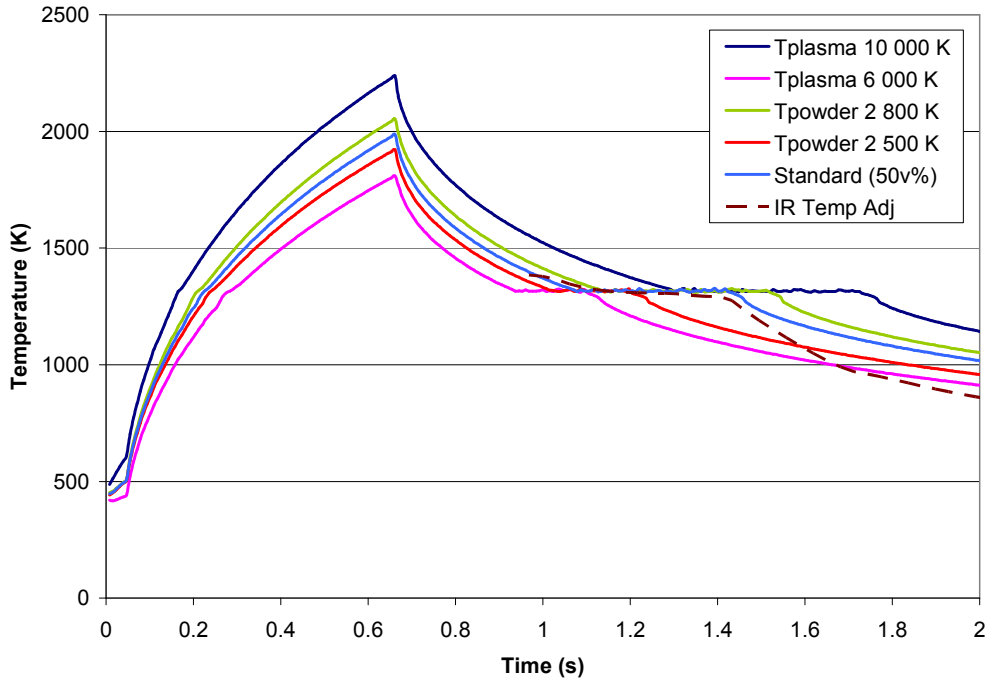

Figure 5.31: Change in temperature profile with changes in temperature of plasma gas and incoming particles.

Table 5.7: Peak temperature, corresponding time and duration of solidification for changes in plasma gas temperature and incoming particle temperature.

Parameter	*Peak Temperature (K)*	*Corresponding Time (s)*	*Onset of solidification (s)*	*Duration of solidification (s)*
Standard (50v%)	1986	0.66	1.09	0.34
Tplasma 10 000 K	2237	0.66	1.30	0.43
Tplasma 6 000 K	1809	0.66	0.93	0.17
Tpowder 2 800 K	2053	0.66	1.12	0.40
Tpowder 2 500 K	1927	0.66	1.02	0.20

Increasing the temperature of the substrate by 100K has a profound effect on the solidification time (Figure 5.32). Although the maximum temperature is not significantly affected, the heat is not dissipated through the substrate at a rate as

quickly as the standard conditions. Thus, the duration of the solidification plateau is increased from 0.34 s to 0.63 s (Table 5.8). In addition, the time to reach the liquidus has increased. Reducing the temperature of the substrate by 100 K reduces the time to reach the liquidus by over 0.1 s and the duration of the solidification plateau to 0.2 s. The effects of altering the thickness of the substrate are only revealed in the duration of the solidification plateau. Both increasing and decreasing the substrate thickness resulted in a decrease in the solidification time. By reducing the substrate thickness, the heat flow due to the isothermal substrate bottom is increased. Increasing the substrate thickness results in increasing the thermal mass of the system, so more heat is absorbed into the substrate.

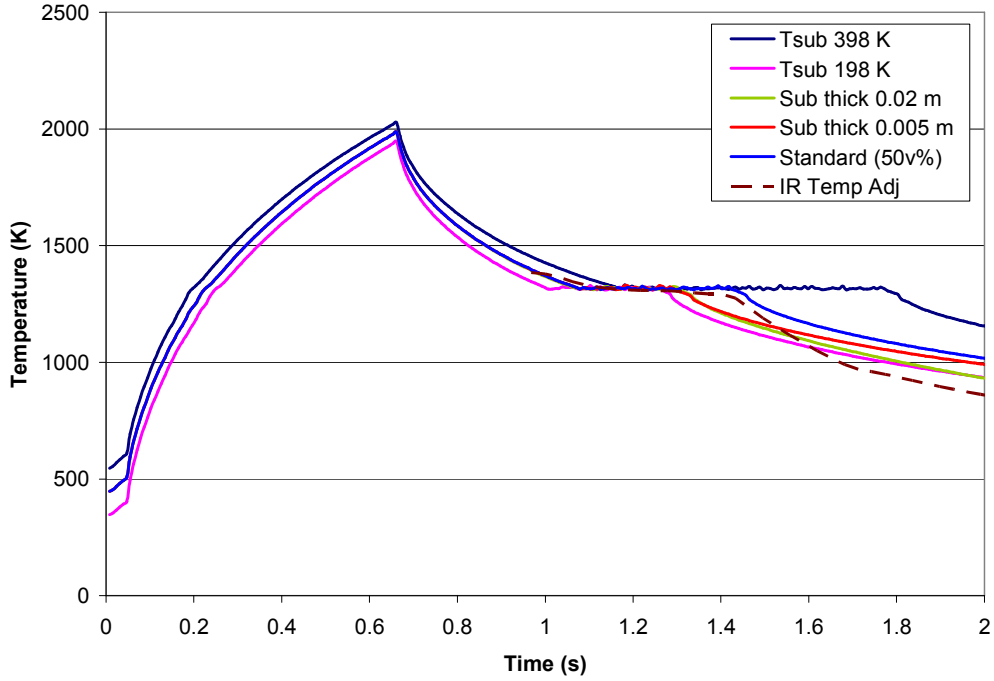

Figure 5.32: Change in temperature profile with changes in temperature of substrate and substrate thickness.

Table 5.8: Peak temperature, corresponding time and duration of solidification for changes in substrate temperature and thickness.

Parameter	*Peak Temperature (K)*	*Corresponding Time (s)*	*Onset of solidification (s)*	*Duration of solidification (s)*
Standard (50v%)	1986	0.66	1.09	0.34
Tsub 398 K	2028	0.66	1.15	0.63
Tsub 198 K	1947	0.66	1.02	0.26
Sub thick 0.02 m	1986	0.66	1.08	0.23
Sub thick 0.005 m	1986	0.66	1.08	0.23

Increasing the powder feed rate decreases the time required for deposition of the coating, increases the maximum surface temperature to 2105 K and decreases the duration of the solidification plateau to 0.22 s (Figure 5.33 and Table 5.9). Because the coating is deposited so quickly, less heat is absorbed into the substrate. This is due to the fact that the heat remains in the deposit and has yet to conduct into the substrate. The cooler substrate acts as a larger heat sink and increases the cooling rate of the deposit, thus, a shorter solidification plateau. A lower powder feed rate requires a longer time for deposition, but results in a lower maximum temperature. This is because there was sufficient time for the heat in the coating to conduct downwards into the substrate. Since the substrate temperature is hotter, the duration of the solidification plateau increased. Also shown in this figure is a reduction in the thickness of the coating. A thinner coating has a lower maximum substrate temperature, a very short solidification time and a rapid cooling of the solid. Less powder deposited results in less heat transfer into the coating thus a lower overall temperature of both the coating and the substrate. A lower overall substrate temperature will decrease the duration of the solidification plateau. The thinner coating will cool faster as there is less distance for heat to conduct from the substrate centre. A thicker coating will result in a higher maximum temperature and a significantly longer deposition time. The cooling time required for a thick coating was so lengthy compared to the standard run that the duration of the solidification plateau was not even considered.

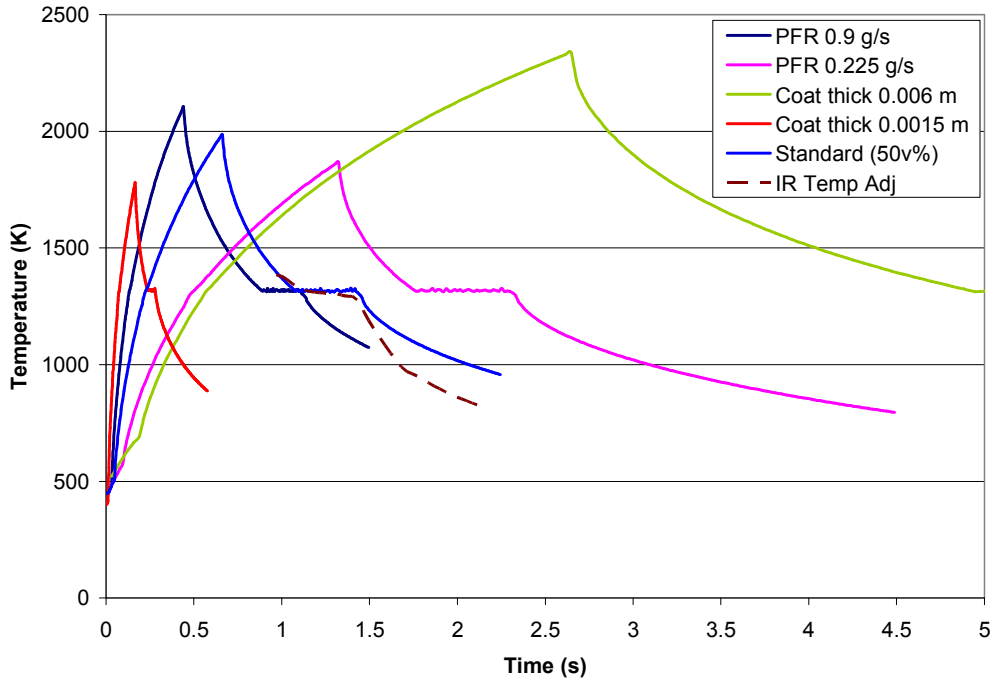

Figure 5.33: Change in temperature profile with changes in powder feed rate and the thickness of the deposit.

Table 5.9: Peak temperature, corresponding time and duration of solidification for changes in powder feed rate and the thickness of the deposit.

Parameter	*Peak Temperature (K)*	*Corresponding Time (s)*	*Onset of solidification (s)*	*Duration of solidification (s)*
Standard (50v%)	1986	0.66	1.09	0.34
PFR 0.9 g/s	2105	0.44	0.91	0.22
PFR 0.225 g/s	1870	1.32	1.78	0.54
Coat thick 0.006 m	2338	2.65	4.95	-
Coat thick 0.0015 m	1788	0.16	0.23	0.05

The effect of the amount of preheat was investigated in terms of no preheat, 0.25 s of preheat (25 steps) and 0.75 s of preheat. Shown in Figure 5.34, less preheat reduces the maximum surface temperature and the duration of the solidification plateau (Table 5.10). More heat is added to the system with the inclusion of preheat which takes time to remove.

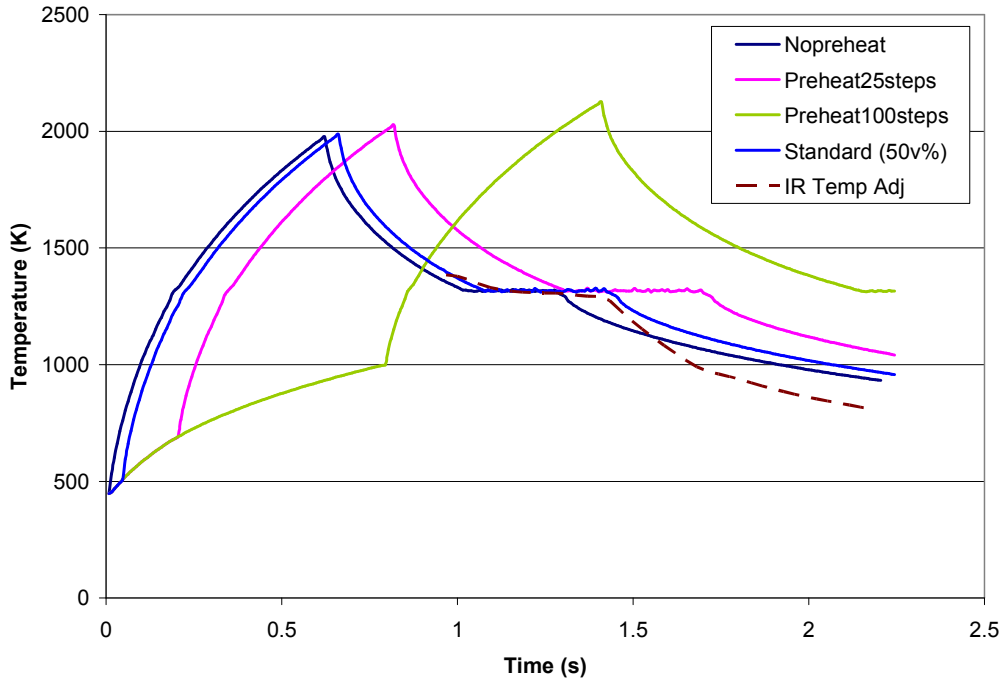

Figure 5.34: Change in temperature profile with changes in the amount of preheat before powder is deposited.

Table 5.10: Peak temperature, corresponding time and duration of solidification for changes in the amount of preheat before powder is deposited.

Parameter	*Peak Temperature (K)*	*Corresponding Time (s)*	*Onset of solidification (s)*	*Duration of solidification (s)*
Standard (50v%)	1986	0.66	1.09	0.34
No preheat	1976	0.62	1.02	0.29
Preheat 25 steps	2027	0.82	1.31	0.39
Preheat 100 steps	2125	1.41	2.15	-

The effect of the particle diameter and shape was investigated, and the results are shown in Figure 5.35. There is very little effect on the thermal profile, with the exception of a small decrease in the duration of the solidification plateau with a decrease in the particle size and shape irregularity of the particle (Table 5.11). A smaller particle size will conduct heat at a faster rate than a larger carbide particle. This conveyance of heat will reduce the duration of the solidification plateau.

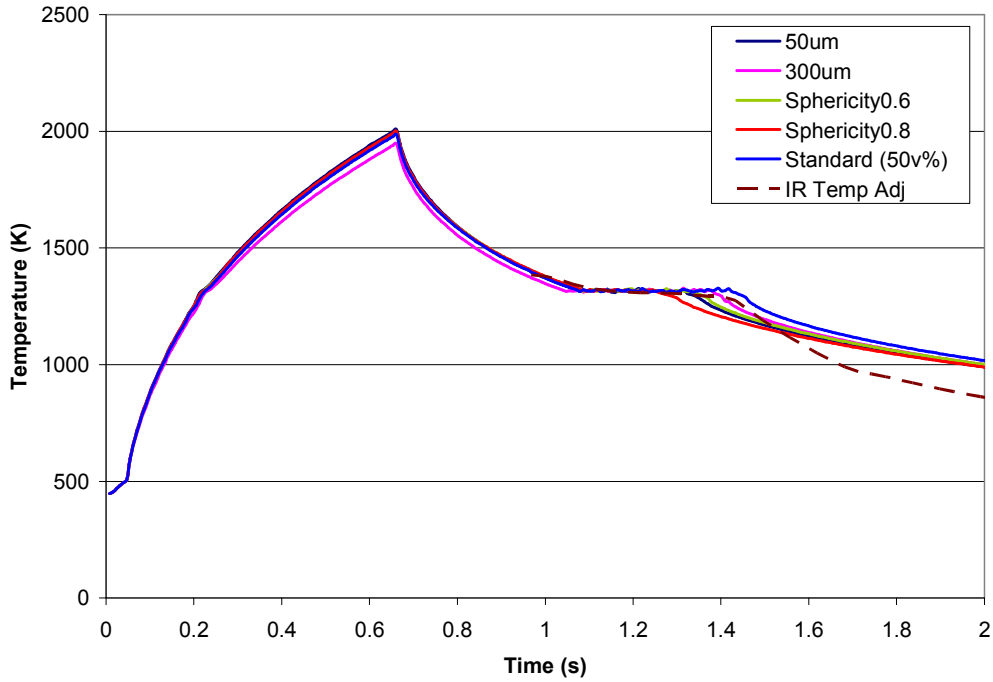

Figure 5.35: Change in temperature profile with changes in particle diameter.

Table 5.11: Peak temperature, corresponding time and duration of solidification for changes in particle diameter.

Parameter	*Peak Temperature (K)*	*Corresponding Time (s)*	*Onset of solidification (s)*	*Duration of solidification (s)*
Standard (50v%)	1986	0.66	1.09	0.34
50µm	2008	0.66	1.06	0.27
300µm	1947	0.66	1.02	0.36
Sphericity0.6	1995	0.66	1.07	0.28
Sphericity0.8	2000	0.66	1.07	0.20

The effect of the heat transfer coefficient on the cooling profile of the deposit is shown in Figure 5.36. Doubling the heat transfer coefficient of the plasma gas to 2400 W/m K has little effect on the profile. This is because the temperature of the plasma is so hot that the increase in *h* has little bearing on the deposit temperature. Reducing the heat transfer coefficient by half to 600 W/m K has a more significant effect. The maximum surface temperature is lower by 160 K and the duration of the solidification plateau has decreased by 0.14 s (Table 5.12). It

appears there is a threshold in *h* of the plasma whereby insufficient heat is transferred into the deposit and subsequently the substrate.

The effect of the heat transfer coefficient of the shielding gas is also shown in Figure 5.36. Lowering the *h* of the shielding gas to 1000 W/m K has little effect on the cooling profile, with the exception that the onset of solidification is delayed slightly as less heat is being removed from the deposit surface. However, increasing the shielding gas heat transfer coefficient to 4000 W/m K or 6000 W/m K the standard value acts to increase the cooling rate, decrease the onset of solidification and decrease the duration of the solidification plateau (Table 5.12). It can be seen that the change between the shielding gas and air occurs just after 1.4 s, located with a change in slope of the cooling curve. This was not apparent with the standard run as the completion of solidification occurred at the same time. However, increasing the heat transfer coefficients to such high levels do not duplicate the temperature measurements obtained by the infrared camera.

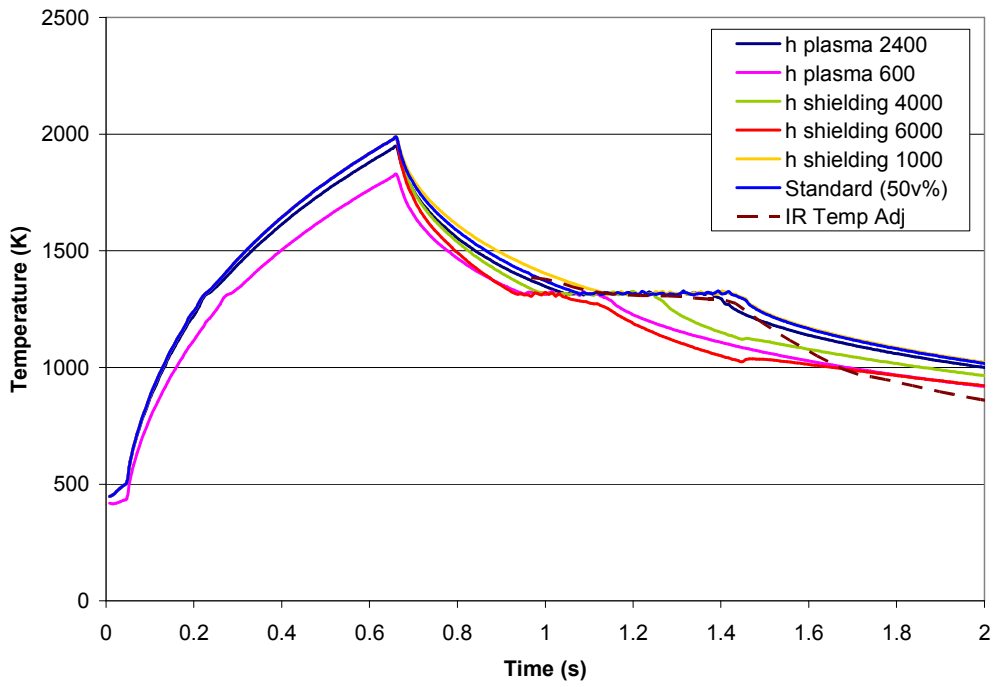

Figure 5.36: Change in temperature profile with changes in heat transfer coefficient of the plasma gas and shielding gas.

Table 5.12: Peak temperature, corresponding time and duration of solidification for changes in heat transfer coefficient of the plasma gas and shielding gas.

Parameter	*Peak Temperature (K)*	*Corresponding Time (s)*	*Onset of solidification (s)*	*Duration of solidification (s)*
50v% (standard)	1986	0.66	1.09	0.34
h plasma 2400	1947	0.66	1.02	0.36
h plasma 600	1827	0.66	0.93	0.20
h shielding 4000	1986	0.66	0.98	0.28
h shielding 6000	1986	0.66	0.92	0.12
h shielding 1000	1986	0.66	1.11	0.33

5.5.3 Analysis of Sensitivity Results

The qualitative results of the sensitivity analysis are summarized in Table 5.13 in terms of changes of the cooling profile of the deposit. The points of interest of the cooling profile are the maximum temperature obtained, the time of the onset of solidification, the duration of the solidification plateau and the slope of the cooling rate after solidification is complete. The severity of the value is indicated by the direction of the arrow and the percent change. The factors which reduce the solidification time, that is, have less time to the onset of solidification and a shorter time for solidification will allow for less particle settling and a more homogeneous deposit, and are highlighted in red. Those factors which indicated faster solidification are:

- lower vol % WC
- lower plasma temperature
- decreasing coating thickness
- significant increase in shielding gas heat transfer coefficient.

The effect of these parameters on the homogeneity will be investigated in the following chapter.

Table 5.13: Summary of sensitivity of modifying model parameters on temperature profile of coating

Parameter	*Maximum Temperature*	*Onset of solidification*	*Duration of solidification*	*Cooling Rate after solidification*
10 vol% WC	↓ 11%	↓ 21%	↓ 41%	-
20 vol% WC	↓ 10%	↓ 21%	↓ 18%	-
30 vol% WC	↓ 8%	↓ 14%	↓ 12%	-
40 vol% WC	↓ 2%	↓ 5%	↓ 9%	-
Plasma Temp ↑	↑ 13%	↑ 19%	↑ 26%	-
Plasma Temp ↓	↓ 9%	↓ 15%	↓ 50%	-
Powder Temp↑	↑ 3%	↑ 3%	↑ 18%	-
Powder Temp↓	↓ 3%	↓ 6%	↓ 41%	-
Substrate Temp↑	↑ 2%	↑ 6%	↑ 85%	-
Substrate Temp↓	↓ 2%	↓ 6%	↓ 23%	-
Substrate Thickness↑	-	-	↓ 32%	-
Substrate Thickness↓	-	-	↓ 32%	-
Powder Feed Rate↑	↑ 6%	↓ 17%	↓ 35%	-
Powder Feed Rate↓	↓ 6%	↑ 63%	↑ 59%	-
Coating thickness↑	↑ 13%	↑ 354%	?	?
Coating thickness↓	↓ 10%	↓ 79%	↓ 85%	↓↓
No preheat	↓ 0.5%	↓ 6%	↓ 15%	-
Preheat↑	↑ 2%	↑ 20%	↑ 15%	-
Preheat↑↑	↑ 7%	↑ 97%	?	?
Particle size↑	↑ 1%	↓ 3%	↓ 20%	-
Particle size↓	↓ 2%	↓ 6%	↑ 6%	-
Sphericity↓	↑ 0.5%	↓ 2%	↓ 18%	-
Sphericity↓↓	↑ 0.7%	↓ 2%	↓ 41%	-
h plasma↑	↓ 2%	↓ 6%	↑ 6%	-
h plasma↓	↓ 8%	↓ 15%	↓ 41%	-
h shielding↓	-	↑ 2%	↓ 3%	-
h shielding↑	-	↓ 10%	↓ 18%	↓
h shielding↑↑	-	↓ 16%	↓ 65%	↓

It should be stated that the model was intended to predict MMC homogeneity, and it will be shown in the following section that the correlation between the experiment and the model is very good. However, there are other factors shown

in Figure 5.26 which reinforce the validity of the thermal portion of model up to full solidification. The duration of the solidification from liquid to solid of the model matches that of the experiment. The solidification occurs in less than 0.5 s, 1 s after the arc is extinguished. Thus, the onset of solidification and the duration of solidification plateau agree.

The value of the incoming temperature of the powder in the solidification model was 2 650 K. The calculations from section 5.1.2.2 estimated that the powder temperature should be between 2 800 K and 3 200 K. These calculations were based on only one particle heating in the gas, whereas there is a steady stream. Thus, the incoming temperature should be lower. However, if the temperature of the incoming particles were increased, the maximum temperature of the top node would increase, the time to onset of solidification would increase and the duration of the solidification plateau would increase. The model fit with the experimental results would no longer be agreeable.

The portion of the model which does not agree well occurs after solidification is complete and the particles are no longer permitted to settle. The heat transfer coefficients for the shielding gas and ambient air, estimated in sections 5.1.1.2 and 5.1.1.3, were no greater than 1600 and 400 W/m K respectively. The model used a heat transfer coefficient of 2000 and 1000 W/m K for shielding gas and air, respectively, which is significantly more than estimated. Since the cooling portion was not matching the experimental results, it was thought that increasing the shielding gas would increase the rate of cooling. However, it was seen that the duration the shielding gas is on ends at full solidification of the deposit. According to the model, the solid is cooled only by air. Increasing the shielding gas heat transfer coefficient acts to speed up the time for onset of solidification and the decrease the duration of solidification. Altering the shielding gas heat transfer coefficient does not improve the correlation between the model and experiment for the cooling portion of the curve. The values necessary to obtain a cooling rate similar to the experimental results are not achievable with the PTAW

equipment. It is conceivable that once full solidification of the deposit is attained that cooling from the sides increases the cooling rate. Also, according to the sensitivity analysis, decreasing the thickness of the deposit by half obtained a cooling rate similar to that seen by the experimental measurements. This indicates that cooling may have a significant 2-dimensional component after solidification.

It was noted in the modeling performed by Murugan et al. [MUR1999] that only during the cooling phases did the temperature of the prediction deviate from the experiments. It was suggested that the combination of heat losses by convection and radiation as well as differences in thermal properties were the contributors to the deviation in the model. Similarly, Ravichandran [RAV2001] experienced lower cooling rates in the model than seen with experiments of keyhole welding by plasma arc welding. The deviation was attributed to higher heat losses than accounted for in the model, uncertainties in material properties and assuming zero velocity of the liquid metal. Zhu and Chao [ZHU2002] suggested that using the correct thermal conductivity has more of an effect on the prediction of transient temperature distributions during welding than density or specific heat. Since the thermal properties of the MMC were taken only as nickel, it can be implied that further enhancements to the model can be implemented with improvements in the thermal properties.

The amount of convective heat transfer by the shielding gas was estimated to be proportional to the temperature of the plasma gas temperature to the power of 1.9 [EVA1998]. If the temperature of the plasma gas were to increase by 2 000 K, the heat of convection would increase by 5%. These changes in convective heat transfer coefficients were not considered in the sensitivity analysis and may have an effect on the modeled cooling rate.

5.5.4 Settling Verification

Experimental and model predictions are shown in Figure 5.37 for 40-50 vol% WC and in Figure 5.38 for 10-30 vol% WC. There is very good agreement between the settling of the particles based on concentration from the model (solid line) and the experiment (marker). The region near the substrate (approaching 100% depth) has a reduced value of carbide since the matrix freezes very quickly and does not allow for particles to settle. The model shows a decrease in carbide near the substrate surface, although not to the degree as the experimental results. As the concentration of carbide is increased towards 50 vol%, the deposit becomes fully packed. The metallographic images of the coatings containing 10 to 50 vol% are shown in Figure 4.11. It is clearly shown that the height of the fully packed region increases with carbide fraction. Thus, the higher the volume fraction of carbide, the greater the coating homogeneity. At 40 vol% WC, the coating is almost homogeneous. When the carbide amount reached 50 vol%, the coating is fully homogeneous, except for the upper 10% of the depth. At 50 vol% WC, circular regions void of carbide can occur. This is due to a metallurgical reaction between the carbide and the matrix that is only seen with carbide fractions greater than 50 vol% WC.

The model agrees very well for carbide concentrations of 40 and 50 vol% (Figure 5.37). The surface is depleted of carbide until approximately 15% of the depth from the surface, at which point the remainder of the deposit is fairly homogeneous. Near the substrate, both the model and experimental results reveal that the amount of carbide is reduced. As previously indicated, this is a result of the quick solidification of the MMC as it is deposited onto the substrate. For carbide concentrations of 50 vol%, the fully packed concentration of 55% is achieved for most of the depth in both the experiment and the model prediction. When the concentration is reduced to 40 vol%, the fully packed concentration is not achieved by the experimental results and for the majority of the model results. This occurs because the material solidifies before settling can achieve the fully packed status.

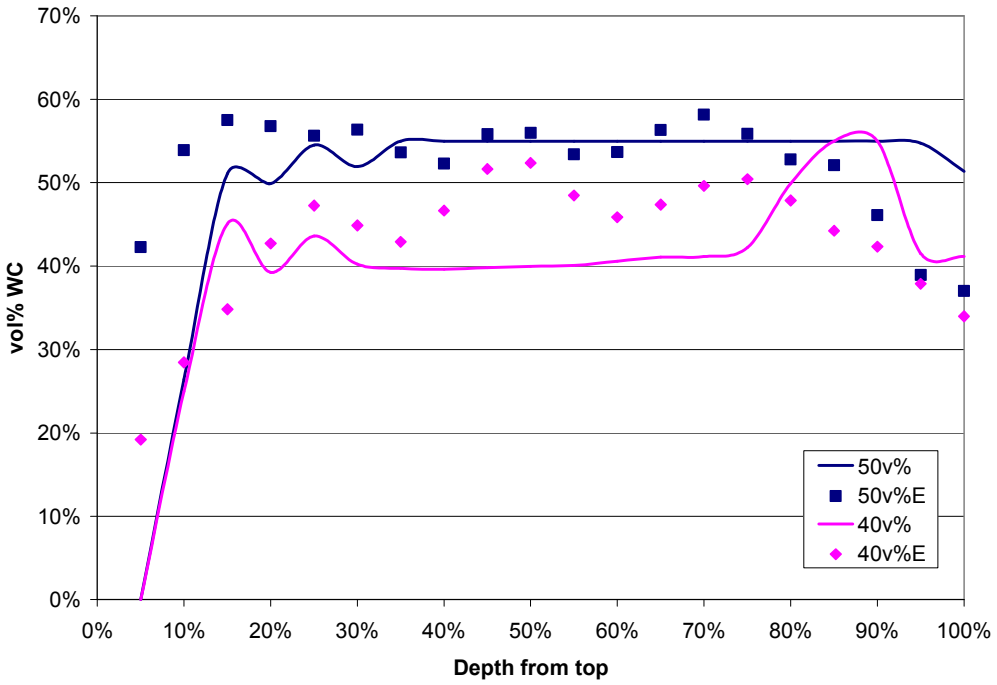

Figure 5.37: Model and experimental results for 40 and 50 v% WC. The experimental results are the points and indicated in the legend by an E.

Near the deposit surface, the model indicates a periodic change in the amount of carbide. According to the model code, as the matrix solidifies in one cell no more carbide is permitted to enter. This results in an instantaneous pile-up of carbide which is not alleviated as the solidification front passes. The hindered settling equation is in the form of an exponential decay. As the carbide concentration decreases, the velocity is more sensitive to changes in concentration. As such, greater fluctuations will occur. The oscillatory behaviour was also seen in packing simulation of spheres of high particle concentration and was attributed to particle packing [CAS1998].

As the carbide level is reduced to 30 vol% and below (Figure 5.38), there is some deviation between the model and the experiment, however the trend is consistent. The depth at which the carbide concentration exceeds 10 vol% for both the model and experiment occurs at approximately 30%, 45% and 60% for 30 vol% WC, 20 vol% WC and 10 vol% WC respectively. The maximum carbide concentration

occurs at 50% of the depth for both the model and experiment with 30 vol%, but decreases to 70% for 20 vol% WC and between 70-80% for 10 vol% WC. The volume percent of carbide at the peak decreases from 50 vol% to 45 vol% to 35 vol% as the initial carbide concentration decreases from 30 to 20 to 10 vol%. At the substrate interface, the initial carbide concentration is maintained. This is because the substrate is colder than the liquid MMC, thus causing the coating to solidify rapidly and not permitting any carbide to settle.

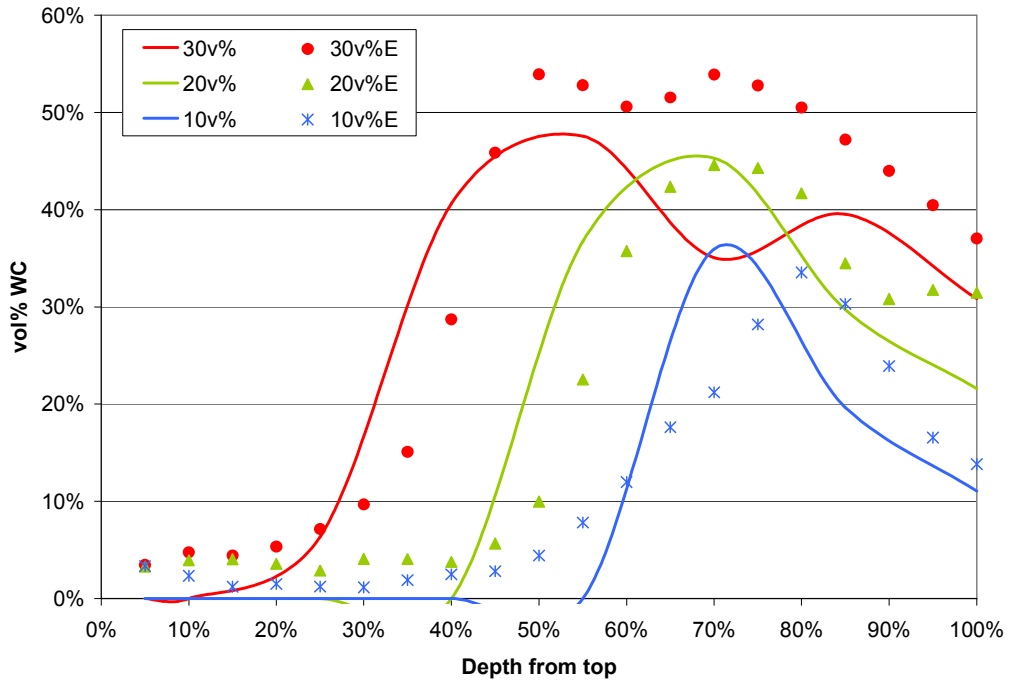

Figure 5.38: Model and experimental results for 10 to 30 vol% WC. The experimental results are the points and indicated in the legend by an E.

The depth of the settling region at the surface gets larger as the carbide concentration decreases. This clearly illustrates from both experiments and model results that there is significant particle settling occurring. The region adjacent to the substrate which depicts a reduction in carbide is also apparent in both the model and the experiment. The model underestimates the amount of carbide at the surface, indicating that the settling is occurring at a slightly faster rate than occurs experimentally. Note that some of the differences between model and

experiments may be due to the particle size of the WC. The particle diameter of the carbide in the model is uniform, whereas the range of carbide in the powder is 50 μm to 300 μm. Larger particles have more mass and will settle at a rate faster than the 150 μm particles used in the model. Thus, the carbide concentration would be higher nearer to the substrate surface. Likewise, smaller particles settle a rate slower than the standard and would occupy a higher concentration near the surface. The effect of particle size will be further explored in the next chapter.

5.6 Chapter Summary

A one dimensional coupled model of solidification of an MMC with particle settling was developed. The MMC consisted of high volume fraction of WC in a nickel alloy matrix, deposited by plasma transfer arc welding. Experiments were carried out to validate the model. Images of the deposit and the volume fraction of the WC in the deposit were quantified as a function of deposit depth. The model had very good agreement with the experimental results of the homogeneity of the carbide as a function of depth. This fundamental model was able to accurately predict the particle homogeneity of an MMC deposited by an extremely complicated process. It was shown that the most important variable leading to a homogeneous coating is to operate at the packing saturation limit of the reinforcement. In the case of the MMC explored, a fully homogeneous coating was obtained with 50 vol% WC in a NiCrBSi matrix.

The next chapter explores the parameters which yield improvements in homogeneity using the model.

6 Prediction of Homogeneity using Modeling

This section utilizes the model developed in the previous chapter in order to predict conditions which yield an improvement in coating homogeneity. The model was run with a carbide concentration of 50 vol% carbide and 30 vol% carbide. The fully packed MMC was chosen in order to determine what operational improvements could be made to eliminate the settling region at the surface. The conditions which decreased the size of the settling region were used on a 30 vol% MMC. At a lower level of carbide, changes in size of the settling region are more apparent. If a fully homogeneous coating could be obtained with a lower carbide fraction, significant cost savings could be obtained.

The effects of carbide settling on MMC systems where the density difference between the reinforcement particle and matrix were minimized was explored. Two systems were considered: an Al-B_4C and a Ni-Cr_3C_2 system. The density of the liquid and the carbide are similar and significantly lower than the Ni-WC MMC in the case of the Al-B_4C. The densities Cr_3C_2 is lower than the Ni to simulate carbide floating.

Finally, the model was expanded to allow for a second pass of MMC over a fully solidified coating and partially cooled substrate. The elimination of the settling region due to remelting and subsequent settling of WC from the second pass into the first pass results in a minor improvement in coating homogeneity.

6.1 Optimization of a 50 vol% WC MMC

For a MMC with 50 vol% carbide, the size of the settling region was calculated from the model results under a variety of operating parameters. Shown in Figure 6.1 are the sizes of the settling region for carbide volume fractions ranging from 10 vol% to 50 vol%. The size of the settling region is measured to the point where the carbide volume fraction exceeds the overall carbide vol%. The most

homogeneous coatings are obtained with a carbide fraction amount of 50 vol%, which is just under the fully packed ratio of carbide. As the carbide level decreases, the size of the settling region grows substantially to 60% at 10 vol% WC. A 600% increase in the size of the settling region occurs over the range of carbide volume fractions explored.

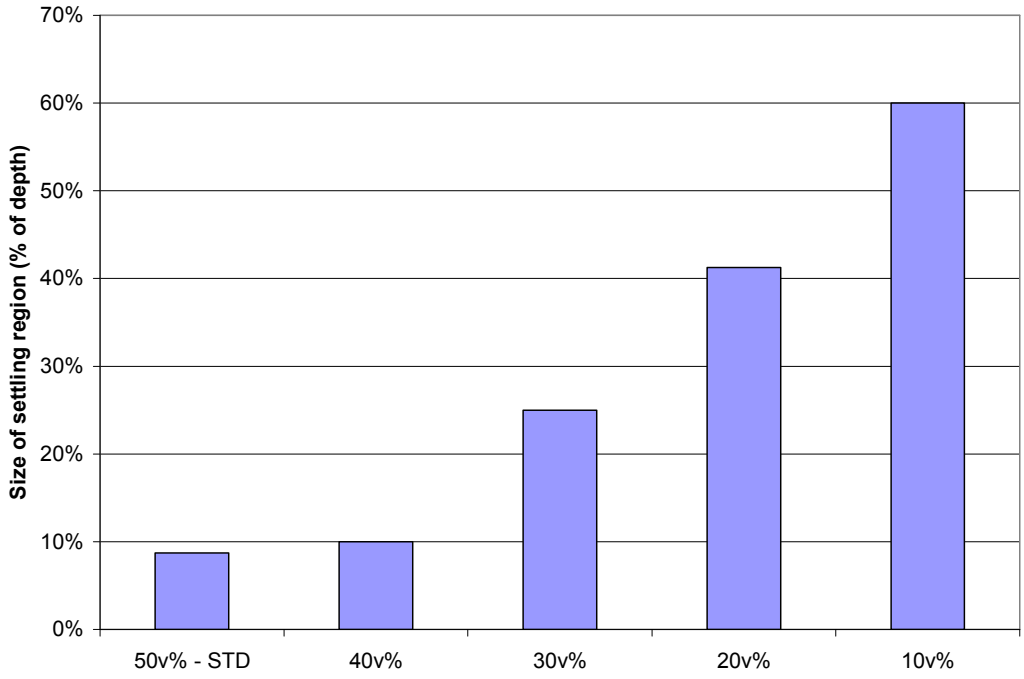

Figure 6.1: Size of settling region for changes in amount of carbide.

The effect of plasma temperature and incoming particle temperature on the carbide profile is shown in Figure 6.2. Both lowering the plasma temperature and the incoming particle temperature improve homogeneity. Reducing the plasma temperature by 2 000 K improves the homogeneity at a level slightly more than reducing the incoming particle temperature by 150 K. The thermal portion of the model indicated that reducing these temperatures result in a decrease of the time to the onset of solidification and a decrease in the duration of the solidification plateau. A decrease in one or either of these two times will allow for less settling of the carbides and a more homogeneous coating. Shown in Figure 6.3, are the sizes of the settling region. A lower plasma gas temperature reduces the size of

the settling region by 30%, from 8.75% to 6.25% of the depth. Similarly, lowering the incoming particle temperature reduces the settling region size by less than 15%, from 8.75% to 7.5% of the depth. In terms of welding operating parameters, the plasma temperature and incoming particle temperature can be reduced by lowering the plasma gas flow, the current and/or the voltage. To account for changes in current in the model, it was shown that the temperature of the plasma gas varies with current according to equation 6.1 [EVA1998]. This empirical relationship states that a drop in plasma temperature from 10 000K to 8000K (2000K) represents a decrease in the current by a factor of 0.92. For example, if the current for the higher plasma arc was 100 A, the cooler arc would have a current of 92 A.

$$T_{plasma} \propto I^{0.3} \tag{6.1}$$

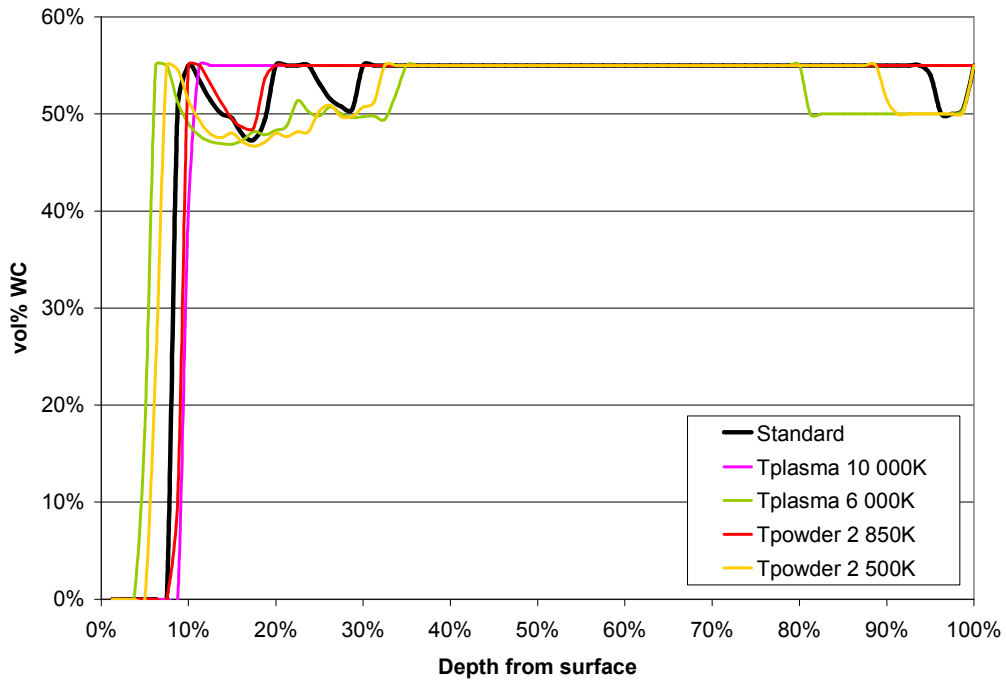

Figure 6.2: Carbide concentration profile due to changes in temperature of the plasma gas and the incoming particles. Initial concentration of carbide is 50 vol% WC in Ni alloy.

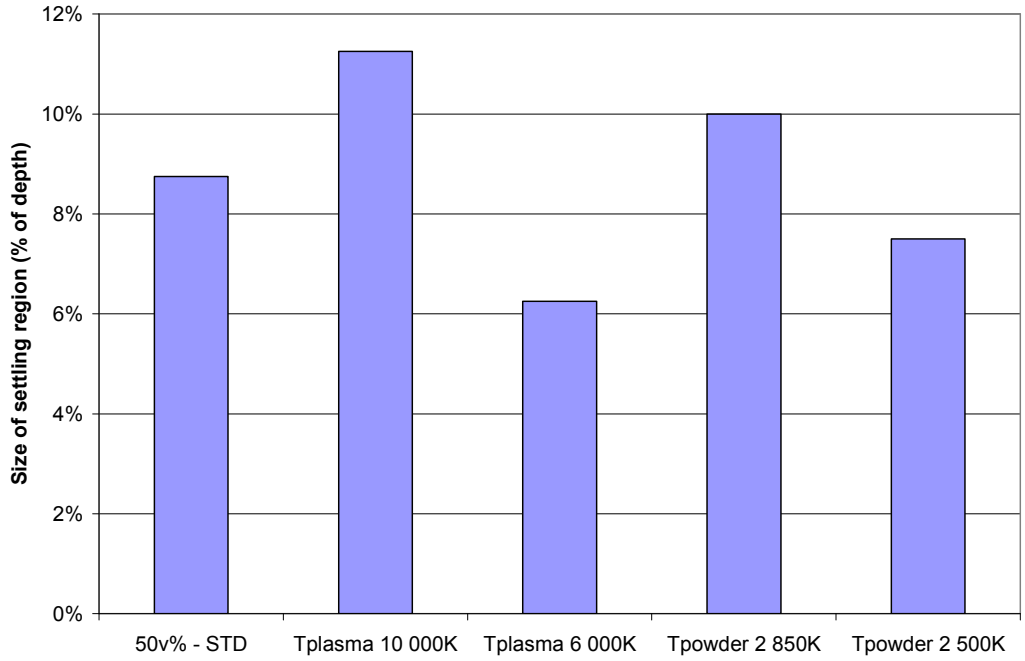

Figure 6.3: Size of settling region for changes in plasma temperature and incoming particle temperature. Initial concentration of carbide is 50 vol% WC in Ni alloy.

The effect the substrate has on the homogeneity of the deposit was investigated in terms of substrate temperature, substrate thickness and degree of preheat. Shown in Figure 6.4 and Figure 6.5 are the settling profiles of the substrate variables. There is very little difference in the carbide fraction profiles between the changes. Increasing the substrate temperature and increasing the amount of preheat results in full settling of all the carbide before solidification of the deposit is completed. Decreasing the substrate temperature has a minimal improvement in homogeneity. Alterations in the degree of preheat have no effect on the settling profile (Figure 6.5). The size of the settling regions is compared in Figure 6.6. The only significant decrease in settling region is due to cooling the substrate temperature. A cooler substrate reduces the settling region by less than 15%, from 8.75% to 7.5% of the depth.

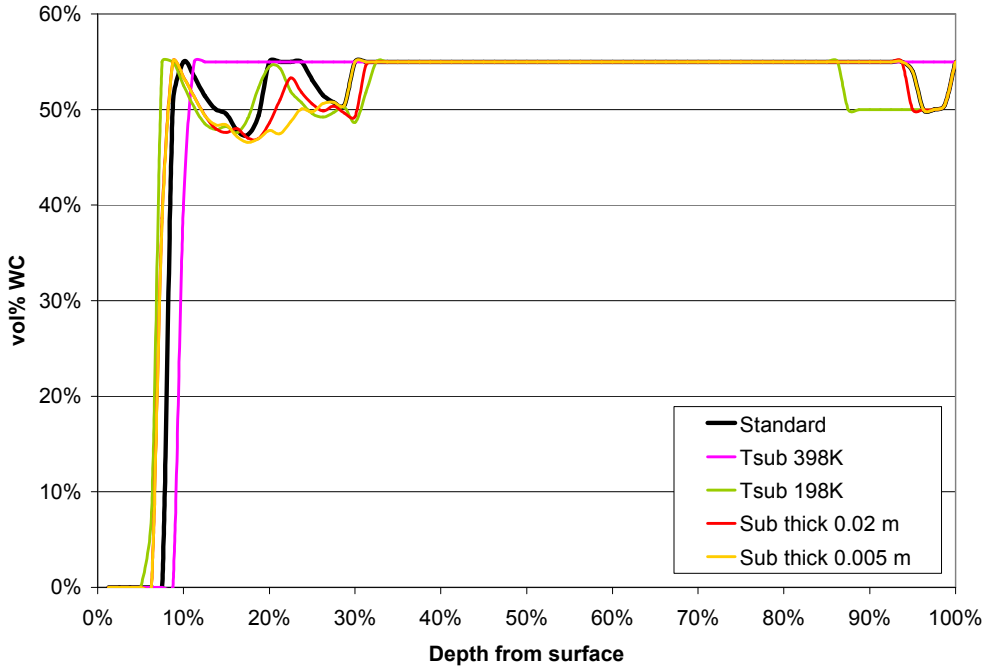

Figure 6.4: Carbide concentration profile with changes in substrate temperature and substrate thickness. Initial concentration of carbide is 50 vol% WC in Ni alloy.

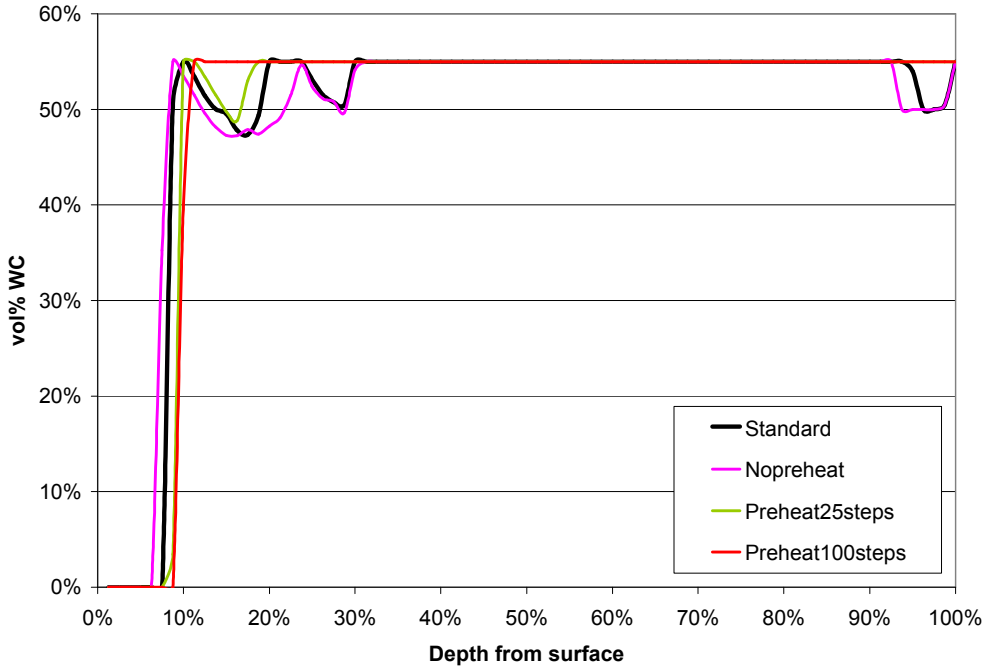

Figure 6.5: Carbide concentration profile with changes in the amount of preheat before powder is deposited. Initial concentration of carbide is 50 vol% WC in Ni alloy.

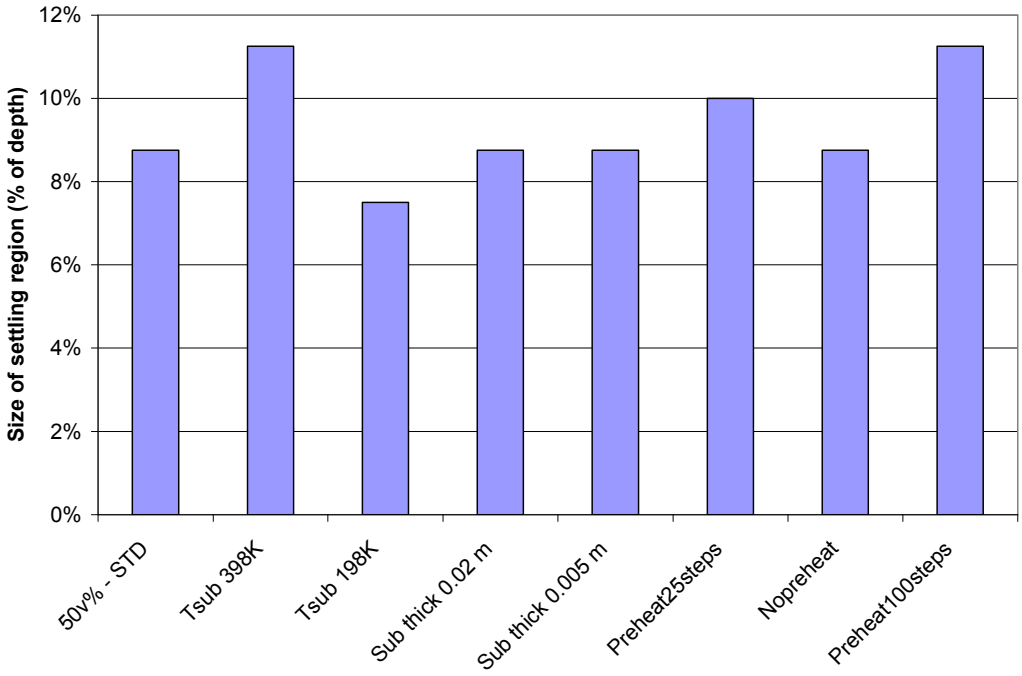

Figure 6.6: Size of settling region for changes in substrate temperature, substrate thickness and degree of preheat on the substrate. Initial concentration of carbide is 50 vol% WC in Ni alloy.

Shown in Figure 6.7, is the carbide fraction profile for changes in powder feed rate and coating thickness. Decreasing the coating thickness was the only parameter in this subset that reduced the size of the settling region. A thinner coating can only be achieved by increasing the travel speed while maintaining the same powder feed rate as the standard case. However, this increase in homogeneity was not seen in the experimental results, presented in Figure 4.8. A combination of the range of travel speeds tested and the variability of the carbide volume fraction may not have revealed differences in the size of the settling region. The measurements of the size of the settling region are shown in Figure 6.8. A significant reduction of the settling region size of almost 60% is obtained when the coating thickness is reduced by half, from 8.75% to 3.75% of the depth. Shown in Table 5.9, the onset of solidification and the duration of the solidification plateau are remarkably decreased when the thickness is reduced.

But most notably, the cooling rate is much higher than all the other parameters. This drastically decreases the time available for settling to occur and as such, produces a more homogeneous coating.

The effect of particle size and sphericity of the settling profile is shown in Figure 6.9. Decreases in particle size from 150 μm to 50 μm as well as reductions in sphericity produce significant improvements in carbide homogeneity. Reducing the sphericity effectively decreases the particle size. According to Equation 5.23, a sphericity of 0.6 and 0.8 on a 150μm sphere reduces the effective particle diameter to 93.75 and 125 μm, respectively. The 300 μm diameter particles settle so quickly that each node from the bottom up reaches its fully packed ratio, resulting in a larger settling zone at the surface.

Quantifying the size of the settling region, Figure 6.10 shows a substantial decrease in the size of the settling zone with smaller diameter particles. Reductions in size of up to 60% of the depth are predicted, from 8.75% to 3.75% of the depth. The gain in homogeneity due to reduction in particle diameter is a result of the particle having less mass, thus not settling as quickly as particles with larger size and mass. The predicted thermal profile was not changed to any significant degree, thus increased solidification rates do not contribute to the improvement in homogeneity. Increasing the particle size is detrimental to achieving a more homogeneous MMC, as the particles have sufficient mass to settle very quickly. This was confirmed previously where the smallest WC particles gave the most homogeneous structure compared to coatings with the coarsest WC particles which revealed relatively large areas of pure metal phase [BER1997].

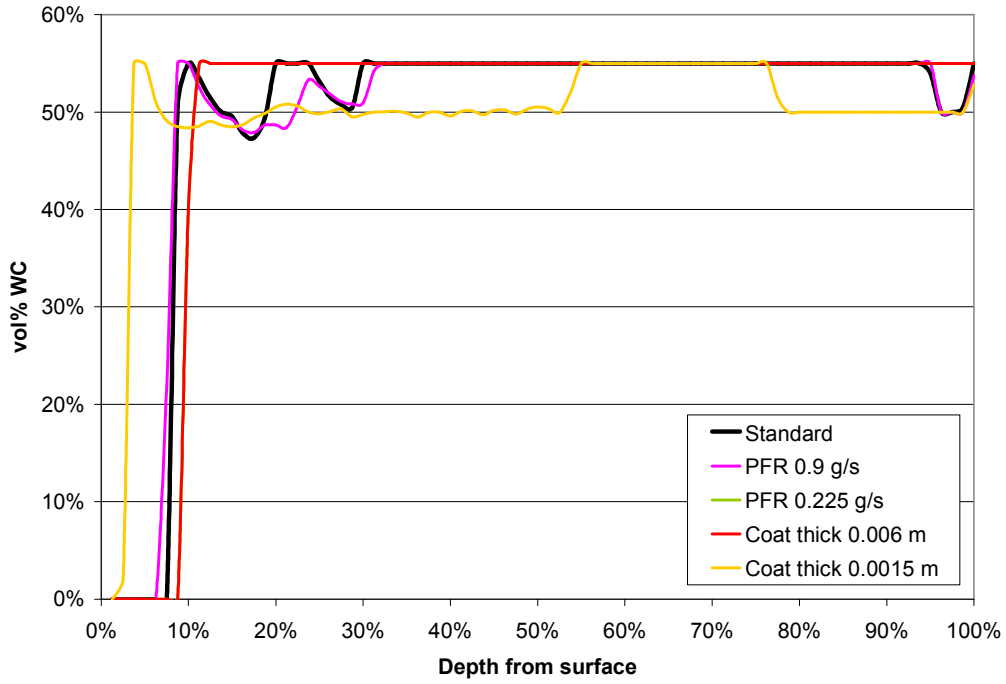

Figure 6.7: Carbide concentration profile with changes in powder feed rate and the thickness of the deposit. Initial concentration of carbide is 50 vol% WC in Ni alloy.

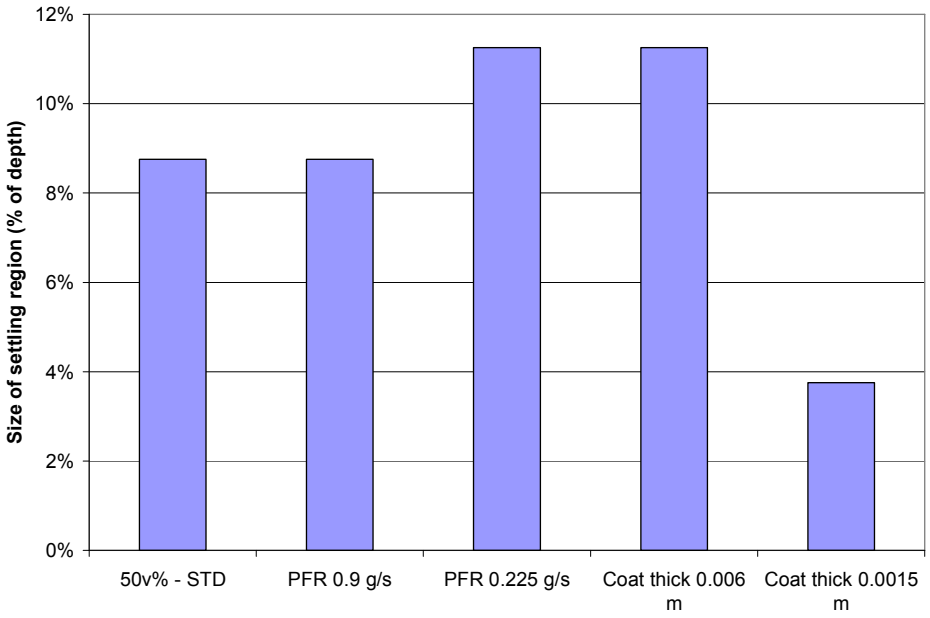

Figure 6.8: Size of settling region for changes in powder feed and coating thickness. Initial concentration of carbide is 50 vol% WC in Ni alloy.

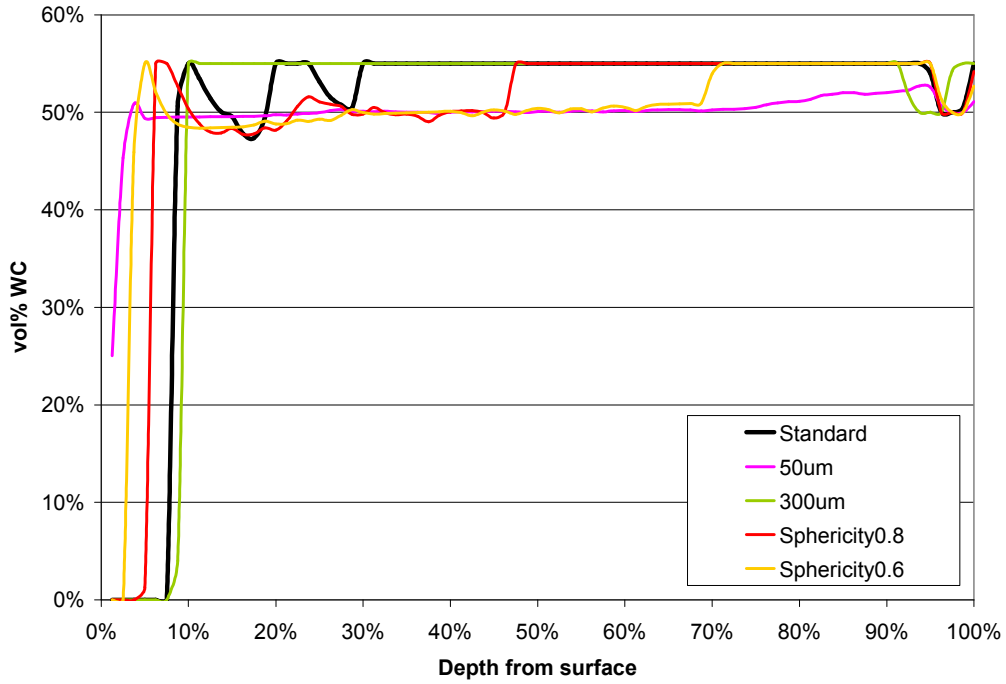

Figure 6.9: Carbide concentration profile with changes in particle diameter and sphericity. Initial concentration of carbide is 50 vol% WC in Ni alloy.

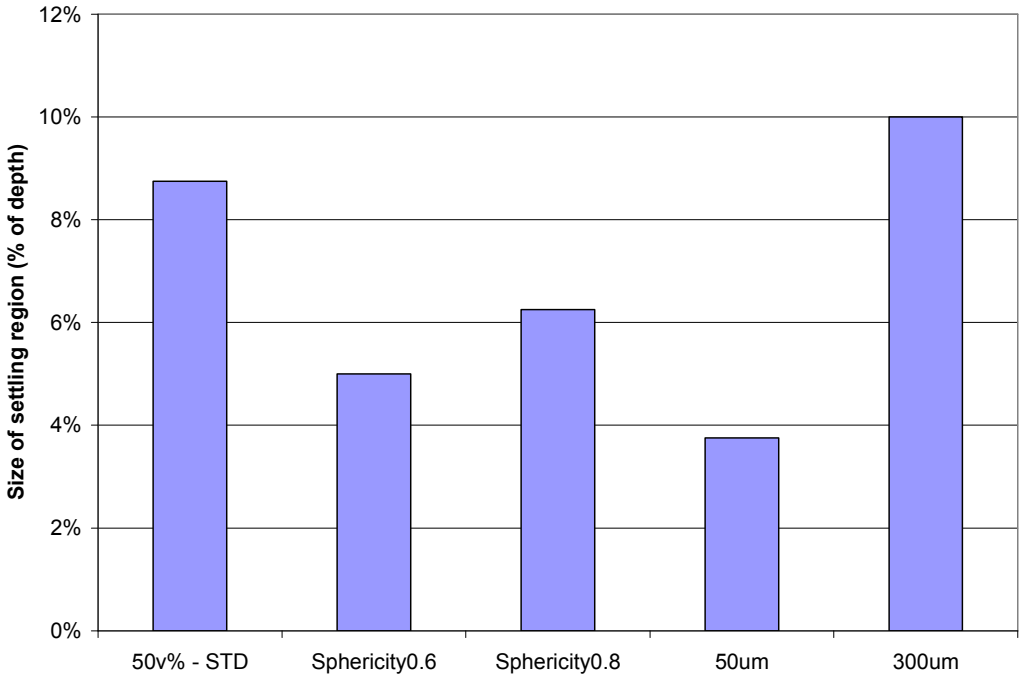

Figure 6.10: Size of settling region for changes in particle size and sphericity. Initial concentration of carbide is 50 vol% WC in Ni alloy.

Decreasing the heat transfer coefficient of the plasma gas and increasing the heat transfer coefficient of the shielding gas produces improvements in homogeneity (Figure 6.11). Reducing the plasma gas and shielding gas heat transfer coefficients degrade homogeneity or have no effect on homogeneity. Shown in Figure 6.12, small reductions in the size of the settling region occur when the plasma gas heat transfer is lowered by half and the shielding gas heat transfer is tripled. These changes lower the onset time to solidification and reduce the duration of the solidification plateau. Both these act to freeze the MMC such that no further particle settling occurs. A maximum reduction in size of the settling region of 30% is shown, from 8.75% to 6.25% of the depth.

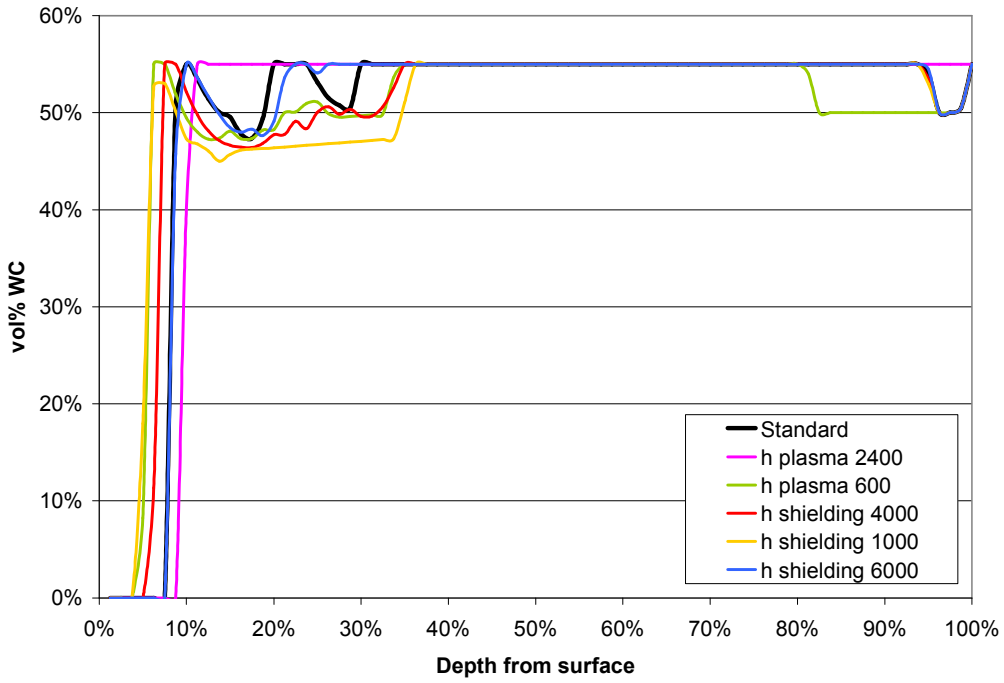

Figure 6.11: Carbide concentration profile with changes in heat transfer coefficient of the plasma gas and shielding gas. Initial concentration of carbide is 50 vol% WC in Ni alloy.

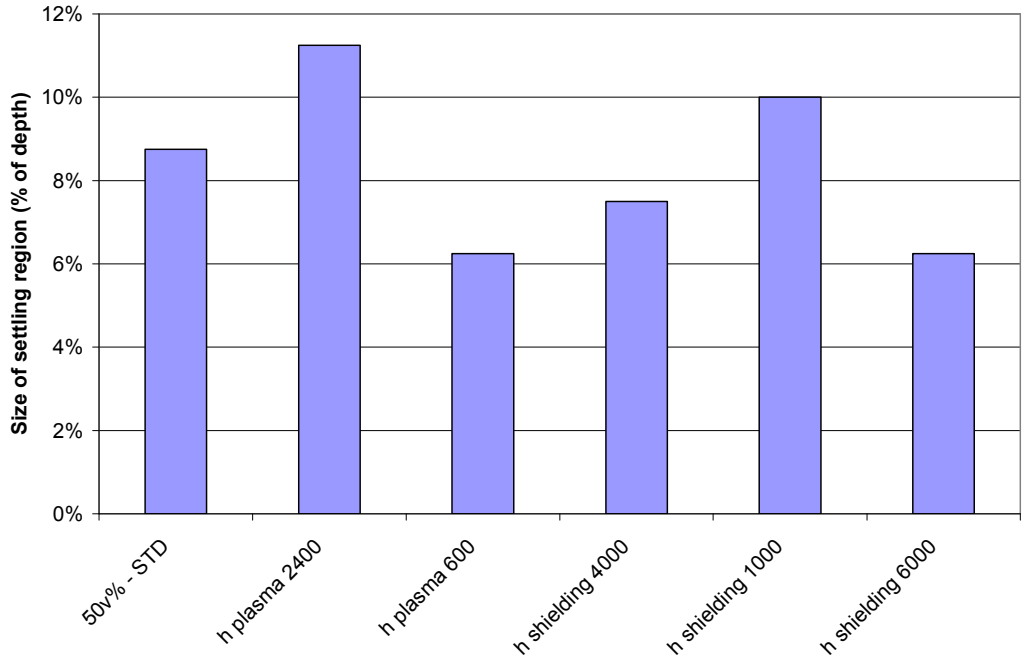

Figure 6.12: Size of settling region for changes in heat transfer coefficient of the plasma gas and shielding gas. Initial concentration of carbide is 50 vol% WC in Ni alloy.

For a 50 vol% MMC, the significant reductions in the size of the settling region and hence improvements in homogeneity are shown in Figure 6.13. The conditions which improve homogeneity, in terms of impact, are:

- reducing the thickness of the coating,
- reducing the sphericity and particle diameter,
- reducing the plasma temperature,
- reducing the plasma gas heat transfer coefficient,
- increasing the shielding gas heat transfer coefficient,
- reducing the incoming particle temperature, and
- lowering the substrate temperature.

The operating conditions which contribute to these changes are listed in

Table 6.1. Of these parameters, the most significant improvements are made by reducing the particle size to 50 μm and halving the coating thickness. Reducing the particle size is a design parameter in the materials selection of the coating and may have significant effects on the wear resistance of the coating. Reducing the thickness of the coating is obtained by increasing the travel speed, which increases welding productivity. However, a thinner coating may not have the desired operational longevity and additional passes would be required, raising cost. Other operating parameters which consistently improve homogeneity are lowering the power by decreasing current, increasing the shielding gas flow rate, increasing plasma gas flow rate and decreasing the welding table temperature.

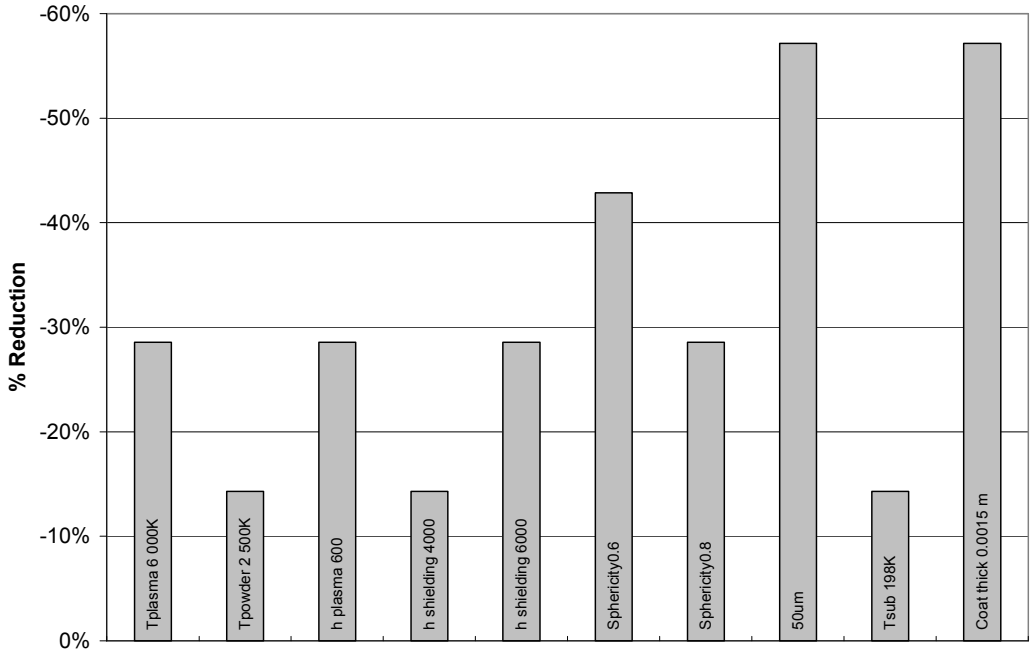

Figure 6.13: Summary of process conditions which yield improvements in homogeneity, in terms of % reduction of the size of the settling region. Initial concentration of carbide is 50 vol% WC in Ni alloy.

Table 6.1: Summary of parameters and resultant operating conditions which yield improvements in homogeneity

Parameter	*Operating Condition*
Reducing plasma temperature	• Increasing plasma gas flow • Lowering power (current/voltage) • Using a gas with a lower ionization potential
Reducing incoming particle temperature	• Increasing plasma gas flow • Lowering current
Reducing plasma gas heat transfer coefficient	• Lowering temperature of plasma gas and increasing velocity of plasma gas (increasing plasma gas flow rate)
Increasing shielding gas heat transfer coefficient	• Increase shielding gas flow rate • Increase size of shielding gas annulus
Reducing sphericity	• More irregular size particles
Reducing particle diameter	• Decreasing mean particle size
Reducing substrate temperature	• More cooling on welding table
Reducing coating thickness	• Increasing torch velocity

6.2 Optimization of a 30vol% MMC

The model parameters which contribute to improved homogeneity, based on a 30v% WC MMC, were explored. This volume fraction was chosen as it would be more sensitive to changes in homogeneity than larger volume fractions. Highlighting conditions that contribute to a homogeneous coating with less carbide could result in cost savings due to the lower amount of carbide used. Caution should be exercised as the wear resistance of homogeneous coatings of 30 vol% WC may be lower than homogeneous 50 vol% WC.

The parameters which yielded improvements in homogeneity for the 50 vol% WC cases were explored for the 30 vol% WC MMC's.

Shown in Figure 6.14, is the carbide concentration profile of a 30 vol% WC MMC comparing reductions in plasma temperature and incoming powder temperature to the standard deposition conditions. Both result in a reduction of the settling region, however, reducing the plasma temperature has a greater effect

in achieving a smaller settling region. This result is similar to that observed with the 50 vol% WC MMC. It is seen that a significant decrease in carbide fraction occurs immediately below the settling region. The carbide pile-up at the bottom of the settling region creates a region of lower concentration just below due to the hindered settling code. This is not seen in the experimental results.

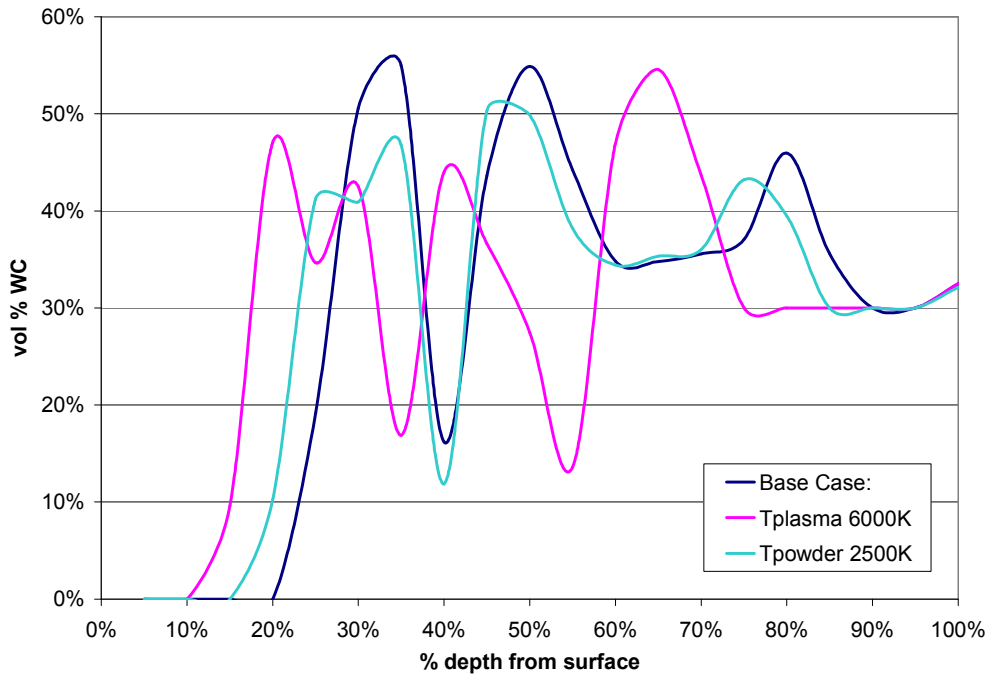

Figure 6.14: Carbide concentration profile due to changes in temperature of the plasma gas and the incoming particles. Initial concentration of carbide is 30 vol% WC in Ni alloy.

The effect of substrate temperature, substrate thickness and degree of preheat on the carbide concentration profile is shown in Figure 6.15. The only variable which appears to improve homogeneity at the surface is reducing the substrate thickness by 100 K. A colder substrate temperature will increase the cooling rate of the deposit and halt settling of the particles within a shorter duration. The maximum temperature and onset solidification and time for solidification of a 30 vol% WC MMC are all lower than that of a 50 vol% WC MMC. Since the

solidification rate is faster than the 50 vol% cases, decreases in substrate thickness and preheat time do not contribute significantly to increasing the cooling rate.

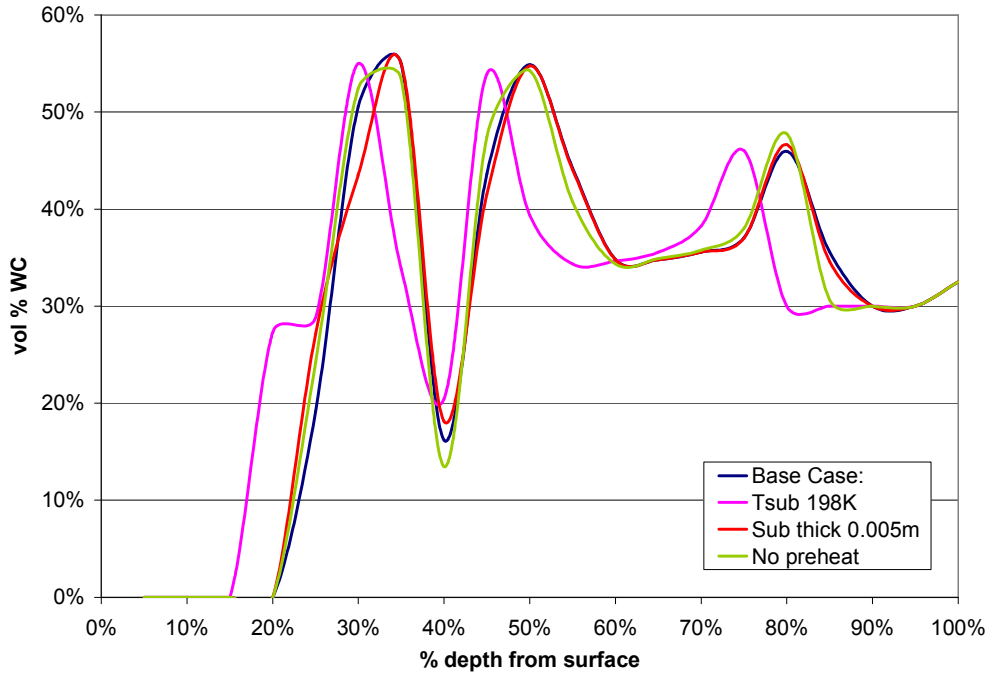

Figure 6.15: Carbide concentration profile with changes in substrate temperature, substrate thickness and preheat time. Initial concentration of carbide is 30 vol% WC in Ni alloy.

Changing the deposit thickness has a dramatic effect on the homogeneity of the coating (Figure 6.16). By halving the thickness, the coating is almost entirely homogeneous. A thinner coating results in faster solidification and reduces the distance the carbide particles are permitted to settle.

Shown in Figure 6.17, if the particle size was reduced from a standard value of 150μm to 50 μm, a uniformly homogeneous coating would be obtained. The small particles are not affected by the instantaneous carbide pile-ups shown by the fact that there are no large fluctuations in concentration throughout the thickness. This is likely a result of the small mass of the particles and the fact that their velocity is smaller than the larger particles. A faster particle would experience a larger change in velocity when exposed to the solidification front. Reducing the

sphericity also resulted in improvements in coating homogeneity, due to the lowered effective diameter.

Surprisingly, changes in the heat transfer coefficient have no effect on the homogeneity of the coating for the 30 vol% WC cases (Figure 6.18). This was not expected as reductions in the size of the settling region for the 50 vol% WC cases were between 15 and 30 %. Similarly to the substrate thickness and preheat cases, it appears that the 30 vol% WC MMC's are not as sensitive to changes in the rate heat is removed rather than heat applied (such as plasma gas temperature and incoming particle temperature).

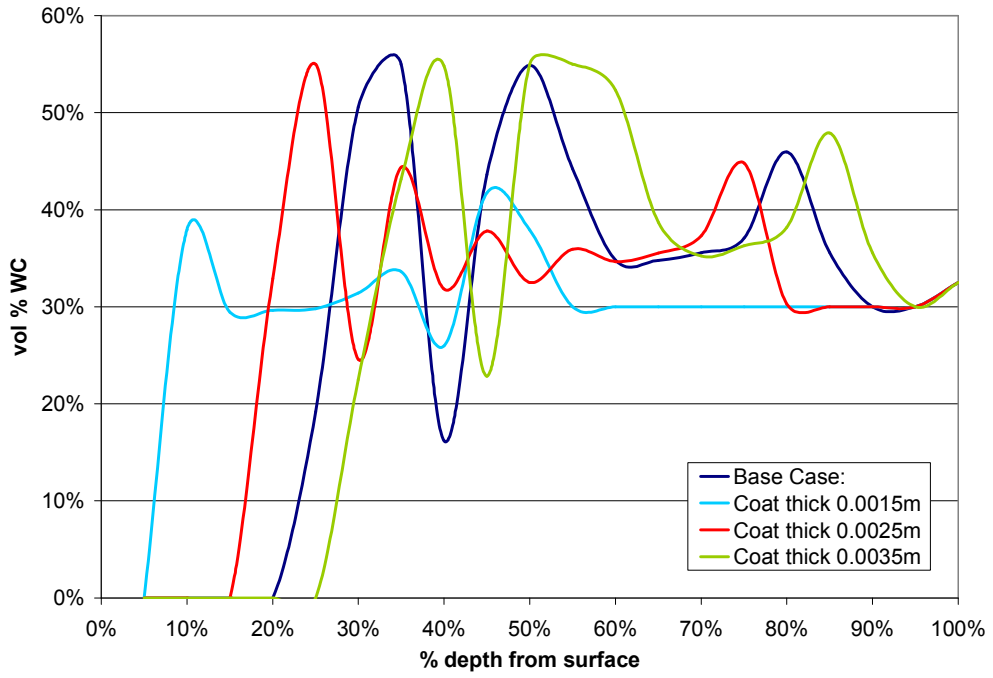

Figure 6.16: Carbide concentration profile with changes in the thickness of the deposit. Initial concentration of carbide is 30 vol% WC in Ni alloy.

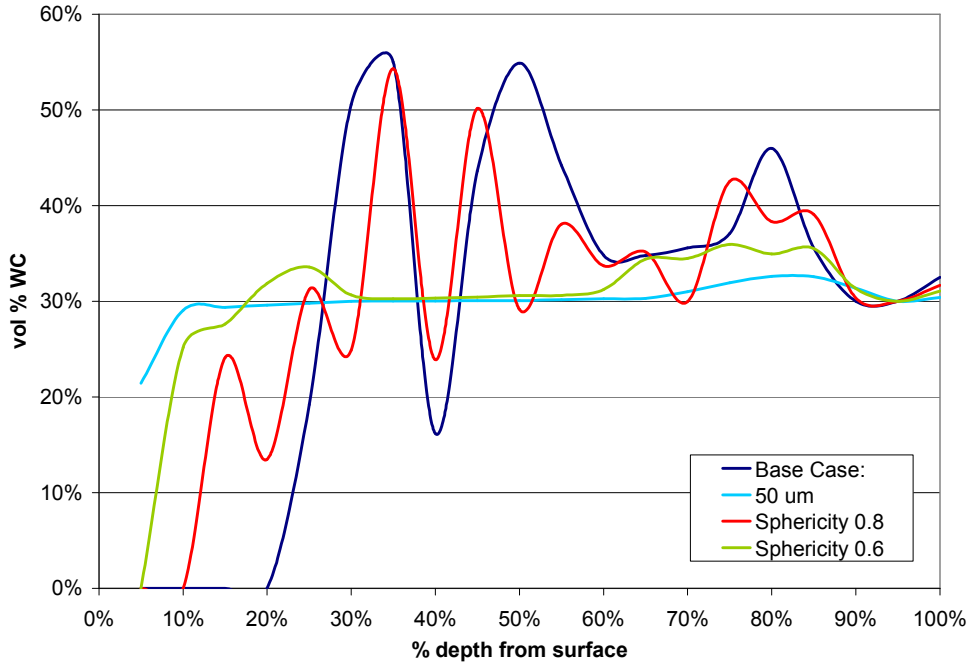

Figure 6.17: Carbide concentration profile with changes in particle diameter and sphericity. Initial concentration of carbide is 30 vol% WC in Ni alloy.

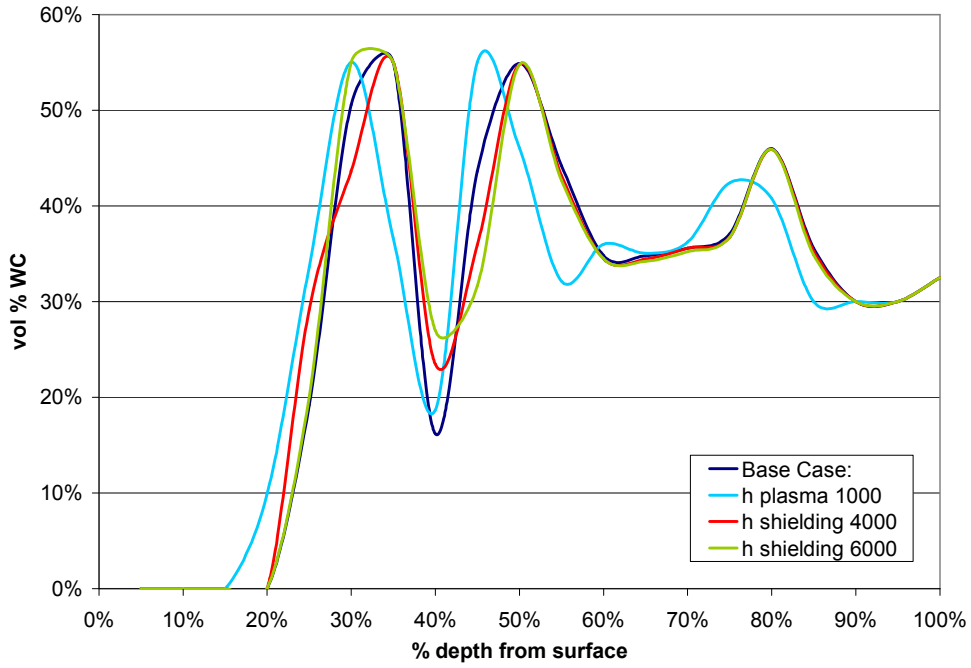

Figure 6.18: Carbide concentration profile with changes in heat transfer coefficient of the plasma gas and shielding gas. Initial concentration of carbide is 30 vol% WC in Ni alloy.

The height of the settling region was measured once the concentration of carbide exceeded 30 vol%. Shown in Figure 6.19 and Figure 6.20 are measurements of the size of the settling region for the cases studied in the 30 vol% WC MMCs. Of all the cases, the most significant decreases in settling region size are obtained with a decrease in the plasma temperature, decrease in deposit thickness, and decrease in particle size. These results are further quantified in Figure 6.21. Notably, over a 70% reduction in the size of the settling region was achieved by reducing the particle size to 50 μm. Compared to the 50 vol% WC cases, there are several options where greater homogeneity was achieved with 30 vol% WC. Larger reductions were obtained with decreasing the plasma temperature, decreasing substrate thickness, decreasing substrate temperature and decreasing particle size. Increasing heat transfer coefficients of plasma and shielding gas had little or no effect on the % reduction of the settling region size.

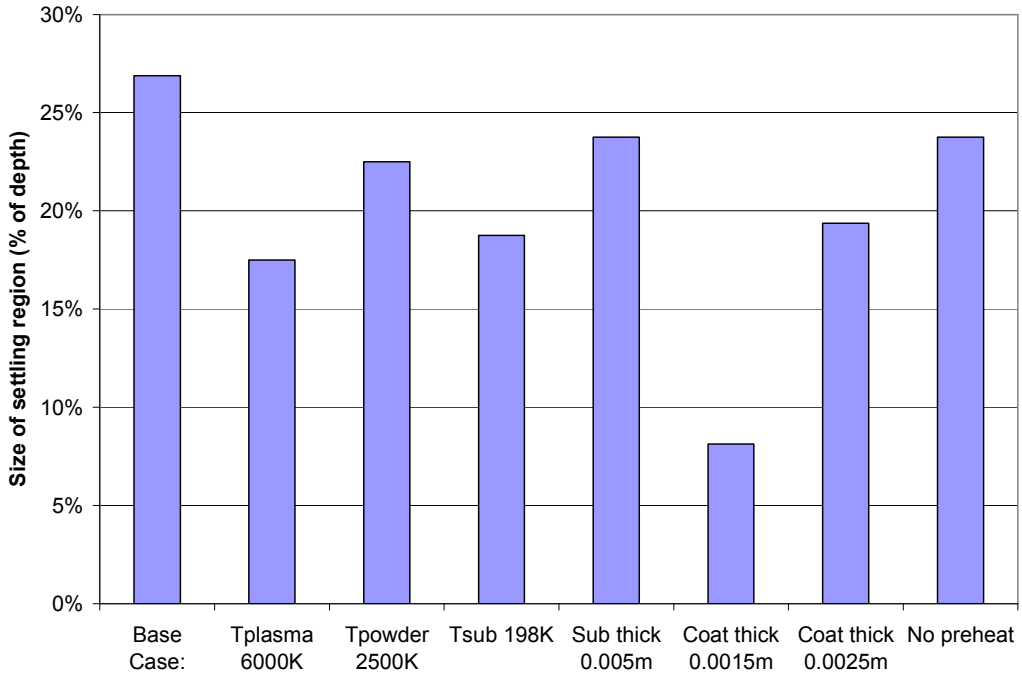

Figure 6.19: Size of settling region for changes incoming plasma temperature, incoming powder temperature, substrate temperature, substrate thickness, deposit thickness and preheat time. Initial concentration of carbide is 30 vol% WC in Ni alloy.

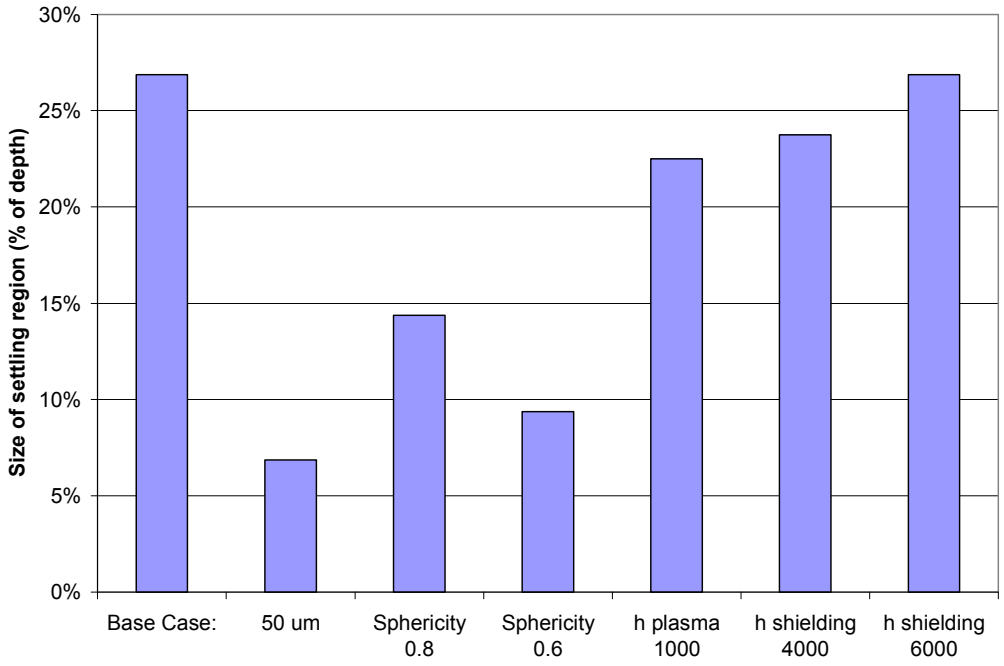

Figure 6.20: Size of settling region for changes in particle size, sphericity, and heat transfer coefficient of plasma gas and shielding gas. Initial concentration of carbide is 30 vol% WC in Ni alloy.

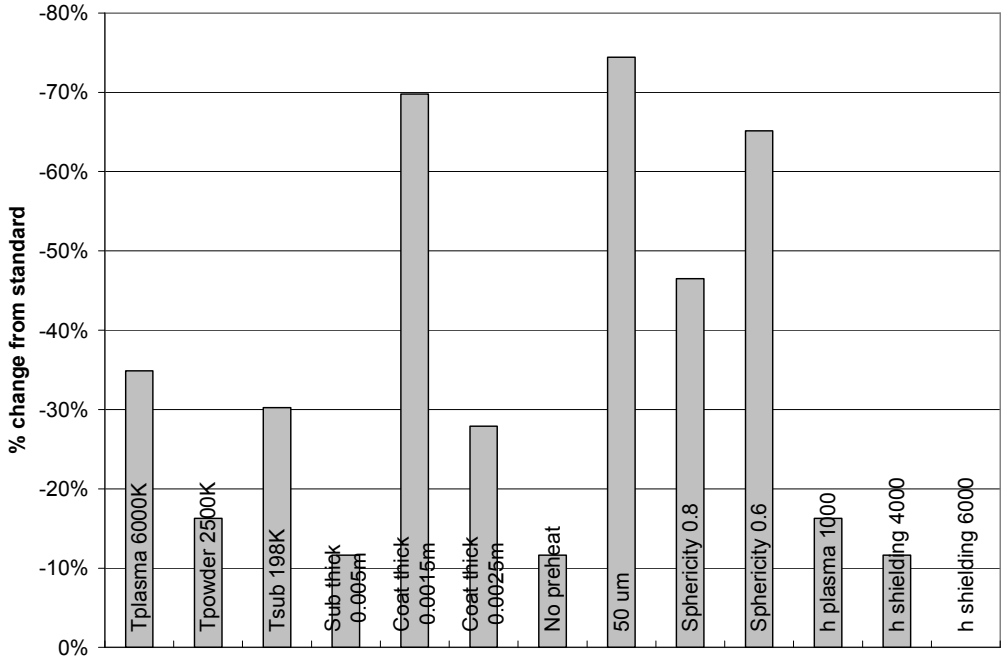

Figure 6.21: Summary of process conditions which yield improvements in homogeneity, in terms of % reduction of the size of the settling region. Initial concentration of carbide is 30 vol% WC in Ni alloy.

It was suggested by Anderson et al. [AND2003] that increasing the powder feed rate at constant heat input improves coating homogeneity. This was assumed a result of faster cooling of the weld. Shown in Figure 5.33, an increase in powder feed rate increases the initial maximum temperature of the coating, reduces the time to onset of solidification and increases the duration of the solidification plateau. For a coating with 50 vol% WC, there is no decrease in the size of the settling region with changes in powder feed rate. When the amount of carbide is reduced to 30 vol% WC, shown in Figure 6.22, there is a small difference in the settling profiles. Decreasing the powder feed rate at constant travel speed increases the homogeneity of the coating. However, this is due to the fact that the thickness of the coating is thinner such that solidification occurred at a faster rate.

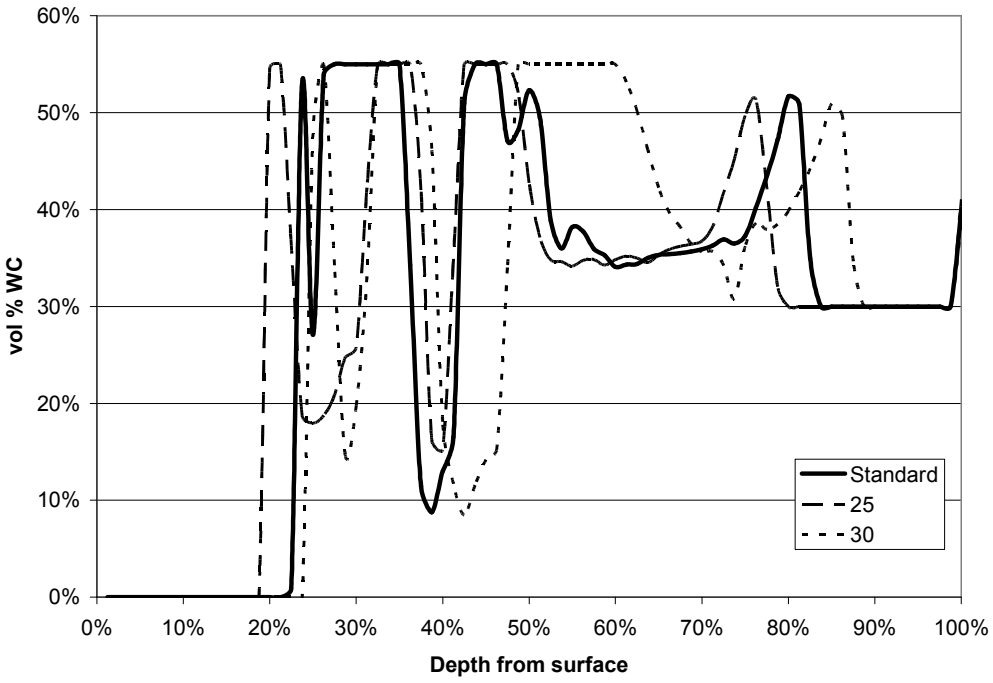

Figure 6.22: Changes in powder feed rate on a 30 vol%, from 25 g/min to 30 g/min. The standard case is 27 g/min.

6.3 Other MMC Systems

The degree of carbide settling for material systems where the density difference between the carbide and matrix was close to zero was explored. Two such common systems are an Al-B_4C and a Ni-Cr_3C_2. The properties for aluminum

and the two carbides are listed in Appendix B. The general modeling assumptions that were made for the Ni-WC system were held, with minor deviations described below. Chemical interactions between the matrix and the carbide are not considered.

6.3.1 Ni-Cr_3C_2 MMCs

This system was selected as the density of the carbide is less than that of the matrix. The density of the carbide is 6700 kg/m3, which is lower than that of the matrix of 8900 kg/m^3. The carbide no longer settles due to gravity, but floats due to buoyancy. The code allows for carbide movement such as settling or floating. When the particles tend to float, the maximum carbide concentration of the surface node is restricted to the loose random packing fraction. This value was kept at 0.55 as in the Ni-WC cases, as the particle size and shape for the Cr_3C_2 were retained as the same as the WC particles. The number of nodes used was 80, similar to that used for the early comparisons.

Shown in Figure 6.23 are the model predictions comparing the carbide settling profile of the Ni- Cr_3C_2 system to that of the Ni-WC system. The effect of the particles floating on the carbide profile is evident as there the lack of settling region at the surface and the emergence of a depleted zone near the substrate interface. The lower density of the carbide results in a more homogeneous coating for the majority of the coating depth.

The effect of the lower density carbide on the carbide profile is enhanced when the carbide volume fraction is reduced to 30 vol%. Shown in Figure 6.24 is a near homogeneous coating with Cr_3C_2 compared to WC. The substrate interface becomes significantly depleted of carbide when the carbide levels decrease below 30 vol%, shown in Figure 6.25 (20 vol%) and Figure 6.26 (10 vol%). The carbide concentration was very sensitive to changes in velocity due to hindered settling when the volume fraction was 20 vol%, as shown by the large amount in variation. However, the carbide profile is nevertheless relatively constant with an

overall volume fraction of 20 vol%. As the volume fraction decreases to 10 vol% (Figure 6.26), the size of the region void of carbides is the same for both carbide types. There is no improvement in carbide homogeneity when the concentration is 10 vol%.

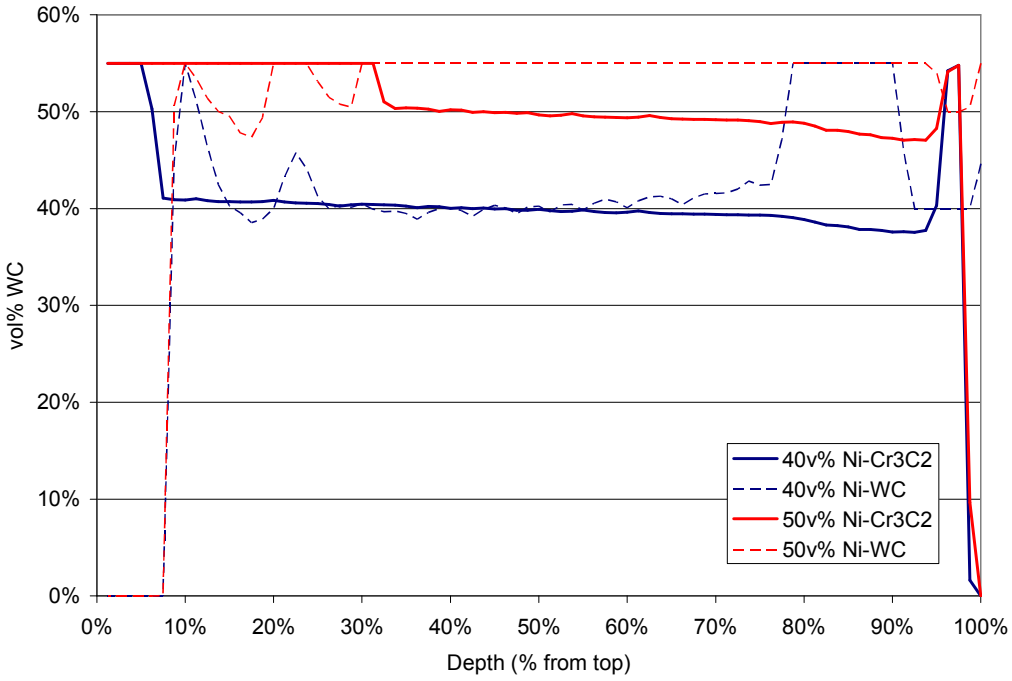

Figure 6.23: Model predictions of carbide settling profile comparing Ni-Cr_3C_2 MMC to Ni-WC MMC for 40 and 50 vol% carbide.

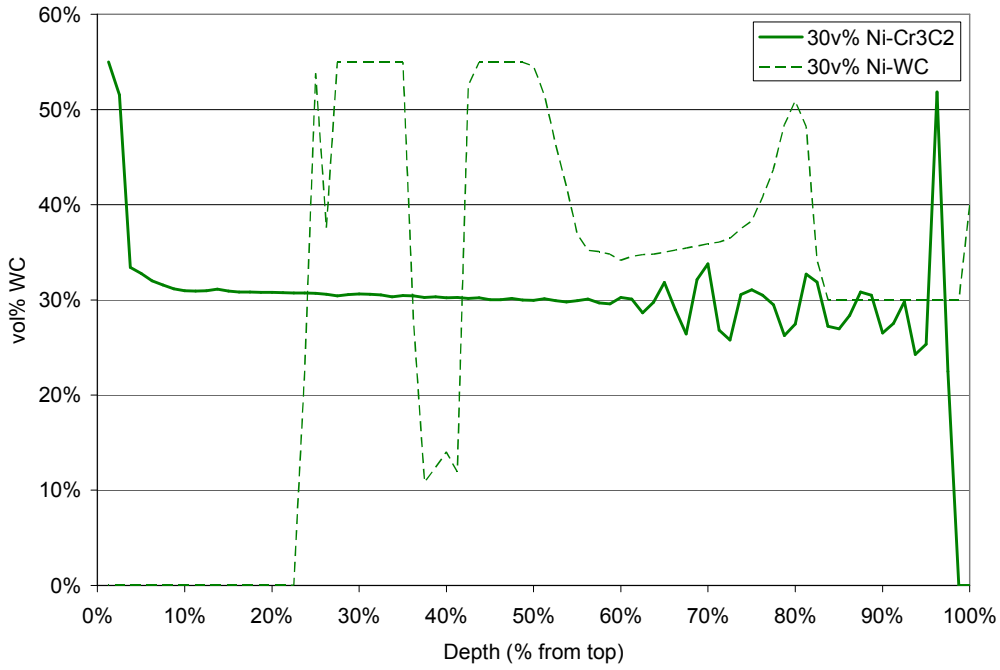

Figure 6.24: Model predictions of carbide settling profile comparing Ni-Cr_3C_2 MMC to Ni-WC MMC for 30 vol% carbide.

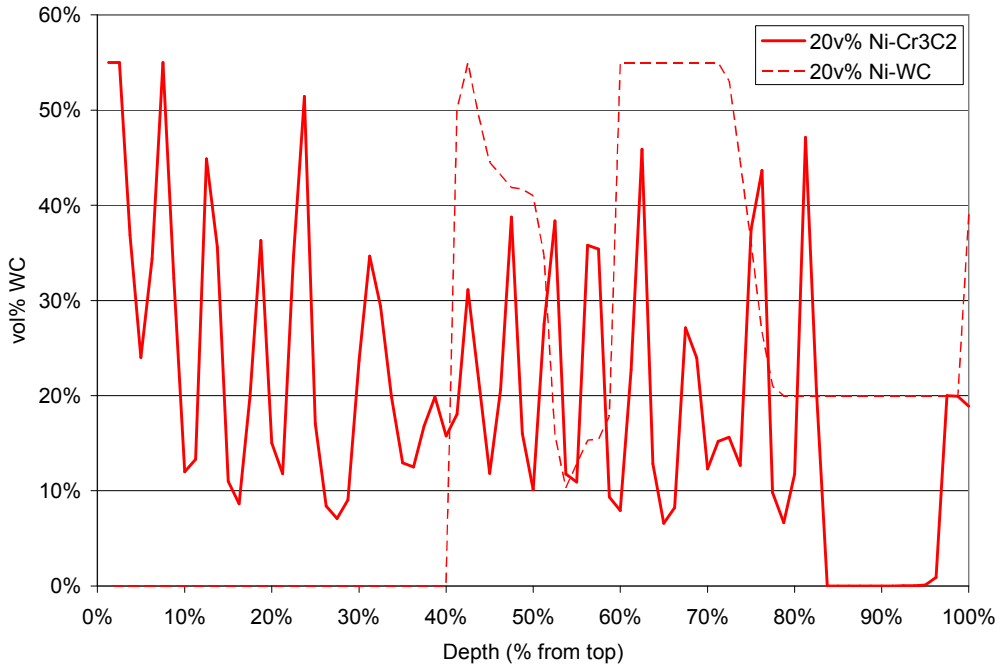

Figure 6.25: Model predictions of carbide settling profile comparing Ni-Cr_3C_2 MMC to Ni-WC MMC for 20 vol% carbide.

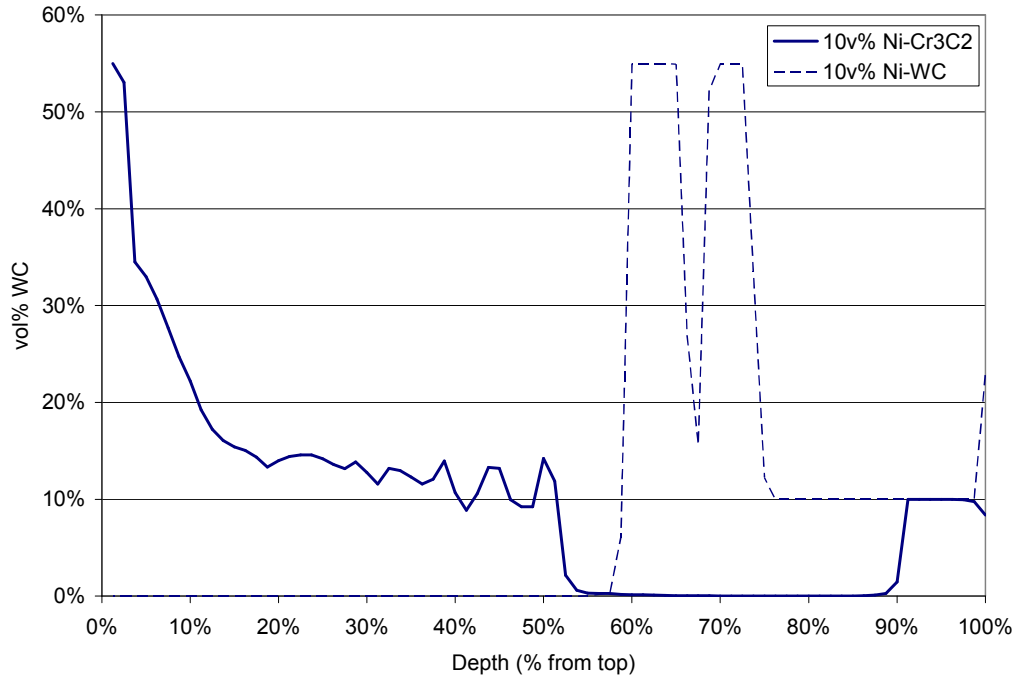

Figure 6.26: Model predictions of carbide settling profile comparing Ni-Cr_3C_2 MMC to Ni-WC MMC for 10 vol% carbide.

6.3.2 Al-B_4C MMC

Aluminum and boron carbide have very similar densities, 2300 and 2500 kg/m^3 respectively. This system is of interest as a replacement for silicon carbide. Since aluminum has a significantly lower melting point than nickel, the temperature of the incoming particles was lowered to 2000 K; other parameters were unchanged. This value is just an estimation. The model does not take into account the actual feasibility of depositing aluminum by PTAW. Only the settling characteristics, as well as the thermal profile were obtained and compared to the Ni-WC predictions.

Shown in Figure 6.27 are the thermal results from the model for Al-B_4C MMC containing up to 50 vol% B_4C. The Ni-WC system containing 50 vol% WC is also shown for comparison. The maximum temperature obtained by the Al- B_4C systems was significantly lower, due to the fact that the incoming particle temperature was lower. A higher peak temperature occurs with increasing B_4C

concentrations. This is because the heat capacity is higher than aluminum and the thermal conductivity is lower, such that more heat is retained. However, the cooling rate and solidification time is also faster, due in part the higher thermal conductivity of aluminum. It would be expected that the coatings would be more homogeneous due to the faster cooling and solidifications rates.

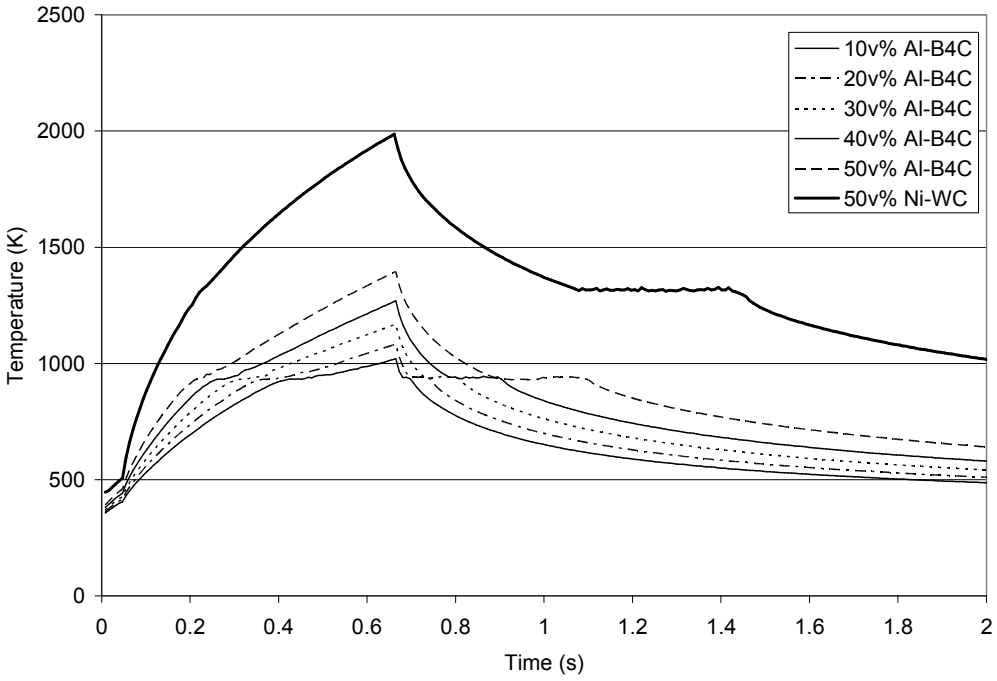

Figure 6.27: Model output of thermal profile of Al-B_4C MMCs with carbide volume fractions ranging from 10 to 50 vol% B_4C. The dark line is the output for the 50vol% Ni-WC system.

Shown in Figure 6.28 and Figure 6.29 are the carbide profiles comparing Al- B_4C to Ni-WC for 10 to 50 vol% carbide. The thick line is the Al- B_4C system and the broken line is the Ni-WC system. No settling of B_4C occurs for any of the carbide systems. This is a result of the similar densities of the matrix and carbide and the fast solidification.

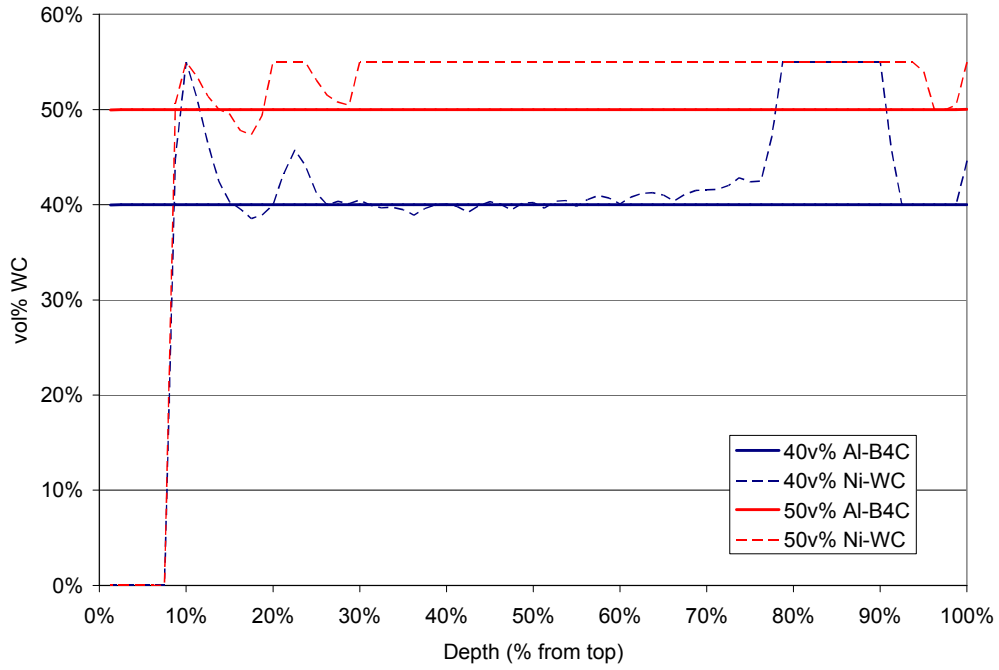

Figure 6.28: Model output of carbide profile of Al-B_4C MMCs with carbide volume fractions of 40 and 50 vol% B_4C (thick line). The broken line is the output for the corresponding Ni-WC system.

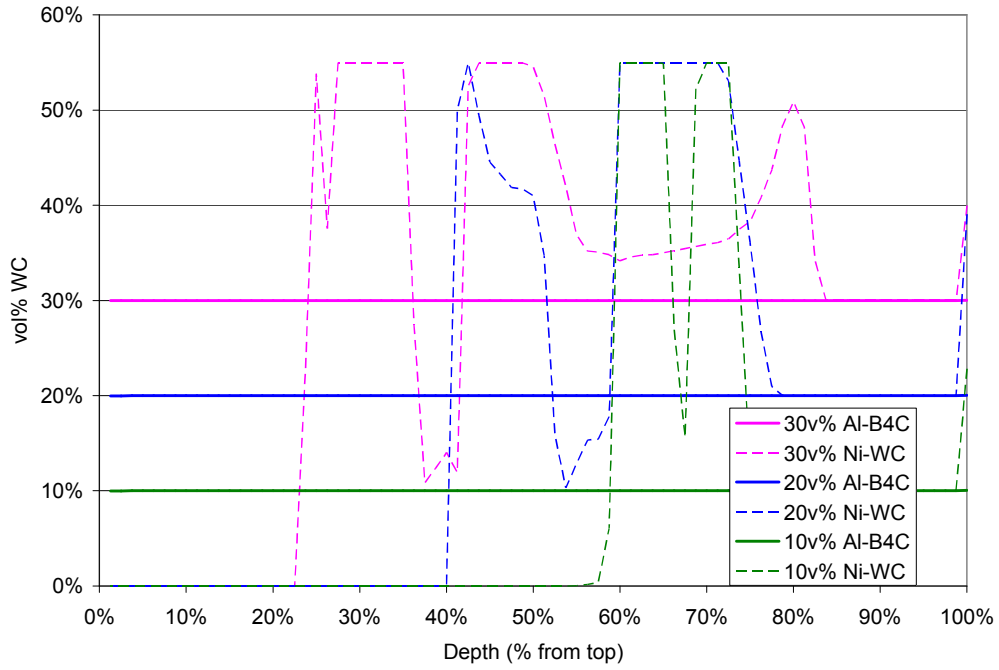

Figure 6.29: Model output of carbide profile of Al-B_4C MMCs with carbide volume fractions of 10, 20 and 30 vol% B_4C (thick line). The broken line is the output for the corresponding Ni-WC system.

It was shown that decreasing the particle density results in a more homogeneous coating. The effect of buoyancy and drag in the settling of the particles is negligible compared to gravity. In early MMC research, it was found that the low density of TiC caused the particles to float in the overlay, whereas WC had the opposite problem: dispersed carbides tended to sink [SAL1985] [DEU1998]. However, the liquid velocity becomes significantly more important as the particle size and density decrease. Particle pushing is dominant in SiC/Al composites [LIN1999]. The liquid velocity should be studied to improve the model for system where the density difference is not as large as the Ni-WC system.

6.4 Two-Pass Homogeneity

The model was enhanced to allow for a second layer of MMC to be added onto the first one. The carbide concentration for each node of the first pass was saved and added to the substrate before the second pass was added. The preheat as the second pass was laid was 500 K. This was chosen based on the temperature of the first coating as measured by the IR camera about 5 seconds after arc was extinguished. The second pass contained the same volume fraction as the first pass. The material system investigated was the Ni-WC system with carbide levels of 10 to 50 vol% WC.

Shown in Figure 6.30 is the model prediction for 40 and 50 vol% WC in a two pass scenario. As the second pass was added, a small amount of the surface was remelted, allowing for carbide from the second pass to settle into. This is shown as the peak between 50 and 60% of the depth from the top. Both two pass coatings with 40 and 50 vol% WC have good homogeneity. In comparison with the experimental results, the peak due to remelting occurs at a greater depth, around 60-70%. In addition, the volume fraction of the experiment was expected to be 50 vol%, however, it can be seen that the actual volume fraction is less at around 45 vol%. This was shown previously with other experimental runs not having the same amout of carbide as indicated by the manufacturer.

As the level of carbide decreases to 30 vol% and below, the model results show that insufficient melting of the top of the first coating occurs. The carbide of the second layer is not permitted to settle into the remelted first layer in order to reduce the size of the settling region. Thus, a layered two pass carbide coating is deposited. Shown in Figure 6.31 are the carbide profiles for two pass Ni-WC coatings with carbide volume fractions between 10 and 30 vol%. The carbide distribution for both passes containing 10 vol% WC are identical. This concluded heat of the arc and second pass were insufficient to penetrate far enough into the first pass increase coating homogeneity. As the carbide volume fraction increases to 20 and 30 vol%, the peak of carbide fraction for the top layer is higher than the first layer. This is due to the addition heat in the system from the preheat of the first layer. The time for solidification is longer, thus allowing for more settling to occur. The loose packing fraction was obtained above the interface between the first and second layers in both the 20 and 30 vol% WC cases. The lack of a homogeneous two pass coating is seen when compared to the 2 pass experimental results.

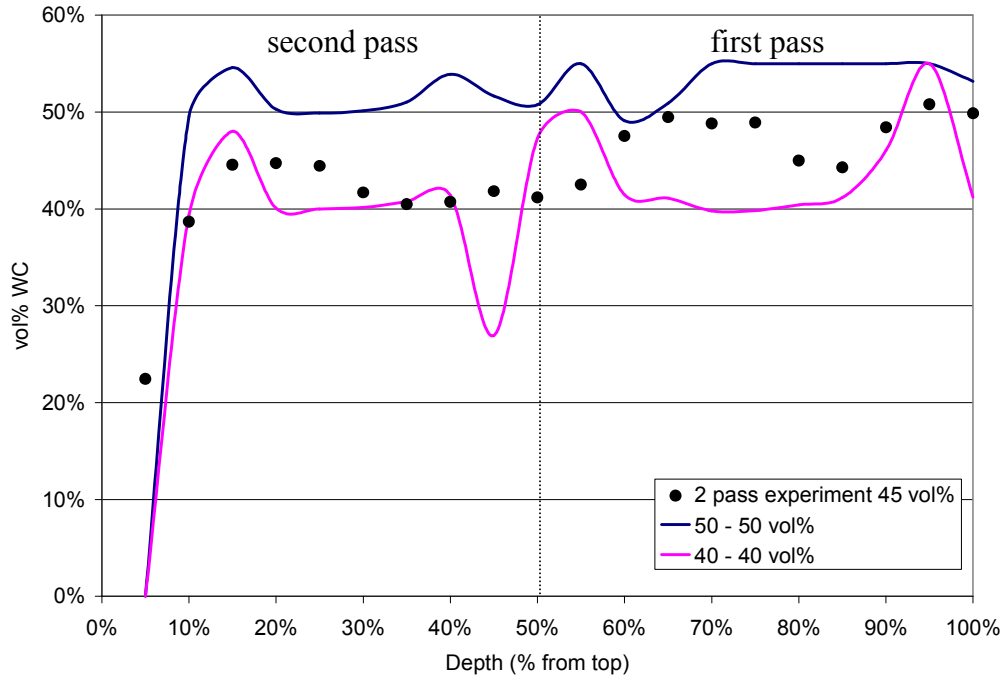

Figure 6.30: Model prediction of carbide homogeneity of 2 passes of Ni-WC with volume fractions of 40 and 50 vol%. The measured experimental results for a 2 pass MMC are shown for comparison.

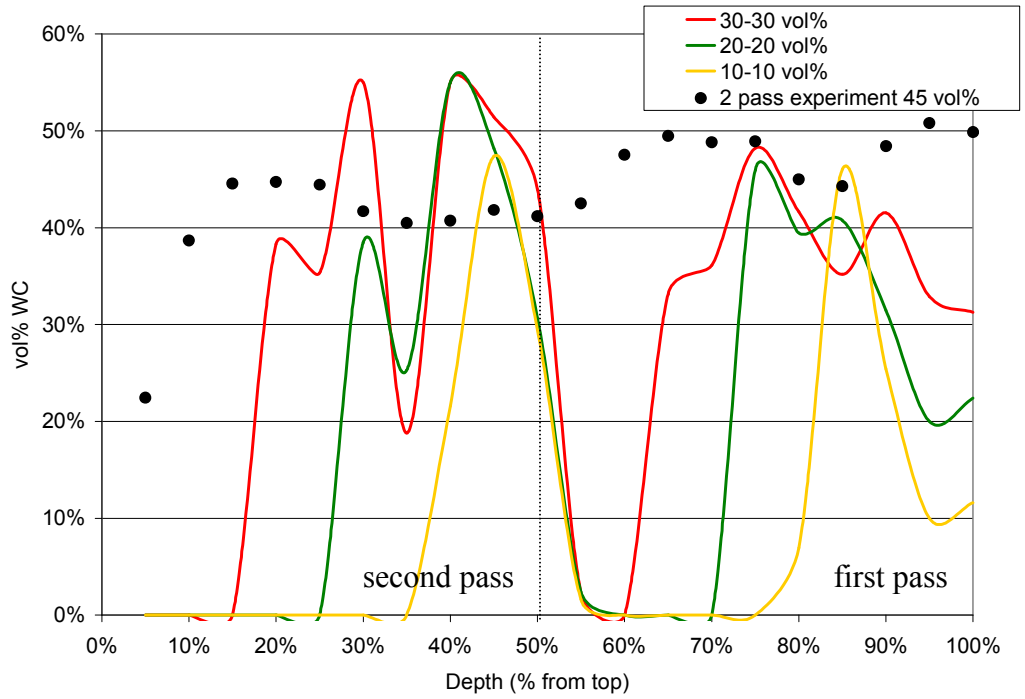

Figure 6.31: Model prediction of carbide homogeneity of 2 passes of Ni-WC with volume fractions of 10 to 30 vol%. The measured experimental results for a 2 pass MMC are shown for comparison.

6.5 Chapter Summary

The operating parameters which yielded an improvement in homogeneity of the carbides throughout the deposit thickness were predicted using the model presented in the previous chapter.

For a 50 vol% WC MMC, the factors which yielded the most significant improvement in homogeneity in terms of reducing the size of the settling region were:

- Reducing the thickness of the coating by half, which can lead to reduced productivity by having to apply more coatings even if the travel speed is increased;
- Decreasing the particle size to 50 μm, which may have significant effects on the wear performance;

- Reducing the plasma gas temperature by 2 000 K by lowering the current, voltage or plasma gas flow rate;
- Reducing the heat transfer coefficient of the plasma gas by half, lowering the current, voltage or plasma gas flow rate;
- Tripling the heat transfer coefficient of the shielding gas, by increasing the shielding gas flow rate;

The 30 vol% WC MMC obtained greater improvements in homogeneity than the 50 vol% WC MMC case when the plasma temperature was decreased, the deposit thickness decreased and the particle size decreased. No improvements were seen with changes in heat transfer coefficients of plasma and shielding gases, reducing substrate thickness or eliminating substrate preheat. This is a result of the lower maximum temperature and shorter solidification times seen with the 30 vol% WC compared to the 50 vol% WC MMCs. Enhancing the extraction of heat from the system produced no improvements in homogeneity for the 30vol% WC cases, unlike the 50 vol% WC cases. The improvements were seen when the amount of heat added to the system was lowered.

In centrifugal casting of MMCs, the factors that resulted in a more homogenous casting were a small density difference between particle and liquid, a small particle diameter size, and a longer pouring time [LAJ1988].

Homogeneous coatings were simulated when the difference between liquid and particle density was decreased, shown in Ni-Cr_3C_2 and Al-B_4C systems. The Ni-Cr_3C_2 had a density lower than the Ni and the carbides exhibited a tendency to float. When the carbide level was above 30 vol%, a homogeneous coating was obtained. A homogeneous coating was obtained for all cases studied in the Al-B_4C system. This is due to the similar densities of Al and B_4C, as well as the faster solidification rate due to the higher heat conductivity of Al.

A second pass was added to simulate multi-pass coatings. Homogeneous coatings were obtained for carbide values of 40vol% and above. A peak in carbide fraction was found just below the interface between the two passes. When the carbide fraction was decreased to 30 vol% and below, the settling region of the first pass was not eliminated and homogeneous coatings were not obtained.

7 Conclusions and Future Work

A one dimensional coupled model of solidification of an MMC with particle settling has been developed. The MMC consisted of a high volume fraction of WC in a nickel alloy matrix, deposited by plasma transfer arc welding. Experiments were carried out to validate the model. Images of the deposit and the volume fraction of the WC in the deposit were quantified as a function of deposit depth. Surface temperatures of the weld deposit were acquired using infrared thermography.

The model had very good agreement with the experimental results. This fundamental model was able to accurately predict the particle homogeneity of an MMC deposited by an extremely complicated process. It was shown that the most important variable leading to a homogeneous coating was to operate at the random loose packing fraction of the reinforcement particles. The amount of carbide in the powder is proportional to the degree of settling of the carbide in the coating. In the case of the MMC explored, a near homogeneous coating was obtained with 50 vol% of WC in a NiCrBSi matrix. In terms of selecting operational parameters which improve homogeneity, reducing the current/voltage, increasing shielding gas flow rates, increasing plasma gas flow rates, increasing travel speed all lead to improvements. The MMC design parameters which yield improvements in homogeneity are a reduction in particle size, a thinner coating, and using more irregular shaped particles. Reducing the density difference between the two particles also significantly improves the homogeneity of the coating.

At 30 vol% WC, a homogenous deposit was achieved when the particle size and the coating thickness were reduced. Operational parameters that improved homogeneity were low pool superheat and a cooler substrate temperature. Below 30 vol% WC, homogeneous distribution of WC was not achieved and the model has shown reasonable agreement with the experimental results.

There is no current research evaluating the surface temperatures of welding coatings using infrared technology, most notably in plasma transferred arc welding. Infrared cameras are currently used to measure the heat affected zone of the substrate. It was shown that IR temperature measurements are complex to obtain in the arc region for welding applications. Interference with the arc and surface reflections made it impossible to measure the real weld pool temperature. Temperatures in that area could be obtained when the arc was extinguished; however, evaluation of the real temperature became complicated due to emissivity changes. The emissivity of the MMC was measured using laser reflectometry and was found to decrease from 0.8 to 0.3 between 900°C and 1200°C. The temperatures obtained from the infrared camera were corrected using an iterative approach with the measured emissivities. It was shown that the surface temperatures increased with increasing current and voltage and with decreasing shielding gas flow rate.

Plasma arc shape is a good indicator of heat transfer into the weld and substrate. Exhaustive models have been produced to capture the plasma temperature and velocity gradients. Very few have been validated. These images show that PTAW with powder addition cannot be modeled as a Gaussian distribution – as all current models are.

The WC particles react with the Ni-based matrix. A microscopic evaluation showed that as the heat input increased, the morphology of the secondary W-based carbide changed from dendritic to acicular. A herringbone structure was also identified which is produced with higher heat inputs, which allows for more degradation of the primary WC. Spherical eutectic carbides with free tungsten and carbon degrade when deposited by PTAW and are not recommended.

7.1 Future Work

There are several improvements to the model that can be explored to provide a better fit with experimental results. It was shown that the fit between cooling of the solid should be improved. The following suggestions may result in better model prediction.

- The development of a 2D model to incorporate heat transfer from the sides of the coating. Heat is lost not only from the surface of the deposit, but from the sides as well, specifically during cooling after solidification.
- It was discussed that the accuracy of the thermal properties increase the fit of the model. The properties used were from Ni only since no data exists for the complex matrix of NiCrBSi. The properties of this alloy should be acquired to improve the model.
- The emissivity at liquidus/solidus points changed rapidly and was not investigated exhaustively. A controlled experiment should be conducted to collect emissivity data in these regions. In addition, emissivity can vary significantly with surface roughness of the material. For a Ni/Al 95/5, the emissivity varied between 0.18 and 0.47 as the surface got rougher [FRI2001]. This difference in emissivity can drastically alter the temperature values measured from the infrared camera.
- The apparent viscosity of liquid aluminum was shown to increase with volume fraction of SiC [HAS2002]. The viscosity of the liquid nickel in the model was a function of temperature, but not of volume fraction carbide since data does not exist for this system and for particle volume fractions greater than 30 vol%. The viscosity of the MMC at various WC volume fractions should be experimentally determined in order to improve the properties used in the model.
- Automatic adjustments for increase in shielding gas and substrate temperature when increasing plasma gas temperature due to increase in current should be included. In addition, changes in voltage and plasma gas velocity result in an increase of the incoming particle temperature.

- The liquid velocity plays a role in the settling of particles as the size and density decrease. Further studies in the effect of liquid velocity should be pursued.

In terms of coating design, it was reported that fully homogeneous coatings were obtained in microgravity environments [VAN2000]. Gravity is the most considerable force on the settling of the reinforcement particles. Although the elimination of gravity during the deposition process is impossible, the selection of system where the density difference is minimal can mimic a low gravity environment.

The effect of the wear resistance due to the morphology of the secondary tungsten based carbide is unknown. Quantification of the type and volume fraction of the carbide morphology and the resultant mass loss from ASTM G65 abrasion testing would be required. The cause of the circular denuded zones is currently not known. An investigation into the stability of various tungsten carbides at high temperatures should be conducted.

8 References

[AHM2001] Ahmed I, Bergman TL, (2001), Simulation of Thermal Plasma Spraying of Partially Molten Ceramics: Effect of Carrier Gas on Particle Deposition and Phase Change Phenomena, *Transactions of ASME*, volume 123: pp. 188-196

[AIT1998] Aithal SM, Subramaniam VV, Pagan J, Richardson RW, (1998), Numerical Model of a Transferred Plasma Arc, *Journal of Applied Physics*, volume 84, number 7: pp. 3506-3517

[AME2007] American Conference of Governmental Industrial Hygienists, (2007), *Industrial ventilation : a manual of recommended practice for design, 26th Edition*, Cincinnati, Ohio.

[AND1998] Anderson M, Chiovelli S, Reid D, (1998), Wear resistant materials for use in the oil sands hydraulic transportation process, *Materials for Resource Recovery & Transport*, Collins L (ed.), CIM: pp. 451–465

[AND2003] Anderson M, Chiovelli S, Llewellyn R, (2003), The use of tungsten carbide materials for oilsand wear applications, *ITSC 2003: International Thermal Spray Conference 2003: Advancing the Science and Applying the Technology*; Orlando, FL, USA; 5-8 May 2003: pp. 509-518

[ARA1993] Araki T, Nishida M, Hirose A, Yano K, Fujita H, (1993), Abrasive Wear Resistance of Overlay Composite Alloy with Addition of Carbide Powders, *Transactions of the Japan Welding Society*, volume 24: pp. 74-80

[ASTME1933] ASTM E1933-99a, (2005), *Standard Test Methods for Measuring and Compensating for Emissivity Using Infrared Imaging Radiometers*, American Society for Testing and Materials International, Pennsylvania, USA.

[ASTMG65] ASTM G65 -04, (2004), *Standard Test Method for Measuring Abrasion Using the Dry Sand/Rubber Wheel Apparatus*, American Society for Testing and Materials International, Pennsylvania USA.

[BAB1986] Babiak Z, Dudzinski W, (1986), Tungsten carbide stability in plasma weld surfacing, *Surfacing Journal International*, volume 1 number 3: pp. 87-90

[BAB2002] Babu SS, Martukanitz RP, Parks KD, David SA, (2002), Toward Prediction of Microstructural Evolution during Laser Surface Alloying, *Metals and Materials Transactions A*, volume 33A: pp. 1189-1200

[BAD2008] Badisch E, Kirchgaβner M, (2008), Influence of welding parameters on microstructure and wear behaviour of a typical NiCrBSi hardfacing alloy reinforced with tungsten carbide, *Surface and Coatings Technology*, volume 202: pp. 6016-6022

[BAK1992] Baker H (ed.), (1992), *ASM Handbook, 10th ed., v3 - Phase Diagrams*, Materials Park, OH, ASM International.

[BAL2004] Baldock TE, Tomkins MR, Nielsen P, Hughes MG, (2004), Settling velocity of sediments at high concentrations, *Coastal Engineering*, volume 51: pp. 91-100

[BEJ2003] Bejan A, Kraus AD, (2003), *Heat Transfer Handbook*, John Wiley & Sons: pp. 500-515, Online version available at: http://knovel.com.login.ezproxy.library.ualberta.ca/web/portal/browse/display?_EXT_KNOVEL_DISPLAY_bookid=725&VerticalID=0

[BER2000] Bertrand P, Ignatiev M, Flamant G, Smurov I, (2000), Pyrometry applications in thermal plasma processing, *Vacuum*, volume 56: pp. 71-76

[BER1997] Berget J, Bardal E, Rogne T, (1997), Influence of WC particle size and matrix composition on the behavior of WC-Co-Cr coatings sprayed by the HVOF process, *Thermal Spray: a United Forum for Scientific and Technological Advances*, Indianapolis, Indiana; USA; 15-18 Sept. 1997: pp. 783-789

[BER2001] Berget J, Bardale E, Rogne T, (1998), Effects of powder composition on the erosion, corrosion and erosion-corrosion properties of HVOF sprayed WC coatings, *Proceeding of the 15th International Thermal Spray Conference*, Nice, France, 25-29 May 1998: pp. 305-312

[BIR1960] Bird RB, Stewart WE, Lightfoot EN, (1960), *Transport Phenomena*, Wiley New York NY: pp. 340-342

[BOU2001] Bounds WM, (2001), A Mathematical Model for Solids Settling, *Light Metals 2001*, Anjier JL (ed.), TMS: pp. 65-69

[BRO1950] Brown GG, (1950), *Unit Operations*, Wiley: pg 22

[BRO1981] Brooks JA, Dini JW, Johnson HR, (1981), Causes of Weld Porosity in Electroformed Nickel, *Metal Finishing*, volume 79, number 5: pp. 41-45

[BUC1991] Bucher F, Sainte-Catherine C, Jeandin M, Montagnon JP, Pantelis D, (1991), Microstructural study of tungsten carbide reinforced Ni-based superficial composite obtained by laser melt-injection processing, *Memoires et Etudes Scientifiques Revue de Metallurgie*, May 1991, volume 88: pp. 279-282

[BUD1988] Budinski KG, (1988), *Surface Engineering for wear resistance*, Prentice Hall, Englewood Cliffs NJ.

[BUS2001] Buschow KH, Cahn RW, Flemings MC, Ilschner B, Kramer EJ, Mahajan S, (2001), *Encyclopedia of Materials - Science and Technology, Volumes 1-11*, Elsevier.

[CAM2007] Camenen B, (2007), Simple and General Formula for the Settling Velocity of Particles, *Journal of Hydraulic Engineering*, Feb 2007: pp. 229-223

[CAS1998] Castier M, Delgado Cuellar O, Tavares FW, (1998), Monte Carlo simulation of particle segregation, *Powder Technology*, volume 97: pp. 200 -207

[CHE1982] Chen X, Pfender E, (1982), Heat Transfer to a Single Particle Exposed to a Thermal Plasma, *Plasma Chemistry and Plasma Processing*, volume 2, number 2: pp. 185-212

[CHE1983] Chen X, Pfender E, (1983), The effect of the Knudsen Number on Heat Transfer to a Particle Immersed into a Thermal Plasma, *Plasma Chemistry and Plasma Processing*, volume 3, number 1: pp. 97-113

[CHE1990] Chen W, Chin BA, (1990), Monitoring Joint Penetration Using Infrared Sensing Techniques, *Welding Journal*, volume 69: pp. 181s-185s

[CHE1997] Cheng NS, (1997), Effect of concentration of settling velocity of sediment particles, *Journal of Hydraulic Engineering*, volume 123, number 8: pp. 728-731

[CHI1983] Chin BA, Madsen NH, Goodling JS, (1983), Infrared Thermography for Sensing the Arc Welding Process, *Welding Journal*, volume 62: pp. 227s-234s

[CHO1990] Choo RTC, Szekely J, Westhoff RC, (1990), Modeling of High Current Arcs with Emphasis on Free Surface Phenomena in the Weld Pool, *Welding Journal*, volume 69: pp. 346s-361s

[CHU2004] Chu SC, Lian SS, (2004), Numerical analysis of temperature distribution of plasma arc with molten pool in plasma arc melting, *Computational Materials Science*, volume 30: pp. 441-447

[COB1955] Cobine JD, Burger EE, (1955), Analysis of electrode phenomena in the high current arc, *Journal of Applied Physics*, volume 26, issue 7: pp.895-900

[COB2007] Cobo A, Mirapeix J, Conde OM, Garcia-Allende PB, Madruga FJ, Lopez-Higuera JM, (2007), Arc welding process control based on back face thermography: Application to the manufacturing of nuclear steam generators, *Proceedings of SPIE - The International Society for Optical Engineering, v 6541, Thermosense XXIX*: pp. 65410F1-11

[COC1997] Cockeram BV, Buck RF, Wilson WL, (1997), Laboratory galling tests of several commercial cobalt-free weld hardfacing alloys, *Surface and Coatings Technology*, volume 94-95: pp. 495-500

[COC2002] Cockeram BV, (2002), The fracture toughness and toughening mechanisms of nickel-base wear materials, *Metals and Materials Transactions A*, volume 33A: pp. 33-56

[COL2003] Colaço R, Vilar R, (2003), Abrasive wear of metallic matrix reinforced materials, *Wear*, volume 255: pp. 643-650

[COR1986] Correa SM, Sundell RE, (1986), Computational and Experimental Study of the Fluid Flow in Weld Pools, *Modeling and Control of Casting and Welding Processes, Proceedings of the Third Conference*, Santa Barbara, CA, USA, Metallurgical Soc of AIME: pp. 211-227

[COU1993] Coudert JF, Delalondre C, Roumilhac P, Simonin O, Fauchais P, (1993), Modelling and Experimental study of a transferred arc stabilized with argon and flowing in a controlled atmosphere chamber filled with argon at atmospheric pressure, *Plasma Chemistry and Plasma Processing*, volume 13, number 3: pp. 399-432

[DAS2005] Das CR, Albert SK, Bhaduri AK, Sudha C, Terrance ALE, (2005), Characterisation of nickel based hardfacing deposits on austentic stainless steel, *Surface Engineering*, volume 21: pp. 290-296

[DAV1996] Davis RH, (1996), Velocities of Sedimenting Particles in Suspension, chapter 6, *Sedimentation of Small Particles in a Viscous Liquid*, Troy EM (ed.), Computational Mechanics Publications UK.

[DEH1968] DeHoff RT, Rhines FN, (1968), *Quantitative Microscopy, 1st Ed.*, McGraw-Hill Book Company, New York: pp. 45-53

[DEU1997A] Deuis RL, Yellup JM, Subramanian C, (1997), Aluminium composite coatings produced by plasma transferred arc surfacing technique, *Materials Science Technology*, volume 13, number 6: pp. 511-522

[DEU1997B] Deuis RL, Bee JV, Subramanian C, (1997), Investigation of interfacial structures of Plasma Transferred Arc deposited Aluminium-based composites by Transmission Electron Microscopy, *Scripta Materialia*, volume 37, number 6: pp. 721-727

[DEU1998] Deuis RL, Yellup JM, Subramanian C, (1998), Metal-matrix composite coatings by PTA surfacing, *Composites Science and Technology*, volume 58: pp.299-309.

[DIL2001] Dilthey U, Balachov B, Kabatnik I, (2001), Processing of Characterization of Graded Aluminium components with high hardness and improved wear behaviour using Plasma Transferred Arc Welding (PTAW) processes, *Ceramic Transactions*, volume 114: pp. 151-158

[DOU1990] Doumandis CC, Hardt DE, (1990), Simultaneous In-Process Control of Heat-Affected Zone and Cooling Rate during Arc Welding, *Welding Journal*, volume 6: pp. 186s-196s

[DOW1994] Dowden J, Kapadia P, (1994), Plasma arc welding: a mathematical model of the arc, *Journal of Physics D: Applied Physics*, volume 27: pp. 902-910

[DUP1995] DuPont JN, Marder AR, (1995), Thermal Efficiency of Arc Welding Processes, *Welding Journal*, volume 74: pp. 406s-416s

[EAS1969] Eastwood J, Matzen EJP, Young MJ, Epstein N, (1969), Random loose porosity of packed beds, *British Chemical Engineering*, volume 14, number 11: pp. 1542-1545

[EPS1962] Epstein N, Young MJ, (1962), Random Loose Packing of Binary Mixtures of Spheres, *Nature*, volume 196: pp. 885-886

[EVA1998] Evans DM, Huang D, McClure JC, Nunes AC, (1998), Arc Efficiency of Plasma Arc Welding, *Welding Journal*, Feb 1998: pp. 53s-58s

[FAN1999] Fan HG, Kovacevic R, (1999), Keyhole formation and collapse in plasma arc welding, *Journal of Physics D: Applied Physics*, volume 32: pp. 2902-2909

[FAN2003] Fan H, Ravala NK, Wilke III HC, Chin BA, (2003), Low-cost infrared sensing system for monitoring the welding process in the presence of plate inclination angle, *Journal of Materials Processing Technology*, volume 140: pp. 668-675

[FAR1998] Farson D, Richardson R, Li X, (1998), Infrared Measurement of Base Metal Temperature in Gas Tungsten Arc Welding, *Welding Journal*, volume 77: pp. 396s-401s

[FAU2004] Fauchais P, (2004), Understanding plasma spraying, *Journal of Physics D: Applied Physics*, volume 37: pp. R86-R108

[FEL1997] Feller RJ, Beckermann C, (1997), Modeling of solidification of metal matrix particulate composites with convection, *Metallurgical and Materials Transactions B*, volume 28B: pp. 1165-1183

[FIR2001] Firedrich CJ, Gadow R, Killinger A, Li C, (2001), IR Thermographic Imaging – a Powerful Tool for On-line Process Control for Thermal Spraying, *Thermal Spray 2001: New Surfaces for a New Millenium*, Berndt CC, Khor KA, Lugschieder EF (eds.), ASM International, Materials Park OH: pp. 779-786

[FIS1979] Fiszdon JK, (1979), Melting of Powder Grains in a Plasma Flame, *International Journal of Heat and Mass Transfer*, volume 22: pp. 749-761

[FLE1974] Flemings MC, (1974), Solidification Processing, *Metallurgical Transactions*, volume 5, October 1974: pp. 2121-2134.

[FRI1975] Friedman E, (1975), Thermomechanical analysis of the welding process using the finite element model, *Transactions of the ASME, Journal of Pressure Vessel Technology*, volume 97, Series J (3), August 1975: pp. 206-213

[FUD1997] Fudolig AM, Nogami H, Yagi J, (1997), Numerical Analysis of the Flow Characteristics and Temperature Distribution in Metal Beads subjected to Transferred Arc Plasma Impingement, *ISIJ International*, volume 37, number 6: pp. 630-636

[GAN1998] Ganz B, Krebs W, Koch R, Wittig S, (1998), Spectral Emissivity Measurements of Thermal Barrier Coatings, *AIAA/ASME Joint Thermophysics and Heat Transfer Conference*, volume 1: pp. 291-296

[GAO2001] Gao JW, Wang CY, (2001), Transport Phenomena During Solidification Processing of Functionally Graded Composites by Sedimentation, *Journal of Heat Transfer,* volume 123: pp. 368-375

[GAR1962] Gardon R, Cobonpue J, (1962), Heat Transfer between a Flat Plate and Jets of Air Impinging on It, *International Developments in Heat Transfer*, ASME, New York: pp. 454-460

[GAU1995] Gauthier M, (1995), *Engineered Materials Handbook*, Materials Park, OH, ASM International.

[GLI1979] Glickenstein SS, (1979), *Arc Physics and Weld Pool Behaviour*, Cambridge: The Welding Institute: pp. 1-16

[GOL1984] Goldak J, Chakravarthi A, Bibby M, (1984), A New Finite Element Model for Welding Heat Sources, *Metallurgical Transactions B*, volume 15B: pp. 299-305

[GOL1986] Goldak J, Bibby M, Moore J, House R, Patel B, (1986), Computer Modeling of Heat Flow in Welds, *Metallurgical Transactions B*, volume 17B: pp. 587-600

[GOO1998] Goodarzi M, Choo R, Takasu T Toguri JM, (1998), The effect of the cathode tip angle on the gas tungsten arc welding arc and weld pool: II, The mathematical model for the weld pool, *Journal of Physics D: Applied Physics*, volume 31: pp. 569-583

[GRE2008] Green DW, Perry RH, (2008), *Perry's Chemical Engineers' Handbook (8th Edition)*. McGraw-Hill.

[GRI1995] Grigorescu IC, Di Rauso C, Drira-Halouani R, Lavelle B, Di Giampaolo R, Lira J, (1995), Phase Characterization in Ni alloy-hard carbide composites for fused coatings, *Surface and Coatings Technology*, volume 76-77; pp. 494-498.

[GUB2005] Gubish M, Liu Y, Krischok S, Ecke G, Spiess L, Schaefer JA, Knedlik C**,** (2005), Tribological characteristics of WC1−x, W2C and WC tungsten carbide films, *Tribology and Interface Engineering Series*, Volume 48: pp. 409-417

[GUR2007] Gurumoorthy K, Kamaraj M, Prasad Rao K, Sambasiva Rao A, Venugopal S, (2007), Microstructural aspects of plasma transferred arc surface Ni-based hardfacing alloy, *Materials Science Engineering A*, volume 456: pp. 11-19

[GUT1975] Guthrie RIL, Clift R, Henein H, (1975), Contacting problems associated with aluminum and ferro-alloy additions in steelmaking-hydrodynamic aspects, *Metallurgical Transactions B*, volume 6B: pp. 321-329

[GUT1976] Guthrie RL, Gourtsoyannis L, Henein H, (1976), An experimental and mathematical evaluation of shooting methods for projecting buoyant alloy additions into liquid steel baths, *Canadian Metallurgical Quarterly*, volume 15, number 2: pp. 145-153

[HAL1992] Hallen H, Mathesius H, Ait-Mekideche A, Hettiger F, Morkramer U, Lugscheider E, (1992), New Applications for High Power PTA Surfacing in the Steel Industry, *Proc. Int. Thermal Spray Conference*, Orlando, Florida, 28 May-5 June 1992, ASM International: pp. 899-902

[HAM1992] Hamar-Thibault S, Valignat N, Lebaili S, (1992), Composition of M_6C carbides formed in nickel-based hardfacing alloys, *International Congress of X-ray Optics and Microanalysis*, Manchester, Inst. Phys. Conf. Ser. No. 130, chapter 2: pp. 189-192

[HAN1992] Hanumanth GS, Irons GA, Lafreniere S, (1992), Particle Sedimentation during Processing of Liquid Metal-Matrix Composites, *Metallurgical Transactions B*, volume 23B: pp. 753-762

[HAN1996] Hanumanth GS, Irons GA, (1996), Solidification of Particle-Reinforced Metal-Matrix Composites, *Metallurgical and Materials Transactions B*, volume 27B: pp. 663-671

[HAS2002] Hashim J, Looney L, Hashmi MSJ, (2002), Particle distribution in cast metal matrix composites – Part I, *Journal of Materials Processing Technology*, volume 123: pp. 251-257

[HER1993] Herrström C, Hallen H, Ait-Mekideche A, Lugscheider E, (1993), Factorial analysis applied to the PTA process, *TS93 Thermal Spraying Conference Proceedings*, DVS Berichte, number 152, Aachen; 3-5 Mar. 1993: pp. 409-412

[HIC1991] Hicken GK, Campbell RD, Daumeyer GJ, Madigan RB, Marburger SJ and Young B, (1991), Gas Tungsten Arc Welding, *AWS Welding Handbook, 8th Edition*, volume 2, chapter 3, American Welding Society: pp. 74-107

[HOL1992] Holman JP, (1992), *Heat Transfer, 7th Ed.*, London, McGraw-Hill.

[HOS2008] Private communication with S. Hoskins, Syncrude Canada Inc. (2008).

[HSU1983] Hsu KC, Etemadi K, Pfender E, (1983), Study of the free-burning high-intensity argon arc, *Journal of Applied Physics*, volume 54, number 3: pp. 1293-1301

[HSU1988] Hsu YF, Rubinksy B, (1988), Two dimensional heat transfer study on the keyhole plasma arc welding process, *International Journal of Heat and Mass Transfer*, volume 31: pp. 1409-1421

[HUA2007] Huang RS, Liu LM, Song G, (2007), Infrared temperature measurement and interference analysis of magnesium alloys in hybrid laser TIG welding process, *Materials Science and Engineering A*, volume 447: pp. 239-243

[INC1996] Incropera FP, DeWitt DP, (1996), *Fundamentals of Heat and Mass Transfer, 4th Ed.*, John Wiley and Sons, Inc.

[IRO1995] Irons GA, Owusu-Doahen K, (1995), Settling and Clustering of Silicon Carbide Particles in Aluminum Metal Matrix Composites, *Metallurgical and Materials Transactions B*, volume 26B: pp. 981-989

[JEN2001] Jenney CL, O'Brien A (ed.), (2001), *Welding Handbook, 9th Edition*, Volume 1 - Chapter 3: Heat Flow in Welding, American Welding Society, Miami Florida.

[JIL2003] Jiluan P, (2003), Summary of colorimetric imaging method, *Arc Welding Control*, CRC Press, Boca Raton FL.

[JON1994] Jonsson PG, Szekely J, Choo RTC, Quinn TP, (1994), Mathematical models of transport phenomena associated with arc-welding processes: a survey, *Modelling and Simulation in Materials Science and Engineering*, volume 2: pp. 995-1016

[JOU2003] Jou M, (2003), Experimental Study and Modeling of GTA Welding Process, *Journal of Manufacturing Science and Engineering*, volume 125: pp. 801-808

[KAM1991] Kammer PA, Weinstein M, DuMola RJ, (1991), Characteristics and Applications for Composite Wear-Resistant Overlays, *Proc.4th Nat. Thermal Spray Conference*, Pittsburgh, PA, USA, 4-10 May 1991, ASM Int. 1991: pp. 513-518

[KEA1993] Keanini RG, Rubinsky B, (1993), Three dimensional simulation of the plasma arc welding process, *International Journal of Heat and Mass Transfer*, volume 36: pp. 3283-3298

[KEY1993] Key, FJ, (1993), Arc Physics of Gas-Tungsten Arc Welding, *ASM Handbook Volume 6 – Welding and Joining*, ASM International Pub.

[KIM1997A] Kim WH, Fan HG, Na SJ, (1997), A mathematical model of gas tungsten arc welding considering the cathode and the free surface of the weld pool, *Metallurgical Transactions B*, volume 28B, August 1997: pp. 679-686

[KIM1997B] Kim WH, Fan HG, Na SJ, (1997), Effect of various driving forces on heat and mass transfer in arc welding, *Numerical Heat Transfer Part A*, volume 32: pp. 633-652

[KIM1999] Kim HJ, Kim YJ, (1996), Wear and Corrosion Resistance of PTA Weld Surfaced Ni and Co Based Alloy Layers, *Surface Engineering*, volume 15 number 6: pp. 495-501

[KIM2001] Kim BH, Suhr DS, (2001), Characteristics of HVOF-Sprayed WC-Co Cermet Coatings Affected by WC Particle Size and Fuel/Oxygen Ratio, *Materials Transactions*, volume 42, number 5: pp. 833-837

[KIM2003] Kim CH, Zhang W, DebRoy T, (2003), Modeling of temperature field and solidified surface profile during gas-metal arc fillet welding, *Journal of Applied Physics*, volume 94: pp. 2667-2679

[KNO1981] Knotek O, Reimann H, Lohage P, (1981), Reactions between Ni-Cr-B-Si matrixes and carbide additives in coatings during fusion treatment, *Thin Solid Films*, volume 83: pp. 361-367

[KOB1999] Kobayashi M, Ono A, Otsuki M, Sakate H, Sakuma F, (1999), A database of normal spectral emissivities of metals at high temperatures, *International Journal of Thermophysics*, volume 20: pp. 299-308

[KOU 1985] Kou S, Sun KK, (1985), Fluid flow and weld penetration in stationary arc welds, *Metallurgical Transactions A*, volume 16A number 2, February 1985: pp. 203-213

[KRA1989] Kraus HG, (1989), Experimental Measurement of Stationary SS 304, SS 316L and 8630 GTA Weld Pool Surface Temperatures, *Welding Journal*, volume 68: pp. 269s-279s

[KRE1998] Kreye H, Schwetzke R, Buschinelli A, Boccanera L, (1998), Cavitation erosion resistant coatings produced by thermal spraying and by weld cladding, *Proc. 15th Int. Thermal Spray Conference*, Nice, France, 25-29 May 1998: pp. 269-273

[KRE2005] Kreith F, Goswami DY (eds.), (2005), *The CRC handbook of mechanical engineering [electronic resource]*, 2nd ed., Boca Raton, FL, CRC Press.

[KRI1968] Krivosheya VE, (1968), Influence of deoxidizing agents on weld porosity in argon-arc welding of nickel, *Chem & Petroleum Eng (English translation of Khimicheskoe i Neftyanoe Mashinostroenie)*, number 11-12: pp. 918-920

[KUR2006] Kurlov AS, Gusev AI, (2006), Tungsten Carbides and W-C Phase Diagram, *Inorganic Materials*, volume 42: pp. 156-163

[LAJ1988] Lajoye L, Suery M, (1988), Modelling of particle segregation during centrifugal casting of Al-matrix composites, *Cast Reinforced Metal Composites*, Fishman SG, Dhingra AK (ed), ASM Materials Park, OH: pp. 15-20

[LAN1959] Landau LD, Lifshitz EM, (1959), *Fluid Mechanics*, Pergamon Press, London.

[LAN1986] Lancaster JF, (1986), *The Physics of Welding, 2nd Ed*., Pergamon, Oxford.

[LEE1985] Lee YC, Chyou YP, Pfender E, (1985), Particle Dynamics and Particle Heat and Mass Transfer in Thermal Plasmas. Part II. Particle Heat and Mass Transfer in Thermal Plasmas. *Plasma Chemistry and Plasma Processing*, volume 5, number 4: pp. 391-414

[LEE1988] Lee HE, (1988), Heat transfer of particles in plasma flow, *Journal of Physics D: Applied Physics*, volume 21: pp. 73-78

[LEE2002] Lee JH, Cho YT, Na SJ, (2002), A numerical analysis of a gas tungsten arc welding considering the current density and temperature distribution on the electrode surface, *Journal of Engineering Manufacture*, volume 216: pp. 1151-1121

[LEW1973] Lewis JA, Gauvin WH, (1973), Motion of Particles Entrained in a Plasma Jet, *AIChE Journal*, volume 19: pp. 982-990

[LI1997] Li ZY, Wu CS, (1997), Analysis of the transport phenomena in the interfacial region between TIG arcs and weld pools, *Computational Materials Science*, volume 8: pp. 243-250

[LI1999] Li Q, Lei TC, Chen WZ, (1999), Microstructural characterization of WC_p reinforced Ni-Cr-B-Si-C composite coatings, *Surface and Coatings Technology*, volume 114: pp. 285-291

[LI2000] Li PJ, Zhang YM, (2000), Analysis of an Arc Light Mechanism and its application in sensing of the GTAW process, *Welding Journal*, Sept 2000: pp. 252s-260s

[LI2001] Li P, Zhang Y, (2001), Robust Sensing of Arc Length, *IEEE Transactions on Instrumentation and Measurement*, volume 50, number 3, June 2001: pp. 697-704

[LIA1997] Liang C, Lin ST, (1997), Sintering of injecton moulded WC-7wt% Ni in a hydrogen atmosphere, *Journal of Materials Science*, volume 32: pp. 3207-3212

[LIM1998B] Lim LC, Ming Q, Chen ZD, (1998), Microstructures of laser-clad nickel-based hardfacing alloys, *Surface and Coatings Technology*, volume 106: pp. 183-192

[LIN1986] Lin ML, Eagar TW, (1986), Pressures produced by gas tungsten arcs, *Metallurgical Transactions B*, volume 17B: pp. 601-607

[LIN1999] Lin CH, Wu CL, Chiang CH, (1999), Analysis of mold flow and microstructures of die casting in Al alloy/SiC (p) composites, *Journal of Materials Science*, volume 34: pp. 2229-2240

[LOU2003] Lou D, Hellman J, Luhulima D, Liimatainen J, Lindroos VK, (2003), Interactions between tungsten carbide (WC) particulates and metal matrix in WC-reinforced composites, *Materials Science and Engineering A*, volume 340: pp. 155-162

[LUK1982] Lukens WE, Morris RA, (1982), Infrared Temperature Sensing of Cooling Rates for Arc Welding Control, *Welding Journal*, volume 61: pp. 27-33

[MAN1986] Mandersloot WGB, Scott KJ, Geyer CP, (1986), Sedimentation in the hindered settling regime, In: Muralindhara HS (Ed.), *Advances in Solid-Liquid Separation*, Battelle Press, Columbus, OH: pp. 63-77

[MAT2009] Matteï S, Grevey D, Mathieu A, Kirchner L, (2009), Using infrared thermography in order to compare laser and hybrid (laser+MIG) welding processes, *Optics and Laser Technology*, volume 41: pp. 665-670

[MCK1986] McKelliget J, Szekely J, (1986), Heat Transfer and Fluid Flow in the Welding Arc, *Metallurgical Transactions A*, volume 17A: pp. 1139-1148

[MCK1997] McKee B, Wu JBC, (1997) An overview of wear-resistant alloys for the mining industry, *CIM Bulletin*, volume 90, number 1012: pp. 71-74.

[MEN1999] Mendez PF, Niece KL, Eagar TW, (1999), Humping formation in high current GTA welding, *Proceedings of the International Conference in Joining of Advanced and Specialty Materials II*, Cincinnati OH, November 1999.

[MER1999] Mercer T, Bissel PR, Gotaas JA, Gilson RG, (1999), Hindered settling of particulate dispersions, *Journal Magnetism and Magnetic Materials*, volume 193: pp. 284-287

[MET1975] Metcalfe JC, Quigley MBC, (1975), Heat Transfer in Plasma-Arc Welding, *Welding Journal*, volume 54: pp. 99s-103s

[MIL1960] Milner DR, Salter GR, Wilkinson JB, (1960), Arc Characteristics and their Significance in Welding, *British Welding Journal*, volume 7, number 2: pp 73 – 88

[MIL1968] Milner DR, Apps RL, (1968), *Introduction to Welding & Brazing*, Pergamon Press Publications.

[MOR1999] Mortensen D, (1999), Mathematical Model of the Heat and Fluid Flows in Direct-Chill Casting of Aluminum Sheet Ingots and Billets, *Metallurgical and Materials Transactions B*, volume 30B: pp. 128

[MOS1980] Moskowitz LN, Klar E, (1980), Spray-and-Fuse Self-Fluxing Alloy Powders, *United States Patent 4192672*, March 11, 1980.

[MUR1999] Murugan S, Kumar PV, Gill TPS, Raj B, Bose MSC, (1999), Numerical modeling and experimental determination of temperature distribution during manual metal arc welding, *Science and Technology of Welding and Joining*, volume 4, number 6: pp. 357-364

[NES1962] Nestor OH, (1962), Heat Intensity and Current Density Distribution at the Anode of High Current, Inert Gas Arcs, *Journal of Applied Physics*, volume 33, number 5: pp. 1638-1648

[NEV2006] Neville A, Reza F, Chiovelli S, Revega T, (2006), Assessing Metal Matrix Composites for Corrosion and Erosion-Corrosion Applications in the Oil Sands Industry, *Corrosion*, volume 62: pp. 657-675

[NRC1987] Associate Committee on Tribology, (1987), *A Strategy for Tribology in Canada, Enhancing Reliability and Efficiency Through the Reduction of Friction and Wear*, National Research Council, Canada Report Number 26556.

[OBE1992] Oberländer BC, Lugscheider E, (1992), Comparison of properties of coatings produced by laser cladding and conventional methods, *Materials Science and Technology*, volume 8 : pp. 657-665.

[OGA1996] Ogawa K, Hijikata K, (1996), Experimental and Theoretical study on heat transfer of an impinging plasma jet, *Transport Phenomena in Materials Processing, ASME Heat transfer division (Publications HTD)*, volume 336: pp. 1-8

[OKA1988] Okada A, Kasugai T, Hiraoka K, (1988), Heat source model in arc welding and evaluation of weld heat affected zone, *Transactions of the Iron and Steel Institute of Japan*, volume 28: pp. 876-882

[OLS1963] Olsen HN, (1963), The electric arc as a light source for quantitative spectroscopy, *Quantitative Spectroscopy and Radiative Transfer*, volume 3: pp. 305-333

[OME2007] OMEGA, (2007), http://www.omega.com/literature/transactions/volume1/emissivitya.html

[OUR2001] Ourdjini A, Chew KC, Khoo BT, (2001), Settling of silicon carbide particles in cast metal matrix composites, *Journal of Materials Processing Technology*, volume 116: pp. 72-76

[PAL1975] Paley Z, Hibbert PD, (1975), Computation of Temperatures in Actual Weld Designs, *Welding Journal*, Nov 1975: pp. 385s-392s

[PAT1998] Patchett BM, Welding Metallurgy, (1998), *The Metals Blue Book – Welding Filler Metals, 2nd ed.*, CASTI Publication and American Welding Society.

[PAV1969] Pavelic V, Tanbakuchi R, Uyehara OA, Myers PS, (1969), Experimental and Computed Temperature Histories in Gas Tungsten Arc Welding of Thin Plates, *Welding Journal*, volume 48: pp. 295s-305s

[PIE1996] Pierson HO, (1996), *Handbook of Refractory Carbides and Nitrides*, William Andrew Publishing.

[PIN1973] Pinfold BE, Jubb JEM, (1973), Welding Technology Data Sheet 39--Plasma-Arc Welding. Pt. 1, *Welding and Metal Fabrication*, volume 41, number 11, November 1973: pp. 391-393

[PLA2005] *http://www.plasmateam.com/Products/PTA_torch/Torch-Principle/a_pta5-eng.gif*, accessed October 27, 2005

[POS1986] Posthill JB, Edmonds DV, (1986), Matrix and interfacial precipitation in the W-Ni-Fe system, *Metallurgical and Materials Transactions A*, volume 17A, Number 11 : pp. 1921-1934

[QIA1998] Qian Ming, Lim LC, Chen ZD, (1998), Laser cladding of nickel-based hardfacing alloys, *Surface and Coatings Technology*, volume 106: pp. 174-182

[QUI1973] Quigley MBC, Richards PH, Swift-Hook DT, Gick AEF, (1973), Heat flow to the workpiece from a TIG welding arc, *Journal of Physics D: Applied Physics*, volume 6: pp. 2250-2259

[RAI2007] Rai R, Roy GG, DebRoy T, (2007), A computationally efficient model of convective heat transfer and solidification characteristics during keyhole mode laser welding, *Journal of Applied Physics*, volume 101: pp. 054909

[RAL2008] Ralchenko Y, Kramida AE, Reader J and NIST ASD Team (2008), *NIST Atomic Spectra Database* (version 3.1.5), [Online]. Available: http://physics.nist.gov/asd3 [2009, August 23]. National Institute of Standards and Technology, Gaithersburg, MD.

[RAN1986] Rangaswamy S, Herman H, Metallurgical Characterization of WC-Co coatings, *Advances in Thermal Spraying*, Pergamon Press, 1986, 101-110.

[RAT1981] Ratanapupech P, Bautista RG, (1981), Normal spectral emissivities of liquid iron, liquid nickel, and liquid iron-nickel alloys, *High Temperature Science*, volume 14: pp. 269-283

[RAV2001] Ravichandran G, (2001), Solidification behaviour in plasma arc welding, *Sãdhanã*, volume 26, parts 1 & 2, February-April 2001: pp. 199-211

[REI1965] Reif F, (1965), *Fundamentals of Statistical and Thermal Physics*, McGraw-Hill, Boston.

[RIC1954] Richardson JF, Zaki WN, (1954), Sedimentation and fluidization: part 1, *Transactions of the Institute of Chemical Engineering*, volume 32: pp. 35-53

[ROS1941] Rosenthal D, (1941), Mathematical Theory of Heat Distribution During Welding and Cutting, *Welding Journal*, volume 20: pp. 220s-234s

[ROS1946] Rosenthal D, (1946), The theory of moving sources of heat and its application to metal treatments, *Transactions of the ASME*, volume 68, number 8: pp. 849-866

[RUL1995] Rulison AJ, Rhim WK, (1995), Constant pressure specific heat to hemispherical total emissivity ratio for undercooled liquid nickel, zirconium, and silicon, *Metallurgical and Materials Transactions B*, volume 26B: pp. 503-508

[RYK1974] Rykalin NN, (1974), Energy sources used for welding, *Welding in the world*, volume 9/10: pp. 227-248

[SAL1985] Salzman GA, Aufderhaar WB, (1985), New antiwear coatings applied by plasma transferred arc wear surfacing, *Lubrication Engineering*, volume 41, issue 4: pp. 233-241

[SAL1986] Saltzman GA, (1986), Carbides Add Muscle to PTA Antiwear Coatings, *Metal Progress*, volume 129: pp. 25-30

[SCH1991] Schneider Jr. SJ, Shaffer PTB, (1991), Engineering Properties of Carbides, *Engineered Materials Handbook*, Volume 4, ASM International: pp. 804-811

[SIE1981] Siegel R, Howell JR, (1981), *Thermal Radiation Heat Transfer, 2nd ed*, Hemisphere Publishing Company, New York, NY

[SIN2000] Singh N, Razafinimanana M, Hlina J, (2000), Determination of plasma velocity from light fluctuations in a dc plasma torch, *Journal of Physics D: Applied Physics*, volume 33: pp. 275-279

[STO1880] Stokes G, (1880), *Mathematical and physical papers*, volume 1, Cambridge University Press, Cambridge, UK.

[SU1997A] Su YL, Chen KY, (1997), Effect of Alloy Additions on Wear resistance of Nickel Based Hardfacing, *Welding Journal*, volume 76: pp. 43s-150s

[SU1997B] Su YL, Chen KY, (1997), The influence of niobium, chromium, molybdenum and carbon on the sliding wear behavior of nickel-base hardfacing alloys, *Wear*, volume 209: pp. 160-170

[SUD2008] Sudha D, Shankar P, Subba Roa RV, Thirumurugesan R, Mijayalakshmi V, Raj B, (2008), Microchemical and microstructural studies in a PTA weld overlay of NiCrBSi alloy on AISI 304L stainless steel, *Surface and Coatings Technology*, volume 202: pp. 2103-2112

[TAJ1993] Tajima S, Hirano S, (1993), Synthesis and properties of Fe_3C film by r.f. magnetron sputtering, *Journal of Materials Science*, Volume 28, Number 10, Jan 1993: pp. 2715-2720

[TAN1999] Tanaka M, Ushio M, (1999), Plasma state in free burning argon arc and its effect on anode heat transfer, *Journal of Physics D: Applied Physics*, volume 32: pp. 1153-1162

[TAN2002] Tanaka M, Terasaki H, Ushio M, Lowke JJ, (2002), A Unified Numerical Modelling of Stationary Tungsten Inert Gas Welding Process, *Metallurgical Transactions A*, volume 33A: pp. 2043-2052

[THE1999] Thevik HJ, Mo A, Rusten T, (1999), A Mathematical Model for Surface Segregation in Aluminum Direst Chill Casting, *Metallurgical and Materials Transactions B*, volume 30B: pp. 139.

[TOM1998] Tomita T, Takatani Y, Okita K, Harada Y, (1998), Improvement of wear property of NbC/high Cr-high Ni overlay alloy coating formed by PTA welding process, *Proceedings from the 15th International Thermal Spray Conference, volume 1*, Nice, France: pp. 253-258

[TOU1970] Toulokian, YS (ed.), (1970), *Thermophysical properties of matter; [the TPRC data series; a comprehensive compilation of data.]*, volume 7, New York, IFI/Plenum.

[TSA1985] Tsai NS, Eagar TW, (1985), Distribution of the Heat and Current Fluxes in Gas Tungsten Arcs, *Metallurgical Transactions B*, volume16B: pp. 841-846

[TU2006] Tu SY, Jean MD, Wang JT, Wu CS, (2006), A robust design in hardfacing using a plasma transfer arc, *International Journal of Advanced Manufacturing Technology*, volume 27: pp. 889-896

[USH1982] Ushio M, Matsuda F, (1982), Mathematical Modelling of Heat Transfer of Welding Arc (Part 1), *Transactions of JWRI*, volume 11: pp. 7-15

[VAN2000] van Vugt L, Froyen L, (2000), Gravity and temperature effects on particle distribution in Al-Si/SiC composites, *Journal of Materials Processing Technology*, volume 104: pp. 133-144

[VER1998] Verma A, Jog MA, (1998), Analysis of Heat Transfer to a Spectrum of Particles in Plasma Spray Coating Process, *Proceedings of the ASME Heat Transfer Division, HTD*, volume 361-4: pp. 287-294

[WAN1998] Wan YP, Prasad V, Wang GX, Sampath S, (1998), Modeling of Powder Particle Heating, Melting and Evaporation in Plasma Spraying Processes, *Proceedings of the ASME Heat Transfer Division, HTD*, volume 361-4: pp. 67-77

[WAN1999] Wan YP, Prasad V, Wang GX, Sampath S, Fincke JR, (1999), Model and Powder Particle Heating, Melting, Resolidification and Evaporation in Plasma Spraying Processes, *Journal of Heat Transfer*, volume 121: pp. 691-699

[WEN2003] Wen Y, Jog MA, (2003), Effect of Temperature Dependent Properties and Particle Shape on Heat Transfer in Plasma Flow, *Proceedings of the ASME Heat Transfer Division, HTD*, volume 374-3: pp. 217-220

[WIL2006] Wilden J, Bergmann JP, Frank H, (2006), Plasma Transferred Arc Welding – Modeling and Experimental Optimization, *Journal of Thermal Spray Technology*, volume 15, number 4: pp. 779-784

[WLO1993] Wlosinski W, Mustafa AS, Pikor N, (1993), Plasma arc hardfacing of steel by used composite powders, *Proceedings of the 6th International Conference of Joining of Materials*, Denmark, 5-7 Apr 1993, JOM-Inst. (Denmark): pp. 229-233

[WU1991] Wu MK, McFeaters JS, Welch BJ, Stephens RL, (1991), Heat transfer to a particle in a thermal plasma, *Chemical Engineering Research and Design*, volume 69, number 1: pp. 21-24

[WU2001] Wu S, Nakae H, Kanno T, You Y, (2001), Zone-melted unidirectional solidification of particulate dispersed composites, *Journal of Materials Science*, volume 36: pp. 225-229

[WU2003] Wu P, Zhou CZ, Tang XN, (2003), Microstructural characterization and wear behaviour of laser cladding nickel-based and tungsten carbide composite coatings, *Surface and Coatings Technology*, volume 166: pp. 84-88

[WU2004] Wu CS, Zhao PC, Zhang YM, (2004), Numerical Simulation of Transient 3-D Surface Deformation of a Completely Penetrated GTA Weld, *Welding Journal*, volume 83: pp. 330s-335s

[XIA2009] Xiao B, Xing JD, Feng J, Zhou CT, Li YF, Su W, Xie XJ, Cheng YH, (2009), A comparative study of Cr_7C_3, Fe_3C and Fe_2B in cast iron both from *ab initio* calculations and experiments, *Journal of Physics D: Applied Physics,* volume 42: pp. 115415

[XIB1998] Xibao W, Hua L, (1998), Metal powder thermal behaviour during the plasma transferred-arc surfacing process, *Surface and Coatings Technology*, volume 106: pp. 156-161

[XIO2006] Xiong HB, Ma Y, Zheng LL, (2006), Multiphase flow in directional solidification of metal matrix particulate composites, *Modelling and Simulation of Materials Science and Engineering*, volume 14: pp. 445-463

[XU2003] Xu DY, Wu XC, Chen X, (2003), Motion and heating of non-spherical particles in a plasma jet, *Surface and Coatings Technology*, volume 171: pp. 149-156

[YAR2005] Yarmuch MAR, (2005), *Effect of Welding Parameters on the Plasma Transferred Arc Welding (PTAW) Process for Autogeneous Beads and 410SS-WC Overlays*, MSc thesis, University of Alberta, Edmonton, Canada.

[YU1993] Yu AB, Standish N, (1993), Characterisation of non-spherical particles from their packing behaviour, *Powder Technology*, volume 74: pp. 205-213

[ZHA2003] Zhang YM, Hida M, Sakakibara A, Takemoto Y, (2003), Effect of WC addition on microstructures of laser melted Ni-based alloy powder, *Surface and Coatings Technology*, volume 169-170: pp. 384-387

[ZHA2006] Zhao M, Liu A, Guo M, Liu D, Wang Z, Wang C, (2006), WC reinforced surface metal matrix composite produced by plasma melt injection, *Surface and Coatings Technology*, volume 201: pp. 1655-1659

[ZHU1995] Zhu P, Lowke JJ, Morrow R Haidar J, (1995), Prediction of anode temperature of free burning arcs, *Journal of Physics D: Applied Physics*, volume 28: pp. 1369-1376

[ZHU2002] Zhu XK, Chao YJ, (2002), Effects of temperature-dependent material properties on welding simulation, *Computers and Structures*, volume 80: pp. 967-976

[ZOU1996] Zou RP, Yu AB, (1996), Evaluation of the packing characteristics of mono-sized non-spherical particles, *Powder Technology*, volume 88: pp. 71-79

Appendix A - Powder

A.1 Conversion between volume and mass percent of WC

The conversion between vol% WC and mass% of Ni and WC is shown in Table A.1. This conversion is required for accurately mixing powders with a varying amount of WC.

Table A.1: Conversion between volume percent WC and mass percent WC

vol%WC	*mass%WC*	*mass%Ni*
0	0.0	100.0
5	8.6	91.4
10	16.6	83.4
15	24.0	76.0
20	30.9	69.1
25	37.3	62.7
30	43.4	56.6
35	49.0	51.0
40	54.4	45.6
45	59.4	40.6
50	64.1	35.9
55	68.6	31.4
60	72.8	27.2
65	76.8	23.2
70	80.7	19.3
75	84.3	15.7
80	87.7	12.3

A.2 Sieve Analysis Results

The matrix and carbide powders were sieved to measure the particle size range. The results are shown in Figures A.2 through A.4.

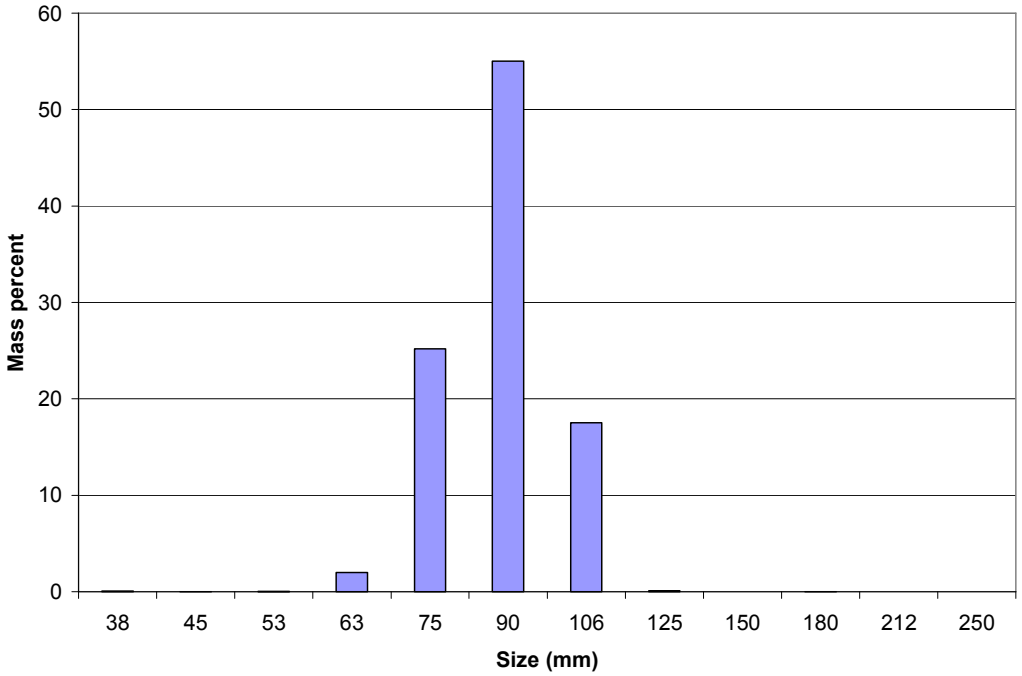

Figure A.1: Sieve analysis for angular WC powder.

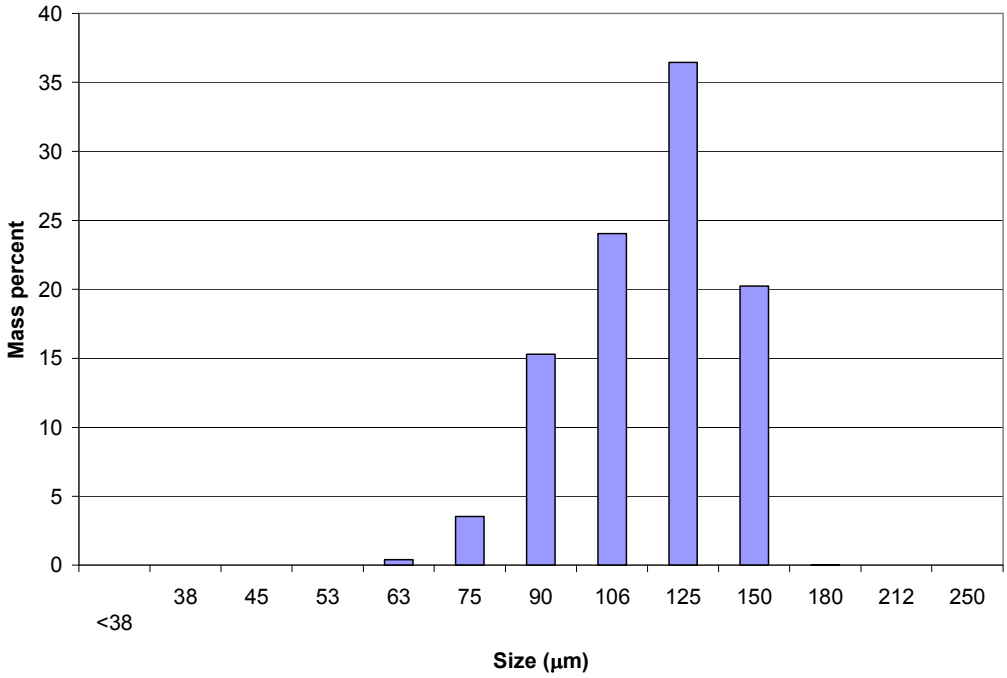

Figure A.2: Sieve analysis for NiCrBSi powder.

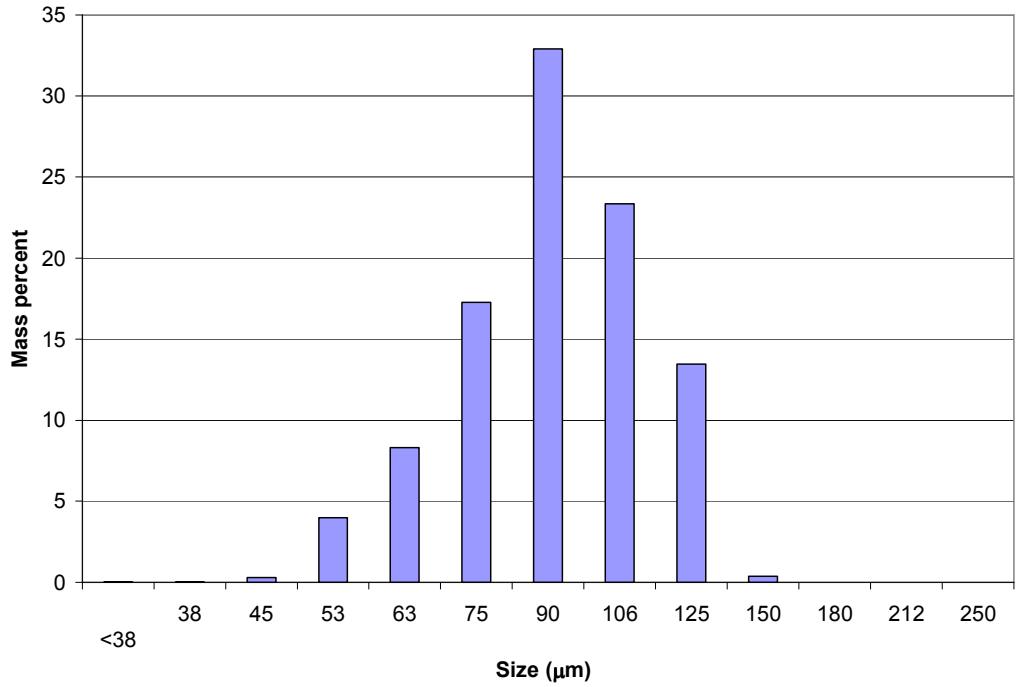

Figure A.3: Sieve analysis for commercial pre-mixed WC-NiCrBSi powder.

A.3 Complex Carbide in 50 vol%WC-NiCrBSi

Shown in Figure A.4 is the spectrum for the thread-like complex carbide found in the voided area of the 50%WC sample. Two issues arise from this spectrum:

1. Overlap of Si and W

   Since W overlaps the only Si peak, it cannot be concluded that Si is indeed present in the spectrum. A comparison of the peak heights can indicate trace amounts of Si, however, the value is small and is likely not accurate. If no Si was present in the powder, it could be stated that Si artifacts are introduced. If no higher W peaks were apparent, then the peak at 1.74 keV would have been attributed only to Si.

2. Presence of Fe, Ti (and Nb)

   Not all the elements identified in the spectrum were present in the chemical composition certification of the original powder. The powder was laid on a steel substrate, with up to 5% dilution occurring. Interactions between Fe, W and Ni are thermodynamically feasible and

favoured. Nb and Ti are found in microalloyed steels and are strong carbide formers. The amount of C freed from the dissolution of WC is quickly formed as a carbide.

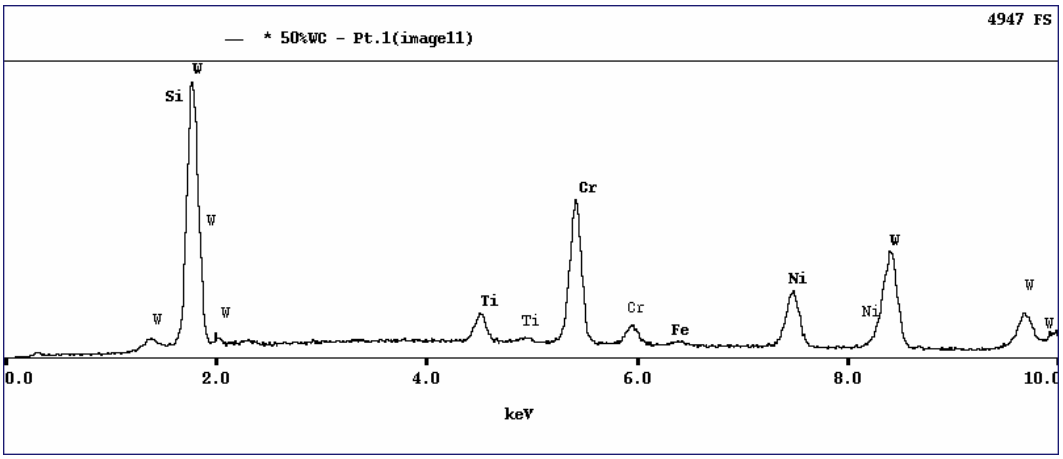

Figure A.4: EDX spectrum of a complex carbide from a 50% WC sample

Appendix B – Properties

B.1 Argon

The properties of the argon gas at elevated temperatures are shown in Figures B.1-B.6. These properties are critical in determining the fluid mechanics of the gas. It can be seen that they vary significantly over the range of temperatures explored. The curves were fit with a polynomial function such that the R-squared value exceeded 0.99. A summary of the property equations is listed in Table B.1. Data was obtained from **Tekna Plasma Systems Inc.**, 2935 boul. Industriel, Sherbrooke, Québec, J1L 2T9, Canada.

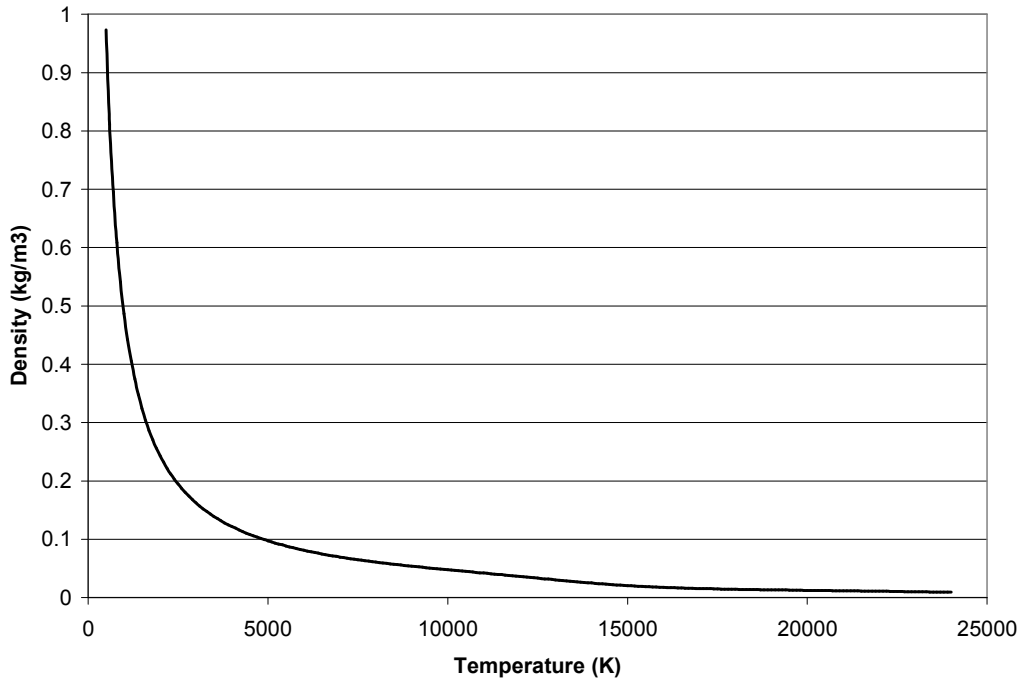

Figure B.1: Density of argon gas at elevated temperatures.

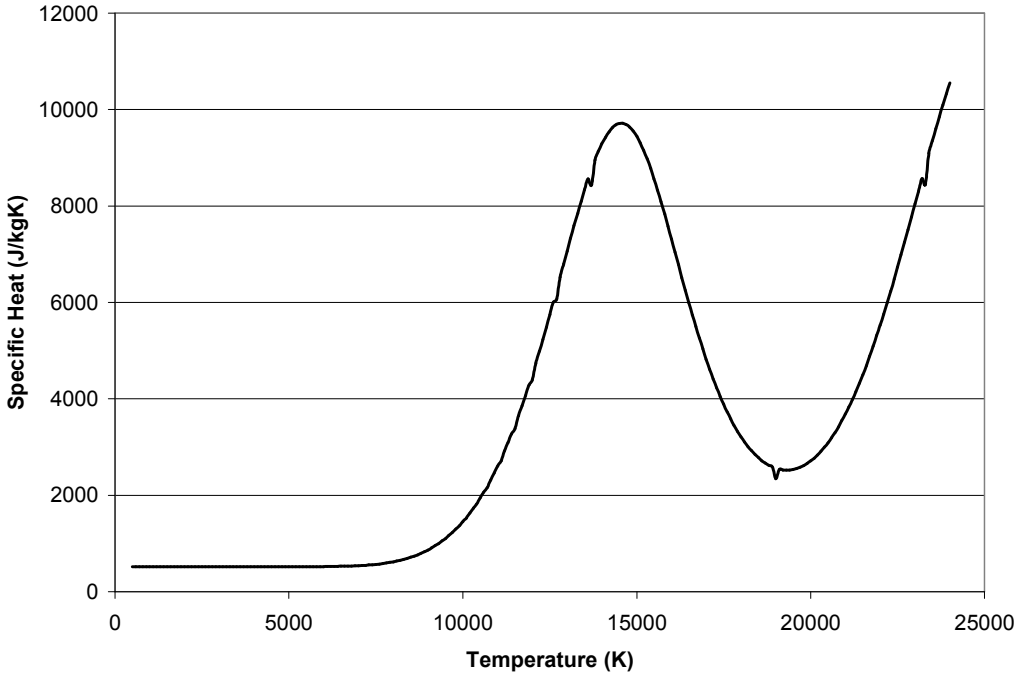

Figure B.2: Specific heat of argon gas at elevated temperatures

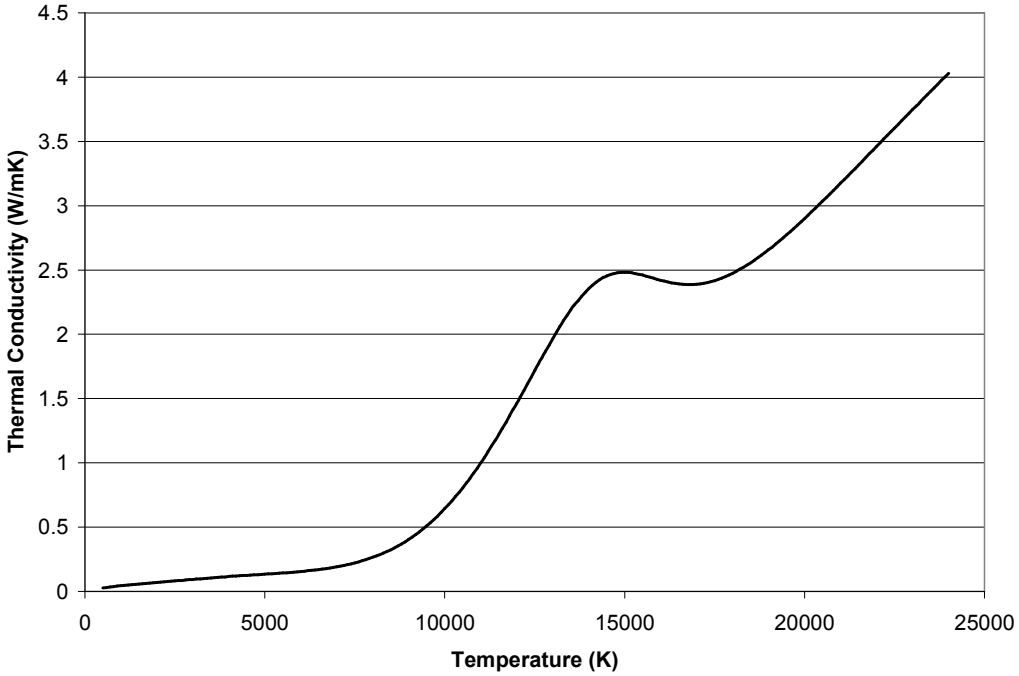

Figure B.3: Thermal conductivity of argon gas at elevated temperatures.

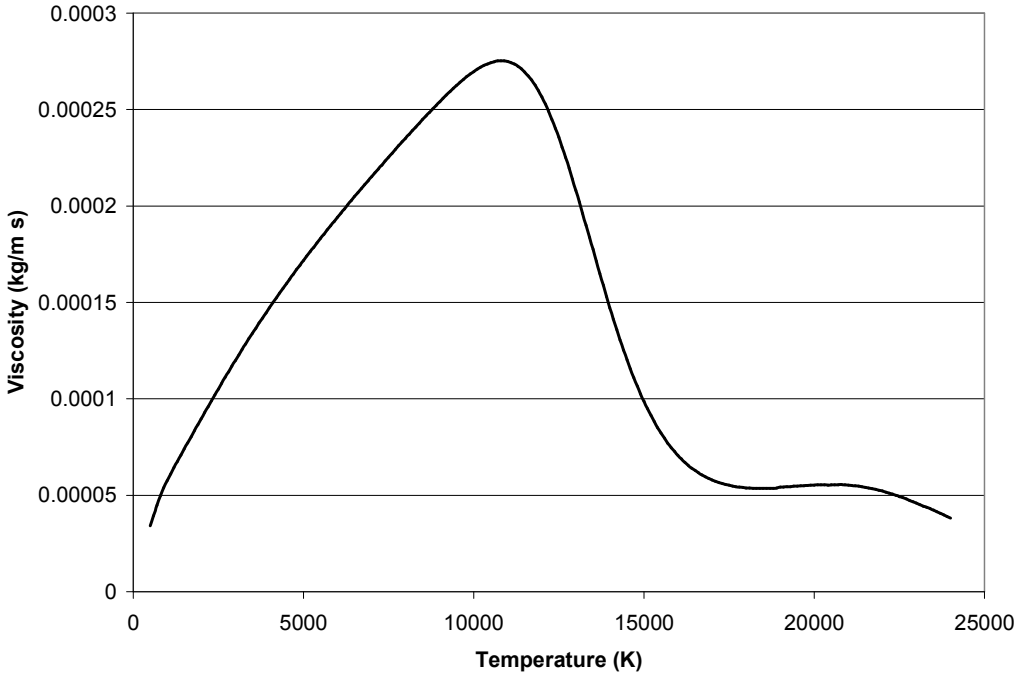

Figure B.4: Viscosity of argon gas at elevated temperatures.

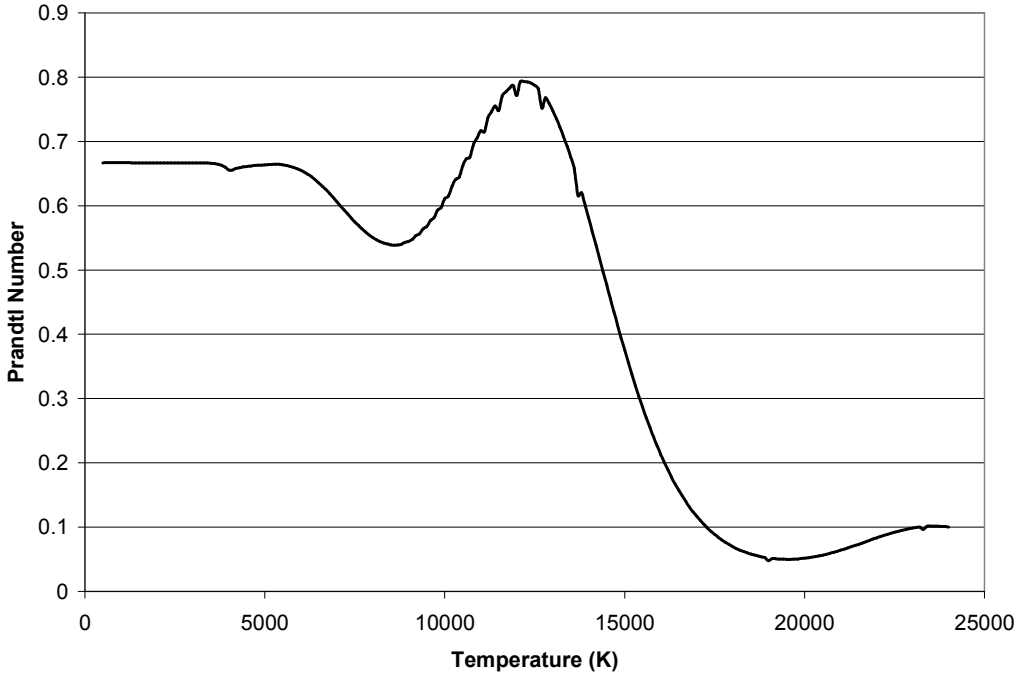

Figure B.5: Pradtl number of argon gas at elevated temperatures.

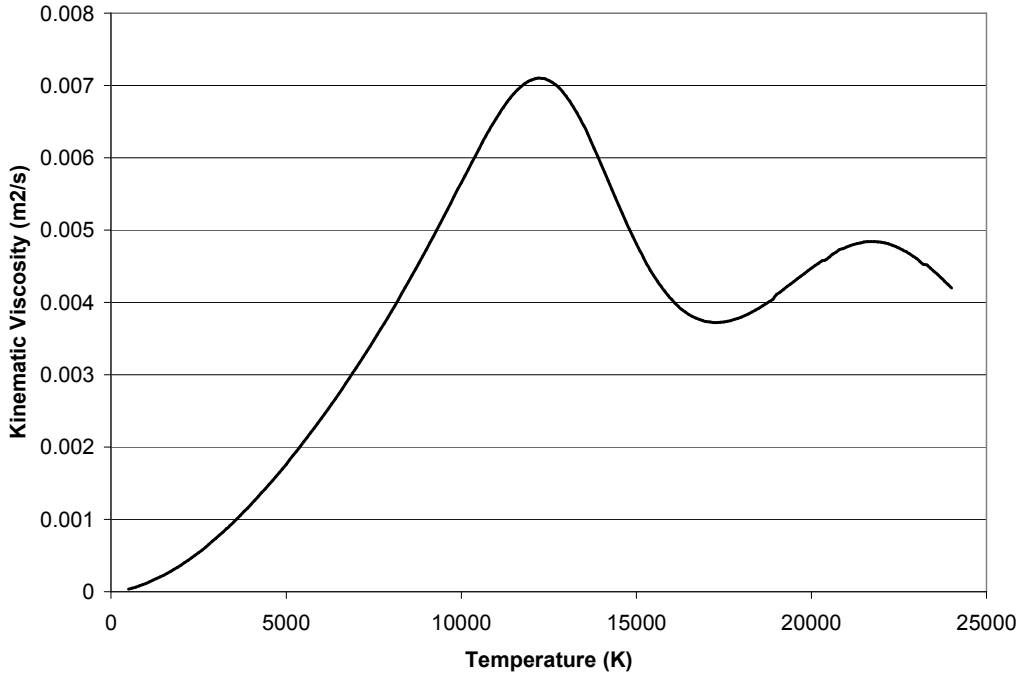

Figure B.6: Kinematic viscosity of argon gas at elevated temperatures.

Table B.1: Polynomial fit of argon property data in the temperature range of 500-20000K.

Property	***Temperature Range (K)***	***Equation***
Density (kg/m^3) ρ	T>5000	$\rho = 3.591E\text{-}10T^2 - 1.422E\text{-}05T + 1.536E\text{-}01$
	T<5000	$\rho = 1.281E\text{-}14T^4 - 1.683E\text{-}10T^3 + 8.070E\text{-}07T^2 - 1.723E\text{-}03T + 1.585E+00$
Viscosity (kg/m s) μ	T>5000	$\mu = -1.9222E\text{-}27T^6 + 1.3250E\text{-}22T^5 - 3.5711E\text{-}18T^4 + 4.7825E\text{-}14T^3 - 3.3714E\text{-}10T^2 + 1.2146E\text{-}06T - 1.6006E\text{-}03$
	T<5000	$\mu = -8.6976E\text{-}26T^6 + 1.6091E\text{-}21T^5 - 1.1869E\text{-}17T^4 + 4.4284E\text{-}14T^3 - 8.8524E\text{-}11T^2 + 1.2137E\text{-}07T - 9.3274E\text{-}06$
Specific heat (J/kg K) c_p	T>14500	$c_p = -3.2609E\text{-}11T^4 + 2.3386E\text{-}06T^3 - 6.2306E\text{-}02T^2 + 7.2952E+02T - 3.1563E+06$
	T<14500	$c_p = -1.4660E\text{-}15T^5 + 6.6124E\text{-}11T^4 - 1.1394E\text{-}06T^3 + 9.4984E\text{-}03T^2 - 3.8504E+01T + 6.1364E+04$
Thermal Conductivity (W/m K) k	T>5000	$k = 1.2249E\text{-}19T^5 - 7.2191E\text{-}15T^4 + 1.5882E\text{-}10T^3 - 1.6067E\text{-}06T^2 + 7.5859E\text{-}03T - 1.3394E+01$
	T<5000	$k = 8.1700E\text{-}20T^5 - 1.4153E\text{-}15T^4 + 9.0473E\text{-}12T^3 - 2.7282E\text{-}08T^2 + 6.2667E\text{-}05T + 1.5051E\text{-}03$

B.2 Nickel, Tungsten Carbide and Steel

The material properties were thermally dependent, shown in Figure B.7 and are listed in Table B.2.

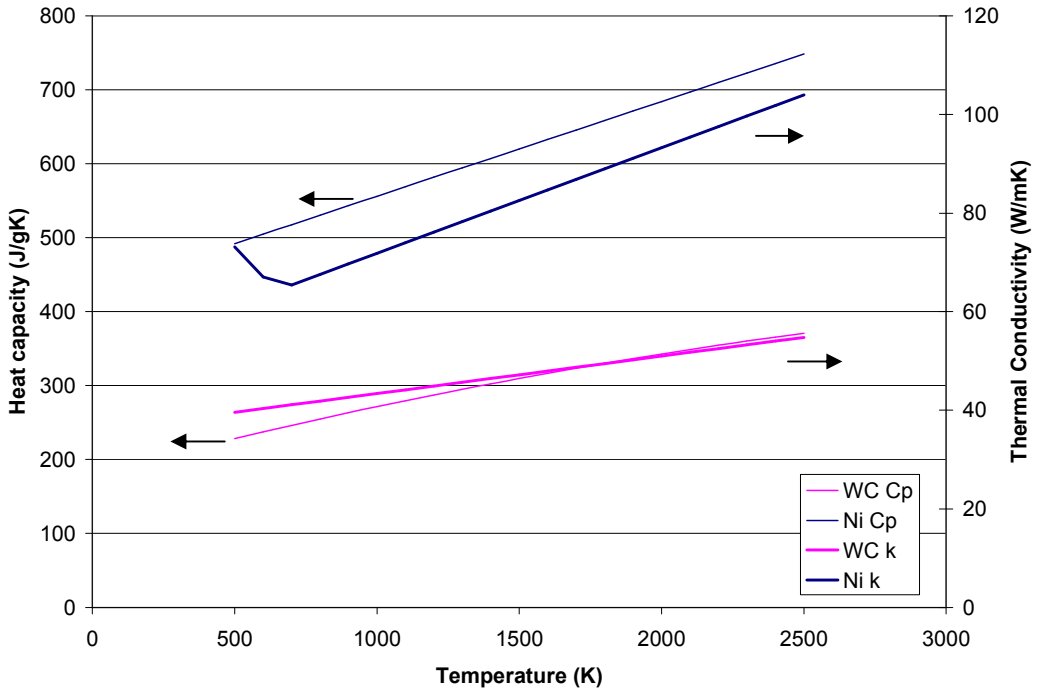

Figure B.7: Heat capacity (thin lines) and thermal conducitivity (thick lines) of WC and Ni [TOU1970].

Table B.2: Temperature dependent thermal material properties for Ni, WC and steel.

Property	*Nickel Matrix*	*WC*	*Steel*
Thermal Conductivity (W/m K) k	-0.0615T+103.91 (T<650K) 0.0214T+50.46 (T≥650K)	0.0076T+35.784	36
Specific heat (J/kg K) c_p	71.2777(6+1.8E-3T)	$-1E-5T^2 + 0.1013T + 180.1$	486
Density (kg/m^3) ρ	8900	15900	7700
Viscosity (kg/m s) μ	$906.418/(T^{1.6779})$	-	-

B.3 Other systems

The carbide distribution profile of other MMC systems was acquired using the settling and solidification code developed for the Ni-WC system. The materials properties used are listed below in Table B.3.

Table B.3: Temperature dependent thermal material properties for Al [MOR1999] [THE1999], B_4C [PIE1996] and Cr_3C_2 [PIE1996]

Property	***Aluminum***	***B_4C***	***Cr_3C_2***
Thermal Conductivity (W/m K) k	102 (T<933 K) 208.67 - 0.0289T (T≥933 K)	3E-06T^2 - 0.0137T + 31.8	3E-05T^2 - 0.024T + 15.252
Specific heat (J/kg K) c_p	878.28 + 0.5198T (T<933 K) 1175 (T≥933 K)	-0.0003 T^2 + 1.6721T + 482.5	0.001 T^2 - 0.6095T + 516.16
Density (kg/m^3) ρ	2300	2500	6700
Viscosity (kg/m s) μ	0.1492exp(1984.5/T)	-	-
Emissivity	0.1 (T≥933 K) 0.2 (T<933 K)	-	-
Melting points (K)	936, 930	-	-
Latent heat (J/kg)	321000	-	-

Appendix C - MATLAB CODE

C.1 Thermal Solidification and Settling Code

```
clear
global x Tinf tempsub rho subnode Width numsteps nodenum
preheattime initconc epsilon

g = 9.81; %m/s2
Vl = 0; %fluid velocity
rhol = 8900; %kg/m3 fluid density
rhos = 15900; %kg/m3 solid density 15900
D = 150e-6;  %m particle size ranges from 50 to 350 micron,
standard 150 um
Tinfafter=298; % ambient temp is 25C after welding
Tinfweld=8000; %ambient temperature during welding, standard
8000K
Tstart=2650; %initial Ni/WC liquid temperature - standard 2650K
tempsub = 298;  %the substrate boundary condition is held at this
temperature, standard 298 K
subsurf = 300; %the initial substrate surface temperature, due to
plasma heating, standard 300K

rhosub = 7700; %7830; %density of substrate material
mufstart = 906.418/(Tstart^1.6779); %kg/ms fluid viscosity - temp
dependent viscosity 906.418*T(celsius)^-1.6779
gamma = rhol/rhos;
Powflowrate = 0.45e-3; %kg/s 0.45e-3
density = 12600; %kg/m3, based on 60w% WC (15400) and 40w% Ni
(8400)
Volumeflowrate = Powflowrate/density;
Width = 0.0025; %0.0025, 2.5mm
Thickness = 0.003; %0.003, 3mm
Linearflowrate = Volumeflowrate/(Width*Thickness);%m/s

depthick = 0.003; %thickness is 3mm
nodenum = 80;  %this the number of nodes
x = depthick/nodenum; %this is the delta in the x direction

subthick = 0.01; % substrate thickness in m - 0.010
subnode=round(subthick/x);
percentdepth=0.00;
subheat = round(percentdepth*subnode); %number of nodes (depth)
to pre-heat substrate

tstepdiv=100; %increment/division of the time step (needs to be
at least 100)
tstep = (x/Linearflowrate); %cooling time step
settlingtime=200; %time steps for settling & cooling after
material addition is finshed, 180
preheattime=5; % time steps for preheat before welding begins, 5
initpart=2; % initial particle velocity, 1.5
```

```
initconc=.5; % initial particle concentration vol%, standard 50%
maxconc=.55; %maximum particle concentration vol%
sphericity = 1;
exp=2;

if sphericity < 1
    D=D/(sphericity*exp);
end

volsphere=4/3*pi*(D/2)^3;
volnode=x*Width*Thickness;

Yend=zeros(nodenum+settlingtime,nodenum);
Tnode=zeros(subnode+1,1); %initialize Tnode as a column vector
rho=zeros(subnode+1,1); %initialize rho as a column vector
Toptemp=zeros(nodenum+settlingtime,2); %initialize a matrix for
the temp in the top cell + time
Tnode(1:subnode-subheat) = tempsub; %set initial substrate
temperature below pre-heat zone
%set initial substrate temperature in pre-heat zone
for idx=subnode-subheat+1:subnode
    Tnode(idx) = tempsub + (subsurf-tempsub)*(idx^2)/(subnode^2);
end
Tnode(subnode+1) = Tstart;  %set the initial weld temperature
muf=mufstart*ones(nodenum,1);  %set the initial viscosity
rho(1:subnode) = rhosub; %initialize substrate density
rho(subnode+1) = rhol*(1-initconc)+rhos*initconc; %initialize
weld node density

epsilonsave=zeros(nodenum+settlingtime+preheattime,nodenum); %
variable to store concentrations at each time step
vpsave=zeros(nodenum+settlingtime+preheattime,nodenum); % to
store particle velocities at each time step
epsilon(1:subnode)=0;
epsilon(subnode+1)=initconc; %initial particle concentration
Vp(1:subnode)=0;
Vp(subnode+1) = initpart; %initial particle velocity

scrsz = get(0,'ScreenSize');
figure('Position',[1 10 scrsz(3)-5 scrsz(4)-80])

for numsteps=1:nodenum+settlingtime+preheattime
    weldnodes=min(max(1,numsteps-preheattime),nodenum);
    curnodes=subnode+weldnodes;
    for tdiv=1:tstepdiv %iterate time step divisions (time steps
are smaller to capture settling better)
        for curcell=subnode+1:curnodes
            muf(curcell)=906.418/(real(Tnode(curcell)^1.6779));
%set viscosity based on current temperature
            rho(curcell)=rhol*(1-
epsilon(curcell))+rhos*epsilon(curcell);

            Re=abs((Vp(curcell)-Vl))*rho(curcell)*D/muf(curcell);
            Cd=24/Re*(1+0.15*Re^0.681)+0.407/(1+(8710/Re));
```

```
            if Re <0.2
                a=4.65+19.5*(D/Width);
            else if Re < 1
                    a=(4.35+17.5*(D/Width))*Re^-0.03;
                else if Re<200
                        a=(4.45+18*(D/Width))*Re^-0.1;
                    else if Re<500
                            a=4.45*Re^-0.1;
                        else
                            a=2.39;
                        end
                    end
                end
            end

            if Tnode(curcell)<1284
                Vt=1e-10;
            else
            Vt=(4/3*(1-gamma)*g*D/(gamma*Cd))^0.5;
            end

            %Vp(curcell)=((1.0-epsilon(curcell))^(a))*Vt;
%original Vp code
            Vp(curcell)=max(((1.0-epsilon(curcell))^(a)),.1)*Vt;
%proposed Vp code, setting minimum Vp at 10% of Vt
        end

        for curcell=subnode+2:curnodes
            % set particle velocity to weighted average of
surrounding
            % nodes, for calculation of particle movements. This
prevents
            % static 'piling up' and allows voids to form & move.
            % Vpart=Vp(curcell); %would be 'standard' settling
velocity
            if curcell < curnodes
                Vpart=(3*Vp(curcell)+Vp(curcell-
1)+Vp(curcell+1))/5;
            else
                Vpart=(Vp(curcell)+Vp(curcell-1))/2;
            end

            Dist=Vpart*tstep/tstepdiv;
            Partmove=Dist/x;

            numpart=epsilon(curcell)*volnode/volsphere;
            nstar=numpart*Partmove;

            if epsilon(curcell-
1)+(nstar*volsphere/volnode)>=maxconc
                epsilon(curcell)=max(epsilon(curcell)-(maxconc-
epsilon(curcell-1)),0);
                epsilon(curcell-1)=maxconc;
            else
                epsilon(curcell)=max(epsilon(curcell)-
(nstar*volsphere/volnode),0);
```

```
                epsilon(curcell-1)=epsilon(curcell-
1)+(nstar*volsphere/volnode);
            end
        end
    end

    % update Tinf depending on whether welding is still underway
    if numsteps<(nodenum+preheattime)
        Tinf=Tinfweld;
    else
        Tinf=Tinfafter;
    end

    % call cooling function and update temperature matrix
    [T,Y] = ode45(@odefunc2,[0 tstep],Tnode);
    %disp(numsteps)
    Ysize=size(Y);
    for idx=1:Ysize(2)
        Tnode(idx)=real(Y(Ysize(1),idx));
        Yend(numsteps,idx)=real(Y(Ysize(1),idx));
    end

    Toptemp(numsteps,2)=Y(Ysize(1),curnodes);

    % update plot
    plot(epsilon(subnode:curnodes),subnode:curnodes) %plot
concentration
    line(((Tnode-tempsub)/(Tstart-
tempsub)),1:curnodes,'Color','r') % plot temperature
    line([((1284-tempsub)/(Tstart-tempsub)) ((1284-
tempsub)/(Tstart-tempsub))],[subnode+1
subnode+nodenum],'Color','g') % plot solidus line
    line([0 1],[subnode subnode],'Color',[.5 .5 .5])
    grid on
    % display current step number as well as time in seconds on
plot
    title(['Settling, Step ',num2str(numsteps-1),' - Time (s):
',num2str(numsteps*tstep)])
    set(gca,'XColor','b') % set x-axis for concentration blue to
match plot colour
    xlim([0 1])
    ylim([1 subnode+nodenum])
    % create new axes and labels for temperature data

text(0,subnode+nodenum,num2str(tempsub),'Color','r','HorizontalAl
ignment','center','VerticalAlignment','bottom')

text(1,subnode+nodenum,num2str(Tstart),'Color','r','HorizontalAli
gnment','center','VerticalAlignment','bottom')


    pause(0.25)
    epsilonsave(numsteps,1:curcell)=epsilon(1:curcell);
    vpsave(numsteps,1:curcell)=Vp(1:curcell);
```

```
    % add cells to concentration, velocity and temp matrices
    if curnodes<(nodenum+subnode) && numsteps>preheattime
        epsilon(curnodes+1)=initconc;
        Vp(curnodes+1)=initpart;
        Tnode(curnodes+1)=Tstart;
        rho(curnodes+1) = rhol*(1-initconc)+rhos*initconc;
    end
end
epsilonend=epsilon(subnode+1:nodenum+subnode);
Toptemp(1:numsteps)=tstep*(1:numsteps);

figure,
plot(tstep*(1:numsteps),Toptemp(1:numsteps,2)),title('Temperature
of surface over time')
```

C.2 Heat conduction program (odefunc2)

This subprogram is called upon in C.1 Thermal Solidification and Settling Code

```
    %This function computes the finite difference equations for
the general
%heat conduction equation in 1D for the ode solver

function dy = odefunc2(t,y)

global x Tinf tempsub rho subnode Width numsteps nodenum
preheattime initconc epsilon
%disp(999)
sizey=size(y);
n=sizey(1);

F= zeros(n,1);

%build the equation matrix

k=zeros(n,1);
c_p=zeros(n,1);
f_l=zeros(n,1);
alpha=zeros(n,1);
k_WC=zeros(n,1);
k_Ni=zeros(n,1);
c_p_WC=zeros(n,1);
c_p_Ni=zeros(n,1);


for j=1:subnode % steel properties
    k(j) = 36; %73-(40/1700)*y(j); % W/mK (conductivity)36, 54
    c_p(j)= 465; %660; % J/kgK (heat capacity) 486

end

%make conversion from initconc to wt% here for the properties.
```

```
% wt_WC=-0.5644*initconc^2 + 1.5407*initconc + 0.0132;
% wt_Ni=1-wt_WC;


for j=subnode+1:n % Ni/WC properties
    wt_WC=-0.5644.*epsilon.^2 + 1.5407.*epsilon + 0.0132;
    wt_Ni=1-wt_WC;

%k(j) = (0.7 + 3.407e-2*y(j) - 3.083e-5*y(j)^2 + 1.580e-
8*y(j)^3)*1.5; %(*1.5 to include WC) conductivity
      k_WC(j) = 0.0076*y(j)+35.784; %W/mK
      if y(j)<650
          k_Ni(j) = -0.0615*y(j)+103.91;
      else
          k_Ni(j) = 0.0214*y(j)+50.46;
      end
    k(j) = wt_Ni(j)*k_Ni(j) + wt_WC(j)*k_WC(j);
%

    %c_p(j)= (-7E-05*y(j)^2 + 0.3017*y(j) + 358.58)/1.4; % (/1.4
to give average of nickel & WC) J/kgK (heat capacity)
      c_p_WC(j) = -1E-5*y(j)^2 + 0.1013*y(j) + 180.1; %J/kgK
      c_p_Ni(j) = (6+1.8e-3*y(j))*4.184*1000/58.7; %J/kgK
%     %c_p(j)=(6+1.8*10^-3*y(j))*4.184/58.7; %Cp for nickel in
J/g
     c_p(j) = wt_Ni(j)*c_p_Ni(j) + wt_WC(j)*c_p_WC(j);

end

alpha = k./(rho.*c_p);

boltz=5.669e-8;
emiss_plasma=0.012; %0.012


%latent heat calculation - treated as a source enthalpy term;
T_liq = 1309; %K
T_sol = 1284; %K
%L = 38100;%79410 ; %J/kg

%plasma conditions at surface
T_plasma = 10000; %K
V_plasma = 100; %m/s
k_plasma = 0.644;
Re_plasma = 176.88;
Pr_plasma = 0.61;
Nu_plasma = 0.664*Re_plasma^(1/2)*Pr_plasma^(1/3);
%h_plasma = Nu_plasma*k_plasma/Width;
h_plasma = 1200;%1200;
h_shielding = 2000;%2000;
h_air = 1000;%1000;

%h for a turbulent jet
% C1=0.516;
% C2=0.491;
```

```
% m_jet=0.5;
% n_jet=0.532;
% Nu_plasma=C1*Re_plasma

heatingtime = 100;%350

for j=1:n
    if ((y(j)<T_liq) && (y(j)>T_sol))

        emiss_MMC=45.075*exp(-0.0045*(y(j)+273));
        f_l(j)= 0.04*y(j)-51.36;
        L(j)=-64305*wt_WC(j)+79410;

        if j==1
           F(j) = alpha(j)/(1+0.04*f_l(j)*L(j)/c_p(j))*(y(j+1)-
2*y(j)+tempsub)/x^2;
        elseif j==n
           if numsteps<nodenum+preheattime
            h=h_plasma;
            F(j) = alpha(j)/(1+0.04*f_l(j)*L(j)/c_p(j))*((y(j-1)-
((2*x/k(j))*((h*(y(j)-Tinf))+ boltz*emiss_plasma*(y(j)^4-
Tinf^4))))-2*y(j)+ y(j-1))/x^2;  %with radiation
           else
            if numsteps<nodenum+preheattime+heatingtime
                h = h_shielding;
                F(j) =
alpha(j)/(1+0.04*f_l(j)*L(j)/c_p(j))*((y(j-1)-
((2*x/k(j))*((h*(y(j)-Tinf))+ boltz*emiss_MMC*(y(j)^4-Tinf^4))))-
2*y(j)+ y(j-1))/x^2;  %with radiation
            else
                h = h_air;
                %h = 1.32*abs(y(j)-Tinf)^0.25; %heat transfer
coefficient
                F(j) =
alpha(j)/(1+0.04*f_l(j)*L(j)/c_p(j))*((y(j-1)-
((2*x/k(j))*((h*(y(j)-Tinf))+ boltz*emiss_MMC*(y(j)^4-Tinf^4))))-
2*y(j)+ y(j-1))/x^2;  %with radiation
            end
           end

           %F(j) = a(j)/(1+0.04*f_l(j)*L/c_p(j))*((y(j-1)-
(2*h*x/k(j))*(y(j)-Tinf))-2*y(j)+ y(j-1))/x^2;

        else
           F(j) = alpha(j)/(1+0.04*f_l(j)*L(j)/c_p(j))*(y(j+1)-
2*y(j)+ y(j-1))/x^2;
        end

    else
        if y(j)>=T_liq
            emiss_MMC=0.3;
        else
            emiss_MMC=0.75;
        end
```

```
        if j==1
            F(j) = alpha(j)*(y(j+1)-2*y(j)+tempsub)/x^2;
        elseif j==n
           if numsteps<nodenum+preheattime
            h=h_plasma;
            F(j) = alpha(j)*((y(j-1)-((2*x/k(j))*((h*(y(j)-
Tinf))+ boltz*emiss_plasma*(y(j)^4-Tinf^4))))-2*y(j)+ y(j-
1))/x^2;  %with radiation
            %F(j) = alpha(j)/(1+0.04*f_l(j)*L/c_p(j))*((y(j-1)-
((2*x/k(j))*((h*(y(j)-Tinf))+ boltz*emiss_plasma*(y(j)^4-
Tinf^4))))-2*y(j)+ y(j-1))/x^2;  %with radiation
           else
            if numsteps<nodenum+preheattime+heatingtime
                h = h_shielding;
                F(j) = alpha(j)*((y(j-1)-((2*x/k(j))*((h*(y(j)-
Tinf))+ boltz*emiss_MMC*(y(j)^4-Tinf^4))))-2*y(j)+ y(j-1))/x^2;
%with radiation
                %F(j) = alpha(j)/(1+0.04*f_l(j)*L/c_p(j))*((y(j-
1)-((2*x/k(j))*((h*(y(j)-Tinf))+ boltz*emiss_MMC*(y(j)^4-
Tinf^4))))-2*y(j)+ y(j-1))/x^2;  %with radiation
            else
                h = h_air;
                %h=1.32*abs(y(j)-Tinf)^0.25; %heat transfer
coefficient
                F(j) = alpha(j)*((y(j-1)-((2*x/k(j))*((h*(y(j)-
Tinf))+ boltz*emiss_MMC*(y(j)^4-Tinf^4))))-2*y(j)+ y(j-1))/x^2;
%with radiation
            end
            %h = 1.32*abs(y(j)-Tinf)^0.25; %heat transfer
coefficient
            %F(j) = a(j)/(1+0.04*f_l(j)*L/c_p(j))*((y(j-1)-
((2*x/k(j))*((h*(y(j)-Tinf))+ boltz*emiss_MMC*(y(j)^4-Tinf^4))))-
2*y(j)+ y(j-1))/x^2;  %with radiation
           end
            %F(j) =a(j)/(1+0.04*f_l(j)*L/c_p(j))*((y(j-1)-
(2*h*x/k(j))*(y(j)-Tinf))-2*y(j)+ y(j-1))/x^2;

        else
            F(j) = alpha(j)*(y(j+1)-2*y(j)+ y(j-1))/x^2;
        end

    end
end

dy=F;
```

C.3 Multi-pass

C.3.A Main program

```
 clear
global x Tinf tempsub rho subnode numsteps nodenum preheattime
epsilon node1pass

node1pass=0;
g = 9.81; %m/s2
Vl = 0; %fluid velocity
rhol = 8900; %kg/m3 fluid density 8900
rhos = 15900; %kg/m3 solid density 15900
D = 150e-6;  %m particle size ranges from 50 to 350 micron,
standard 150 um
Tinfafter=298; % ambient temp is 25C after welding
Tinfweld=8000; %ambient temperature during welding, standard
8000K
Tstart=2650; %initial Ni/WC liquid temperature - standard 2650K
tempsub = 298;  %the substrate boundary condition is held at this
temperature, standard 298 K
subsurf = 300; %the initial substrate surface temperature, due to
plasma heating, standard 300K

rhosub = 7700; %7830; %density of substrate material
mufstart = 906.418/(Tstart^1.6779); %kg/ms fluid viscosity - temp
dependent viscosity 906.418*T(celsius)^-1.6779
gamma = rhol/rhos;
% Powflowrate, Width, depthick and travelspeed are not
mathematically
% linked in this model, so the user must ensure that if one value
is
% changed, that the others are changed to match as required.  For
example,
% if travelspeed is doubled, and Width and depthick are held the
same, then
% Powflowrate must also be doubled.
Powflowrate = 0.45e-3; %powder flow rate in kg/s - default:
0.45e-3
Width = 0.0025; %2.5mm is the nominal weld width
depthick = 0.003; %deposit thickness in m - default: 0.003

nodenum = 80;  %nodenum is the number of nodes of weld material
x = depthick/nodenum; %x is the height of one node in m

subthick = 0.01; % substrate thickness in m - default: 0.010
subnode=round(subthick/x); % subnode is the number of substrate
nodes
percentdepth=0.00; % precent depth to pre-heat substrate -
default is zero
subheat = round(percentdepth*subnode); %number of nodes (depth)
to pre-heat substrate
```

```
initconc=.2; % initial particle concentration vol%, standard 50%
maxconc=.55; %maximum particle concentration is 55vol%
travelspeed = .0038;%default: 3.8mm/s (speed used in experiments
at Syncrude)
tstepdiv=100; %increment/division of the time step for settling
calcs (needs to be at least 100)
tstep = (travelspeed/.006)/nodenum; %time step = time to deposit
one node of weld
settlingtime=180; %time steps for settling & cooling after
material addition is finished, 180
preheattime=5; % time steps for preheat before welding begins -
default: 5 time steps
initpart=2; % initial particle velocity - default: 2m/s

sphericity = 1;
exp=2;
if sphericity < 1
    D=D/(sphericity*exp);
end

volsphere=4/3*pi*(D/2)^3;
volnode=x*Width*depthick;

Yend=zeros(nodenum+settlingtime,nodenum); %initialize matrix to
record node temperatures at each time step
Tnode=zeros(subnode+1,1); %initialize Tnode as a column vector
rho=zeros(subnode+1,1); %initialize rho as a column vector
Toptemp=zeros(nodenum+settlingtime,2); %initialize a matrix for
the temp in the top cell + time
Tnode(1:subnode-subheat) = tempsub; %set initial substrate
temperature below pre-heat zone
%set initial substrate temperature in pre-heat zone
for idx=subnode-subheat+1:subnode
    Tnode(idx) = tempsub + (subsurf-tempsub)*(idx^2)/(subnode^2);
end
Tnode(subnode+1) = Tstart;  %set the initial weld temperature
muf=mufstart*ones(nodenum,1);  %set the initial viscosity
rho(1:subnode) = rhosub; %initialize substrate density
rho(subnode+1) = rhol*(1-initconc)+rhos*initconc; %initialize
weld node density

epsilonsave=zeros(nodenum+settlingtime+preheattime,nodenum); %
variable to store concentrations at each time step
vpsave=zeros(nodenum+settlingtime+preheattime,nodenum); % to
store particle velocities at each time step
epsilon(1:subnode)=0;
epsilon(subnode+1)=initconc; %set initial particle concentration
Vp(1:subnode)=0;
Vp(subnode+1) = initpart; %initial particle velocity

scrsz = get(0,'ScreenSize');
figure('Position',[1 10 scrsz(3)-5 scrsz(4)-80])

for numsteps=1:nodenum+settlingtime+preheattime
    weldnodes=min(max(1,numsteps-preheattime),nodenum);
    curnodes=subnode+weldnodes;
```

```
    for tdiv=1:tstepdiv %iterate time step divisions (time steps
are smaller to capture settling better)
        for curcell=subnode+1:curnodes
            muf(curcell)=906.418/(real(Tnode(curcell)^1.6779));
%set viscosity based on current temperature
            rho(curcell)=rhol*(1-
epsilon(curcell))+rhos*epsilon(curcell);

            Re=abs((Vp(curcell)-Vl))*rho(curcell)*D/muf(curcell);
            Cd=24/Re*(1+0.15*Re^0.681)+0.407/(1+(8710/Re));

            if Re <0.2
                a=4.65+19.5*(D/Width);
            else if Re < 1
                    a=(4.35+17.5*(D/Width))*Re^-0.03;
                else if Re<200
                        a=(4.45+18*(D/Width))*Re^-0.1;
                    else if Re<500
                            a=4.45*Re^-0.1;
                        else
                            a=2.39;
                        end
                    end
                end
            end

            if Tnode(curcell)<1284
                Vt=1e-10;
            else
            Vt=(4/3*(1-gamma)*g*D/(gamma*Cd))^0.5;
            end

            %Vp(curcell)=((1.0-epsilon(curcell))^(a))*Vt;
%original Vp code
            Vp(curcell)=max(((1.0-epsilon(curcell))^(a)),.1)*Vt;
%proposed Vp code, setting minimum Vp at 10% of Vt
        end

        for curcell=subnode+2:curnodes
            % set particle velocity to weighted average of
surrounding
            % nodes, for calculation of particle movements. This
prevents
            % static 'piling up' and allows voids to form & move.
            % Vpart=Vp(curcell); %would be 'standard' settling
velocity
            if curcell < curnodes
                Vpart=(3*Vp(curcell)+Vp(curcell-
1)+Vp(curcell+1))/5;
            else
                Vpart=(Vp(curcell)+Vp(curcell-1))/2;
            end

            Dist=Vpart*tstep/tstepdiv;
            Partmove=Dist/x;
```

```
            numpart=epsilon(curcell)*volnode/volsphere;
            nstar=numpart*Partmove;

            if epsilon(curcell-
1)+(nstar*volsphere/volnode)>=maxconc
                epsilon(curcell)=max(epsilon(curcell)-(maxconc-
epsilon(curcell-1)),0);
                epsilon(curcell-1)=maxconc;
            else
                epsilon(curcell)=max(epsilon(curcell)-
(nstar*volsphere/volnode),0);
                epsilon(curcell-1)=epsilon(curcell-
1)+(nstar*volsphere/volnode);
            end
        end
    end

    % update Tinf depending on whether welding is still underway
    if numsteps<(nodenum+preheattime)
        Tinf=Tinfweld;
    else
        Tinf=Tinfafter;
    end

    % call cooling function and update temperature matrix
    [T,Y] = ode45(@odefunc2,[0 tstep],Tnode);
    %disp(numsteps)
    Ysize=size(Y);
    for idx=1:Ysize(2)
        Tnode(idx)=real(Y(Ysize(1),idx));
        Yend(numsteps,idx)=real(Y(Ysize(1),idx));
    end

    Toptemp(numsteps,2)=Y(Ysize(1),curnodes);

    % update plot
    plot(epsilon(subnode:curnodes),subnode:curnodes) %plot
concentration
    line(((Tnode-tempsub)/(Tstart-
tempsub)),1:curnodes,'Color','r') % plot temperature
    line([((1284-tempsub)/(Tstart-tempsub)) ((1284-
tempsub)/(Tstart-tempsub))],[subnode+1
subnode+nodenum],'Color','g') % plot solidus line
    line([0 1],[subnode subnode],'Color',[.5 .5 .5])
    grid on
    % display current step number as well as time in seconds on
plot
    title(['Settling, Step ',num2str(numsteps-1),' - Time (s):
',num2str(numsteps*tstep)])
    set(gca,'XColor','b') % set x-axis for concentration blue to
match plot colour
    xlim([0 1])
    ylim([1 subnode+nodenum])
    % create new axes and labels for temperature data
```

```
text(0,subnode+nodenum,num2str(tempsub),'Color','r','HorizontalAl
ignment','center','VerticalAlignment','bottom')

text(1,subnode+nodenum,num2str(Tstart),'Color','r','HorizontalAli
gnment','center','VerticalAlignment','bottom')


    pause(0.25)
    epsilonsave(numsteps,1:curcell)=epsilon(1:curcell);
    vpsave(numsteps,1:curcell)=Vp(1:curcell);

    % add cells to concentration, velocity and temp matrices
    if curnodes<(nodenum+subnode) && numsteps>preheattime
        epsilon(curnodes+1)=initconc;
        Vp(curnodes+1)=initpart;
        Tnode(curnodes+1)=Tstart;
        rho(curnodes+1) = rhol*(1-initconc)+rhos*initconc;
    end
end
epsilonend=epsilon(subnode+1:nodenum+subnode);
epsilonend=epsilonend.';
Toptemp(1:numsteps)=tstep*(1:numsteps);

figure,
plot(tstep*(1:numsteps),Toptemp(1:numsteps,2)),title('Temperature
of surface over time')

save('epsilon1pass.mat','epsilonend','depthick')

     %This function computes the finite difference equations for
the general
%heat conduction equation in 1D for the ode solver
```

C.3.A ODEFUNC2 – required for Multi-pass

```
function dy = odefunc2(t,y)

global x Tinf tempsub rho subnode numsteps nodenum preheattime
epsilon node1pass
sizey=size(y);
n=sizey(1);

F= zeros(n,1);

%build the equation matrix

k=zeros(n,1);
c_p=zeros(n,1);
f_l=zeros(n,1);
alpha=zeros(n,1);
```

```
k_WC=zeros(n,1);
k_Ni=zeros(n,1);
c_p_WC=zeros(n,1);
c_p_Ni=zeros(n,1);


for j=1:subnode % steel properties
    k(j) = 36; %73-(40/1700)*y(j); % W/mK (conductivity)36, 54
    c_p(j)= 465; %660; % J/kgK (heat capacity) 486

end

%make conversion from initconc to wt% here for the properties.
% wt_WC=-0.5644*initconc^2 + 1.5407*initconc + 0.0132;
% wt_Ni=1-wt_WC;


for j=subnode+1:n % Ni/WC properties
    wt_WC=-0.5644.*epsilon.^2 + 1.5407.*epsilon + 0.0132;
    wt_Ni=1-wt_WC;

%k(j) = (0.7 + 3.407e-2*y(j) - 3.083e-5*y(j)^2 + 1.580e-
8*y(j)^3)*1.5; %(*1.5 to include WC) conductivity
      k_WC(j) = 0.0076*y(j)+35.784; %W/mK
      if y(j)<650
          k_Ni(j) = -0.0615*y(j)+103.91;
      else
          k_Ni(j) = 0.0214*y(j)+50.46;
      end
    k(j) = wt_Ni(j)*k_Ni(j) + wt_WC(j)*k_WC(j);
%

    %c_p(j)= (-7E-05*y(j)^2 + 0.3017*y(j) + 358.58)/1.4; % (/1.4
to give average of nickel & WC) J/kgK (heat capacity)
      c_p_WC(j) = -1E-5*y(j)^2 + 0.1013*y(j) + 180.1; %J/kgK
      c_p_Ni(j) = (6+1.8e-3*y(j))*4.184*1000/58.7; %J/kgK
%     %c_p(j)=(6+1.8*10^-3*y(j))*4.184/58.7; %Cp for nickel in
J/g
     c_p(j) = wt_Ni(j)*c_p_Ni(j) + wt_WC(j)*c_p_WC(j);

end

alpha = k./(rho.*c_p);

boltz=5.669e-8;
emiss_plasma=0.012; %0.012


%latent heat calculation - treated as a source enthalpy term;
T_liq = 1309; %K
T_sol = 1284; %K
%L = 38100;%79410 ; %J/kg

%plasma conditions at surface
```

```
T_plasma = 10000; %K
V_plasma = 100; %m/s
k_plasma = 0.644;
Re_plasma = 176.88;
Pr_plasma = 0.61;
Nu_plasma = 0.664*Re_plasma^(1/2)*Pr_plasma^(1/3);
%h_plasma = Nu_plasma*k_plasma/Width;
h_plasma = 1200;%1200;
h_shielding = 2000;%2000;
h_air = 2000;%1000;

%h for a turbulent jet
% C1=0.516;
% C2=0.491;
% m_jet=0.5;
% n_jet=0.532;
% Nu_plasma=C1*Re_plasma

heatingtime = 100;%350

for j=1:n
    if ((y(j)<T_liq) && (y(j)>T_sol))

        emiss_MMC=45.075*exp(-0.0045*(y(j)+273));
        f_l(j)= 0.04*y(j)-51.36;
        L(j)=-64305*wt_WC(j)+79410;

        if j==1
           F(j) = alpha(j)/(1+0.04*f_l(j)*L(j)/c_p(j))*(y(j+1)-
2*y(j)+tempsub)/x^2;
        elseif j==n
           if numsteps<node1pass+nodenum+preheattime
            h=h_plasma;
            F(j) = alpha(j)/(1+0.04*f_l(j)*L(j)/c_p(j))*((y(j-1)-
((2*x/k(j))*((h*(y(j)-Tinf))+ boltz*emiss_plasma*(y(j)^4-
Tinf^4))))-2*y(j)+ y(j-1))/x^2;  %with radiation
           else
            if numsteps<node1pass+nodenum+preheattime+heatingtime
                h = h_shielding;
                F(j) =
alpha(j)/(1+0.04*f_l(j)*L(j)/c_p(j))*((y(j-1)-
((2*x/k(j))*((h*(y(j)-Tinf))+ boltz*emiss_MMC*(y(j)^4-Tinf^4))))-
2*y(j)+ y(j-1))/x^2;  %with radiation
            else
                h = h_air;
                %h = 1.32*abs(y(j)-Tinf)^0.25; %heat transfer
coefficient
                F(j) =
alpha(j)/(1+0.04*f_l(j)*L(j)/c_p(j))*((y(j-1)-
((2*x/k(j))*((h*(y(j)-Tinf))+ boltz*emiss_MMC*(y(j)^4-Tinf^4))))-
2*y(j)+ y(j-1))/x^2;  %with radiation
            end
           end

           %F(j) = a(j)/(1+0.04*f_l(j)*L/c_p(j))*((y(j-1)-
(2*h*x/k(j))*(y(j)-Tinf))-2*y(j)+ y(j-1))/x^2;
```

```
        else
           F(j) = alpha(j)/(1+0.04*f_l(j)*L(j)/c_p(j))*(y(j+1)-
2*y(j)+ y(j-1))/x^2;
        end

    else
        if y(j)>=T_liq
            emiss_MMC=0.3;
        else
            emiss_MMC=0.75;
        end

        if j==1
            F(j) = alpha(j)*(y(j+1)-2*y(j)+tempsub)/x^2;
        elseif j==n
           if numsteps<node1pass+nodenum+preheattime
            h=h_plasma;
            F(j) = alpha(j)*((y(j-1)-((2*x/k(j))*((h*(y(j)-
Tinf))+ boltz*emiss_plasma*(y(j)^4-Tinf^4))))-2*y(j)+ y(j-
1))/x^2;  %with radiation
            %F(j) = alpha(j)/(1+0.04*f_l(j)*L/c_p(j))*((y(j-1)-
((2*x/k(j))*((h*(y(j)-Tinf))+ boltz*emiss_plasma*(y(j)^4-
Tinf^4))))-2*y(j)+ y(j-1))/x^2;  %with radiation
           else
            if numsteps<node1pass+nodenum+preheattime+heatingtime
                h = h_shielding;
                F(j) = alpha(j)*((y(j-1)-((2*x/k(j))*((h*(y(j)-
Tinf))+ boltz*emiss_MMC*(y(j)^4-Tinf^4))))-2*y(j)+ y(j-1))/x^2;
%with radiation
                %F(j) = alpha(j)/(1+0.04*f_l(j)*L/c_p(j))*((y(j-
1)-((2*x/k(j))*((h*(y(j)-Tinf))+ boltz*emiss_MMC*(y(j)^4-
Tinf^4))))-2*y(j)+ y(j-1))/x^2;  %with radiation
            else
                h = h_air;
                %h=1.32*abs(y(j)-Tinf)^0.25; %heat transfer
coefficient
                F(j) = alpha(j)*((y(j-1)-((2*x/k(j))*((h*(y(j)-
Tinf))+ boltz*emiss_MMC*(y(j)^4-Tinf^4))))-2*y(j)+ y(j-1))/x^2;
%with radiation
            end
            %h = 1.32*abs(y(j)-Tinf)^0.25; %heat transfer
coefficient
            %F(j) = a(j)/(1+0.04*f_l(j)*L/c_p(j))*((y(j-1)-
((2*x/k(j))*((h*(y(j)-Tinf))+ boltz*emiss_MMC*(y(j)^4-Tinf^4))))-
2*y(j)+ y(j-1))/x^2;  %with radiation
           end
            %F(j) =a(j)/(1+0.04*f_l(j)*L/c_p(j))*((y(j-1)-
(2*h*x/k(j))*(y(j)-Tinf))-2*y(j)+ y(j-1))/x^2;

        else
            F(j) = alpha(j)*(y(j+1)-2*y(j)+ y(j-1))/x^2;
        end

    end
end
```

```
dy=F;
```

C.3.C Second pass

```
clear
global x Tinf tempsub rho subnode numsteps nodenum preheattime
epsilon node1pass

load epsilon1pass.mat % file containing settling data from first
weld pass
node1pass=length(epsilonend);

g = 9.81; %m/s2
Vl = 0; %fluid velocity
rhol = 8900; %kg/m3 fluid density 8900
rhos = 15900; %kg/m3 solid density 15900
D = 150e-6;  %m particle size ranges from 50 to 350 micron,
standard 150 um
Tinfafter=298; % ambient temp is 25C after welding
Tinfweld=8000; %ambient temperature during welding, standard
8000K
Tstart=2650; %initial Ni/WC liquid temperature - standard 2650K
tempsub = 298;  %the substrate boundary condition is held at this
temperature, standard 298 K
coat_temp = 500;  %the temperature of the coating after 1 pass,
standard 500 K
%subsurf = 600; %the initial substrate surface temperature, due
to plasma heating, standard 300K

rhosub = 7700; %7830; %density of substrate material
mufstart = 906.418/(Tstart^1.6779); %kg/ms fluid viscosity - temp
dependent viscosity 906.418*T(celsius)^-1.6779
gamma = rhol/rhos;
% Powflowrate, Width, depthick and travelspeed are not
mathematically
% linked in this model, so the user must ensure that if one value
is
% changed, that the others are changed to match as required.  For
example,
% if travelspeed is doubled, and Width and depthick are held the
same, then
% Powflowrate must also be doubled.
Powflowrate = 0.45e-3; %powder flow rate in kg/s - default:
0.45e-3
Width = 0.0025; %2.5mm is the nominal weld width
depthick = 0.003; %deposit thickness in m - default: 0.003

nodenum = 80;  %nodenum is the number of nodes of weld material
x = depthick/nodenum; %x is the height of one node in m

subthick = 0.01; % substrate thickness in m - default: 0.010
```

```
subnode=round(subthick/x); % subnode is the number of substrate
nodes

initconc=.2; % initial particle concentration vol%, standard 50%
maxconc=.55; %maximum particle concentration is 55vol%
travelspeed = .0038;%default: 3.8mm/s (speed used in experiments
at Syncrude)
tstepdiv=100; %increment/division of the time step for settling
calcs (needs to be at least 100)
tstep = (travelspeed/.006)/nodenum; %time step = time to deposit
one node of weld
settlingtime=250; %time steps for settling & cooling after
material addition is finished, 180
preheattime=5; % time steps for preheat before welding begins -
default: 5 time steps
initpart=2; % initial particle velocity - default: 2m/s

sphericity = 1;
exp=2;
if sphericity < 1
    D=D/(sphericity*exp);
end

volsphere=4/3*pi*(D/2)^3;
volnode=x*Width*depthick;

Yend=zeros(nodenum+settlingtime,node1pass+nodenum); %initialize
matrix to record node temperatures at each time step
Tnode=zeros(subnode+node1pass+1,1); %initialize Tnode as a column
vector
rho=zeros(subnode+node1pass+1,1); %initialize rho as a column
vector
Toptemp=zeros(nodenum+settlingtime,2); %initialize a matrix for
the temp in the top cell + time
Tnode(1:subnode) = tempsub; %set initial substrate temperature
Tnode(subnode+1:subnode+node1pass) = coat_temp; %set initial
coating temperature
Tnode(subnode+node1pass+1) = Tstart;  %set the initial weld
temperature
muf=mufstart*ones(node1pass+nodenum,1);  %set the initial
viscosity
rho(1:subnode) = rhosub; %initialize substrate density
rho(subnode+1:subnode+node1pass+1) = rhol*(1-
initconc)+rhos*initconc; %initialize weld node density

epsilonsave=zeros(nodenum+settlingtime+preheattime,node1pass+node
num); % variable to store concentrations at each time step
vpsave=zeros(nodenum+settlingtime+preheattime,node1pass+nodenum);
% to store particle velocities at each time step
epsilon(1:subnode)=0; % no particles in substrate
epsilon(subnode+1:subnode+node1pass)=epsilonend; % set
concentrations in first pass nodes
epsilon(subnode+node1pass+1)=initconc; %initial particle
concentration
Vp(1:subnode+node1pass)=0;
Vp(subnode+node1pass+1) = initpart; %initial particle velocity
```

```
scrsz = get(0,'ScreenSize');
figure('Position',[1 10 scrsz(3)-5 scrsz(4)-80])

for
numsteps=node1pass+1:node1pass+nodenum+settlingtime+preheattime
    weldnodes=min(max(node1pass+1,numsteps-
preheattime),node1pass+nodenum);
    curnodes=subnode+weldnodes;
    for tdiv=1:tstepdiv %iterate time step divisions (time steps
are smaller to capture settling better)
        for curcell=subnode+1:curnodes
            muf(curcell)=906.418/(real(Tnode(curcell)^1.6779));
%set viscosity based on current temperature
            rho(curcell)=rhol*(1-
epsilon(curcell))+rhos*epsilon(curcell);

            Re=max(.00001,abs((Vp(curcell)-
Vl))*rho(curcell)*D/muf(curcell));
            Cd=24/Re*(1+0.15*Re^0.681)+0.407/(1+(8710/Re));

            if Re <0.2
                a=4.65+19.5*(D/Width);
            else if Re < 1
                    a=(4.35+17.5*(D/Width))*Re^-0.03;
                else if Re<200
                        a=(4.45+18*(D/Width))*Re^-0.1;
                    else if Re<500
                            a=4.45*Re^-0.1;
                        else
                            a=2.39;
                        end
                    end
                end
            end

            if Tnode(curcell)<1284
                Vt=1e-10;
            else
            Vt=(4/3*(1-gamma)*g*D/(gamma*Cd))^0.5;
            end

            %Vp(curcell)=((1.0-epsilon(curcell))^(a))*Vt;
%original Vp code
            Vp(curcell)=max(((1.0-epsilon(curcell))^(a)),.1)*Vt;
%proposed Vp code, setting minimum Vp at 10% of Vt
        end

        for curcell=subnode+2:curnodes
            % set particle velocity to weighted average of
surrounding
            % nodes, for calculation of particle movements. This
prevents
            % static 'piling up' and allows voids to form & move.
```

```
            % Vpart=Vp(curcell); %would be 'standard' settling
velocity
            if curcell < curnodes
                Vpart=(3*Vp(curcell)+Vp(curcell-
1)+Vp(curcell+1))/5;
            else
                Vpart=(Vp(curcell)+Vp(curcell-1))/2;
            end

            Dist=Vpart*tstep/tstepdiv;
            Partmove=Dist/x;

            numpart=epsilon(curcell)*volnode/volsphere;
            nstar=numpart*Partmove;

            if epsilon(curcell-
1)+(nstar*volsphere/volnode)>=maxconc
                epsilon(curcell)=max(epsilon(curcell)-(maxconc-
epsilon(curcell-1)),0);
                epsilon(curcell-1)=maxconc;
            else
                epsilon(curcell)=max(epsilon(curcell)-
(nstar*volsphere/volnode),0);
                epsilon(curcell-1)=epsilon(curcell-
1)+(nstar*volsphere/volnode);
            end
        end
    end

    % update Tinf depending on whether welding is still underway
    if numsteps<(node1pass+nodenum+preheattime)
        Tinf=Tinfweld;
    else
        Tinf=Tinfafter;
    end

    % call cooling function and update temperature matrix
    [T,Y] = ode45(@odefunc2,[0 tstep],Tnode);
    %disp(numsteps)
    Ysize=size(Y);
    for idx=1:Ysize(2)
        Tnode(idx)=real(Y(Ysize(1),idx));
        Yend(numsteps,idx)=real(Y(Ysize(1),idx));
    end

    Toptemp(numsteps,2)=Y(Ysize(1),curnodes);

    % update plot
    plot(epsilon(subnode:curnodes),subnode:curnodes) %plot
concentration
    line(((Tnode-tempsub)/(Tstart-
tempsub)),1:curnodes,'Color','r') % plot temperature
    line([((1284-tempsub)/(Tstart-tempsub)) ((1284-
tempsub)/(Tstart-tempsub))],[subnode+1
subnode+nodenum],'Color','g') % plot solidus line
```

```
    line([0 1],[subnode subnode],'Color',[.5 .5 .5])
    grid on
    % display current step number as well as time in seconds on
plot
    title(['Settling, Step ',num2str(numsteps-1),' - Time (s):
',num2str(numsteps*tstep)])
    set(gca,'XColor','b') % set x-axis for concentration blue to
match plot colour
    xlim([0 1])
    ylim([1 subnode+node1pass+nodenum])
    % create new axes and labels for temperature data

text(0,subnode+nodenum+node1pass,num2str(tempsub),'Color','r','Ho
rizontalAlignment','center','VerticalAlignment','bottom')

text(1,subnode+nodenum+node1pass,num2str(Tstart),'Color','r','Hor
izontalAlignment','center','VerticalAlignment','bottom')



    pause(0.25)
    epsilonsave(numsteps,1:curcell)=epsilon(1:curcell);
    vpsave(numsteps,1:curcell)=Vp(1:curcell);

    % add cells to concentration, velocity and temp matrices
    if curnodes<(node1pass+nodenum+subnode) &&
numsteps>preheattime+node1pass
        epsilon(curnodes+1)=initconc;
        Vp(curnodes+1)=initpart;
        Tnode(curnodes+1)=Tstart;
        rho(curnodes+1) = rhol*(1-initconc)+rhos*initconc;
    end
end
epsilonend=epsilon(subnode+1:nodenum+subnode+node1pass);
epsilonend=epsilonend.';
Toptemp(1:numsteps)=tstep*(1:numsteps);

figure,
plot(tstep*(1:numsteps),Toptemp(1:numsteps,2)),title('Temperature
of surface over time')
```

C.4 Particle Velocity in Liquid

This stand-alone program tracks the velocity and position of a single sphere settling through a liquid.

```
[S,D] = ode45(@sphere5,[0 1],[.01 0]);

plot(S,D(:,1),'-',S,D(:,2),'-.')

function dy = sphere5(t,y)
```

```
d = 150e-6; %diameter of particle, in m
rho_l = 8900; %kg/m3
rho_s = 15900; %kg/m3
k_mu = 0.537e-6; %m2/s
mu_l= 4.09e-3; %Ns/m2
gamma = rho_s/rho_l;
liquidvel=-1;
g = 9.81; %m/s2
Ca = 0.5;

Re = rho_l/mu_l*(y(1)-liquidvel)*d;

Cd = 24/Re;
%Cd = 16.6*Re^(-0.75) + 0.2;


dy = zeros(2,1);    % a column vector
dy(1) = [-(1-gamma)*g/(gamma+Ca)]-[3*Cd*(y(1)-
liquidvel)*abs(y(1)-liquidvel)/(4*d*(gamma+Ca))];
dy(2) = y(1);
```

C.5 Particle Temperature and Velocity in Plasma Fluid

```
%This stand-alone program calculates the temperature and velocity
of a Nickel or WC
%particle through the plasma field

clear

global n

n=100;
inittemp = 298*ones(n,1);
initpos = [0.8; 0]; % initial velocity is 0.8 m/s, initial z
position is zero
initcond = [inittemp; initpos];
timespan = [0; .006];

[T,Y] = ode15s(@particlefunc,timespan,initcond);

plot(T,Y(:,1),'-',T,Y(:,2),'-.')


function dy = particlefunc(t,T)
global n

%T = 298*ones(n,1);
r_p = 75e-6; %meters
h=r_p/n;
g = 9.81;
d = r_p*2;
s = size(T,1);
```

```
% %particle properties for nickel
% for i=1:n
% %k(i)= 7E-06*T(i)^2 + 0.0073*T(i) + 11.768; %W/mK
% k(i) = 0.7 + 3.407e-2*T(i) - 3.083e-5*T(i)^2 + 1.580e-8*T(i)^3;
%
% if T(i)<650
%           k(i) = -0.0615*T(i)+103.91;
%       else
%           k(i) = 0.0214*T(i)+50.46;
% end
%
% rho(i)=8900; %kg/m3
% cp(i) = (6+1.8e-3*T(i))*4.184*1000/58.7; %J/kgK
% end

%particle properties for tungsten carbide - if using, please
comment latent
%terms below!
for i=1:n
 k(i)= 0.0076*T(i)+35.784; %W/mK
 rho(i)= 15900; %kg/m3
 cp(i) = -1E-5*T(i)^2 + 0.1013*T(i) + 180.1; %J/kgK
end

%plasma properties
%UNITS  cp - J/kg K, rho - kg/m3, mu - kg/m s, k - W/m K
SurfaceT = T(n);
T_g = 13000; %K
T_m = (T_g + T(n))/2;

%properties at film temperature
if T_m < 14500
    cp_m =  -1.4660E-15*T_m^5 + 6.6124E-11*T_m^4 - 1.1394E-
06*T_m^3 + 9.4984E-03*T_m^2 - 3.8504E+01*T_m + 6.1364E+04;
else
    cp_m = -3.2609E-11*T_m^4 + 2.3386E-06*T_m^3 - 6.2306E-
02*T_m^2 + 7.2952E+02*T_m - 3.1563E+06;
end

rho_m = 3.591E-10*T_m^2 - 1.422E-05*T_m + 1.536E-01;
mu_m =  -1.9222E-27*T_m^6 + 1.3250E-22*T_m^5 - 3.5711E-18*T_m^4 +
4.7825E-14*T_m^3 - 3.3714E-10*T_m^2 + 1.2146E-06*T_m - 1.6006E-
03;
k_m = 1.2249E-19*T_m^5 - 7.2191E-15*T_m^4 + 1.5882E-10*T_m^3 -
1.6067E-06*T_m^2 + 7.5859E-03*T_m - 1.3394E+01;

%properties at gas temperature
mu_g =  -1.9222E-27*T_g^6 + 1.3250E-22*T_g^5 - 3.5711E-18*T_g^4 +
4.7825E-14*T_g^3 - 3.3714E-10*T_g^2 + 1.2146E-06*T_g - 1.6006E-
03;
if T_g < 14500
    cp_g =  -1.4660E-15*T_g^5 + 6.6124E-11*T_g^4 - 1.1394E-
06*T_g^3 + 9.4984E-03*T_g^2 - 3.8504E+01*T_g + 6.1364E+04;
else
    cp_g = -3.2609E-11*T_g^4 + 2.3386E-06*T_g^3 - 6.2306E-
02*T_g^2 + 7.2952E+02*T_g - 3.1563E+06;
```

```
end
rho_g = 3.591E-10*T_g^2 - 1.422E-05*T_g + 1.536E-01;
k_g = 1.2249E-19*T_g^5 - 7.2191E-15*T_g^4 + 1.5882E-10*T_g^3 -
1.6067E-06*T_g^2 + 7.5859E-03*T_g - 1.3394E+01;

%properties at surface temperature
if T(n) < 5000
    cp_s = 520;
    rho_s = 1.281E-14*T(n)^4 - 1.683E-10*T(n)^3 + 8.070E-
07*T(n)^2 - 1.723E-03*T(n) + 1.585E+00;
    mu_s = -8.6976E-26*T(n)^6 + 1.6091E-21*T(n)^5 - 1.1869E-
17*T(n)^4 + 4.4284E-14*T(n)^3 - 8.8524E-11*T(n)^2 + 1.2137E-
07*T(n) - 9.3274E-06;
    k_s = 8.1700E-20*T(n)^5 - 1.4153E-15*T(n)^4 + 9.0473E-
12*T(n)^3 - 2.7282E-08*T(n)^2 + 6.2667E-05*T(n) + 1.5051E-03;
elseif T(n) < 14500
    cp_s =  -1.4660E-15*T(n)^5 + 6.6124E-11*T(n)^4 - 1.1394E-
06*T(n)^3 + 9.4984E-03*T(n)^2 - 3.8504E+01*T(n) + 6.1364E+04;
    rho_s = 3.591E-10*T(n)^2 - 1.422E-05*T(n) + 1.536E-01;
    mu_s =  -1.9222E-27*T(n)^6 + 1.3250E-22*T(n)^5 - 3.5711E-
18*T(n)^4 + 4.7825E-14*T(n)^3 - 3.3714E-10*T(n)^2 + 1.2146E-
06*T(n) - 1.6006E-03;
    k_s = 1.2249E-19*T(n)^5 - 7.2191E-15*T(n)^4 + 1.5882E-
10*T(n)^3 - 1.6067E-06*T(n)^2 + 7.5859E-03*T(n) - 1.3394E+01;
else
    cp_s = -3.2609E-11*T(n)^4 + 2.3386E-06*T(n)^3 - 6.2306E-
02*T(n)^2 + 7.2952E+02*T(n) - 3.1563E+06;
    rho_s = 3.591E-10*T(n)^2 - 1.422E-05*T(n) + 1.536E-01;
    mu_s =  -1.9222E-27*T(n)^6 + 1.3250E-22*T(n)^5 - 3.5711E-
18*T(n)^4 + 4.7825E-14*T(n)^3 - 3.3714E-10*T(n)^2 + 1.2146E-
06*T(n) - 1.6006E-03;
    k_s = 1.2249E-19*T(n)^5 - 7.2191E-15*T(n)^4 + 1.5882E-
10*T(n)^3 - 1.6067E-06*T(n)^2 + 7.5859E-03*T(n) - 1.3394E+01;
end


%plasma velocity
V_g = 185; %m/s -2E+7*T(s-1)^2+58695*T(s-1)+1178.3



%drag coefficient Cd = 16.6*Re^-0.75 + 0.2, valid for Re=0.4-10
dy1_dt = g + (16.6*(rho_g*(V_g-T(s-1))*d/mu_g)^-0.75 +
0.2)/(12*d)*rho_g/rho(n/2)*(V_g - T(s-1))^2;
dy2_dt = T(s-1);

dvel = [dy1_dt; dy2_dt];

Pr = cp_m*mu_m/k_m;
Re = 2*rho_m*r_p*(V_g-T(s-1))/mu_m;
Nu = 2+0.6*Re^(1/2)*Pr^(1/3);
f_prop = rho_g*mu_g/(rho_s*mu_s);
Nu_adj = Nu*f_prop^0.6*(cp_g/cp_s)^0.38;
h_m = Nu_adj*k_m/(2*r_p); %W/m2 K
```

```
F = zeros(n,1);

r = h*ones(n,1);
for j=2:n
    r(j) = r(j-1) + h;
end

for i=1:n
alpha(i) = k(i)/(rho(i)*cp(i));
end

% %latent heat calculation - treated as a source enthalpy term,
for Nickel only;
% T_liq = 1309; %K
% T_sol = 1284; %K
% L = 79410; %J/kg

for j=1:n
%     if ((T(j)<T_liq) && (T(j)>T_sol))
%
%         f_l(j)= 0.04*T(j)-51.36;
%
%         if j==1
%            F(j) =
alpha(j)/(1+0.04*f_l(j)*L(j)/c_p(j))*(2*T(j+1)-2*T(j))/h^2;
%         elseif j==n
%            T_n1 = 2*h*h_m/k(n)*(T_g - T(j)) + T(j-1);
%            F(j) = alpha(j)/(1+0.04*f_l(j)*L(j)/c_p(j))*((T_n1-
T(j))/(r(j)*h) + (T_n1-2*T(j)+T(j-1))/h^2);
%         else
%             F(j) =
alpha(j)/(1+0.04*f_l(j)*L(j)/c_p(j))*((T(j+1)-T(j-1))/(r(j)*h) +
(T(j+1)-2*T(j)+T(j-1))/h^2);
%         end
%     else


        if j==1
            F(j) = alpha(j)/h^2*(2*T(j+1)-2*T(j));
        elseif j==n
            T_n1 = 2*h*h_m/k(n)*(T_g - T(j)) + T(j-1);
            F(j) = alpha(j)*((T_n1-T(j))/(r(j)*h) + (T_n1-
2*T(j)+T(j-1))/h^2);
        else
            F(j) = alpha(j)*((T(j+1)-T(j-1))/(r(j)*h) + (T(j+1)-
2*T(j)+T(j-1))/h^2);
        end
%     end
end

dy=[F;dvel];
```

C.6 Image Analysis for Quantification of Homogeneity

C.6.A Generate Outlines

```
%program to generate a binary image of outlines in metallography
images
[FileName,PathName] = uigetfile('*.jpg','Select greyscale file to
process:')
img=imread(fullfile(PathName,FileName));
%img=imresize(img,.5);
%img = rgb2gray(img);
img=imadjust(img,[0 1],[1 0]);

img_adapthisteq = adapthisteq(img,'NumTiles',[64
64],'clipLimit',0.02,'Distribution','rayleigh','alpha',.6);

figure, imshow(img);
title('Original');
%figure, imshow(img_adapthisteq);
%title('Adapthisteq');

level=graythresh(img);
BW = im2bw(img,level);
%figure, imshow(BW);
%title('BW Original');

lighten=0;
level=graythresh(img_adapthisteq);
BW4 = im2bw(img_adapthisteq,level);
figure, imshow(BW4);
while lighten<3
    BW4 = im2bw(img_adapthisteq,level);
    imshow(BW4);
    title(['Current Binary Conversion ',num2str(level)]);
    lighten=menu('Lighten, darken or accept
image?','Lighten','Darken','Accept');
    if lighten == 1
        level=level+.01;
    elseif lighten == 2
        level=level-.01;
    end
end


%speckchoice = menu('Enter Maximum Speckle Size to
Remove:','400','500','600','700','800','900','1000')
speckchoice=2;
specksize=[200,250,300,500,600,700,1000];
BW10 = bwareaopen(BW4,specksize(speckchoice),4);
figure, imshow(BW10);
title(specksize(speckchoice));

Fname = strtok(FileName,'.')
Ext='.bmp';
```

```
Fnamearea=strcat(Fname,Ext);
imwrite(BW10,Fnamearea,'bmp');

BW10fill = imfill(BW10,'holes');
figure, imshow(BW10fill);
title('BW fill');
Fnamefill=strcat(Fname,'fill',Ext);
imwrite(BW10fill,Fnamefill,'bmp');
```

C.6.B Fill Outlines

```
%program to fill outlines in binary metallography images
[FileName,PathName] = uigetfile('*.bmp','Select binary file to
process:')
img=imread(fullfile(PathName,FileName));
Fname = strtok(FileName,'.')
Ext='.bmp';

figure, imshow(img);
title('BW outline');
imgfill = imfill(img,'holes');
figure, imshow(imgfill);
title('BW fill');
Fnamefill=strcat(Fname,'fill',Ext);
imwrite(imgfill,Fnamefill,'bmp');
```

C.6.C Erode

```
%program to erode filled outlines in binary metallography images
[FileName,PathName] = uigetfile('*.bmp','Select binary file to
process:')
img=imread(fullfile(PathName,FileName));
Fname = strtok(FileName,'.')
Ext='.bmp';

figure, imshow(img);
title('BW outline');

se=strel('disk',1)
imgerod = imerode(img,se);
figure, imshow(imgerod);
title('BW erode1');
Fnameerod=strcat(Fname,'erode1',Ext);
imwrite(imgerod,Fnameerod,'bmp');

se=strel('disk',2)
imgerod = imerode(img,se);
figure, imshow(imgerod);
title('BW erode2');
Fnameerod=strcat(Fname,'erode2',Ext);
imwrite(imgerod,Fnameerod,'bmp');

se=strel('disk',3)
imgerod = imerode(img,se);
```

```
figure, imshow(imgerod);
title('BW erode3');
Fnameerod=strcat(Fname,'erode3',Ext);
imwrite(imgerod,Fnameerod,'bmp');
```

C.6.D Section and count pixels

```
%program to slice and count binary images
[FileName,PathName] = uigetfile('*.bmp','Select binary file to
process:')
img=imread(fullfile(PathName,FileName));
Fname = strtok(FileName,'.')
Ext='.bmp';

vslicenum=20;
hslicenum=4;
imgdim=size(img)
tottung=bwarea(img)/(imgdim(1)*imgdim(2))
sliceht=floor(imgdim(1)/(vslicenum))
slicelen=floor(imgdim(2)/(hslicenum))
x=1;
y=1;
x2=slicelen-1;
y2=sliceht-1;
clear tungsten
for vslicecount=1:vslicenum
    for hslicecount=1:hslicenum
        slice=imcrop(img,[x y x2 y2]);
%        figure, imshow(slice);
%        title(vslicecount);
        tungsten(vslicecount,hslicecount)=bwarea(slice);
        x=x+slicelen;
    end
    y=y+sliceht;
    x=1;
end
tungsten=tungsten/(slicelen*sliceht);
Fnametung=strcat(Fname,'tungstencount.txt');
save (Fnametung, 'tungsten', '-ascii', '-tabs');

x=1;
y=1;
x2=slicelen-1;
y2=sliceht-1;
figure, imshow(img);
Figtitle=strcat(Fname,' Slices');
title(Figtitle);
for vslicecount=1:vslicenum
    for hslicecount=1:hslicenum
        rectangle('Position',[x,y,x2,y2])
        x=x+slicelen;
    end
    y=y+sliceht;
    x=1;
end
```

```
Fnamegrid=strcat(Fname,'grid',Ext);
saveas(gcf,Fnamegrid,'bmp');
```

C.7 Image Analysis for Plasma Arc Intensity

This stand-alone program maps the pixel and grey scale level of the plasma arc image.

```
%program to analyze arc images
[FileName,PathName] = uigetfile('*.bmp','Select plasma picture to
process:')
img=imread(FileName);
Fname = strtok(FileName,'.')
Ext='.bmp';
clrimg=img;
img = rgb2gray(img);

imgdim=size(img)
xcentre=imgdim(2)/2;
ystart=0;
counter=0;
while ystart<40 % loop finds the approximate top of the arc by
intensity
   counter=counter+1;
   ystart=improfile(img,[xcentre-10 xcentre+10],[counter
counter]);
end
counter=counter+6; % lower current y position for better top of
arc position

imgaccept=1;
while (imgaccept==1)
   figure, imshow(img);
   title('Select top of weld and hit Enter');
   line([1 imgdim(2)],[counter counter])
   [botx boty]=getpts;
   boty=boty-3; %move selection up slightly to stay away from
reflections in intensity calcs
   line([1 imgdim(2)],[boty boty])
   imgaccept = menu('Is the top of the weld correctly
selected?','No, Try Again','Yes');
end

% user selects arc length to store in file
figure, imshow(img);
title('Select top and bottom of arc for arc length, and then hit
Enter');
[arcx arcy]=getpts;
arclength(1)=abs(arcy(1)-arcy(2));
line(arcx,arcy)
```

```
sliceht=8; % pixel height of slice to use in image analysis
slicenum=floor((boty-counter)/sliceht)+1;
y=counter; %set starting y value for analysis
arccentre = zeros(slicenum,1);
centreindex = zeros(slicenum,1);
lwid = zeros(slicenum,1);
rwid = zeros(slicenum,1);
lineintensity = zeros(slicenum,1);

for slicecount=1:slicenum
   xline=[1 imgdim(2)];
   yline=[y y];
   arcprofile=improfile(img,xline,yline);%get intensity profile
of current slice
   [arccentre(slicecount),centreindex(slicecount)] =
max(arcprofile); %find most intense point (centre) in current
slice
   % find edges of arc by intensity < 40
   for x=2:imgdim(2)-1
       if (arcprofile(x)>=40) && (arcprofile(x+1)>=40) &&
(x<centreindex(slicecount))
           if (arcprofile(x-1)<40)
               lwid(slicecount)=x;
           end
       end
       if (arcprofile(x)>=40) && (arcprofile(x+1)<40) &&
(x>centreindex(slicecount))
           if (arcprofile(x+2)<40)
               rwid(slicecount)=x;
           end
       end
   end

lineintensity(slicecount)=sum(arcprofile(lwid(slicecount):rwid(sl
icecount))); %total intensity of arc slice
   y=y+sliceht;
end
Fnamearc=strcat(Fname,'arcprofile.txt');
lpos=centreindex-lwid; %distance from centre to left edge of arc
rpos=rwid-centreindex; %distance from centre to right edge of arc
svdata=[arccentre centreindex lpos rpos arclength lineintensity];
save (Fnamearc, 'svdata', '-ascii','-tabs');

% Plot arc slices with detected centres and edges
y=min(arcy)+5;
figure, imshow(clrimg);
Figtitle=strcat(Fname,' Slices');
title(Figtitle);
for slicecount=1:slicenum
    line([1 imgdim(2)],[y y])
    rectangle('Position',[centreindex(slicecount)-1,y-
1,2,2],'Curvature',[1,1],'FaceColor','r')
    rectangle('Position',[lwid(slicecount)-1,y-
1,2,2],'Curvature',[1,1],'FaceColor','b')
    rectangle('Position',[rwid(slicecount)-1,y-
1,2,2],'Curvature',[1,1],'FaceColor','b')
```

```
    y=y+sliceht;
end
Fnamelines=strcat(Fname,'lines',Ext);
saveas(gcf,Fnamelines,'bmp');
```